

Functional roles of the chemokine CCL17 in skin and brain immunity

Dissertation

zur

Erlangung des Doktorgrades (Dr. rer. nat.)

der

Mathematisch-Naturwissenschaftlichen Fakultät

der

Rheinischen Friedrich-Wilhelms-Universität Bonn

vorgelegt von

Lorenz Marc Michael Fülle

aus

Starnberg

Bonn, August 2018

Angefertigt mit Genehmigung der Mathematisch-Naturwissenschaftliche Fakultät
der Rheinischen Friedrich-Wilhelms-Universität Bonn

Erstgutachter: Prof. Dr. Irmgard Förster
Zweitgutachter: Prof. Dr. Waldemar Kolanus

Tag der Promotion: 23.11.2018
Erscheinungsjahr: 2019

Eidesstattliche Erklärung

Hiermit erkläre ich an Eides statt, dass

die vorgelegte Arbeit

– abgesehen von den ausdrücklichen bezeichneten Hilfsmitteln –

persönlich, selbstständig und ohne Benutzung anderer als der angegebenen Hilfsmittel angefertigt wurde,

die aus anderen Quellen direkt oder indirekt übernommenen Daten und Konzepte unter Angabe der Quelle kenntlich gemacht sind,

die vorgelegte Arbeit nicht bereits anderweitig als Dissertation eingereicht worden ist,

ich keine früheren Promotionsversuche unternommen habe,

für die Erstellung der vorgelegten Arbeit keine fremde Hilfe, insbesondere keine entgeltliche Hilfe von Vermittlungs- oder Beratungsdiensten in Anspruch genommen wurde.

Bonn, den _____

Lorenz Marc Michael Fülle

Teile der vorliegenden Dissertationsschrift sind bereits veröffentlicht:

Fülle L*, Steiner N*, Funke M*, Gondorf F*, Pfeiffer F, Siegl J, Opitz FV, Haßel SK, Erazo AB, Schanz O, Stunden HJ, Blank M, Gröber C, Händler K, Beyer M, Weighardt H, Latz E, Schultze JL, Mayer G, and Förster I. *RNA Aptamers Recognizing Murine CCL17 Inhibit T Cell Chemotaxis and Reduce Contact Hypersensitivity In Vivo.* Molecular Therapy doi: 10.1016/j.ymthe.2017.10.005.
*contributed equally

Fülle L, Offermann N, Hansen JN, Breithausen B, Erazo AB, Schanz O, Radau L, Gondorf F, Knöpper K, Alferink J, Zeinab A, Neumann H, Weighardt H, Henneberger C, Halle A, and Förster I. *CCL17 exerts a neuroimmune modulatory function and is expressed in hippocampal neurons.* GLIA (accepted)

Table of contents

<i>Publikationen</i>	<i>I</i>
<i>Zusammenfassung</i>	<i>II</i>
<i>Abstract</i>	<i>IV</i>
<i>List of Abbreviations</i>	<i>VI</i>
<i>Index of Figures</i>	<i>IX</i>
<i>Index of Tables</i>	<i>XI</i>
1. Introduction	1
1.1 The immune system	1
1.2 Immunity in the skin	3
1.2.1 The skin as a barrier organ	3
1.2.2 Inducible skin-associated lymphoid tissue	10
1.3 Allergic contact dermatitis	11
1.3.1 Immunological mechanisms of ACD	11
1.3.2 Mouse model of ACD	13
1.3.3 The role of the chemokine CCL17 in skin allergy	13
1.4 Immunity in the brain	16
1.4.1 Barrier sites in the CNS	16
1.4.2 Microglia - Principal immune cells of the brain	16
1.4.3 Neuronal monitoring of peripheral immune responses	20
1.5 The hippocampus	22
1.5.1 The trisynaptic circuit	23
1.5.2 Chemokines in the hippocampus	24
1.6 Epilepsy	25
1.6.1 Temporal lobe epilepsy	26
2. Aim of the thesis	27
3. Materials	28
3.1 Equipment	28
3.1 Consumables	30
3.2 Chemicals, reagents and recombinant proteins	31
3.3 Solutions and buffers	33

3.4	ELISA Kits	34
3.5	Antibodies	34
3.5.1	Antibodies for flow cytometry	34
3.5.2	Antibodies for Immunohistology	35
3.6	Kits	35
3.7	PCR primer sequences	36
3.8	Software	36
3.9	Enzymes	37
3.10	Mice strains used for experiments	37
3.11	Generation of CCL17/CCL22-double-deficient mice	38
4.	Methods	39
4.1	Histology	39
4.1.1	Immunohistology of murine ears	39
4.1.2	Perfusion and immunohistology of the murine brain	39
4.1.3	Hematoxylin and Eosin staining of brain paraffin sections	40
4.1.4	Morphological analysis of microglia	40
4.2	Intravital microscopy of murine ears	41
4.3	Isolation and flow cytometry of skin immune cells	42
4.4	Isolation and flow cytometry of CNS mononuclear cells	43
4.5	Transwell migration assay	44
4.5.1	DNFB-induced contact hypersensitivity assay	45
4.6	TLR-ligand stimulation	45
4.7	Real Time semi-quantitative PCR (semi-qPCR)	46
4.7.1	RNA isolation	46
4.7.2	Determination of RNA concentration	46
4.7.3	cDNA synthesis and RPS6 PCR	46
4.7.4	semi-qPCR	47
4.8	Generation of primary hippocampal neurons	48
4.9	Electrophysiological recordings of acute brain slices	49
4.10	DT-mediated ablation of CCL17-expressing neurons	50
4.11	EEG recordings	50
4.12	Statistical Analysis	51

5. Results	52
5.1 Analysis of CCL17⁺ cells in murine skin	52
5.1.1 CCL17 ⁺ cells are present in solvent and DNFB-treated murine skin	52
5.1.2 Two behaviorally distinct CCL17 ⁺ cell populations are present in the murine dermis	54
5.1.3 CCL17 is expressed in defined subpopulations of skin-resident myeloid cells	55
5.1.4 Skin-resident monocytes and macrophages harbor substantial numbers of CCL17 ⁺ cells	57
5.1.5 GM-CSF signaling differentially regulates CCL17 expression in skin dendritic cells and macrophages	59
5.1.6 CCL17-deficiency has only moderate effects on skin T cell numbers	62
5.2 Inhibition of CCL17 ameliorates symptoms of contact hypersensitivity <i>in vivo</i>	63
5.2.1 MF11 and MF35 inhibit CCL17-dependent chemotaxis of BW cells	64
5.2.2 CCL17-deficient mice are protected from CHS pathology	65
5.2.3 Aptamer-mediated inhibition of CCL17 reduces symptoms of CHS <i>in vivo</i>	66
5.3 Opposing roles of CCR4 and its two known ligands in the context of contact hypersensitivity	70
5.4 Analysis of immune cell infiltrates after DNFB application	72
5.4.1 Analysis of T cells in ears of CCR4 ^{-/-} , CCL17 ^{E/E} and CCL17 ^{E/E} /22 ^{-/-} mice after DNFB treatment	72
5.4.2 Analysis of myeloid cells in ears of CCR4 ^{-/-} , CCL17 ^{E/E} and CCL17 ^{E/E} /22 ^{-/-} mice after DNFB treatment	74
5.4.3 Analysis of monocyte populations in ears of CCR4 ^{-/-} , CCL17 ^{E/E} and CCL17 ^{E/E} /22 ^{-/-} mice after DNFB treatment	76
5.5 CCL17 is a neuromodulatory chemokine in the CNS	80
5.5.1 CCL17 is expressed in a subset of hippocampal CA1 neurons	80
5.5.2 Systemic inflammation induced by LPS upregulates expression of <i>Ccl17</i> and <i>Ccl22</i> in the brain	82
5.5.3 Weak expression of CCL17 in cortical cells	84
5.5.4 CCL17 is secreted from <i>in vitro</i> cultured hippocampal neurons	86
5.5.5 Local TNF signaling regulates LPS-induced <i>Ccl17</i> expression in the hippocampus	87
5.5.6 Cytokines rather than MyD88 signaling regulate the LPS-induced expression of <i>Ccl22</i> in the hippocampus	91
5.5.7 LPS-induced septic shock is not affected by the loss of CCL17	92
5.5.8 Absence of CCL17 reduces the number of microglia in the brain and affects monocyte activation	93
5.5.9 Hippocampal microglia acquire an altered morphology in the absence of CCL17	97
5.5.10 CCL17 ^{E/E} mice display an increased synaptic transmission at CA3-CA1 Schaffer collaterals	101
5.6 CCL17-DTR mice as a model system for the analysis of inducible neuroinflammation	104
5.6.1 Strong fluctuations of body weight in DT-treated CCL17 ^{DTR/+} mice	104
5.6.2 DT-induced ablation of CCL17 ⁺ neurons takes approximately 14 days	106

5.6.3	Ablation of CCL17 ⁺ neurons causes severe micro- and astrogliosis in the hippocampus	108
5.6.4	DT-treated CCL17 ^{DTR/+} mice develop epileptic seizures after an initial silent phase	111
6.	Discussion	113
6.1	CCL17 in the context of skin immunity	114
6.1.1	Analysis of CCL17-expressing cells in the murine skin	114
6.1.2	GM-CSF regulates CCL17 expression in dDCs and monocytes	118
6.1.3	CCL17 regulates the abundance of dermal $\gamma\delta$ T cells	119
6.1.4	Aptamer-mediated inhibition of CCL17 represents a promising treatment strategy for ACD	120
6.1.5	Opposing roles of CCR4 and its two known ligands CCL17 & CCL22	122
6.1.6	Increased abundance of CCL17-expressing macrophages during CHS	124
6.2	CCL17 in the context of brain immunity	126
6.2.1	CCL17 is expressed in hippocampal CA1 neurons and affects microglia morphology and synaptic transmission	126
6.2.2	Locally produced TNF regulates <i>Ccl17</i> expression in the brain	129
6.2.3	<i>Ccl22</i> is expressed in microglia and regulated by GM-CSF signaling	129
6.2.4	Synaptic transmission is altered in the absence of CCL17	130
6.3	CCL17-DTR mice can be used as a new model for the analysis of temporal lobe epilepsy	132
7.	Acknowledgments	136
8.	References	138

Publikationen

2018

Fülle L, Offermann N, Hansen JN, Breithausen B, Erazo AB, Schanz O, Radau L, Gondorf F, Knöpper K, Alferink J, Zeinab A, Neumann H, Weighardt H, Henneberger C, Halle A, and Förster I. *CCL17 exerts a neuroimmune modulatory function and is expressed in hippocampal neurons*. GLIA (accepted)

2017

Fülle L*, Steiner N*, Funke M*, Gondorf F*, Pfeiffer F, Siegl J, Opitz FV, Haßel SK, Erazo AB, Schanz O, Stunden HJ, Blank M, Gröber C, Händler K, Beyer M, Weighardt H, Latz E, Schultze JL, Mayer G, and Förster I. *RNA Aptamers Recognizing Murine CCL17 Inhibit T Cell Chemotaxis and Reduce Contact Hypersensitivity In Vivo*. Molecular Therapy doi: 10.1016/j.ymthe.2017.10.005.

*contributed equally

2014

Globisch T, Steiner N*, **Fülle L***, Lukacs-Kornek V, Degrandi D, Dresing P, Alferink J, Lang R, Pfeiffer K, Beyer M, Weighardt H, Kurts C, Ulas T, Schultze JL, Förster I. *Cytokine-dependent regulation of dendritic cell differentiation in the splenic microenvironment*. Eur J Immunol doi: 10.1002/eji.201343820

*contributed equally

Zusammenfassung

Die Chemokine CCL17 und CCL22 sind Liganden von CCR4 und werden hauptsächlich von dendritischen Zellen (DCs) und Makrophagen produziert. Für CCL17 wurde gezeigt, dass es verschiedene entzündliche und allergische Erkrankungen fördert. Im Gegensatz dazu, wird CCL22 eher mit einer immunsuppressiven Wirkung assoziiert. Diese gegenläufigen Funktionen spiegeln sich ganz besonders in der Fähigkeit wider, nur bestimmte Immunzellen zu Entzündungsherden zu rekrutieren. Während CCL17 die Chemotaxis von Effektor-T-Zellen induziert und eine Interaktion von T-Zellen und DCs erleichtert, wird CCL22 hauptsächlich mit der Rekrutierung regulatorischer T-Zellen, z.B. in das Tumormikromilieu, in Verbindung gebracht. Im Vergleich zu CCL17 führt CCL22 außerdem zu einer schnelleren Desensibilisierung und Internalisierung von CCR4, was eine gewisse funktionelle Selektivität (engl. biased agonism) von CCL17 und CCL22 für CCR4 impliziert.

In der vorliegenden Arbeit wurden neu generierte CCL17/22-doppelt defiziente Mäuse (CCL17^{E/E}/22^{-/-}) dazu verwendet, die differentielle Funktion von CCL17 und CCL22 weitergehend zu untersuchen. Interessanterweise entwickelten CCL17^{E/E}/22^{-/-} Mäuse genau wie CCL17-defiziente (CCL17^{E/E}) Mäuse eine deutlich reduzierte Kontakthypersensitivitäts-(CHS)-Reaktion im Vergleich zu wildtypischen (WT) Kontrollmäusen, während CCR4^{-/-} Mäuse eine verstärkte allergische Reaktion ausbildeten. Somit konnte gezeigt werden, dass der schon bekannte Unterschied zwischen CCR4^{-/-} und CCL17^{E/E}-Mäusen im CHS Modell nicht durch die in CCL17^{E/E} Mäusen verbleibende Wirkung von CCL22 erklärt werden kann. Darüber hinaus wurden intravitale Mikroskopie (IVM) und Durchflusszytometrie angewandt, um CCL17-positive Zellen in der Haut von CCL17-EGFP Reporter (CCL17^{E/+}) Mäusen in der An- bzw. Abwesenheit von GM-CSF zu charakterisieren. Hier konnte eine GM-CSF-abhängige Expression von CCL17 in DCs der Haut gezeigt werden, wohingegen die Regulation von CCL17 in Makrophagen unabhängig von GM-CSF war. Ferner konnten mittels IVM zwei verschiedene CCL17-positive Zelltypen in der Haut nachgewiesen werden. Neben einer sessilen CCL17-positiven Zellpopulation, welche in der Nähe von dermalen Blutgefäßen lokalisiert war und möglicherweise zu den perivaskulären Makrophagen gehört, wurde eine zweite, durch das Interstitium wandernde CCL17-positive Zellpopulation beobachtet, bei der es sich wahrscheinlich um DCs handelt.

Um neue Möglichkeiten zur Behandlung von Allergien zu entwickeln, wurden zwei neuartige RNA-Aptamere auf ihre Fähigkeit hin getestet, CCL17 *in vitro* und *in vivo* zu neutralisieren. Mithilfe eines Zell-Migrationstests konnte gezeigt werden, dass beide Aptamere die gerichtete Migration der CCR4⁺-Lymphom-Zelllinie BW5147.3 entlang eines CCL17-Gradienten dosisabhängig hemmen. Außerdem konnte in Aptamer-behandelten WT Mäusen eine deutlich reduzierte T-Zell-Infiltration und eine verringerte Ohrschwellung gemessen werden. Des Weiteren konnte in Inhibitionsexperimenten gezeigt werden, dass CCL17 eine vielversprechende Zielstruktur zur Behandlung von allergischen und möglicherweise auch anderen entzündlichen Krankheiten darstellt.

Im zweiten Teil der Arbeit wurde die Expression und Funktion von CCL17 im murinen Gehirn untersucht. CCL17-exprimierende Neuronen konnten vor allem in der hippocampalen CA1 Region identifiziert werden, während im Kortex nur wenige CCL17-produzierende Neuronen nachgewiesen wurden. Systemische Gabe von Lipopolysaccharid (LPS) führte zu einer stark erhöhten Expression von *Ccl17* und *Ccl22* im Hippocampus. Interessanterweise war die LPS-induzierte Expression von *Ccl17* abhängig von lokal produziertem Tumornekrosefaktor (TNF), während GM-CSF die Expression von *Ccl22* regulierte. Eine genaue Untersuchung der Gehirne von LPS-behandelten CCL17^{E/E}- und WT-Mäusen und entsprechenden Kontrolltieren ergab eine stark reduzierte Anzahl von Mikroglia in Hippocampi von CCL17^{E/E} Mäusen. Des Weiteren konnte mittels konfokaler Mikroskopie und einer computergestützten morphologischen Analyse gezeigt werden, dass Mikroglia in naiven CCL17^{E/E} Mäusen, im Vergleich zu WT Mäusen, ein deutlich reduziertes Zellvolumen und einen stärker polarisierten Prozessbaum aufweisen. Außerdem ähnelten die Gesamtverzweigung (engl. ramification), die Zelloberfläche und die Gesamtbaumlänge der Mikroglia von naiven CCL17^{E/E}-Mäusen denen der Mikroglia von LPS-behandelten WT-Mäusen. Des Weiteren wiesen elektrophysiologische Messungen an akuten Gehirnschnitten aus naiven WT- und CCL17^{E/E}-Mäusen darauf hin, dass CCL17 die basale synaptische Übertragung zwischen den Schaffer-Kollateralen der CA3-CA1 Region reprimiert. Damit konnte CCL17 erstmalig als ein neues, homöostatisches und induzierbares neuromodulatorisches Chemokin identifiziert werden, welches sowohl die Häufigkeit und Morphologie von Mikroglia als auch die synaptische Übertragung im Hippocampus beeinflusst.

Abstract

The chemokines CCL17 and CCL22 represent ligands of CCR4 and are mainly produced by dendritic cells (DCs) and macrophages (Mφs) in the immune system. CCL17 was found to promote various inflammatory and allergic diseases, whereas CCL22 has more often been associated with an immunosuppressive environment. These differential functions are reflected by preferential recruitment of distinct subsets of immune cells to sites of inflammation. Whereas CCL17 induces chemotaxis of effector T cells and facilitates T cell-DC interactions, CCL22 appears to be involved in the recruitment of regulatory T cells. In addition, CCL22 induces a more rapid desensitization and internalization of CCR4 than CCL17, implying biased agonism of CCL17 and CCL22.

In this thesis, newly generated CCL17/22-double-deficient ($CCL17^{E/E}/22^{-/-}$) mice were used to further explore the differential function of CCL17 and CCL22. In agreement with previous reports in the literature, CCR4-deficient mice displayed an exaggerated contact hypersensitivity (CHS) response. In contrast, $CCL17^{E/E}/22^{-/-}$ and CCL17-single deficient ($CCL17^{E/E}$) mice were protected from CHS. Thus, the opposing phenotypes of CCR4KO- versus $CCL17^{E/E}$ mice cannot be explained by residual CCL22 signaling in $CCL17^{E/E}$ mice. Furthermore, intravital microscopy (IVM) and flow cytometry were performed to characterize $CCL17^+$ cells in the skin of CCL17-EGFP reporter ($CCL17^{E/+}$) mice in a wild-type (WT) and GM-CSF-deficient background. Whereas expression of CCL17 in skin DCs was GM-CSF-dependent, transcription of CCL17 in skin Mφs occurred independently of GM-CSF. In line, two distinct $CCL17^+$ cell types could be identified in the skin by IVM as judged by their motility: a population of sessile $CCL17^+$ cells in close proximity to dermal blood vessels, presumably representing perivascular Mφs, and a migratory cell population resembling DCs in the interstitium.

To develop novel strategies for treatment of contact allergy, two RNA aptamers were validated *in vitro* and *in vivo* for their capability to neutralize CCL17. The two aptamers effectively inhibited the directed migration of the CCR4⁺ lymphoma line BW5147.3 towards CCL17 in a dose-dependent manner. In the CHS model, systemic application of either one of the aptamers significantly prevented the ear swelling response and reduced T cell infiltration into the ears. These experiments provide proof-of-principle that CCL17-specific aptamers may potentially be used therapeutically in humans to treat allergies and perhaps other inflammatory diseases.

In the second part of the thesis, the expression and function of CCL17 in the murine brain was investigated. $CCL17/EGFP^+$ neurons were primarily detected in a subset of hippocampal CA1 neurons, whereas only few cortical neurons stained positive for CCL17/EGFP. The basal *Ccl17* expression in hippocampal neurons strongly increased by peripheral challenge with lipopolysaccharide (LPS) in a tumor necrosis factor (TNF) dependent manner. In addition, *Ccl22* was also detected in the hippocampus, but its LPS-dependent upregulation required GM-CSF. Analysis of brains from $CCL17^{E/E}$ mice revealed a diminished microglia density in the hippocampus under homeostatic and

inflammatory conditions. A combination of confocal microscopy and computer-assisted morphological analyses demonstrated that microglia from naïve CCL17^{E/E} mice displayed a reduced cellular volume and a more polarized process tree compared to WT controls. Furthermore, overall branching, cell surface area and total tree length of microglia from naïve CCL17^{E/E} mice were similar to that of microglia from LPS-treated WT mice. In addition, electrophysiological recordings of acute slices from naïve WT and CCL17^{E/E} mice indicated a downmodulation of basal synaptic transmission at CA3-CA1 Schaffer collaterals through CCL17. In conclusion, the work presented in this thesis identifies CCL17 as a homeostatic and inducible neuromodulatory chemokine which affects the abundance and morphologic appearance of microglia as well as synaptic transmission in the hippocampus.

List of Abbreviations

ACD	Allergic contact dermatitis
ACKR	Atypical chemokine receptors
AD	Atopic dermatitis
ALD	Alzheimer's disease
AMP	Antimicrobial peptide
APC	Antigen-presenting cell
ARC	Hypothalamic arcuate nucleus
ASD	Autism spectrum disorder
BBB	Blood-brain barrier
BECs	Blood endothelial cells
CA	Cornu Ammonis
CCR	CC chemokine receptor
CD	Cluster of differentiation
cDC	conventional Dendritic cell
CHS	Contact Hypersensitivity
CLA	Cutaneous lymphocyte-associated antigen
CNS	Central nervous system
CSF	Cerebrospinal fluid
CSF-1R	Colony stimulating factor 1 receptor
CTLs	Cytotoxic T leukocytes
CVO	Circumventricular organs
DAMP	Danger-associated molecular pattern
DARC	Duffy Antigen Receptor for Chemokines
DC	Dendritic cell
dDC	dermal Dendritic cell
DETC	Dendritic epidermal T cell
DG	Dentate Gyrus
DNFB	1-Fluor-2,4-dinitrobenzol
DT	Diphtheria toxin
DTR	Diphtheria toxin receptor
EAE	Experimental autoimmune encephalomyelitis
EC	Entorhinal cortex
EEG	Electroencephalography
ELISA	Enzyme-linked Immunosorbent Assay

EMP	Erythro-myeloid progenitor
FLT3L	Fms-related tyrosine kinase ligand
GFAP	Glial fibrillary acidic protein
GM-CSF	Granulocyte-macrophage colony-stimulating factor
GPCR	G Protein-coupled seven transmembrane receptor
HBSS	Hanks' Balanced Salt solution
i.p.	intraperitoneal
IBA-1	ionized calcium-binding adapter molecule 1
IC50	Half maximal inhibitory concentration
IFN	Interferon
Ig	Immunoglobulin
IL	Interleukin
ILC	Innate lymphoid cell
IRF	Interferon regulated factor
iSALT	inducible skin associated lymphoid tissue
IVM	Intravital microscopy
KA	Kainic acid
KC	Keratinocyte
LC	Langerhans cell
LECs	Lymphatic endothelial cells
LN	Lymph node
LPS	Lipopolysaccharide
LTP	Long-term potentiation
M-CSF	Macrophage colony-stimulating factor
MFI	Mean fluorescence intensity
MHCII	Major histocompatibility complex
MMP	Matrix metalloproteinase
MNC	Mononuclear cells
moDC	Monocyte-derived dendritic cell
Mϕ	Macrophage
NAMP	Neurodegenerative-associated molecular pattern
NDD	Neurodegenerative disease
NFκb	Nuclear factor kappa-light-chain-enhancer of activated B cells
NK cell	Natural Killer cell
NO	Nitric oxide

PAMP	Pathogen-associated molecular pattern
PBS	Phosphate-buffered saline
pDC	plasmacytoid Dendritic cell
PRR	Pattern recognition receptor
ROS	Reactive oxygen species
SALT	Skin-associated lymphoid tissue
SE	Status epilepticus
SGZ	Subgranular zone
SRS	Spontaneous recurrent seizures
SVZ	Subventricular zone
TCR	T-cell receptor
TF	Transcription factor
TGF	Transforming growth factor
TLE	Temporal lobe epilepsy
TLR	Toll-like receptor
TNF	Tumor necrosis factor
TNFR	TNF receptor
TRIF	TIR-domain-containing adapter-inducing interferon- β
TSLP	Thymic stromal lymphopietin

Index of Figures

FIGURE 1.1 COMPONENTS OF THE INNATE AND ADAPTIVE IMMUNE RESPONSE. _____	2
FIGURE 1.2 ANATOMY AND CELLULAR COMPONENTS OF MURINE AND HUMAN SKIN. _____	4
FIGURE 1.3 ORIGIN AND SOURCE OF SKIN LCS AND MΦS. _____	6
FIGURE 1.4 MAJOR APC POPULATIONS PRESENT IN THE HEALTHY SKIN. _____	7
FIGURE 1.5 FORMATION OF INDUCIBLE SKIN-ASSOCIATED LYMPHOID TISSUE (iSALT). _____	10
FIGURE 1.6 CELLULAR RESPONSES IN ACD. _____	12
FIGURE 1.7 INNATE AND ADAPTIVE IMMUNE RESPONSES IN THE SKIN. _____	14
FIGURE 1.8 CNS MYELOID CELLS. _____	17
FIGURE 1.9 EMBRYONIC DEVELOPMENT OF MICROGLIA. _____	18
FIGURE 1.10 OVERVIEW OF MICROGLIA FUNCTIONS IN THE CNS. _____	19
FIGURE 1.11 CYTOKINE-COMMUNICATION PATHWAYS OF THE CNS AND THE PERIPHERAL IMMUNE SYSTEM. _____	21
FIGURE 1.12 COMPARISON OF HIPPOCAMPAL ANATOMY IN HUMANS AND MICE. _____	23
FIGURE 1.13 OVERVIEW OF CHEMOKINE FUNCTIONS IN THE MURINE HIPPOCAMPUS. _____	24
FIGURE 4.1 OVERVIEW OF THE ESTABLISHED 2P-IVM SETUP. _____	41
FIGURE 4.2 SCHEMATIC OVERVIEW OF THE CUSTOM-MADE STAGE USED FOR IVM. _____	42
FIGURE 4.3 DNFB APPLICATION ONTO THE SHAVED ABDOMEN OF THE MOUSE. _____	45
FIGURE 4.4 PRIMARY MURINE HIPPOCAMPAL NEURONS. _____	49
FIGURE 4.5 SCHEMATIC OVERVIEW OF THE SETUP USED FOR ELECTROPHYSIOLOGICAL RECORDINGS OF MURINE ACUTE BRAIN SLICES. _____	50
FIGURE 5.1 CCL17 ⁺ CELLS LOCALIZE TO LYMPHATIC AND BLOOD VESSELS IN THE MURINE SKIN. _____	53
FIGURE 5.2 IDENTIFICATION OF DIFFERENT CCL17 ⁺ CELLS IN THE MURINE SKIN. _____	54
FIGURE 5.3 GATING STRATEGY TO IDENTIFY CCL17 ⁺ MYELOID CELL POPULATIONS IN THE MURINE SKIN. _____	56
FIGURE 5.4 CCL17 ⁺ CELLS ARE PRESENT IN SKIN MYELOID CELL POPULATIONS. _____	57
FIGURE 5.5 GATING STRATEGY TO IDENTIFY CCL17 ⁺ SKIN MONOCYTE POPULATIONS. _____	58
FIGURE 5.6 IDENTIFICATION OF CCL17 ⁺ CELLS IN SKIN MONOCYTES AND MACROPHAGES. _____	59
FIGURE 5.7 GM-CSF REGULATES EXPRESSION OF CCL17 IN SKIN MYELOID CELLS. _____	60
FIGURE 5.8 GM-CSF-DEPENDENT REGULATION OF CCL17 EXPRESSION IN SKIN MONOCYTE POPULATIONS. _____	61
FIGURE 5.9 GATING STRATEGY TO IDENTIFY SKIN-RESIDENT T CELL POPULATIONS. _____	62
FIGURE 5.10 LOSS OF CCL17 AFFECTS SKIN-RESIDENT $\gamma\delta$ T CELLS. _____	63
FIGURE 5.11 APTAMERS INHIBIT CCL17-DEPENDENT CELL MIGRATION IN VITRO. _____	65
FIGURE 5.12 CCL17-DEFICIENT MICE ARE PROTECTED FROM CONTACT HYPERSENSITIVITY. _____	66
FIGURE 5.13 MF11.46.M AND MF35.47.M EFFICIENTLY INHIBIT CCL17-DEPENDENT CELL MIGRATION <i>IN VITRO</i> . _____	67
FIGURE 5.14 APTAMER MEDIATED INHIBITION OF CCL17 REDUCES EAR SWELLING AND LEUCOCYTE INFILTRATION. _____	69
FIGURE 5.15 OPPOSING CHS REACTIONS IN CCR4-DEFICIENT AND CCL17/22-DOUBLE-DEFICIENT MICE. _____	71
FIGURE 5.16 QUANTIFICATION OF SKIN T CELL SUBSETS AFTER DNFB TREATMENT. _____	73
FIGURE 5.17 QUANTIFICATION OF SKIN MYELOID CELL SUBSETS AFTER DNFB TREATMENT. _____	75
FIGURE 5.18 PERCENTAGES OF CCL17/EGFP ⁺ CELLS WITHIN SKIN MYELOID POPULATIONS AFTER DNFB TREATMENT. _____	76
FIGURE 5.19 QUANTIFICATION OF SKIN MONOCYTE AND MACROPHAGE SUBSETS AFTER DNFB TREATMENT. _____	77
FIGURE 5.20 PERCENTAGES OF CCL17/EGFP ⁺ CELLS WITHIN SKIN MONOCYTE POPULATIONS AFTER DNFB TREATMENT. _____	79
FIGURE 5.21 IDENTIFICATION OF CCL17 ⁺ CELLS IN THE DISTAL HIPPOCAMPAL CA1 REGION. _____	81

FIGURE 5.22 SYSTEMIC LPS TREATMENT ENHANCES <i>Ccl17</i> AND <i>Ccl22</i> EXPRESSION IN THE HIPPOCAMPUS. _____	83
FIGURE 5.23 SYSTEMIC LPS CHALLENGE ENHANCES <i>Ccl17</i> AND <i>Ccl22</i> EXPRESSION IN THE HIPPOCAMPUS. _____	84
FIGURE 5.24 LOCALIZATION OF CCL17/EGFP ⁺ CELLS IN DIFFERENT REGIONS OF THE MURINE BRAIN. _____	85
FIGURE 5.25 TNF AND LPS TREATMENT OF HIPPOCAMPAL NEURONS INDUCES SECRETION OF CCL17 AND CX ₃ CL1 IN VITRO. _____	87
FIGURE 5.26 INCREASED PRODUCTION OF PRO-INFLAMMATORY CYTOKINES IN THE SERUM AND CNS AFTER SYSTEMIC LPS TREATMENT. _____	88
FIGURE 5.27 DOSE-RESPONSE RELATIONSHIP BETWEEN SYSTEMIC LPS TREATMENT AND HIPPOCAMPAL EXPRESSION OF <i>Tnf</i> , <i>Il-1β</i> , <i>Ccl17</i> AND <i>Ccl22</i> . _____	89
FIGURE 5.28 PERIPHERAL INJECTION OF RMTNF DOES INDUCE <i>Ccl17</i> EXPRESSION IN THE HIPPOCAMPUS. _____	90
FIGURE 5.29 TNFR-DEFICIENCY ABROGATES LPS-INDUCED EXPRESSION OF CCL17 IN THE HIPPOCAMPUS. _____	90
FIGURE 5.30 THE CYTOKINE GM-CSF DIFFERENTIALLY REGULATES <i>Ccl17</i> AND <i>Ccl22</i> EXPRESSION IN THE HIPPOCAMPUS. _____	91
FIGURE 5.31 MYD88-DEPENDENT SIGNALING PATHWAYS DIFFERENTIALLY REGULATE <i>Ccl17</i> AND <i>Ccl22</i> EXPRESSION IN THE HIPPOCAMPUS. _____	92
FIGURE 5.32 LPS-INDUCED SEPTIC SHOCK IS COMPARABLE IN WT AND CCL17-DEFICIENT ANIMALS. _____	93
FIGURE 5.33 GATING STRATEGY FOR IDENTIFICATION OF MICROGLIA AND IMMUNE CELL INFILTRATES IN THE BRAIN. _____	94
FIGURE 5.34 CCL17-DEPENDENT MODULATION OF RESIDENT AND INFLAMMATORY IMMUNE CELLS IN THE BRAIN. _____	95
FIGURE 5.35 QUANTIFICATION OF HIPPOCAMPAL MICROGLIA AND IBA-1 EXPRESSION IN CCL17 ^{+/+} AND CCL17 ^{E/E} MICE. _____	96
FIGURE 5.36 MORPHOLOGICAL ANALYSIS OF HIPPOCAMPAL MICROGLIA IN CCL17 ^{+/+} AND CCL17 ^{E/E} MICE. _____	98
FIGURE 5.37 ALTERED MORPHOLOGY OF MICROGLIA IN CCL17 ^{E/E} MICE. _____	100
FIGURE 5.38 BASAL SYNAPTIC TRANSMISSION IS INCREASED IN CCL17 ^{E/E} MICE UNDER HOMEOSTATIC CONDITIONS. _____	102
FIGURE 5.39 AFTER SYSTEMIC LPS CHALLENGE NEURONAL SIGNALING IS COMPARABLE IN WT AND CCL17 ^{E/E} MICE. _____	103
FIGURE 5.40 FEMALE AND MALE CCL17 ^{DTR/+} MICE SHOW BODY WEIGHT FLUCTUATIONS AFTER DT TREATMENT. _____	105
FIGURE 5.41 NUMBERS OF HIPPOCAMPAL PYRAMIDAL CELLS ARE REDUCED IN CCL17 ^{DTR/+} MICE FOLLOWING LONG-TERM TREATMENT WITH DT. _____	106
FIGURE 5.42 DT TREATMENT INDUCES APOPTOSIS OF HIPPOCAMPAL CCL17 ⁺ NEURONS IN CCL17 ^{DTR/E} MICE. _____	107
FIGURE 5.43 DT TREATMENT INDUCES MICROGLIOSIS IN CCL17 ^{DTR/+} MICE. _____	109
FIGURE 5.44 DT TREATMENT INDUCES ASTROGLIOSIS IN CCL17 ^{DTR/+} MICE. _____	110
FIGURE 5.45 DT-TREATED CCL17 ^{DTR/+} MICE DEVELOP EPILEPTIC SEIZURES AFTER DT TREATMENT. _____	112
FIGURE 6.1 <i>Ccl22</i> EXPRESSION IN DIFFERENT MURINE BRAIN CELL TYPES. _____	130

Index of Tables

TABLE 3-1 EQUIPMENT	28
TABLE 3-2 CONSUMABLES	30
TABLE 3-3 CHEMICALS, REAGENTS AND RECOMBINANT PROTEINS	31
TABLE 3-4 SOLUTIONS AND BUFFERS	33
TABLE 3-5 ELISA KITS	34
TABLE 3-6 FLOW CYTOMETRY ANTIBODIES	34
TABLE 3-7 IMMUNOHISTOLOGY ANTIBODIES	35
TABLE 3-8 KITS	35
TABLE 3-9 PCR PRIMER SEQUENCES	36
TABLE 3-10 SOFTWARE	36
TABLE 3-11 ENZYMES	37
TABLE 3-12 OVERVIEW OF THE USED MICE STRAINS	37
TABLE 4-1 HEMATOXYLIN AND EOSIN STAINING PROTOCOL	40
TABLE 4-2 ANTIBODY STAINING PANELS USED TO CHARACTERIZE IMMUNE CELLS IN THE MURINE SKIN	43
TABLE 4-3 ANTIBODIES USED TO CHARACTERIZES BRAIN LEUKOCYTES	44
TABLE 4-4 RPS6 PCR MASTER MIX AND CYCLER PROGRAM	47
TABLE 4-5 SEMI-QPCR MASTER MIX AND CYCLER PROGRAM	47
TABLE 5-1 OVERVIEW OF THE TESTED TLR LIGANDS	82

For everyone!

"I have no special talents. I am only passionately curious"

Albert Einstein, 1952

"The dark Religions are departed & sweet Science reigns"

From "Vala, or The Four Zoas"

William Blake, 1893

1. Introduction

1.1 The immune system

Immunity is defined as the ability of an organism to cope with potentially harmful substances or disease-causing organisms collectively called pathogens¹.

Besides foreign pathogens, the immune system also constantly eliminates various endogenous threats, such as tumor cells² or autoreactive immune cells¹. The different types of threats commonly possess specific molecular patterns, distinguished by the immune system as pathogen-, danger- or neurodegeneration-associated molecular patterns (PAMPs, DAMPs or NAMPs, respectively)³⁻⁵. A very delicate and complex interplay of immune cells and effector molecules is required to distinguish and eliminate the presented threat⁶. Thus, the immune system has evolved several cooperative strategies that are constantly refined to prepare for a very dynamic and hostile environment⁷. First, a simple avoidance behavior of potentially dangerous substances (e.g., to not eat rotten fruit) is common to many invertebrates and vertebrates and provides a basic opportunity for defense^{8,9}. It is sometimes also referred to as the 'behavioral immune system'¹⁰. Such a behavioral adaptation generally benefits from past experiences of the host and will advance over an organism's life.

Next, anatomical barriers - such as the epithelium lining the skin, the lung or the gut - will provide a first line of defense and protect the host from immediate threats¹. Once these physical barriers are passed, a third, more elaborate system is activated, the innate immune system. Innate immunity represents the evolutionarily conserved arm of the immune system and is found across all species¹¹. It generates rapid, non-specific inflammatory responses and is primarily initiated once anatomical barriers are disrupted. A central element of innate immunity is the immediate production and secretion of immune effector molecules, such as antimicrobial peptides (AMPs), cytokines, chemokines, and reactive oxygen species (ROS). Chemokines are chemotactic cytokines which recruit immune cells to sites of inflammation. Another key element of the innate immune system is the complement system which uses small serum proteins to activate phagocytes, attract other immune cells, or activate the cell-killing membrane attack complex¹. These and other effector molecules are mainly produced by innate immune cells, such as mononuclear phagocytes, neutrophils, innate lymphoid cells (ILCs), natural killer cells (NK cells), or mast cells¹ (see **Fig. 1.1**). Professional phagocytes such as macrophages (Mφs) can directly engulf and degrade microbes. In contrast, NK cells are able to recognize and eliminate virus-infected host cells via a highly specialized set of receptors. Professional antigen-presenting cells (APCs), such as Langerhans cells (LCs) or dendritic cells (DCs) are also phagocytic, but are able to present small pathogen-derived peptide fragments (antigens) via the major histocompatibility complex II (MHCII) on their surface. Once APCs have encountered antigens they will leave their site of residence and migrate to secondary lymphoid organs, such as the spleen or draining lymph nodes (LNs). Here, APCs will present antigens to the cells of the adaptive immune system and

activate the adaptive immune system¹. Innate immune cells are equipped with a set of different pattern recognition receptors (PRRs). These PRRs can recognize specific PAMPs or DAMPs and activate important downstream signaling cascades¹². One of the best-characterized groups of PRRs is the Toll-like receptor (TLRs) family. In humans, eleven different TLR family members have been identified, whereas in mice thirteen TLRs are found¹². Upon binding of their respective ligand, the TLR engages in a distinct intracellular signaling cascade, which originates from a cytoplasmic Toll/IL-1 receptor domain

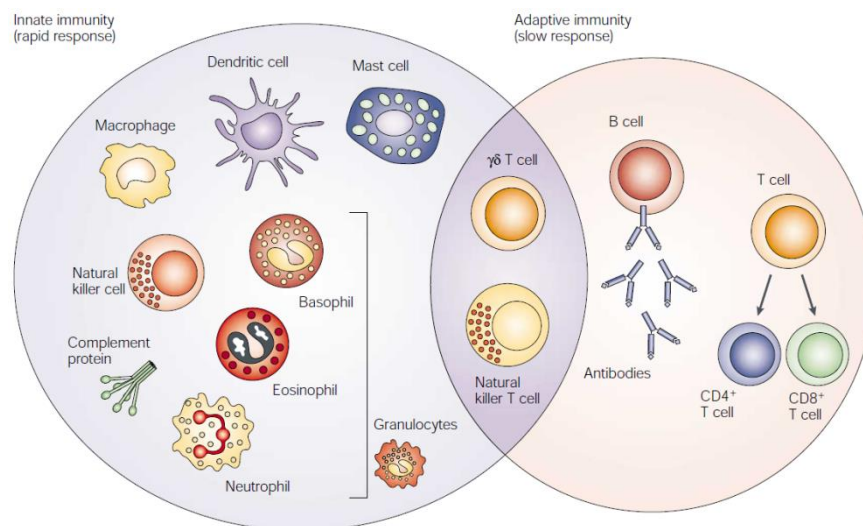


Figure 1.1 | Components of the innate and adaptive immune response.

Innate immunity (left) represents the organism's first line of defense against many environmental threats (e.g. pathogens or toxins). Innate immune cells such as granulocytes (basophils, eosinophils and neutrophils), macrophages, dendritic cells, mast cells and natural killer cells act rapidly either by directly engulfing the pathogen or through the production of soluble immune mediators (cytokines, chemokines etc.). In contrast, adaptive immune responses (right) propagate more slowly, but show a high degree of specificity and eventually result in immunological memory. The two central cell types in adaptive immunity are $CD4^+$ and $CD8^+$ T lymphocytes and B cells. Natural killer T cells and T cells possess both innate and adaptive traits. *Image taken from [2].*

(TIR)¹³. The sub-sequent recruitment of the adaptor protein MyD88 propagates the downstream signaling cascade and activates the transcription factor nuclear factor κ B (NF- κ B) and mitogen-activated protein kinases (MAPKs)¹³. NF- κ B and MAPKs in turn induce the expression of various pro- and anti-inflammatory cytokines¹³. The MyD88-dependent activation of NF κ B is shared among the majority of human and murine TLRs, whereas

TLR3 uses only the MyD88-independent TRIF (TIR-domain-containing adapter-inducing interferon- β) pathway¹³. Interestingly, TLR4 is able to use both pathways. Attributed to the diversity of microorganisms, TLRs are either expressed on the cell surface (e.g. TLR1, TLR2, and TLR4) or are located intracellularly in organelles called endosomes (TLR3, TLR7, and TLR9)^{12,13}. The NLR gene family (nucleotide-binding domain, leucine-rich repeat-containing) also belongs to the PRRs. With the exception of NOD-1 and NOD-2, activation of NLRs results in the assembly of a large multiprotein complex called the inflammasome¹⁴. Inflammasome assembly causes in the activation of caspase-1, which subsequently triggers the release of the pro-inflammatory cytokines interleukin 1 β (IL-1 β) and IL-18¹⁵. For a long time, it was assumed that the innate immune system exists as a purely mechanistic system which triggers similar responses irrespective of previous encounters and that immunological memory represents an exclusive feature of the adaptive immune system. Strikingly, however, in the absence of an adaptive immune system mice are still able to develop increased resistance to

reinfections. Thus, the idea of a trainable innate immune system emerged and opened up possibilities for the development of new therapeutic strategies¹⁶.

As activated APCs present antigens to adaptive immune cells, they link innate and adaptive immune responses. Thus, the efficiency of the adaptive immune system strongly relies on information gained during the innate response. T and B lymphocytes represent the most prevalent immune cell types of the adaptive immune system¹. As the generation of highly specific T and B lymphocytes is central to adaptive immunity, the immune system has developed several mechanisms to select and expand only those lymphocytes which are able to distinguish between host and foreign molecules. During this process, autoreactive cells are either removed or tolerized towards self-antigens¹⁷. The thymus and the bone marrow are the principal organs involved in the generation, selection and maturation of T and B cells, respectively. Following maturation in the thymus, functionally different T cell subsets emerge and divide into either CD4⁺ helper T cells or CD8⁺ cytotoxic T cells¹ (see **Fig. 1.1**). Whereas CD4⁺ helper T cells provide signals to assist in the activation of other immune cells (e.g., B cells or DCs), CD8⁺ cytotoxic T cells eliminate cancer cells and (virus-) infected cells. T cells are characterized by the surface expression of a unique T cell receptor (TCR) which enables them to recognize a specific antigen presented by APCs via MHC molecules. The TCR is generated by random gene rearrangement, a process known as V(D)J-recombination which enables the highest possible diversification of generated TCRs¹. In contrast, B cells are generated in the bone marrow and eventually differentiate into antibody-producing plasma cells¹ (see **Fig. 1.1**). Similar to T cells, B cells rearrange their variable region genes to form a B cell receptor (BCR) which is expressed on the surface but can also be secreted in the form of antibodies. Antibodies are key effector molecules generated during an adaptive immune response and are part of the humoral immune response¹. Antibodies mark pathogens for elimination by phagocytes (opsonization) but can also directly neutralize pathogens¹. Some T and B cells will develop into memory cells which will persist and are quickly re-activated in the case of a second infection with the same pathogen.

1.2 Immunity in the skin

1.2.1 The skin as a barrier organ

The skin represents the organism's primary barrier organ providing a first line of defense against a variety of different challenges¹⁸. Potentially dangerous substances include microbial pathogens, chemical, and physical insults as well as environmental toxins. As depicted in **Fig. 1.2** the skin is organized in several layers which all comprise a highly specialized set of immune and non-immune cells^{19,20}. While substantial differences exist between mouse and human skin, two major compartments of the skin can be distinguished: the epidermis and the dermis (see **Fig. 1.2**). The epidermis is the outermost layer of the skin which is constantly exposed to the environment. Keratinocytes are the most prevalent cell type in the epidermis and exist at different stages of differentiation in each

epidermal layer¹⁸. Keratinocytes produce fibrous structural proteins called keratins¹⁹. Keratins are found in each epidermal layer where they provide the starting material to produce key components of the skin (e.g. hairs or horn).

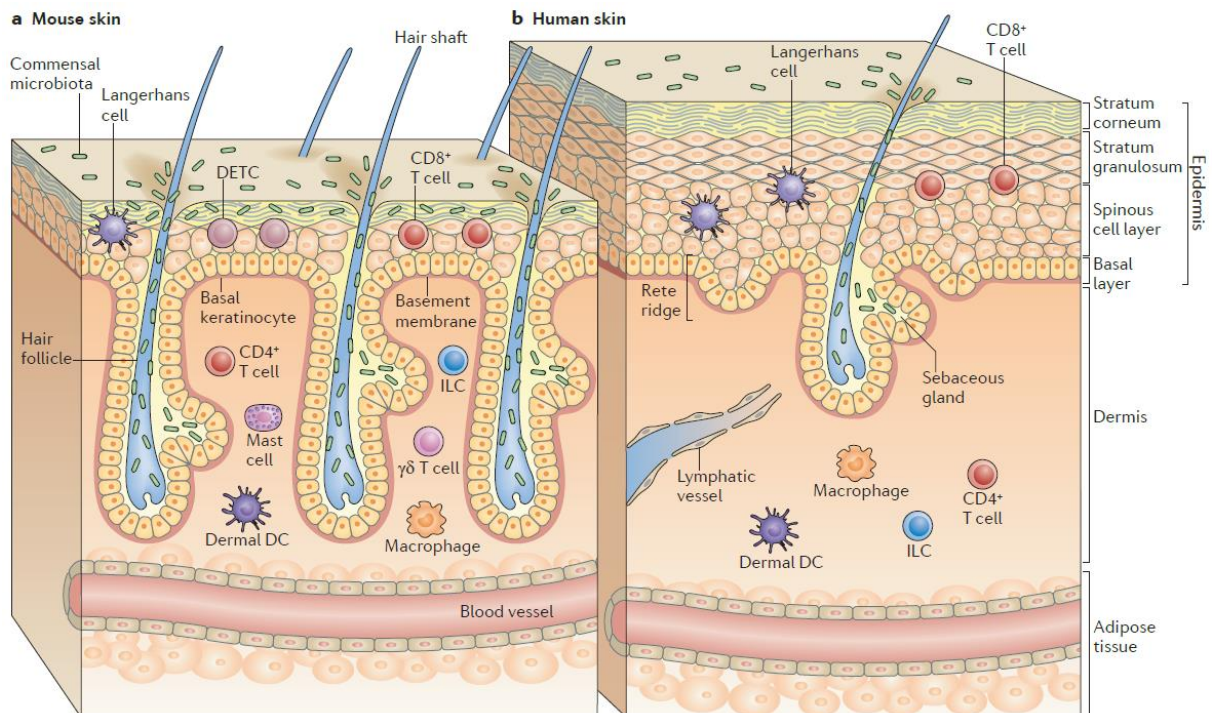


Figure 1.2 | Anatomy and cellular components of murine and human skin.

The side-by-side comparison of murine (a) and human (b) skin reveals some critical differences. Whereas human skin has large areas of interfollicular skin and only few hair follicles, mouse skin contains many densely packed hair follicles. The layered structure of the skin, reflecting its function as a central barrier organ, is comparable in mice and men. However, the human epidermis is much thicker compared to murine skin and is characterized by few downward projections known as epidermal rete ridges. In humans and mice, keratinocytes at different developmental stages make up the majority of epidermal cells. In humans, Langerhans cells and $CD8^+$ T cells are the most prevalent immune cell type in the epidermis, whereas murine skin additionally harbors a prominent population of $V\gamma 5^+$ dendritic epidermal T cells (DETC). The dermis is located beneath the stratum basale and is populated by various dermal DCs, macrophages, mast cells, conventional T cells and few innate lymphoid cells (ILCs). In addition, the dermis is densely traversed by blood and lymphatic vessels, which represent important entry and exit points for immune cells. *Image taken from [20].*

The basement membrane and the stratum basale separate the epidermis from the dermis. The stratum basale consists of only one row of undifferentiated, columnar keratinocytes¹⁹. These basal keratinocytes divide frequently and constantly migrate to the upper layers of the epidermis to mature and differentiate. In humans, the stratum spinosum and granulosum follow the stratum basale and contain more differentiated populations of polygonally shaped keratinocytes¹⁹. In the stratum granulosum, keratinocytes are characterized by the accumulation of lamellar bodies, small secretory organelles that contain various immune effector molecules such as the AMP β -defensin²⁰. In humans and mice, the stratum corneum can be seen as the first-line of defense against many external threats. It is composed of mostly dead keratinocyte-derived cells known as corneocytes¹⁹. Its composition and architecture also prevent significant water-loss¹⁹. Besides keratinocytes, the epidermis also harbors other immune and non-immune cell types. LCs and $CD8^+$ T cells represent the most abundant immune

cell types in the epidermis^{19,20}. The murine epidermis further harbors a unique population of V γ 5⁺ dendritic epidermal T cells (DETCs)¹⁹. Melanocytes are found in human and mouse epidermal layers and are known for their ability to produce the pigment melanin, which is involved in protection against UV-irradiation²⁰.

The dermis represents a distinct compartment of the skin that remains tightly connected to the epidermis by a basement membrane²⁰. The dermis contains several structural components, such as collagen and elastin fibers which form a dense network of rigid and elastic fibers²⁰. Within this network, other dermal components such as hair follicles, sebaceous glands or sweat glands are integrated. In contrast to the epidermis, a far greater diversity of cells is present in the dermis. Fibroblasts for example are known for their capability to produce collagen and elastin¹⁹. The dermis also harbors more specialized immune cell populations, such as distinct populations of dermal DCs (dDCs), dM ϕ s, CD4⁺ T helper cells, $\gamma\delta$ T cells, natural killer T cells, or mast cells^{19,20}. Furthermore, blood and lymphatic vessels ensure a constant supply with O₂ and nutrients and further provide essential entry and exit portals for skin immune cells²¹. In addition, sensory nerve fibers innervate many parts of the skin including the dermis and provide the organism with a sense of touch and temperature²².

The described components render the skin one of the most important organs for the initiation of immune responses. A similar complex network of immune and non-immune cells also protects other barrier organs. From an evolutionary perspective, epithelial surfaces of vertebrates have acquired a central role in host defense as they represent one of the most amenable sites for pathogen entry²⁰.

1.2.1.1 Immune cells of the skin

The skin represents the body's largest interface to the environment and harbors many different types of immune cells all of which participate in maintaining skin integrity (**see Fig. 1.2**). The skin is also heavily colonized by commensal bacteria which are in constant contact with skin cells and thereby also contribute to normal skin function¹.

Langerhans cells. In the epidermis, LCs are among the first cells which come into contact with environmental threats. In homeostasis, LCs are the main resident APCs in the epidermis and make up 3-5% of all epidermal cells²³. Resting LCs possess a branched morphology with extended dendrites that can protrude deep into the stratum corneum to acquire antigens²⁴. LCs are characterized by the expression of high levels of MHCII as well as classical DC and M ϕ markers, such as CD11c and F4/80, respectively²³. In addition, LCs express high levels of CD24 and the epithelial cell adhesion molecule (EpCAM)^{23,25}. Originally, Langerin (CD207) expression was used to unambiguously identify LCs in the skin, however, CD207 expression was also identified on a population of dermal, cross-presenting CD11b⁺XCR1⁺CD103⁺ DCs^{26,27}. LCs are likely to arise from two precursor populations²⁸. During embryogenesis²³, a small population of LCs originates from erythro-myeloid progenitors (EMPs) derived from the yolk sac, whereas the majority of LC precursors comes from the fetal liver²³. It was

demonstrated that LC development, homeostasis, and regeneration rely on signaling through the colony-stimulating factor 1 receptor (CSF-1R)²³. Interestingly, microglia the principal immune cells of the brain also originate from EMPs in the yolk sac in a CSF-1R-dependent manner²⁹. Furthermore, differential functions of the two CSF-1R ligands, CSF-1 and IL-34, were described³⁰. Whereas IL-34 is indispensable for the development and maintenance of LCs and microglia, CSF-1 is required for the repopulation of LCs and microglia following inflammation^{30,31}. In the adult organism, LCs and microglia mostly maintain themselves, but can also be substituted by circulating monocytes and hematopoietic stem cell-derived precursors following inflammation²⁸ (see **Fig. 1.3**). In addition, LCs and microglia are

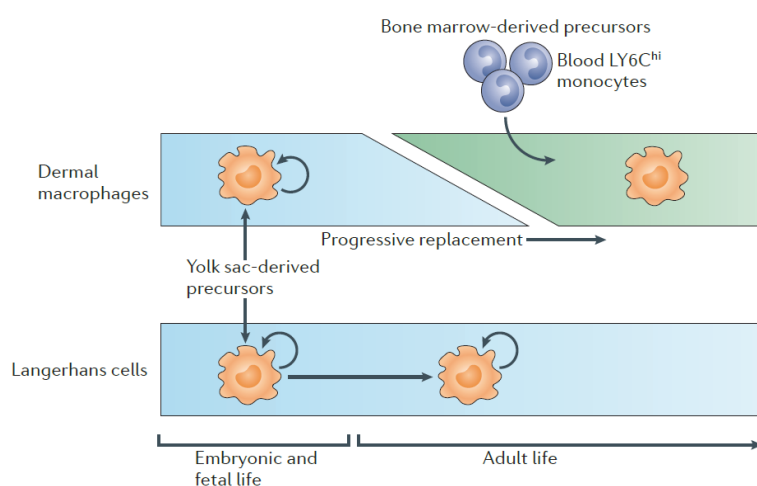


Figure 1.3 | Origin and source of skin LCs and Mφs.

The majority of epidermal LCs and dermal Mφs is established prenatally. (blue panel). However with increasing age of the organism and repeated periods of inflammation, dermal Mφs and to a lesser extent LCs, are replaced by blood Ly6C^{hi} monocytes in a CCR2-dependent manner (green panel). *Image taken from [28].*

both resistant towards ionizing radiation, a feature attributed to the expression of cyclin-dependent kinase inhibitor (CDKN1A) that facilitates the efficient repair of damaged DNA²⁴. LCs were long thought to be instrumental in the progression of allergic skin diseases, such as allergic contact dermatitis (ACD) or psoriasis²⁰. However, the recent analysis of LC-depleted mice revealed conflicting data depending on the model system used or the dose and type of hapten. For example, human Langerin-DTA mice which constitutively lack LCs develop enhanced contact hypersensitivity (CHS) reactions³². In contrast, murine Langerin-diphtheria toxin receptor (DTR) mice which allow ablation of LCs and Langerin⁺ dermal DCs display a diminished CHS response³³. It was further proposed that LCs can induce immune tolerance by inhibiting autoreactive T cells³⁴. In addition, it is of great interest whether tolerogenic and inflammatory LCs are already present in healthy skin or are only generated under inflammatory conditions, as suggested by Seré and colleagues³⁵.

Dermal dendritic cells. DCs were originally identified in the murine spleen by Ralph Steinmann in 1973³⁶ and are primarily derived from hematopoietic stem cells in the bone marrow. In murine skin, the dermis is populated by heterogeneous groups of dermal (dDCs), most of which have equivalent counterparts in other lymphoid and non-lymphoid tissues^{21,24}. In recent years, several DC subsets were identified in the skin and include, among others, type 1 and type 2 conventional DCs (cDC1s & cDC2s), monocyte-DCs (moDCs), plasmacytoid DCs (pDCs) and inflammatory DCs²⁴ (see **Fig. 1.4**). In the murine skin, cDC1s and cDC2s subsets can be generally distinguished by the expression of CD11b. Whereas cDC1s are negative for CD11b, they express the XC-chemokine receptor 1 (XCR1) and

CD207²⁸. Furthermore, they can be separated in a CD103⁺ and CD103⁻ population. CD103⁺ cDC1 represent only a small fraction of dDC, but they are specialized in the cross-presentation of keratinocyte-derived self-antigens to cytotoxic T cells²⁷. In contrast, cDC2 express high levels of CD11b, CD172a, and CX₃CR1²⁴. Besides surface markers, DC subsets can also be identified by expression of distinct transcription factors (TFs) such as Interferon regulated factor 8 (IRF-8) in cDC1 or IRF-4 in cDC2^{24,37}.

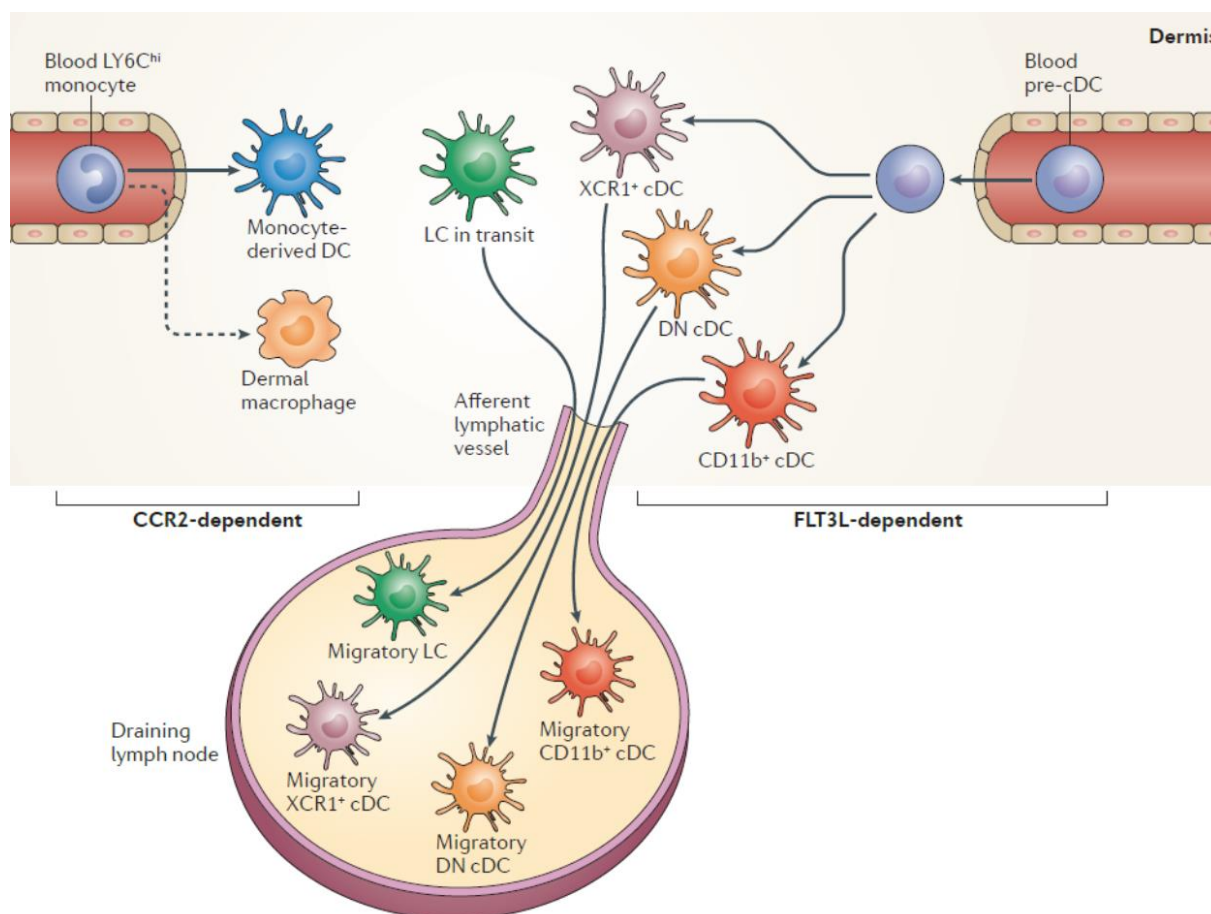


Figure 1.4 | Major APC populations present in the healthy skin.

The dermis is traversed by a dense network of blood and lymphatic vessels which facilitate recruitment of blood-derived cells and allow emigration of dermis-resident cells to skin-draining lymph nodes. CD11b⁺XCR1⁺ cDC1s, CD11b⁺ cDC2s, and double-negative (DN) DCs develop in an Fms-related tyrosine kinase ligand 3 (FLT3L)-dependent manner from blood-derived pre-cDC precursor cells. In contrast, extravasated Ly6C^{hi} CCR2⁺ monocytes develop into dermal monocyte-derived DCs (moDCs) in a CCR2-dependent manner. Dermal macrophages are likely to have a dual origin arising from embryonic progenitors as well as Ly6C^{hi} monocytes²⁸. *Image modified after [28].*

Analysis of DC ontogeny using lineage tracing in mice revealed that commitment to a specific cDC lineage already occurs in the bone marrow³⁸. Here, cDC precursors (pre-cDCs) are genetically imprinted to generate a specific cDC subset in the skin. In contrast to LCs, the development of cDCs depends on Fms-related tyrosine kinase ligand (FLT3L) signaling^{24,39}. In the skin, cDCs have a high turnover rate and approximately 50% of them are replaced by circulating pre-cDCs every seven days²⁸. In contrast, moDCs develop in a CCL2/CCR2-dependent manner and are derived from circulating blood-derived monocytes which enter the skin as Ly6C^{high}, MHCII^{neg} cells, and then gradually loose

Ly6C expression and acquire MHCI²⁴. Whereas the exact identity of moDCs remains controversial, one study demonstrated that mature moDCs possessed a monocytic as well as cDC2-related transcriptomic signature⁴⁰. In line with their genetic relationship to DCs, moDCs are also able to process and present antigens to naïve T cells but are inferior to cDC2s in migrating to skin-draining lymph nodes⁴⁰. In humans, CD14⁺ monocytes resemble murine moDCs to some extent. Whereas substantial numbers of cDCs and moDCs are present in the healthy skin, pDC are only present in the inflamed skin²⁴. Plasmacytoid DCs are known to produce large quantities of IFN- α in response to viral infections. In the skin, however, activated pDCs were implicated in the pathogenesis of systemic lupus erythematosus and psoriasis²⁰.

Dermal macrophages. In the skin, M ϕ s act as important sentinels of the immune system but are also critically involved in maintaining skin homeostasis. In contrast to dDCs, dM ϕ s are long-lived, sessile cells which are superior at phagocytosis but inferior at T cell activation²⁸. Dermal M ϕ s express classical M ϕ markers, such as F4/80, CD11b, and intermediate levels of MHCI but need to be classified with more specific markers, such as CD64, CSF-1R or the proto-oncogene tyrosine-protein kinase MERTK. In general, dM ϕ s do not express CCR2 which sets them apart from monocytes and moDCs^{28,40}. As for all M ϕ populations, development of dM ϕ s requires CSF-1R/CSF-1 signaling²⁸. In mice, dM ϕ s are likely to originate from two distinct precursor populations. Comparable to moDCs, circulating Ly6C^{hi} blood monocytes are a major source of dM ϕ s⁴⁰. However, comparable to other tissue-resident M ϕ s, such as Kupffer cells or microglia, one population of dM ϕ s originates from yolk sac precursors and establishes prenatally²⁸. It has to be noted that over time most dM ϕ s will be of monocytic origin, especially following periods of chronic or frequent inflammation or infection (see **Fig. 1.3**)³⁰. Interestingly, it has been shown that the tissue-resident nature of M ϕ s allows the local microenvironment to shape their epigenetic landscape and consequently refine M ϕ functions^{24,41}. Besides their role in pathogen clearance and tissue repair, dM ϕ s were also shown to be required for the recruitment of neutrophils during skin infection⁴². For example, a population of CD4⁺ dM ϕ s was found to produce chemokines, such as CXCL2 and CXCL10, in close apposition to postcapillary venules to recruit skin-resident and circulating leukocytes^{42,43}.

T cells. The healthy skin contains more than twice as many T cells as the blood, which highlights an important role of T cells in maintaining normal skin function. The skin harbors all major types of conventional (conv) T cells and subsets of unconventional or innate-like T cells. Conventional T cells include all subsets of CD4⁺ helper (TH) and CD8⁺ cytotoxic T cells. They are characterized by the expression of the $\alpha\beta$ T cell receptor ($\alpha\beta$ TCR) which recognizes antigens presented on MHCI or MHCI molecules¹. The majority of conv T cells in the dermis has a memory phenotype and is characterized by high CD44 and CD69 expression and low levels of CD62L⁴⁴. The skin-homing receptor cutaneous lymphocyte-associated antigen (CLA) is expressed on most skin-resident T cells⁴⁴. CLA is an adhesion

molecule that is also found on circulating neutrophils and monocytes. It binds E-selectin on the vascular endothelium and mediates the first step in leukocyte extravasation¹. To facilitate this migration out of the circulatory system, skin-homing CLA⁺ T cells were found to express a set of distinct chemokine receptors, such as CCR4, CCR10, CXCR3 or CCR6⁴⁵. In the inflamed skin, the expression of specific chemokines dictates the recruitment of specific T cell subsets. For example, the chemokines CCL17 and CCL22, both ligands of CCR4, were shown to be induced in the inflamed skin^{46,47} and to mediate the recruitment of CLA⁺CCR4⁺CD4⁺ T_H1, T_H17 and T_H22 cells, as well as CCR4⁺ regulatory T cells⁴⁸. In line, CCL17-deficient mice develop a reduced response in the murine CHS model^{49,50}. In addition, the epidermis harbors a heterogeneous population of tissue-resident CD8⁺ memory T cells that are often found in close proximity to LCs¹⁹. Unconventional or innate-like T cells, such as $\gamma\delta$ T cells or invariant natural killer T cells (iNKT cells) are less frequent in the murine and human skin. In contrast to conv T cells, $\gamma\delta$ T cells are characterized by a distinctive TCR composed of a gamma (γ) and a delta (δ) chain. The antigens that activate $\gamma\delta$ T cells are less well defined, although host-derived lipid antigens were suggested to play an important role in their activation⁴⁴. In humans, $\gamma\delta$ T cells make up only a small proportion of total skin T cells, 2-9% in the dermis and 1-10% in the epidermis¹⁹. In contrast, in the murine epidermis, unconventional V γ 5⁺ DETCs constitute up to 90% of all epidermal T cells¹⁹. DETCs originate from fetal thymic precursors that seed the epidermis during embryonic development⁵¹. Interestingly, DETCs were shown to contribute to local immune surveillance by dampening conv T cell-mediated skin inflammation⁵².

Other skin immune cells. In addition to the cell populations described above, the skin harbors many other types of immune cells, including mast cells, eosinophils, ILCs, or B cells^{19,20}. Mast cells, for example, are activated in responses to allergens and secrete high amounts of pro-inflammatory mediators such as histamines. These mediators are stored in cytoplasmic granules and are released upon binding of allergens, drugs, or IgE antibodies¹. In the skin, B cell-derived antibodies can also directly neutralize pathogens, prevent pathogen binding to epithelial surfaces, opsonize pathogens and antigens, or activate the complement system to initiate direct elimination of the pathogen^{1,20}. Eosinophils represent a minor immune cell population in the healthy skin but are found in high numbers under pathological conditions, especially in parasitic infections²⁰. Innate lymphoid cells (ILCs) represent a heterogeneous group of mucosal lymphocytes that are investigated for their exact roles in skin homeostasis and pathology. In analogy to the different T cell subsets, ILCs are subdivided into three main groups (ILC 1-3) based on their dependence on specific transcription factors and the expression of distinct effector cytokines, such as interferon γ (IFN γ), thymic stromal lymphopoietin (TSLP)/ IL-5 or IL-17/-22, respectively¹⁸. In the skin, ILC2s are the most abundant type of ILC. Furthermore, ILC2 were demonstrated to expand under inflammatory conditions of the skin and to induce a T_H2-dependent immune response⁵³. In contrast, ILC3s were found to be essential for tissue repair in the inflamed skin⁵⁴.

1.2.2 Inducible skin-associated lymphoid tissue

Over the years a growing body of research helped to shed light on the versatile immune responses in the skin under steady state as well as inflammatory conditions. In 1983, Streilein and colleagues proposed the existence of the skin-associated lymphoid tissue (SALT)⁵⁵. The authors recognized for the first time that T cells and DCs both reside in the skin. They further demonstrated that naïve T cells need to be activated in skin-draining LNs before they return to the skin as effector memory T cells. Similar lymphoid structures were also found in specialized submucosal areas, where T and B cells are activated independently of secondary lymphoid organs⁵⁶. The SALT concept reinforced the originally passive barrier function of the skin by a network of different immune cells which help to maintain skin homeostasis and regulate local inflammation. However, the original SALT concept did not consider the complex interactions of immune cells that take place in the skin under pathological conditions like in allergic contact dermatitis (ACD)⁵⁷. Thus, in 2015 Sachiko Ono and Kenji Kabashima proposed that SALT is induced in response to local inflammation of the skin and coined the term inducible SALT or iSALT^{58,59}. Using a murine model of ACD, they found that a sequential activation of different skin-resident immune cells leads to the formation of dense leukocyte clusters around post capillary venules (see **Fig. 1.5**)^{59,60}.

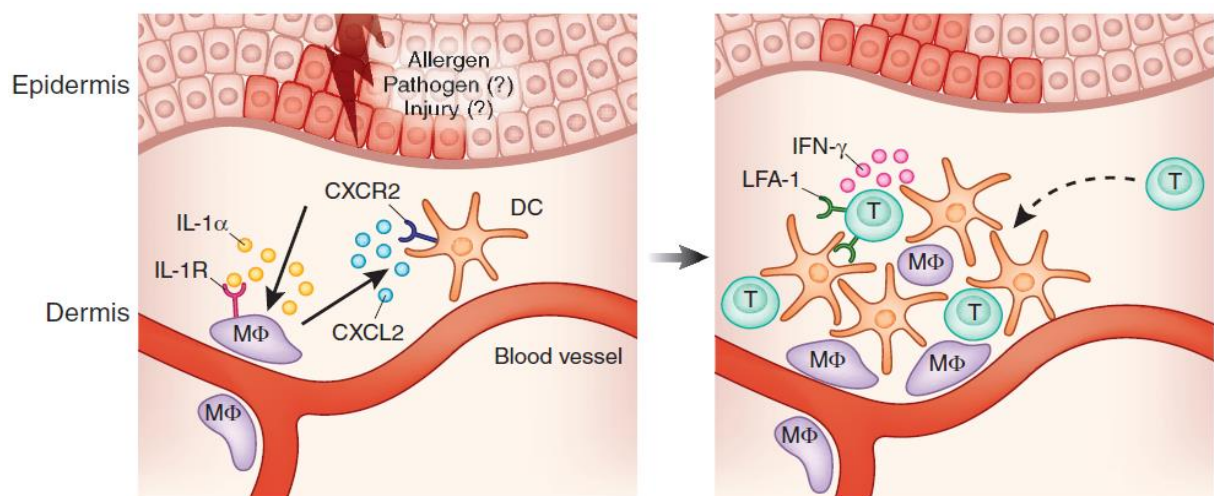


Figure 1.5 | Formation of inducible skin-associated lymphoid tissue (iSALT).

Left: Upon exposure to allergens, and possibly also in response to injury or infection, epidermal keratinocytes produce IL-1 α which activates perivascular M ϕ s to produce increasing amounts of CXCL2. In turn, CXCR2-expressing dermal DCs are recruited towards perivascular M ϕ and form primitive immune cell clusters. Right: Within the cluster, enhanced cell-cell interaction induces the production of further cytokines and chemokines (e.g. IFN γ , CCL17 and CCL22) which will recruit memory and effector T cells to form the terminal (inducible) skin-associated tissue (iSALT). *Image taken from [59].*

Upon exposure to allergens, murine keratinocytes produce the cytokine IL-1 α which in turn activates perivascular M ϕ s to produce the chemokine CXCL2 (C-X-C motif ligand 2). The release of CXCL2 subsequently recruits CXCR2⁺ dDCs to form premature clusters with perivascular M ϕ s (see **Fig. 1.5**). The production of additional cytokines and chemokines, such as CCL17, CCL22 or CCL27 then recruits antigen-specific memory and effector T cells into these clusters^{60,61}. The authors conclude, that iSALT is

necessary to induce local proliferation of T cells and is thus essential for the induction of immune responses⁶². Also, targeting iSALT formation represents a promising strategy to develop new therapies for the treatment of inflammatory skin diseases.

1.3 Allergic contact dermatitis

Allergic reactions of the skin are primarily caused by allergens present in the environment. Repeated exposure to the same environmental allergens can eventually result in mild or severe forms of chronic contact allergies. Contact allergies are a prominent member of ACD. The first indication of ACD is the rapid development of a skin rash at the site of allergen contact. The rash is accompanied by typical symptoms, such as itching, increased sensation of heat, localized swelling, or edema formation^{1,20}. Symptoms related to some form of ACD account for about 20% of all work-related complaints in the U.S. and produce an estimated cost of 400 million US\$ per year⁶³. In addition to the environment, contact allergens are also frequently found in cosmetics, personal care products, biocides, plants, preservatives or jewelry. Due to their small size (<500 Daltons) they can directly penetrate the stratum corneum and react with host proteins in a process called haptization. Thus, most contact allergens belong to the class of haptens which are small, inorganic or organic molecules⁵⁷. To form highly reactive compounds, pre- and pro haptens are oxidized before or after entering the skin, respectively. In contrast, complete haptens can directly react with self-proteins and induce skin inflammation⁵⁷.

1.3.1 Immunological mechanisms of ACD

According to the Gell and Coombs classification, ACD is considered a type IV hypersensitivity reaction being a T cell-mediated inflammatory reaction of the skin⁶⁴. Haptens are not antigenic by themselves but by binding to host proteins; they form highly immunogenic neo-antigens which are recognized by innate immune cells as "altered self"⁵⁷. The development of ACD is broadly separated into two distinct phases. In the sensitization (afferent) phase, epicutaneous exposure to a hapten activates skin innate immunity and results in the priming of hapten-specific effector T cells in skin draining lymph nodes. In the elicitation (efferent) phase, challenging the already sensitized skin with the same hapten induces a rapid recruitment of hapten-specific effector T cells into the skin which then results in clinical manifestations of ACD. In the earliest events of the sensitization phase, hapten-protein complexes induce the local production of reactive oxygen species (ROS) in the skin. This will lead to the release of ATP and the generation of low-molecular-weight hyaluronic acid (lmHA). These molecules activate keratinocytes and induce inflammasome assembly which will subsequently result in the secretion of IL-1 β and IL-18 (see **Fig. 1.6**).

In addition, the release of other immune effector molecules such as histamines and the production of pro-inflammatory cytokines, such as tumor necrosis factor, $\text{IFN}\alpha$ & β , or TSLP, can activate LCs and dDCs to take up hapten-self complexes and transport them to skin-draining LNs⁵⁷. Here, they will induce proliferation and differentiation of antigen-specific T cells which in turn home back to the skin and initiate the efferent phase. Now, repeated contact with the same allergen will activate local antigen-specific memory effector T cells and elicit a severe inflammatory dermatitis, known as ACD.

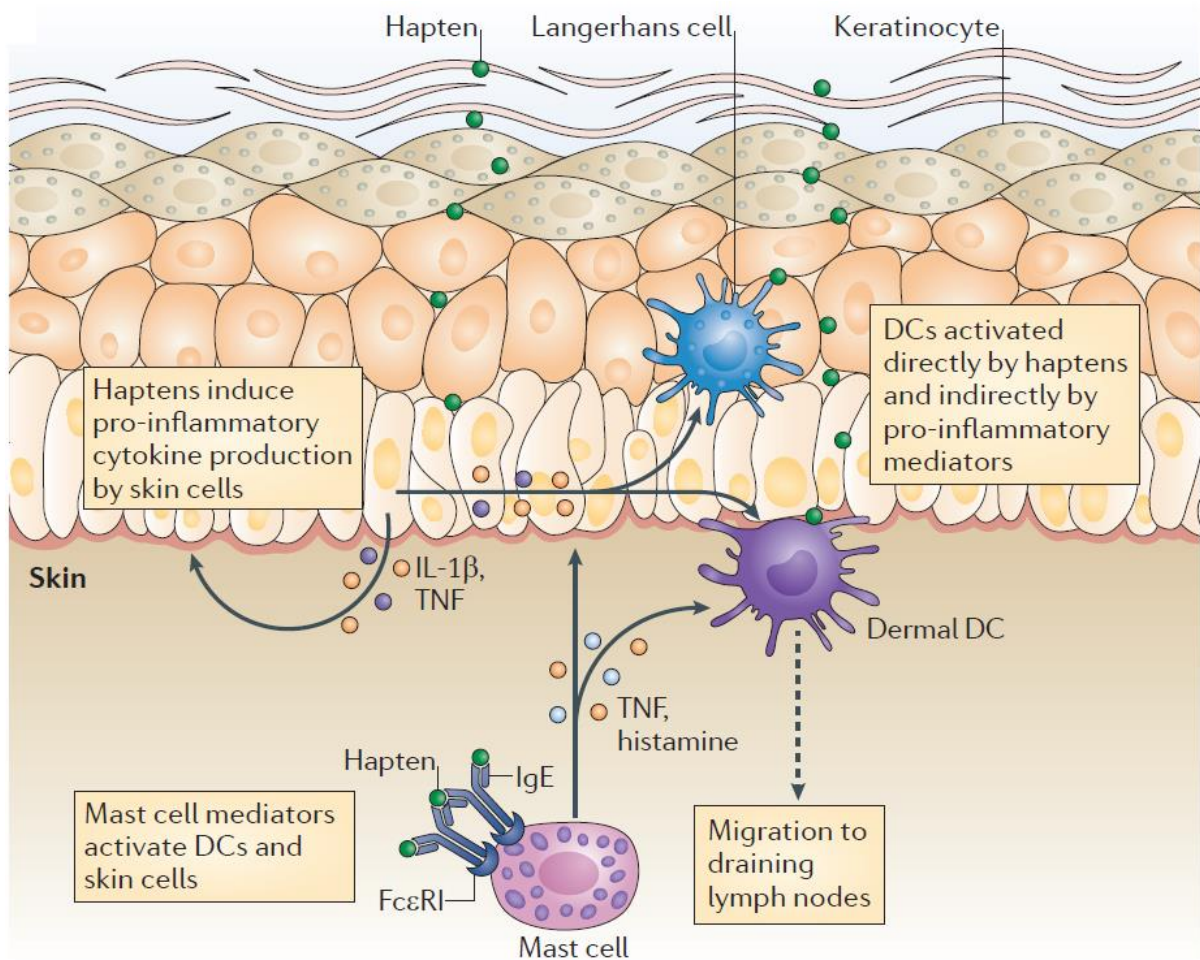


Figure 1.6 | Cellular responses in ACD.

Due to their small size (<500 D) and chemical properties, haptens can directly penetrate the skin. Keratinocytes and mast cells are among the first responding cells which will release a set of pro-inflammatory mediators, such as IL-1 β , TNF or histamine. Professional antigen-presenting cells in the epidermis (LCs) and dermis (dDCs) take up cutaneous antigens and will transport them to skin-draining LNs to present them to and activate antigen-specific effector T cells. *Image taken from [57].*

1.3.2 Mouse model of ACD

Our current knowledge of ACD pathology is mainly derived from animal models in which inflammation is induced by allergen painting on the skin and is referred to as contact hypersensitivity (CHS). In a common model for CHS, the allergen DNFB (1-fluoro-2,4-dinitrobenzene) also called Sanger's reagent is used to induce local inflammation of the murine skin. DNFB is a small lipophilic compound that can directly penetrate the skin⁵⁷. To induce sensitization, DNFB is dissolved in acetone:olive oil (5:1) and applied to the shaved abdominal skin. Following sensitization, which lasts 5-7 days, the animals are challenged with a similar dose of DNFB on the ear (elicitation). The induced ear swelling response can be monitored over three days. As the degree of ear swelling directly correlates with the generated immune effector response, it can be used as a measure to compare transgenic mouse strains or test newly developed drugs. Although substantial differences exist between human ACD and the murine model of CHS, particularly regarding the duration of sensitization, taking much longer in humans, the CHS model is still considered a valuable model for human ACD.

1.3.3 The role of the chemokine CCL17 in skin allergy

Chemokines are small, 8-10 kDa, chemotactic cytokines that regulate leukocyte activation and coordinate their migration under physiological as well as inflammatory conditions. In general, chemokines can be separated in two groups: homeostatic chemokines, which are constitutively expressed, and inducible or inflammatory chemokines⁶⁵. The chemokine superfamily comprises 48 or 40 members in humans and mice, respectively. Based on the specific position of cysteine residues, chemokines are classified into four subtypes: C-C chemokines, C-X-C chemokines, C chemokines and C-X₃-C chemokines. In addition, many chemokines can form homo/heterodimers or oligomers, which adds up to the complexity of chemokine signaling⁶⁶. Recently a chemokine interactome was established describing all homo- and heterophilic chemokine-chemokine interactions⁶⁶. All chemokines interact with one or several of 20 different chemokine receptors, all of which belong to the family of G Protein-coupled seven transmembrane receptors (GPCRs). Chemokines are promiscuous in their interaction with chemokine receptors; as such, one receptor often recognizes several ligands, and one chemokine can often bind to multiple receptors. This promiscuity is most apparent for inflammatory chemokines as homeostatic chemokines appear to be more evolutionary conserved.

The skin harbors a complex network of chemokines which mainly mediate recruitment of leukocytes from the blood (e.g., CXCL10, CCL17 and CCL27)⁶⁷, while also coordinating egress of activated leukocytes via the lymphatics (e.g., CXCL12, CCL21, and CX₃CL1)⁶⁸. A prominent member that was shown to be involved in both processes is the C-C chemokine CCL17, also known as thymus and activation-regulated chemokine or TARC^{49,50,69}. Although CCL17 was initially identified in the thymus⁷⁰; numerous studies have described CCL17 expression in all major barrier organs^{49,71,72} as well as in secondary lymphoid tissues, such as skin-draining LNs or gut-associated lymphoid tissue^{72,73}. In these tissues, cDC2s are the main source of CCL17⁷³. However, alternatively activated Mφs, fibroblasts, and blood endothelial cells were also found to produce CCL17⁷⁴. In the skin, several DC subsets produce high levels of CCL17 after activation (data presented in this thesis). In humans and mice, the designated receptor of CCL17 is CCR4⁷⁵, whereas CCR8 was also found to interact with CCL17 in humans⁷⁶. CCL17 is primarily considered to promote inflammation via the recruitment of immune cells to sites of inflammation. In contrast, CCL22, the second ligand of CCR4, was shown to dampen inflammation by the recruitment of CCR4⁺ regulatory T cells⁷⁷⁻⁷⁹. This might be explained by the fact that CCL17 and CCL22 engage with different binding sites on CCR4 and thus induce differential signaling pathways⁸⁰⁻⁸², a phenomenon referred to as biased agonism⁸³. In addition to regulatory T cells, CCR4 is mainly expressed on T_H1 and T_H2 cells, basophils, and NK cells, whereas some studies also reported

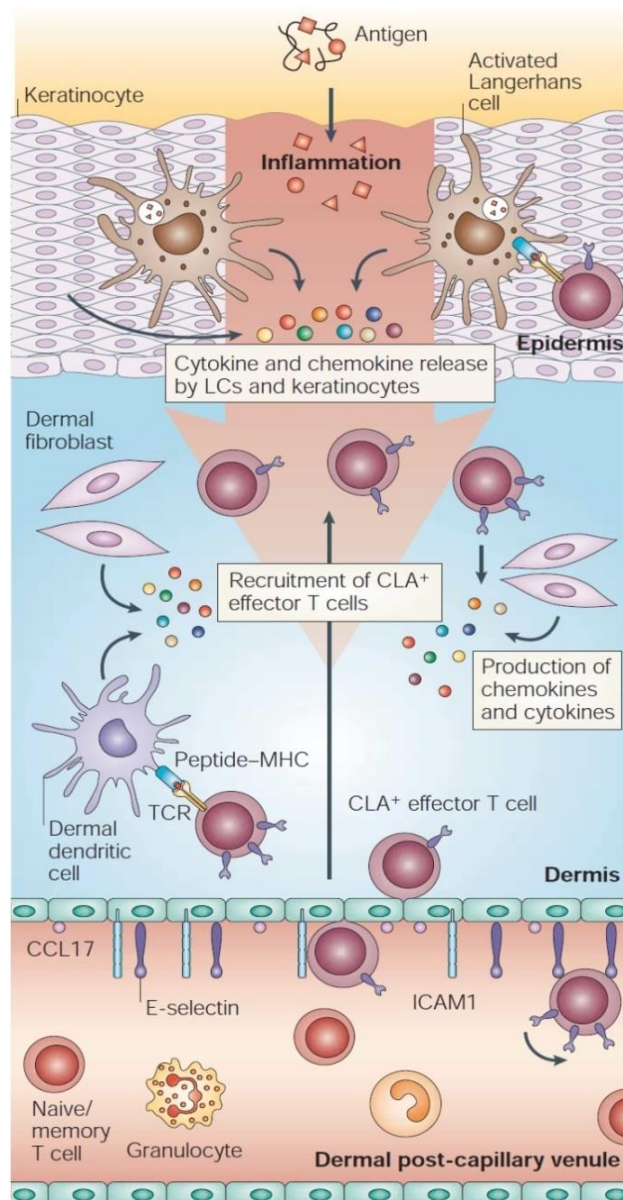


Figure 1.7 | Innate and adaptive immune responses in the skin.

Skin injury activates resident immune and non-immune cells to secrete a multitude of pro- and anti-inflammatory cytokines. Activated LCs and dDCs take up antigens, leave the skin and enter skin-draining lymph nodes to present antigens to naïve and memory T cells. Cytokine production in the skin induces the expression of adhesion molecules, such as E-selectin and ICAM-1, in blood vessel endothelial cells which will result in leukocyte adhesion along the endothelium of dermal post-capillary venules. Chemokines, such as CCL17 or CCL27, direct the extravasation of peripheral immune cells, including neutrophils, eosinophils and T cells. Upon entering the skin, antigen-specific T cells will encounter APCs and start to proliferate further fueling the immune response. ICAM-1, intercellular adhesion molecule 1.

Image modified after [87].

CCR4 expression on DCs, Mφs, and microglia^{84,85}. In the skin, CCL17 was detected on the luminal side of post-capillary venules (see **Fig. 1.7**)^{1,86,87}. Here, CCL17 induces the arrest of skin-homing CLA⁺ T cells that express CCR4 and thereby possibly promotes their extravasation into the dermis^{86,88}. CCL17 was also shown to facilitate DC-T cell interaction⁸⁹ and to promote LC emigration from the skin by enhancing responsiveness to the CCR7 and CXCR4 ligands, CCL21 and CXCL12, respectively⁴⁹. Strikingly, overexpression of CCL17 in the epidermis of transgenic mice induced a more severe T_H2-type associated CHS reaction⁹⁰. In line, the loss of CCL17 was associated with amelioration of skin inflammation in models of CHS^{50,73} and atopic dermatitis (AD)⁴⁹. Intriguingly however, the analysis of CCR4-deficient mice revealed an enhanced inflammatory reaction in a model of oxazolone-induced CHS and no amelioration in DNFB-induced CHS^{48,91}. This might be partially explained by the expression of CCR10 which was also shown to mediate recruitment of skin-homing, CLA⁺ T cells via epidermal expression of CCL27⁶¹. Elevated expression of CCL17 has been generally associated with allergic and inflammatory diseases, including ACD and AD⁶⁹. Interestingly, CCL17 was recently shown to be involved in development of inflammatory pain in a mouse model of collagen- or GM-CSF-induced arthritis⁷⁴, which indicates also non-chemotactic functions of CCL17. Taken together, CCL17 plays pivotal roles in the immune system, in particular in the regulation of barrier organ immunity. Thus, targeting CCL17 represents a promising strategy for the treatment of many inflammatory diseases.

1.4 Immunity in the brain

1.4.1 Barrier sites in the CNS

The original idea of CNS immune privilege is mostly attributed to the blood-brain barrier (BBB) which separates the CNS from the systemic circulatory system. The central function of the BBB is to control the transport of nutrients, signaling molecules, and immune cells into the brain and to further protect the CNS against invading pathogens and toxic substances⁹². The BBB is formed by endothelial cells which are fused together by tight junctions. The endothelium is further shielded by astrocytic endfeet and contractile pericytes which control blood flow within the brain⁹². The BBB has developed sophisticated mechanisms to ensure that brain cells are constantly supplied with nutrients while still preventing the access of pathogens to the brain⁹³. For example, small lipophilic agents can cross endothelial cells using transcellular routes, whereas larger molecules, such as glucose or amino acids, require active transport mechanisms^{92,94}. The protective layers of the BBB are found on most blood vessels in the brain, although some brain regions such as the circumventricular organs (CVOs) lack a functional BBB⁹⁵. CVOs are characterized by an extensive vasculature with highly permeable capillaries that are shielded by an additional layer of glial cells⁹⁵. They are located around the brain ventricles and continuously sample proteins from the plasma and secrete hormones into the bloodstream. In addition to the BBB, two more barrier sites isolate the CNS from the periphery. The blood-cerebrospinal fluid barrier (BCSFB), located at the choroid plexus, and the arachnoid epithelium which forms a barrier between the blood and the cerebrospinal fluid (CSF) of the meninges⁹⁶. In contrast to the BBB, the BCSFB consists of a fenestrated endothelium which allows the direct transport of substances into the CSF. In conclusion, CNS barrier sites not only protect against invading pathogens but also help to maintain homeostasis.

1.4.2 Microglia - Principal immune cells of the brain

Originally discovered at the beginning of the 20th century by Santiago Ramon y Cajal and Pio Del Rio-Hortega, microglia represent the principal immune cells of the brain^{97,98}. Nevertheless, several studies have described the presence of other immune cells in the brain, including DCs⁸⁴, mast cells⁹⁹, and T cells¹⁰⁰. In the healthy CNS, microglia comprise 5-10% of all CNS cells. Microglia are considered the only population of Mφs in the brain parenchyma. However, three other types of Mφs have been identified at the interfaces between the parenchyma and the circulation; perivascular, meningeal and choroid plexus Mφs (see **Fig. 1.8**)^{98,101}. Among these, microglia are the only population that is solely derived from yolk sac erythro-myeloid progenitors (EMPs)^{41,102}.

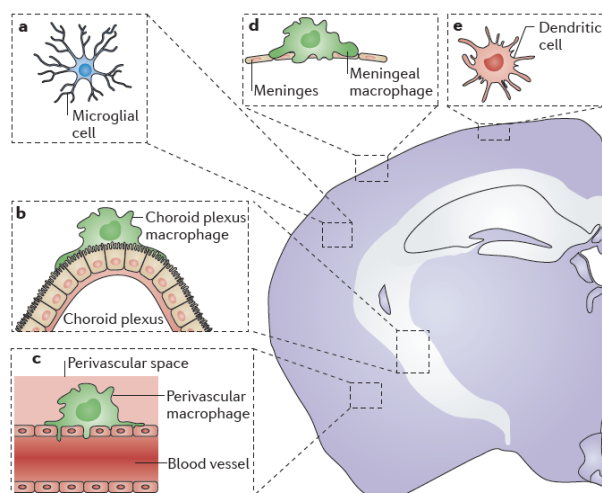


Figure 1.8 | CNS myeloid cells.

a: Under homeostatic conditions microglia are the only immune cells present in the brain parenchyma. b, c, d: Macrophages are located at the outer boundaries of the brain, namely the perivascular space, the meninges and the choroid plexus. In the same locations few blood-derived DCs can be present. *Image taken from Prinz M. & Priller J., Immunity Rev. (2014).*

1.4.2.1 Development of microglia

Much of the knowledge concerning the development of microglia is derived from fate-mapping studies which use fluorescent reporter mouse strains expressing a tissue-specific Cre recombinase fused to the estrogen receptor¹⁰³. By injecting pregnant mice with tamoxifen at distinct time points after ovulation, reporter expression can be switched on at distinct developmental time points. In mice, microglial development starts at approximately embryonic day 7 to E7.5 (E7.0-7.5) (see **Fig. 1.9**)^{103,104}. Here, early yolk sac EMPs start to express the transcription factor RUNX1 (runt-related transcription factor 1) and the receptor tyrosine

kinase c-Kit (CD117). These progenitor cells start to differentiate into yolk sac Mφs by upregulating PU.1 and CSF1R, which are both essential for microglia development and survival¹⁰². Between E8.0 and E9.0, yolk sac Mφs start to express key immune cell and microglia markers, such as CD45 and CX₃CR1, respectively. At E9.0 - 9.5 these early microglia progenitors start to colonize the embryonic brain and continue to do so until the blood-brain barrier (BBB) closes at approximately E13.5⁹⁷. Once inside the brain parenchyma, microglia progenitors will pass through three developmental stages – early microglia (~E10.5), pre-microglia (~E14.5) and adult microglia (P14), each of which is characterized by the expression of distinct surface molecules and a unique transcriptomic signature⁹⁷. A striking feature of adult microglia is their ability to alter their morphology in response to subtle changes in the microenvironment⁹⁷. Strikingly, this dynamic morphological adaptation is already apparent in the embryonic brain. Early microglia are characterized by a round, amoeboid morphology, whereas pre- and adult microglia acquire the typical highly ramified morphology at approximately E14.5 (see **Fig. 1.9**). Microglia continue to proliferate until the end of postnatal week 1 (P7). Subsequently, they slow down their division and acquire a full maturation status at approximately postnatal day 14 (P14)^{97,103,104}.

In the adult brain, neurons and astrocytes produce various growth factors such as transforming growth factor-β (TGF-β) which maintain a homeostatic microenvironment and keep microglia in resting state⁹⁷. Thus, microglia that lack TGF-β receptor signaling adopt a highly activated phenotype and less ramified morphology^{97,105}. In the healthy CNS, microglia are long-lived cells that are capable of self-renewal either by *in situ* proliferation or are derived from local microglia precursor pools¹⁰⁶. It is thought that microglia have a turnover rate of 0.05 cells per hour¹⁰⁵.

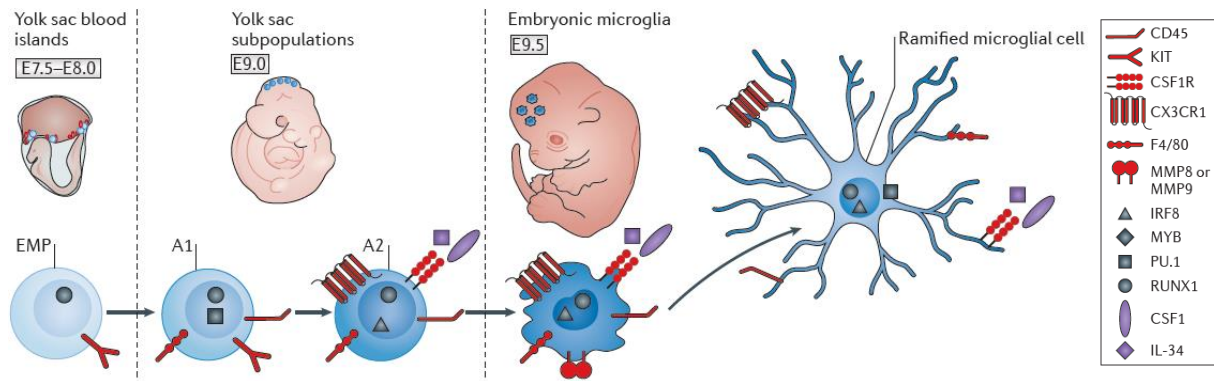


Figure 1.9 | Embryonic development of microglia.

Microglia progenitors develop early during murine embryogenesis. At E7, erythro-myeloid progenitors in the yolk sac start to differentiate into early yolk sac Mφs through the upregulation of specific transcription factors, such as PU.1 and IRF8, and surface markers, such as CD45 and CX₃CR1. From E9.5 onwards yolk sac progenitors start to populate the embryonic brain where they further differentiate into adult microglia and adopt their characteristic ramified morphology. *Image modified after [98].*

1.4.2.2 Microglia functions

In both, the embryonic and adult CNS, microglia form intimate contacts with synapses and astrocytes³¹. In doing so, microglia have been implicated in homeostatic processes, such as the construction of neural circuits or neurogenesis³¹, while also being involved in the degeneration of synapses in neurodevelopmental and neurodegenerative diseases¹⁰⁵. Under homeostatic conditions, microglia function as surveillant immune cells in the brain. They use their fine processes to continuously scan the entire parenchyma every few hours diligently¹⁰⁵. This way they quickly detect small perturbations in the microenvironment. Microglia express several key elements of the complement system, including the complement components C1q and C3 and complement receptors CR3 and CR5^{31,107}. In contrast to the peripheral immune system, microglia have adopted the complement system for a process called 'synaptic pruning'^{107,108}. Here, fragile synapses are tagged with complement components which are then engulfed by microglia. This 'stripping' process shapes synapses and thereby contributes to the formation of functional neural circuits¹⁰⁸. Interestingly, CX₃CR1 was also shown to mediate pruning of CX₃CL1-expressing neurons³¹. Although pruning is most prevalent during embryonic brain development, microglia continue to shape neural circuits in adulthood, particularly in neurogenic regions, such as the subventricular zone (SVZ) and the subgranular zone (SGZ)³¹. At later developmental stages (P1-P14), microglia support neuronal survival through the secretion of several growth factors, such as insulin-like growth factor (IGF) or brain-derived neurotrophic factor (BDNF). Thereby microglia also contribute to learning and memory formation^{107,109}. In the adult animal (>P14), microglia also regulate the proliferation and survival of oligodendrocytes, the myelinating cells of the CNS³¹. Mature microglia preferentially interact with and monitor neurons that show high levels of activity¹⁰⁸. In these neurons, glutamatergic receptor (NMDA)-mediated signaling induces the release of postsynaptic ATP to attract microglial process via the purinergic receptor P2RY12³¹. Whereas this interaction is important to attenuate neuronal activity, its dysregulation was shown to be involved in

the development of neurodevelopmental diseases such as autism spectrum disorder (ASD)¹⁰⁵. Furthermore, microglia-derived mediators, such as cytokines, ROS or nitric oxide (NO), also regulate synaptic plasticity, including long-term potentiation (LTP)³¹.

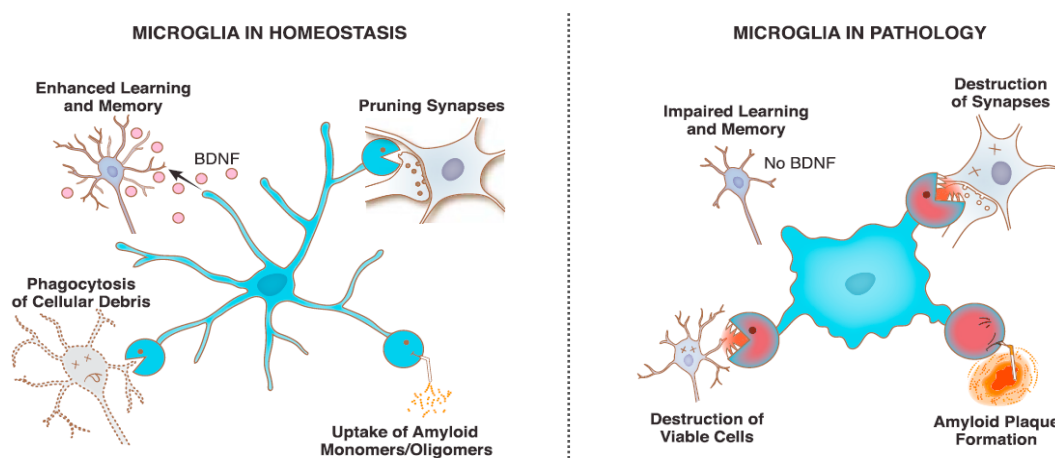


Figure 1.10 | Overview of microglia functions in the CNS.

In the healthy CNS (left), microglia contribute to neuronal health through the secretion of neurotrophic factors (e.g. BDNF). Microglia are also able to prune fragile synapses which is important for embryonic brain development as well as the formation of distinct neural circuits. Furthermore, microglia are highly phagocytic cells which continuously take up senescent cells and slow down the accumulation of protein aggregates such as amyloid- β . Under inflammatory conditions (right), excessive microglia activation results in the degeneration of synapses and a reduced uptake of protein aggregates. Consequently, this promotes the progression of neurodevelopmental diseases and cognitive decline. *Image taken from [101].*

1.4.2.3 Microglia in inflammation and neurodegenerative diseases

As stated earlier, mature microglia acquire a highly ramified morphology representing a 'resting' phenotype associated with brain surveillance³¹. Conversely, activated microglia are characterized by an amoeboid morphology, with larger, rounder cell bodies and shorter, thicker processes. This morphological adaptation is accompanied by an increase in phagocytosis, secretion of pro-inflammatory cytokines, and the expression of a distinct inflammatory transcriptomic signature¹¹⁰. Microglia are for example activated by invading pathogens or by brain tissue damage caused by an ischemic stroke³¹. In addition, microglia are also highly activated in many neurodegenerative diseases (NDD)¹⁰⁷. A hallmark feature of almost all NDD is the progressive accumulation of misfolded endogenous proteins, such as the prion protein PrP^{Sc} in spongiform encephalopathies, amyloid β (A β) in Alzheimer's disease (ALD) or α -synuclein in Parkinson disease¹⁰⁷. In these diseases, aging brain cells accumulate increasing amounts of misfolded proteins, which then start to aggregate and form oligomers and fibrils. These aggregates then deposit as extracellular masses or form intracellular inclusion bodies, both of which will mediate neurotoxicity¹⁰⁷. In the healthy CNS, protein aggregates are readily cleared by microglial phagocytosis, whereas under inflammatory conditions, microglia produce increasing amounts of pro-inflammatory cytokines which promote protein aggregation and amplify neuronal damage¹⁰⁷. Furthermore, it has been reported that peripheral inflammation also influences microglia activation and the progression of NDD¹¹¹⁻¹¹³. Interestingly, the treatment of

systemic inflammation with non-steroidal anti-inflammatory drugs (NSAIDs) is associated with a reduced risk for developing NDD¹¹⁴. Taken together, homeostatic activation of microglia is clearly associated with beneficial responses in the CNS whereas aberrant or excessive microglia activation was shown to contribute to initiation as well as progression of NDDs¹⁰⁷.

1.4.3 Neuronal monitoring of peripheral immune responses

In the brain, a complex interplay of neurons and immune cells is required for the maintenance of homeostasis as well as for the generation of efficient but non-detrimental immune responses. Furthermore, the brain continuously monitors the function of all peripheral organs as well as the immune system. Therefore, the brain has evolved the following mechanisms which enable it to create an exact reflection of the peripheral immune response¹¹⁵⁻¹¹⁹ (see **Fig. 1.11**).

- 1. The humoral pathway.** TLR-expressing Mφs and endothelial cells that reside in CVOs and the choroid plexus respond to circulating pathogens with an increased production of pro-inflammatory cytokines¹⁰¹. As the CVOs bypass the BBB, cytokines can diffuse into the brain parenchyma and activate microglia and neurons to further propagate the signal (see **Fig. 1.11a**).
- 2. The afferent pathway.** Sensory neurons can be activated by local cytokines, such as IL-1β or TNF, produced in response to peripheral infections. Depending on the site of infection, the information is relayed through different primary afferent nerves (see **Fig. 1.11b**). For example, vagal nerves are activated during abdominal or visceral infections, whereas trigeminal nerves respond to orolingual infections¹²⁰.
- 3. Active transport of cytokines across the BBB.** During systemic infections accumulating cytokines are transported across the BBB via saturable transport systems (see **Fig. 1.11c**) and activate local microglia¹¹⁹.
- 4. TLRs and cytokine receptors on brain Mφs and endothelial cells.** Perivascular Mφs and brain endothelial cells express various TLRs and cytokine receptors that respond to circulating, pyrogenic cytokines (see **Fig. 1.11d**)^{119,121}. The activation of this cytokine signaling pathways can for example result in the local production of prostaglandin E2 which is an important regulator of the febrile response¹²⁰.

The overall consequence of this immune-to-brain cross-talk is the increased expression of various pro-inflammatory cytokines and prostaglandins by microglia. The efficient induction of a brain-inflammatory response typically requires two convergent actions; first, rapid activation of sensory neurons at the site of infection which sensitizes target brain regions for the action of cytokines (afferent or neural pathway) and second, the slower propagation of neural cytokine signaling within the brain (humoral pathway). This way, the neural-humoral pathway is able to create a picture of the peripheral immune response that enables the brain to take precise measures of action¹²⁰. For example,

the brain mediates many symptoms of sickness behavior, including fever, fatigue, or loss of appetite. Luckily, however, during most systemic infections the brain is spared from a detrimental immune response which could result in irreversible tissue damage.

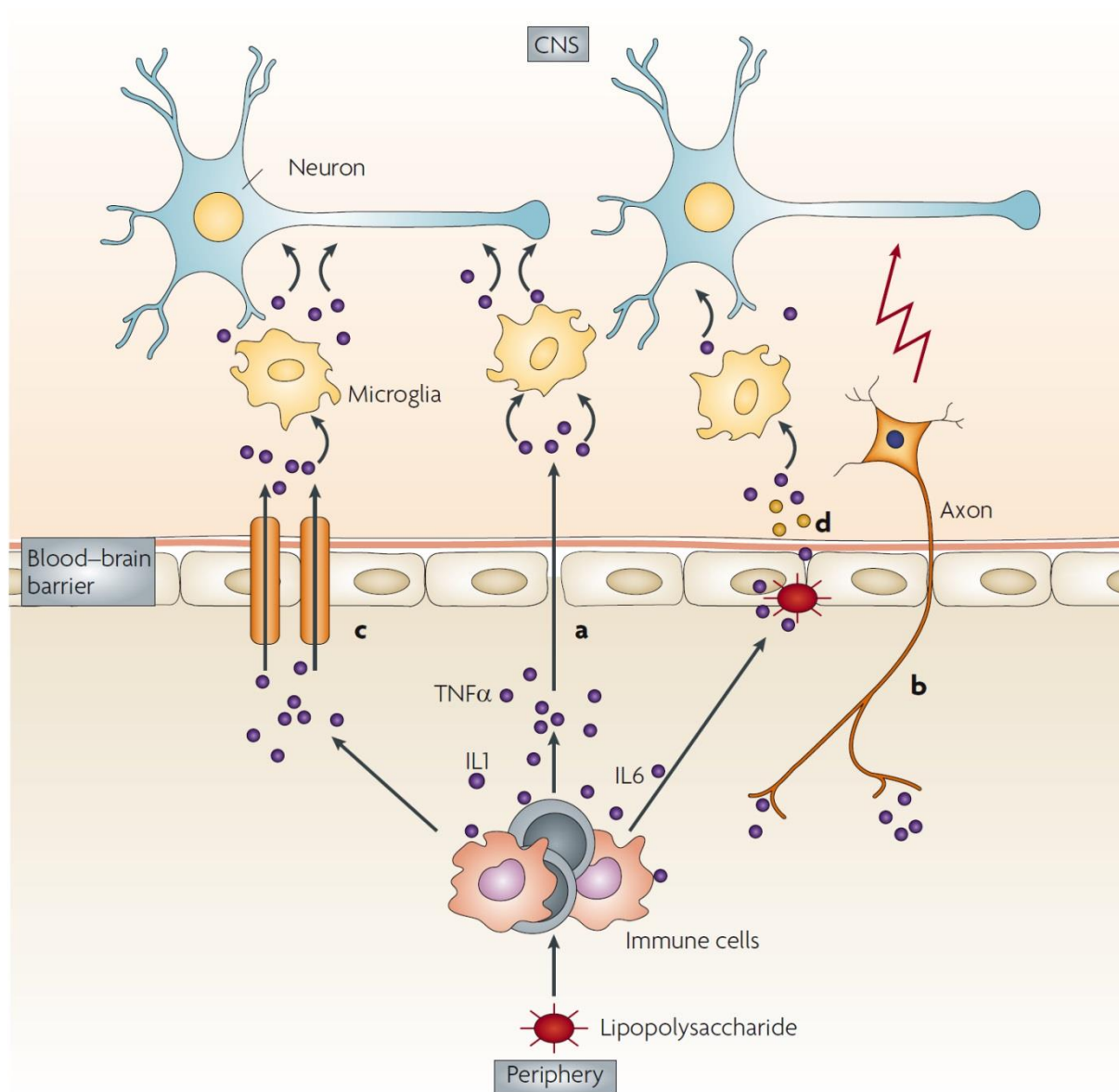


Figure 1.11 | Cytokine-communication pathways of the CNS and the peripheral immune system.

Circulating cytokines represent important signaling molecules facilitating communication of the nervous and immune systems. **a:** At distinct sites in the brain (e.g. CVOs) cytokines can diffuse freely into the brain parenchyma. **b:** Systemic cytokines can directly activate sensory nerve fibers which further propagate the signal across the BBB to activate neurons and brain-resident immune cells. **c:** Some cytokines can be actively transported across the BBB with the help of cytokine transporters. **d:** The expression of distinct cytokine receptors and TLRs allows endothelial cells of the BBB to directly respond to systemically-produced cytokines and pathogens, which will result in an increased production of immune effector molecules. *Image taken from [115].*

1.5 The hippocampus

The hippocampus represents an essential component of the brain of humans and many vertebrates. In most mammals, two hippocampi are found, one in each brain hemisphere^{96,122}. The hippocampus is a medial temporal lobe structure, located under the cerebral cortex. It is a central integral of the limbic system which regulates a variety of functions, including behavior, learning, memory, orientation, emotional state, motivation, and olfaction⁹⁶. The prominent role of the hippocampus in memory formation was initially discovered in patient *H.M.* who suffered severe memory impairments after a bilateral hippocampal resection⁹⁶. These findings resulted in intense studies analyzing the specific role of the hippocampus in the formation of declarative memory which comprises both, episodic and semantic memory⁹⁶. Around the same time, the discovery of hippocampal place cells identified a role for the hippocampus in spatial memory¹²³. As a part of the limbic system, the hippocampus was also demonstrated to mediate emotional memory. The critical involvement of the hippocampus in declarative, spatial and emotional memory resulted in the proposal that different types of memory are wired in distinct intra-hippocampal neural circuits¹²².

Structurally, the hippocampus has a long curved form which runs along a dorsal-to-ventral axis in rodents, corresponding to the posterior-to-anterior axis in humans (see **Fig. 1.12A and B**)¹²². It can roughly be subdivided into three main parts, the dentate gyrus (DG), the hippocampus proper, and the subiculum⁹⁶. Originally, the structure of the hippocampus proper and the DG has been compared to a seahorse and a ram's horn (*Cornu Ammonis*). Its abbreviation CA, is used to distinguish hippocampal subfields in the Ammon's horn (CA1-3). In sagittal brain sections, the hippocampus can be readily identified as an area where the neocortex narrows into a single layer of densely packed pyramidal neurons.

1.5.1 The trisynaptic circuit

The well-defined structure of the hippocampus strongly correlates with the mostly unidirectional flow of information (see **Fig. 1.12B**)^{122,124}. The hippocampus receives significant input from the entorhinal cortex (EC) via the perforant path. The EC is a central part of the parahippocampal gyrus which is reciprocally connected with many cortical and subcortical structures as well as the brainstem. Most axons from the EC project to the granule cell layer in the DG (first synaptic connection). From the DG, information is passed via the mossy fibers to the dendrites of the CA3 pyramidal neurons (second synaptic connection). From there, CA3 axons, called Schaffer collaterals, project to the apical dendrites of cells in the CA1 region whose axons in turn project back to the EC via the subiculum (third synaptic connection). This tripartite unilateral projection system is known as the trisynaptic circuit or loop^{96,122,124}.

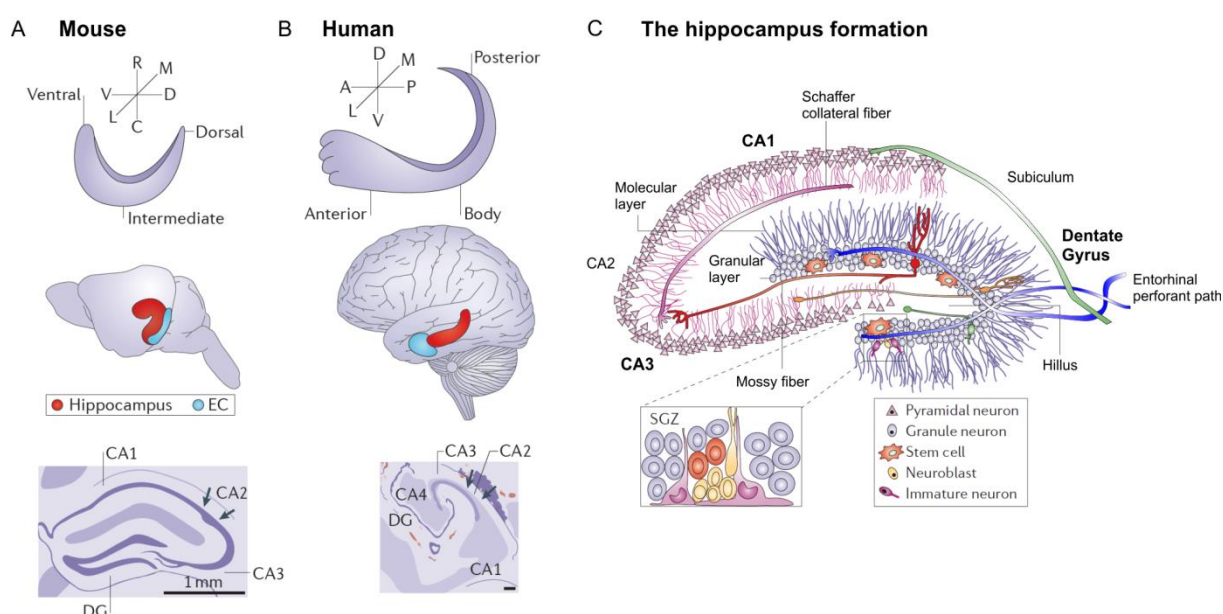


Figure 1.12 | Comparison of hippocampal anatomy in humans and mice.

A, B: Schematic representation of the orientation of the hippocampal longitudinal axis in mice (A) and humans (B). The characteristic long curved form runs along a dorsal-to-ventral axis in mice and a posterior-to-anterior axis in humans. In addition, the exact position of the hippocampus (red) and the entorhinal cortex (EC, blue) in the murine and human brain is depicted. A Nissl cross-section of the murine and human hippocampus proper (CA-CA3) and dentate gyrus (DG) is shown on the lower pictures. **C:** Cellular anatomy of the murine hippocampus. The subgranular zone (SGZ) represents one of only two neurogenic regions in the adult brain. In addition, the well-defined structure is representative of a unidirectional flow of information. The hippocampus initially receives input from the EC via the perforant path connecting to granule cells of the DG. Mossy fibers connect to dendrites of CA3 pyramidal neurons, which in turn project via the Schaffer collaterals to cells of the CA1 region. From here, synaptic information flows back to the EC via the subiculum. *Image modified after [122] (A, B) and [124] (C).*

1.5.2 Chemokines in the hippocampus

There is now a well-established link between environmental stress and hippocampal dysfunction^{120,125-127}. In recent years, several immune effector molecules were found to be essential for healthy brain development and maintenance of homeostasis in the CNS^{119,120}. In particular, cytokines and chemokines were demonstrated to be required for the guidance of synaptogenesis, synaptic pruning, and migration of neurons^{126,128}. In the brain, chemokines and cytokines are mainly produced by microglia and astrocytes and to a lesser extent by neurons, oligodendrocytes and brain endothelial cells^{128,129}. In addition, perivascular Mφs were demonstrated to be a pivotal source of cytokines and chemokines during systemic inflammation⁹⁷. In contrast to other brain regions, the hippocampus

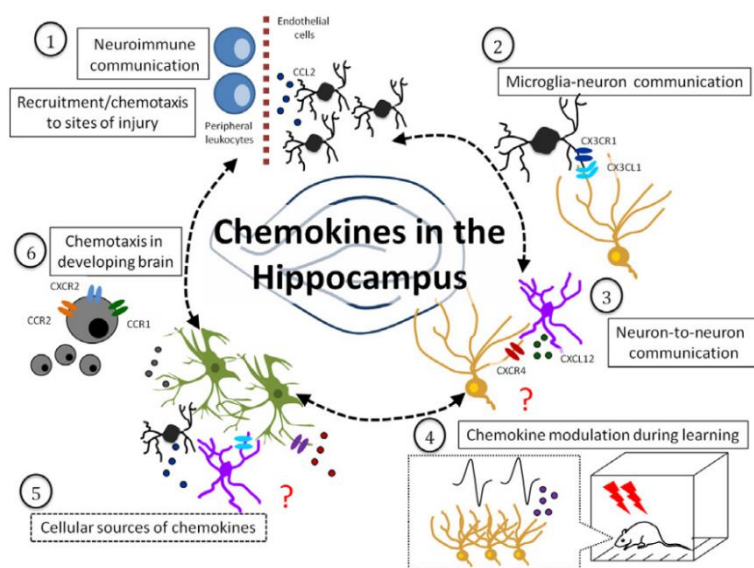


Figure 1.13 | Overview of chemokine functions in the murine hippocampus.

Image taken from [126].

possesses a remarkable plasticity and recapitulates neuronal development well into adulthood¹²⁶. This plasticity combined with the high vascularization render the hippocampus particularly sensitive to perturbations from the environment¹²⁶. For example, the increased production of peripheral cytokines in response to infectious stimuli will rapidly induce changes in hippocampal signaling and the production of cytokines, such as IL-1 β , IL-6 or TNF. In contrast to cytokines, chemokine function in the brain is less well defined. Similar to chemokine function in the periphery, chemokines in the nervous system were also demonstrated to regulate homeostatic as well as neuroinflammatory processes, such as directing chemotaxis of neurons in the embryonic brain, recruitment of peripheral immune cells or facilitating microglia-neuron and neuron-neuron communication (see **Fig. 1.13**)¹²⁶.

Neurogenesis. During embryonic development, neural progenitor cells were shown to express several chemokine receptors, including CCR1, CCR2, CCR5, CCR6, CXCR2, CXCR3, CXCR4, and CX3CR1^{129,130}. In particular, CXCR4 and its ligand CXCL12 were found to play pivotal roles in the migration of CXCR4⁺ granule-neuron progenitor cells in the DG¹³¹. In line, the loss of CXCR4 or CXCL12 in mice led to profound alterations in cerebellar and hippocampal development. In vitro, CXCL12 can directly act as a neurotransmitter and regulate axon guidance, outgrowth, and branching¹³².

Neuronal survival. Chemokines in the brain were also shown to mediate protection against various neurotoxic agents, such as gp120- or amyloid- β -peptide aggregates^{128,133}. So far, CCL5, CCL22, CX₃CL1, and CXCL12 were demonstrated to protect hippocampal neurons from neurotoxicity and apoptosis¹²⁹. Interestingly, a chemokine-dependent induction of matrix metalloproteinases (MMPs) in the CNS is suspected to mediate these neuroprotective effects. MMPs mediate processing of chemokines at the N-terminus and generate various truncated versions of the chemokine. These truncated chemokines could potentially exert opposite effects compared to the full-length protein. For example, a truncated version of CXCL12 (aa5-67) was found to be neurotoxic¹³⁴. Furthermore, N-terminal processing can also inactivate chemokines, as demonstrated for CCL22¹³⁵.

Neuromodulation. Whether chemokines belong to the group of neurotransmitters or neuromodulators is a question related to the physiological effects of both groups. Neurotransmitters propagate neuronal signaling under basal as well as activity-dependent conditions, whereas, neuromodulators have no effect on basal signaling but affect neuronal activity only under certain circumstances¹²⁹. A direct neuromodulatory function of chemokines would require the expression of chemokine receptors at pre- or post-synaptic sites. However, chemokine receptors were only identified at non-synaptic sites^{128,129}. Nonetheless, CXCR4/CXCL12 signaling was shown to suppress depolarization-induced release of dopamine from cultured rat neurons¹²⁹, suggesting a direct neuromodulatory effect of CXCL12. In line, CXCL12 had no effect on the basal neural activity. In addition, several chemokines, including CCL5, CCL22, CXCL12, and CX₃CL1, were also shown to modulate the frequency of spontaneous glutamatergic excitatory postsynaptic currents in cultured hippocampal neurons from rats¹³⁴. The same neurons were also demonstrated to express the receptors necessary to mediate such chemokine-induced neuromodulation (CCR5, CCR4, CXCR4, and CX3CR1, respectively)¹³³. These examples indicate that chemokines in the brain likely represent a new class of modulatory neuropeptides.

1.6 Epilepsy

Epilepsy is a chronic neurological condition of the brain which affects approximately 0.5% of people worldwide^{136,137}. Epileptic patients experience a temporary disruption of normal brain activity, caused by an excessive neural activity in various brain regions. Depending on the brain region, epilepsy can cause multiple symptoms, including loss of consciousness, loss of speech or uncontrollable motor behavior. In the healthy brain, neurons continuously generate action potentials only at distinct time-points. In epilepsy, groups of neurons all fire at the same time leading to the generation of spontaneous recurrent seizures (SRS)¹³⁶. The brain region where the SRS originates is called the epileptogenic focus. The underlying causes for the generation of SRS are mild or severe structural abnormalities in the epileptogenic focus which might be due to genetic factors, infection, head injury, stroke or brain cancer. Based on the underlying cause, different forms of epilepsy are

distinguished^{136,137}. Whereas idiopathic epilepsy is caused by genetic factors, symptomatic epilepsy is caused by a known factor such as stroke. Similarly, different types of SRS are distinctive for a certain form of epilepsy¹³⁷. Whereas partial seizures begin in a localized brain region, generalized seizures affect a widespread area of the cortex. Among generalized seizures, six different types can be distinguished, *absence*, *myoclonic*, *tonic*, *clonic*, *tonic-clonic*, and *atonic* seizures. The most common forms of SRS are *tonic-clonic* seizures, also known as *grand mal*⁹⁶. Tonic-clonic seizures start with sudden stiffening body movements (tonic phase) characterized by the loss of orofacial motor control (tongue biting) and are followed by the typical rhythmic body movements (clonic phase). Over time, epileptic patients may experience prolonged or successive appearance of SRS with no or longer recovery times. This is commonly described as *status epilepticus* (SE) and represents the terminal state of the disease. Although, patients are commonly treated with antiepileptic drugs, only about two-thirds respond to the treatment¹³⁶. Therefore, surgical options, such as the removal or resection of the epileptogenic tissue are often considered the last option in amelioration of the disease.

1.6.1 Temporal lobe epilepsy

One of the most frequent forms of epilepsy is temporal lobe epilepsy (TLE)¹³⁷. TLE is characterized by spontaneous, recurrent, focal seizures that originate in the temporal lobe and further spread to neighboring cortices. It is accompanied by a significant loss of hippocampal neurons and the stepwise development of a chronic gliosis. Comprehension of the underlying pathways and mechanisms that lead to the generation of epileptic seizures are difficult to study in human patients¹³⁸. Thus, our current knowledge is mostly derived from rodent animal models. In rodents, TLE can be induced with the help of neurochemical agents, such as kainic acid (KA) or pilocarpine, optogenetic or electrical stimulation, traumatic injuries, and thermal or hypoxic insults¹³⁸. In addition, the introduction of specific mutations in laboratory mice leads to the spontaneous development of idiopathic or audiogenic-induced seizures¹³⁸. One of the most frequently used models is the kainic acid-induced status epilepticus (KA-SE)¹³⁸. Here, mice receive systemic or intrahippocampal injections of KA to progressively induce limbic SE and the development of chronic seizures¹³⁹. The KA-SE model is often used in the analysis of TLE with hippocampal sclerosis. However, the model presents some critical limitations. For example, a high mortality rate, the incomparability of SRS generation in different animals, and the generally strong neurotoxicity of KA could lead to wrong conclusions concerning the underlying mechanisms of epileptogenesis. Thus, epileptic research strongly depends on the continuous development of new animal models which are less invasive and provide a better approach to study the underlying mechanisms of seizure generation¹³⁸.

2. Aim of the thesis

The chemokines CCL17 and CCL22 represent well-known biomarkers for the diagnosis of atopic diseases. CCL17 has been extensively studied for its role in various allergic and inflammatory diseases, such as atherosclerosis, inflammatory bowel disease, and arthritis. In contrast, CCL22 has more often been associated with an immunosuppressive environment. In mice, both chemokines were shown to interact with the chemokine receptor CCR4 which is expressed on various immune cells, including effector memory T cells and regulatory T cells. In the immune system, CCL17 is probably best-known to attract effector T cells to sites of inflammation⁷⁵, but was also found to facilitate T cell-DC interactions⁸⁹, or to sensitize DCs for CCR7- and CXCR4-dependent migration⁴⁹. Considering the prominent role of CCL17 for leukocyte recruitment its blockade represents a valuable approach for the treatment of various inflammatory diseases.

In previous studies, we demonstrated that CCL17 is expressed in distinct DC subsets of all major barrier organs. Furthermore, CCL17-deficient mice are protected in mouse models of inflammatory skin diseases, such as AD or CHS. In light of these results, we recently developed two highly efficient RNA aptamers with specificity for murine CCL17. Hence, the first aim of this thesis was to further characterize the distinct subsets of CCL17-expressing cells in the murine skin and to validate the two novel RNA aptamers for their capability to neutralize CCL17 *in vitro* and *in vivo*. In addition, others previously demonstrated that CCL22 induces a more rapid desensitization and internalization of CCR4 compared to CCL17⁸⁰⁻⁸² which implies biased agonism of CCL17 and CCL22 for CCR4. In addition, it was shown that CCR4-deficient mice display an exaggerated inflammation of the skin^{91,140} after challenge with a contact sensitizer, whereas CCL17-deficient mice showed amelioration of CHS responses compared to control mice. These results suggested a possible inhibitory role for CCL22 in CCL17-deficient mice. Thus, in the present thesis our recently generated CCL17/22-double-deficient mice should be analyzed in the CHS model and compared to CCR4-deficient and CCL17-deficient mice.

Aside from its expression in immune cells, we also previously detected CCL17 expression in a subset of hippocampal neurons in the murine brain. This expression could be further enhanced upon systemic application of LPS (Bachelor theses, *L. Radau, 2014* and *N. Offermann, 2015*). Furthermore, CCL17 and CCR4 had been previously implicated in the development of experimental autoimmune encephalomyelitis^{84,85}. Thus, in the second part of the thesis the regulatory pathways underlying CCL17 expression and its functional relevance in the murine brain should be investigated.

Taken together, this thesis aimed at providing a more comprehensive insight into the functional roles of CCL17 during regulation of cutaneous immune responses and its impact on neuroimmune cross-talk in the brain.

3. Materials

3.1 Equipment

Table 3-1 | Equipment

Equipment	Article/ Company
Automatic tissue processor	Leica TP1020 (Leica Microsystems, Wetzlar, Germany)
Balances	440-35A (Kern & Sohn, Balingen, Germany) ABJ-NM (Kern & Sohn, Balingen, Germany) EW-N (Kern & Sohn, Balingen, Germany)
Cell counting chamber	Neubauer improved (La Fontaine via Labotec, Göttingen, Germany)
Centrifuges	MicroStar17 (VWR, Wayne, USA), 5415R (Eppendorf, Hamburg, Germany) 5424R (Eppendorf, Hamburg, Germany) 5810R (Eppendorf, Hamburg, Germany) Allegra X-15R (Beckman Coulter, Pasadena, USA)
ELISA washer	CAPP wash 12 (CAPP, Odense, Germany)
Flow Cytometer	BD LSR II Flow (BD Biosciences, Heidelberg, Germany) BD FACSCanto II (BD Biosciences, Heidelberg, Germany)
Freezer (-20°C)	Comfort (Liebherr, Biberach, Germany) Bosch GSD12A20 (Bosch, Gerlingen, Germany) Profi Line GG4310 (Liebherr, Biberach, Germany)
Freezer (-80°C)	New Brunswick Ultra-Low Temperature Freezer (Eppendorf, Hamburg, Germany)
Fridge (+4°C)	KTR16A21/02 (Bosch, Gerlingen, Germany) MediLine LKUexv1610 (Liebherr, Biberach, Germany)
Gel electrophoresis	PerfectBlue Gel System (Peqlab, Erlangen, Deutschland)
Heating devices	TS1 ThermoShaker (Biometra, Göttingen, Germany) Heatingblock Thermostat TH21 (HLC BioTech, Bovenden, Germany) Waterbath WNB 22 (Mettler, Schwabach, Germany)
Homogenizer	Precellys®24 (Peqlab, Erlangen, Germany)
Ice machine	Scotsman Flockeneisbereiter AF200 (Hubbard Systems, Birmingham, USA)
Incubator	CB 150 (Binder, Tuttlingen, Germany)

Incubator shaker	Innova 44 (Eppendorf, Hamburg, Germany)
Intravital microscopy stage	Customized
Laminar flow Workbench	BDK Laminar Flow (BDK, Sonnenbühl, Genkingen, Germany)
Magnetic stirrer	IKA RCT basic (IKA-Werke GmbH & Co. KG, Staufen, Germany)
Measuring cylinder	250ml, 500ml, 1000ml, 2000ml (VWR, Wayne, USA)
Microscope	LSM 780 ZEISS (Carl Zeiss Microscopy GmbH, Jena, Germany)
Microtome	Leica RM2255 (Leica Microsystems, Wetzlar, Germany) Leica HI1210 (Leica Microsystems, Wetzlar, Germany)
Microwave	NN-E235M (Panasonic, Osaka, Japan)
Pipette Controller, cordless	MATRIX CellMate II (Thermo Scientific, Waltham, USA)
Pipettes	10µl, 20µl, 200µl, 1000µl (Eppendorf, Hamburg, Germany) 2,5µl ErgoOne (StarLab, Hamburg, Germany) Multichannel DV8-10, DV12-50, DV8-300 (HTL Lab Solutions, Warszawa, Poland)
Power supply	PowerPac™ (BioRad, Hercules, USA)
Real-Time PCR Detection System	CFX96 TouchReal-Time PCR Detection (Bio-Rad, Munich, Germany)
Spectrophotometer 1 (RNA)	NanoDrop™ ND-1000 (NanoDrop Products, Wilmington, USA)
Spectrophotometer 2 (ELISA)	EL 800 (BioTek, Winooski, USA) infinite M200 (Group Ltd., Männedorf, Switzerland)
Thermal cycler	T100™ (BioRad, Hercules, USA), TProfessional Thermocycler (Biometra, Göttingen, Germany) T1 Thermocycler (Biometra, Göttingen, Germany)
Threaded bottles	100ml, 250ml, 500ml, 1000ml (Schott, Mainz, Germany)
Transilluminator	Transilluminator UST-30M-8R (BioView, Rehovot, Israel) Biostep Dark Hood DH-40/50 (biostep, Burkhaldsdorf, Germany)

Vibratome	VT1000, Leica, Nussloch, Germany
Vortex shaker	Vortex Genie 2 (Scientific Industries, New York, USA)

3.1 Consumables

Table 3-2 | Consumables

Item	Company
BD Plastipak 1ml Sub-Q	BD Medical, Le Pont de Claix Cedex, France
Cell strainer nylon (40µm, 70µm, 100µm)	VWR, Radnor, USA
CellTrics®	Partec, Meckenheim, Germany
Cover slips	Roth, Karlsruhe, Germany
Corning® Costar® Transwell® cell culture inserts	Corning, New York, Vereinigte Staaten
Culture plates (6-well/ 24-well/ 48-well/ 96-well, flat bottom)	Greiner, Frickenhausen, Germany
Disposal bags	Roth, Kalsruhe, Germany
ELISA plate (half-area, 96 K)	Greiner, Kremsmünster, Austria
Eppendorf Tubes® 5ml	Eppendorf, Hamburg, Germany
Filter tips	Sarstedt, Nümbrecht, Germany
Flow cytometry tubes	Sarstedt, Nümbrecht, Germany
Glass beads	Roth, Kalsruhe, Germany
Glass Pasteur pipette	Roth, Kalsruhe, Germany
Gloves	Semperit Technische Produkte GmbH, Wien, Austria
Hard-shell PCR plates	Bio-Rad, München, Germany
Measuring pipettes (5ml, 10ml, 25ml)	Greiner, Kremsmünster, Austria
Micro tube 1.1ml Z-Gel	Sarstedt, Nümbrecht, Germany
Micro tube 2ml + screw cap	Sarstedt, Nümbrecht, Germany
Microplate, 96well (F/U)	Greiner, Frickenhausen, Germany
Microscope slides (Superfrost plus)	Thermo Scientific, Waltham, USA
Multiply® µStrip Pro mix.colour	Sarstedt, Nümbrecht, Germany
Parafilm®	American National Cam, Greenwich, USA
PCR tubes	Sarstedt, Nümbrecht, Germany
Petri dishes	Greiner, Kremsmünster, Austria
Precision wipes	Kimberly-Clark, Reigate, United Kingdom
Reaction tubes (15ml, 50ml)	Greiner, Frickenhausen, Germany
Reagent reservoirs	Thermo Scientific, Waltham, USA
Safe seal reaction tubes (0,5, 1.5ml, 2.0ml)	Sarstedt, Nümbrecht, Germany
Sterican needles (0.90x40mm, 19G x 1½)	Braun, Melsungen, Germany
Sterile filters (Filtopur S 0.45)	Braun, Melsungen, Germany

Surgical disposable scalpel	Braun, Tuttlingen, Germany
Syringe filtration unit (Filtropur S0.2/0.45)	Sarstedt, Nümbrecht, Germany
Syringes Inject-F Tuberkulin (1ml)	Braun, Melsungen, Germany
Syringes Inject® (2ml, 5ml, 10ml, 20ml)	Braun, Melsungen, Germany
Tissue freezing medium	Leica, Nussloch, Germany
Tissue-Tek® Cryomold (15x15mm, 25x20mm)	Sakura Finetek, Torrance, USA
Venofix® A 21G	Braun, Melsungen, Germany
Weighing pans	Roth, Karlsruhe, Germany

3.2 Chemicals, reagents and recombinant proteins

Table 3-3 | Chemicals, reagents and recombinant proteins

Chemical/ reagent	Company
100bp DNA Ladder	New England BioLabs, Ipswich, USA
1-Fluoro-2,4-dinitrobenzene (DNFB)	Sigma-Aldrich, Steinheim, Germany
10x TAE buffer	Invitrogen, Carlsbad, USA
2-Propanol >99.5%	Roth, Karlsruhe, Germany
Acetic acid 100%	Roth, Karlsruhe, Germany
Acetone	VWR, Darmstadt, Germany
Albumin Bovine Fraction V, pH=7.0	SERVA Electrophoresis GmbH, Heidelberg, Germany
Ampuwa	Fresenius Kabi, Bad Homburg, Germany
B-27™ supplement (50X)	Gibco by Life technologies, Carlsbad, USA
CountBright™ absolute counting beads	Life technologies, Carlsbad, USA
CpG ODN 1668	TIB Molbiol, Berlin, Germany
DABCO	Sigma-Aldrich, Steinheim, Germany
Diphtheria Toxin (Unnicked)	Calbiochem by Merck, Darmstadt, Germany
Dithiothreitol (DTT) Molecular Grade	Promega, Fitchburg, USA
DNase/RNase-Free Water	Zymo Research, Irvine, USA
Deoxynucleotide (dNTP) Solution Mix	Peqlab, Erlangen, Germany
Dulbecco's Modified Eagle Medium (DMEM)	ThermoFisher, Waltham, USA
Dulbecco's PBS	Sigma-Aldrich, Steinheim, Germany
Ethanol 70% (methylated)	Roth, Karlsruhe, Germany
Ethanol absolute for molecular biology	ApliChem, Darmstadt, Germany
Ethanol Rotipuran >99.8%	Roth, Karlsruhe, Germany
Ethylenediaminetetraacetic acid (EDTA)	Sigma-Aldrich, St. Louis, USA
FACS Clean Solution	BD Bioscience, Franklin Lakes, USA
FACS Rinse Solution	BD Bioscience, Franklin Lakes, USA
Fetal Bovine Serum	ThermoFischer, Waltham, USA

Fixable Viability Dye eFluor 450/ 780	eBioscience, San Diego, USA
Hair removal Veet®	Reckitt Benckiser Group plc, Slough, England, UK
Hank's Balanced Salt Solution (HBSS) (10x)	Gibco by Life Technologies, Carlsbad, USA
Hemalaun solution	Sigma-Aldrich, St. Louis, USA
HEPES	Sigma-Aldrich, St. Louis, USA
Hydrochloric acid 37%	Roth, Karlsruhe, Germany
Laminin	Sigma-Aldrich, St. Louis, USA
LPS, E. coli 0111:B4	Sigma-Aldrich, St. Louis, USA
Mowiol	Sigma-Aldrich, St. Louis, USA
Murine CCL17	Peprotech, New York, USA
Murine TNF	Peprotech, New York, USA
Neurobasal medium	Gibco by Life Technologies, Carlsbad, USA
Oligo (dT)₁₂₋₁₈ primer	ThermoFisher, Waltham, USA
Olive oil	Sigma-Aldrich, St. Louis, USA
OneComp/ UltraComp ebeads	eBioscience, San Diego, USA
Paraformaldehyde (PFA)	Merck, Darmstadt, Germany
Penicillin-Streptomycin	Gibco by Life Technologies, Carlsbad, USA
Percoll	GE healthcare life science, Chalfont St Giles, Buckinghamshire, GB
peqGOLD Universal Agarose	Peqlab, Erlangen, Germany
Phosphate Buffered Saline Dulbecco	Merck, Darmstadt, Germany
Poly-D-lysine	Invitrogen, Carlsbad, USA
Polyinosinic:polycytidylic acid (poly (I:C))	Invivogen, San Diego, USA
Protease Inhibitor complete Tablets, Mini	Roche, Indianapolis, USA
QIAzol Lysis Reagent	Qiagen, Hilden, Germany
RPMI 1640	ThermoFisher, Waltham, USA
Reverse transcription buffer (5X)	Peqlab, Erlangen, Germany
Sodium hydroxide solution	Roth, Karlsruhe, Germany
Sulfuric acid (H₂SO₄)	Roth, Karlsruhe, Germany
SYBR® DNA Gel Stain	Invitrogen, Carlsbad, USA
Tissue Freezing Medium	Leica Biosystems, Nussloch, Germany
Tetramethylrhodamine isothiocyanate–Dextran, mol wt 155,000 (TRITC-dextran)	Sigma-Aldrich, St. Louis, USA
TritonX-100	ThermoFisher, Waltham, USA
TruStain fcX™ (anti-mouse CD16/32) (Clone: 93)	BioLegend, San Diego, USA
Trypan Blue	Sigma-Aldrich, St. Louis, USA
Trypsin	Gibco by Life technologies, Carlsbad, USA
Tween-20	Roth, Karlsruhe, Germany
Vectashield with DAPI	Vector Labs, Burlingame, California, USA
Xylol	Roth, Karlsruhe, Germany

3.3 Solutions and buffers

Table 3-4 | Solutions and buffers

Solution/buffer	Content
Brain digestion buffer	DMEM DNase I (1 mg/ml) Collagenase (2.5 mg/ml)
Complete RPMI 1640	RPMI Medium 10% FCS 1% Penicillin-Streptomycin
DNFB solution challenge	0.3% DNFB (w/v) in acetone:olive oil (5:1)
DNFB solution sensitization	0.25% DNFB (w/v) in acetone:olive oil (5:1)
EDTA (0.5M)	186.g EDTA approx. 20g NaOH 1000ml H ₂ O pH 7.8-8.0
ELISA stopping solution	25% H ₂ SO ₄ in H ₂ O
ELISA wash buffer	0.05% Tween-20 in PBS
Histology blocking buffer (brain)	PBS 5% BSA 5% normal goat serum 0.5% TritonX-100
Histology primary antibody buffer (brain)	PBS 1% BSA 1% normal goat serum 0.1% TritonX-100
Histology blocking buffer (skin)	PBS 10% normal goat serum 1% CD16/CD32 antibody 0.5% TritonX-100
Lysis buffer (tail lysis)	A. dest 5 mM EDTA, pH 8,0 0,2 % SDS 200 mM NaCl 0,1 mg/ml Proteinase K
MACS buffer	PBS 0.5% BSA 2mM EDTA
PFA (4%)	4g PFA 100ml PBS pH 7.4
Starvation RPMI 1640	RPMI Medium 0.5% FCS 1% Penicillin-Streptomycin

Skin digestion buffer	PBS DNase I (200 U/ml) Liberase™ (0.8 U/ml)
------------------------------	---

3.4 ELISA Kits

Table 3-5 | Elisa Kits

Target molecule/protein	Company
CCL17	R&D Systems, Mineapolis, USA
CX₃CL1	R&D Systems, Mineapolis, USA
IL-1β	R&D Systems, Mineapolis, USA
TNFα	R&D Systems, Mineapolis, USA

3.5 Antibodies

3.5.1 Antibodies for flow cytometry

Table 3-6 | Flow cytometry antibodies

Antigen	Isotype	Clone	Conjugate	Company
B220	rat	RA3-6B2	APC-Cy7	BioLegend
CCR2	rat	475301	APC	R&D Systems
CD3	hamster	145-2C11	APC-Cy7, PE, PerCP	BioLegend
CD4	rat	RM4-5	BV605	BioLegend
CD8a	rat	53-6.7	PE-Cy7	BioLegend
CD11b	rat	M1/70	APC, BV605, PE-Cy7, PerCP	BioLegend
CD11c	hamster	N418	PerCP, APC-Cy7	BioLegend
CD19	rat	eBio1D3	PE	eBiosciences
CD24	rat	M1/69	APC, BV421	BioLegend
CD45	rat	30-F11	PE, BV510	BioLegend
CD64	mouse	X54-5/7.1	PerCP	BioLegend
CD86	rat	GL-1	PE-Cy7	BioLegend
CD103	rat	M290	PE	BD Biosciences
CD206	rat	C068C2	APC	BioLegend
F4/80	rat	BM8	APC, PerCP	BioLegend
Ly-6G	rat	PE, PE-Cy7	1A8	BioLegend
Ly-6C	rat	APC-Cy7, PerCP	HK1.4	BioLegend
MHCII	rat	PE-Cy7, PerCP	M5/114.15.2	BioLegend
NK1.1	mouse	PE	PK136	BioLegend
TCRβ	hamster	PE	H57-597	BioLegend
TCRγd	hamster	APC	GL3	BioLegend
XCR1	mouse	BV421	ZET	BioLegend

3.5.2 Antibodies for Immunohistology

Table 3-7 | Immunohistology antibodies

Antigen	Isotype	Clone	Conjugate	Company
GFP	Rabbit IgG	Polyclonal	purified	Life Technologies
IBA-1	Rabbit IgG	Polyclonal	purified	Wako
Laminin	Rabbit IgG	L9393	purified	Sigma Aldrich
LYVE-1	Rabbit IgG	14917	purified	Abcam
Mouse IgG	Goat IgG	Polyclonal	biotinylated	Dianova
NeuN	Mouse IgG	A60	purified	Merck
Biotin	Streptavidin	-	Cy3	BioLegend
Rabbit IgG	Rabbit IgG	Polyclonal	Alexa Fluor 488	Life Technologies
Rabbit IgG	Rabbit IgG	Polyclonal	Alexa Fluor 594	Life Technologies

3.6 Kits

Table 3-8 | Kits

Name	Company
Absolute qPCR SYBR Green ROX Mix	Thermo Scientific, Waltham, USA
Direct-zol™ RNA MiniPrep Kit	Zymo research, Irvine, USA
LIVE/DEAD® Fixable Violet Dead Cell Stain Kit, for 405 nm excitation	Life Technologies, Carlsbad, USA
MyTaq HS Red DNA Polymerase	Bioline, London, UK
Quick-RNA™ MiniPrep	Zymo research, Irvine, USA

3.7 PCR primer sequences

Table 3-9 | PCR primer sequences

Target		Sequence (5' to 3')
18s rRNA	Fwd	GCA ATT ATT CCC CAT GAA CG
	Rev	GGG ACT TAA TCA ACG CAA GC
CCL2	Fwd	ACG TCC CTG TCA TGC TTC T
	Rev	GGA TCA TCT TGC TGG TGA AT
CCL17	Fwd	TGC TTC TGG GGA CTT TTC TG
	Rev	GAA TGG CCC CTT TGA AGT A
CCL22	Fwd	TCT TGC TGT GGC AAT TCA GA
	Rev	GAG GGT GAC GGA TGT AGT CC
TNF	Fwd	TCT TCT CAT TCC TGC TTG TGG
	Rev	GGT CTG GGC CAT AGA ACT GA
IL-1β	Fwd	TTG ACG GAC CCC AAA AGA T
	Rev	GAA GCT GGA TGC TCT CAT CA
IL-6	Fwd	GCT ACC AAA CTG GAT ATA ATC AGG A
	Rev	CCA GGT AGC TAT GGT ACT CCA GAA

3.8 Software

Table 3-10 | Software

Software	Company
Argus X1	Biostep, Burkhardtsdorf, Germany
BZ-II Analyzer	Keyence, Montabaur, Germany
CFX Manager™ Software	Bio-Rad, Munich, Germany
CorelDRAW Graphics Suite	Corel Corporation, Ottawa, Ontario, Canada
FACS Diva	BD, Franklin Lakes, USA
Fiji (Image J)	Open source scientific analysis program
FlowJo 9.9.7/10.4.1	TreeStar, Inc., Ashland, USA
GraphPad Prism 6	GraphPad, La Jolla, USA
Mendeley Software	Elsevier, Amsterdam, Netherlands
Microsoft Office 2011	Microsoft, Redmond, USA
NanoDrop™ ND-1000	NanoDrop Products, Wilmington, USA
Zen black	Carl Zeiss Microscopy GmbH, Jena, Germany

3.9 Enzymes

Table 3-11 | Enzymes

Enzyme	Company
DNase I	Roche, Basel, Switzerland
Horseradish Peroxidase	Sigma-Aldrich, St. Louis, USA
Liberase™	Roche, Basel, Switzerland
Proteinase K	Sigma-Aldrich, St. Louis, USA
RevertAid Reverse Transcriptase	Thermo Scientific, Waltham, USA
RiboLock RNase Inhibitor	Thermo Scientific, Waltham, USA

3.10 Mice strains used for experiments

Mice were housed under specific pathogen-free (SPF) conditions in the Genetic Resources Center (GRC) of the Life & Medical Sciences (LIMES) Institute, University of Bonn, Germany, if not indicated otherwise. Mice were maintained in standard animal cages under conventional laboratory conditions (12h/12h light/dark cycle, 22 °C), with ad libitum access to food and water. All experiments were performed using male or female 8–12 weeks-old WT (C57BL/6J) or transgenic mice. Littermate controls derived from the same breeding stock as CCL17^{E/E} and CCL17^{E/+} mice are designated as CCL17^{+/+} mice. TNFR1-deficient (Tnfrsf1a^{-/-}) and TNFR1- and TNFR2-deficient (Tnfrsf1a^{-/-}Tnfrsf1b^{-/-}) were bred at the Institute of Molecular Medicine and Experimental Immunology (IMEI), University of Bonn, Germany.

Table 3-12 | Overview of the used mice strains

Mouse line	Genetic background	Reference	Supplier
WT	C57BL/6J-RCCHsd	-	Envigo/ GRC
WT	C57BL/6NCrl	-	Charles river/ GRC
CCL17 ^{E/+}	C57BL/6J-RCCHsd	Alferink et al., 2003 ⁷³	I. Förster
CCL17 ^{E/+} (IVM)	25% C57BL/6J-RCCHsd/ 75% B6N-Tyrc-Brd	I. Förster (unpublished)	I. Förster
CCL17 ^{E/E}	C57BL/6J-RCCHsd	Alferink et al., 2003 ⁷³	I. Förster
Tnfrsf1a ^{-/-}	C57BL/6NCrl	Peschon et al., 1998 ¹⁴¹	Z. Abdullah
Tnfrsf1a ^{-/-} Tnfrsf1b ^{-/-}	C57BL/6NCrl	Peschon et al., 1998 ¹⁴¹	Z. Abdullah
GM-CSF ^{-/-}	C57BL/6J-RCCHsd	Stanley et al., 1994 ¹⁴²	B. Becher
MyD88 ^{-/-}	C57BL/6J-RCCHsd	Adachi et al., 1998 ¹⁴³	S. Akira
CCL17 ^{DTR/+}	C57BL/6J-RCCHsd	I. Förster (unpublished)	I. Förster
CCL17 ^{DTR/E}	C57BL/6J-RCCHsd	I. Förster (unpublished)	I. Förster

CCL17^{E/+} and CCL17^{E/E}, CCL17^{DTR/+}, GM-CSF^{-/-}, and MyD88^{-/-} mice were backcrossed into the C57BL/6J-RCCHsd background for at least 4 generations. All experiments were approved by the government of North Rhine-Westphalia (Az. 87-51.04.2010.A260, Az. 84-02.04.2011.A074, and 84-02.04.2016.A226).

3.11 Generation of CCL17/CCL22-double-deficient mice

Using the TALEN (Transcription activator-like effector nuclease) technology, new CCL17/CCL22-double-deficient mice were generated by Philip Hatzfeld by targeting the second exon of CCL22 in CCL17^{E/E} mice. This strategy presented several advantages. First, only one TALEN construct targeting the CCL22 locus had to be designed and injected. Second, the resulting offspring would still contain the EGFP construct in the *Cc/17* locus, allowing a rapid identification of CCL17-expressing cells using EGFP fluorescence. Genomic sequencing of all successfully targeted animals revealed that the (TAL)endonuclease had introduced eight different mutations ('A'-'H') in the second exon of the CCL22 locus. It was decided to use mice harboring the mutation 'F' or 'G' for all further experiments. Whereas mutation 'F' resulted in the deletion of 13 nucleotides (position 119'-131'), thereby inducing a frameshift mutation and early termination of translation, mutation 'G' was identified as an in-frame deletion of 18 nucleotides (position 115'-132'). Both mutations resulted in the deletion of the first two cysteines which are essential for the formation of the tertiary structure of all CC chemokines. It has to be taken into account, that mutation 'F' led to the production of a truncated version of CCL22, whereas mutation 'G' produced a nearly full length version of CCL22. However, during the initial characterization process neither of them could be detected in BM-DC supernatants by ELISA (data not shown). Furthermore, they did not induce migration of BW cells (data not shown). Thus, it was decided to compare both strains in the *in vivo* CHS assay.

4. Methods

4.1 Histology

4.1.1 Immunohistology of murine ears

Whole-mount samples of the ear dermis and epidermis were prepared for confocal microscopy. Mice were killed by cervical dislocation and ears were carefully excised. Hairs were removed using a hair-removal cream. Ears were separated into dorsal and ventral halves and placed dermis-side down in 1 ml 1% PFA and fixed for 12 h at 4°C. Following fixation, ear halves were washed 3 times with PBS for 5 min. Blocking and permeabilization was performed with 10% NGS (normal goat serum), 1% anti-CD16/CD32 antibody, and 0.5% Triton X-100 diluted in 1x PBS. Sheets were placed on rocker at RT for 2 h. For antibody-mediated staining sheets were incubated with primary rabbit-anti-mouse antibodies against Laminin (1:300, clone L9393) or LYVE-1 (1:500, clone 14917) for 2 h at RT. Following staining, ear halves were washed 3 times with PBS for 15 min before application of a secondary polyclonal goat anti-rabbit Alexa594 (1:500). Secondary antibody was incubated for another 2 h at RT. Following incubation, ear halves were washed as before (3 x 15 min). For mounting, sheets were shortly placed into distilled H₂O to remove any remaining PBS. Ears were briefly air-dried before mounting in between two coverslips to enable imaging from the epidermal as well as dermal site. For mounting Mowiol was freshly mixed with DABCO on the day of the experiment. Samples were dried overnight at RT and stored at 4°C until imaging. Z-stacks were acquired using a ZEISS LSM 780 Laser scanning microscope equipped with objective LCI Plan Neofluar 25x/0.8 DIC M27 or objective Plan-Apochromat 63x/1.4 Oil DIC M27.

4.1.2 Perfusion and immunohistology of the murine brain

For perfusion, mice were anesthetized with ketamine/xylazine. Mice were transcardially perfused sequentially with 25 ml of ice-cold PBS and 4% paraformaldehyde (PFA) in PBS. Next, brains were carefully removed from the skull and fixed in 4% PFA for 48 h at 4°C. 40 µm sagittal brain slices were prepared using a vibratome and stored in PBS until further use (0.1% sodium azide was added for long-term storage). Five slices were kept in one well of a 12-well plate. For antibody staining, 2 slices were transferred to one well of 24-well plate and initially washed 3 times with PBS for 5 min using a rocker. Next, slices were permeabilized and blocked in 500 µl 0.3% Triton-X100/5% BSA/5% NGS in PBS for 2 h at RT. Following blocking, the primary antibodies polyclonal rabbit anti-GFP (1:300), monoclonal mouse anti-NeuN (1:100) and polyclonal rabbit anti-IBA-1 (1:500) were diluted in 0.1% TritonX-100/1% BSA/1% serum in 480 µl PBS per well (240 µl per slice) and incubated at 4°C for 16 h. Following incubation, slices were washed 3 times for 15 min with PBS using a rocker. Next, polyclonal goat anti-rabbit Alexa594 or Alexa488 (both 1:500) or biotinylated anti-mouse IgG secondary antibodies were applied and incubated for 2 h at RT (480µl per well/ 240µl per slice). Sections stained

with anti-NeuN and biotinylated anti-mouse IgG were additionally treated with streptavidin-Cy3 (1:300 in PBS) for 1h at RT. Finally, sections were mounted using Vectashield containing DAPI. Sections were dried overnight at RT and stored at 4°C until imaging. All z-stacks of murine brains were acquired using a ZEISS LSM 780 Laser scanning microscope equipped with objective LCI Plan Neofluar 25x/0.8 DIC M27 or objective Plan-Apochromat 63x/1.4 Oil DIC M27.

4.1.3 Hematoxylin and Eosin staining of brain paraffin sections

Perfused and PFA-fixed brains were placed into plastic cassettes and dehydrated in a series of ascending alcohol concentrations using a benchtop tissue processor. Following dehydration, brains were embedded into paraffin, placed on a cooling plate and stored at RT until processing. 5 µm saggital brain slices were prepared using a rotary microtome. Sections were carefully transferred to pre-warmed (40°C) water bath to enable mounting on microscope slides. Slides were dried on a heating plate set to 37°C for 2 h. Slides were kept in microscopy boxes at RT until proceeding with Hematoxylin and eosin (H&E) staining. The H&E staining protocol is depicted in **Tab. 4.1**.

Table 4-1 | Hematoxylin and Eosin staining protocol

Step	Treatment	Time	Step	Treatment	Time
1	Xylol	10 min	10	Tap water	3 min
2	Xylol	10 min	11	Alcoholic Eosion Y solution	30 sec
3	100% Ethanol	5 min	12	Tap water	10 sec
4	100% Ethanol	5 min	13	95% Ethanol	10 sec
5	95% Ethanol	2 min	14	95% Ethanol	10 sec
6	70% Ethanol	2 min	15	100%Ethanol	10 sec
7	Aqua dest.	1 min	16	100% Ethanol	10sec
8	Mayer's hemalaun solution	3 min	17	Xylol	5 min
9	0.1% HCL	2 sec	18	Xylol	5 min

4.1.4 Morphological analysis of microglia

Semi-automatic morphological analysis of microglia was performed using custom-written ImageJ plug-ins. Tools were provided by J. Hansen and Dr. A. Halle from the German Center for Neurodegenerative Diseases (DZNE). Details on the plugins can be found in Fülle et al.¹⁴⁴. In brief, single IBA-1⁺ microglia were selected out of a z-stack to generate single cell images. Size-filtered (particles smaller than 100 voxel were removed prior to analysis) binary images were used for the reconstruction of the surface area, volume, and convex hull. Cell skeleton parameters were obtained by Gauss-filtering of the same image with subsequent skeleton reconstruction and analysis using the

plugins by Arganda-Carreras and colleagues¹⁴⁵. The ramification index was calculated as the ratio of the surface area of an individual cell (soma and processes) to the surface area of a sphere containing the same volume as the cell¹⁴⁴. This ratio equals the minimum possible surface area the specific cell could achieve:

$$\text{ramification index} = \frac{\text{cell surface area}}{4\pi \cdot \left(\frac{3 \cdot \text{cell volume}}{4\pi}\right)^{\frac{2}{3}}}$$

The polarity index reflects the unbalance of the distribution of microglial processes from the soma and was obtained by normalizing the displacement of convex hull center and cell center to the size of the individual convex hull¹⁴⁴:

$$\text{polarity index} = \frac{|\text{convex hull center} - \text{cell center}|}{2 \cdot \sqrt[3]{3 \cdot \text{convex hull volume} / 4\pi}}$$

4.2 Intravital microscopy of murine ears

To analyze the migratory behavior of CCL17/EGFP⁺ cells in the murine skin 2-photon (2P) intravital microscopy (IVM) was performed using albino CCL17^{E/+} mice, which were generated by backcrossing CCL17^{E/+} C57BL/6J mice into the B6N-Tyrc-Brd/BrdCrCrI background for 2 generations. An overview of the IVM setup is depicted in **Fig. 4.1**. For IVM, mice were placed in an anesthetic induction chamber previously filled with 3% isoflurane mixed with oxygen (~4.1 L/min) and carbogen (~1.9 L/min). Anesthesia depth was assessed via a toe pinch. Before putting on the nose cone delivering the anesthetic gas (1.7-2.1% isoflurane depending on the respiratory rate of the mouse) the eyes were treated with a lubricant to prevent eye damage. The nose cone was carefully fixed on the head of the mouse using adhesive tape. For IVM, ear hairs were removed using hair-removal cream (Veet®). Hair-removal cream was applied using a cotton swab and incubated for 2' before carefully removing the hairs using tissue paper.

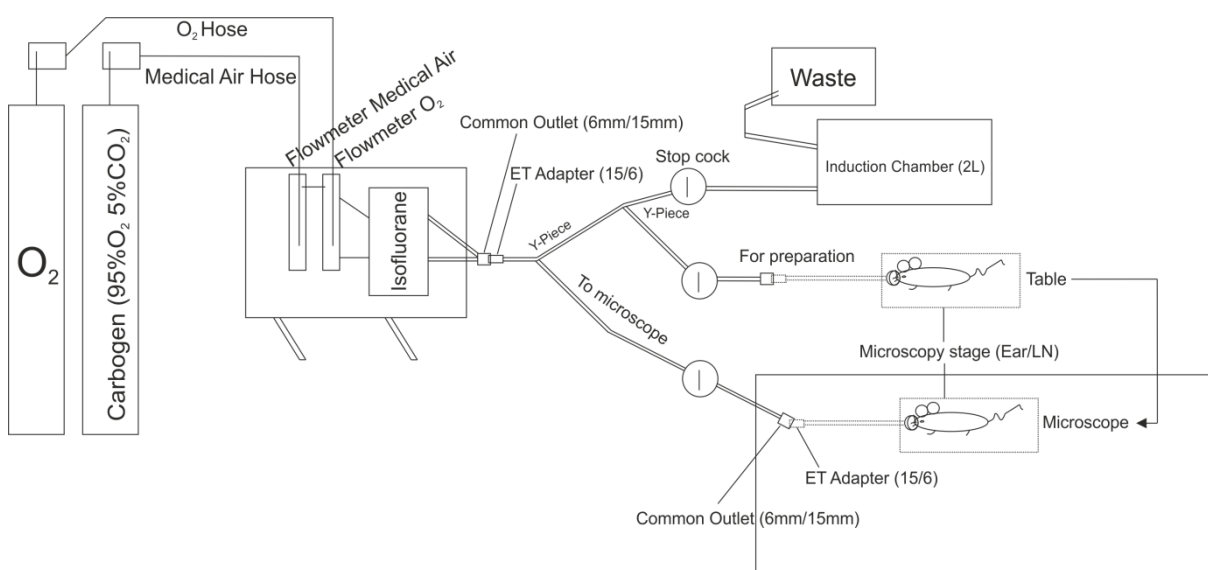


Figure 4.1 | Overview of the established 2P-IVM setup.

Next, the mouse was carefully placed on a custom-made IVM stage. The design of the IVM stage was adapted from a construction provided by Prof. Dr. W. Kastenmüller. To visualize dermal blood

vessels, 100 μ l of a 7 μ M TRITC-dextran (155 kDa) solution were injected i.v. 30 min before imaging. The mouse was prepared for IVM as described by Li et al.¹⁴⁶. In brief, the mouse was fixed with adhesive tape on the IVM stage and the ear was gently fed through the slit of the IVM stage (see **Fig. 4.2**). Next, tissue-grease was spread around the ear, covering the slit of the IVM stage. One drop of PBS was added on the dorsal side of the ear and on the underside of a coverslip before a coverslip was placed on the ear. A second square of tissue-grease was applied on to the coverslip. The IVM stage was carefully transferred to the pre-heated (\sim 37°C) 2P imaging chamber. The tissue-grease square on top of the coverslip was filled with distilled H₂O and the LCI Plan Neofluar 25x/0.8 DIC M27 objective was carefully lowered until it touched the liquid phase. After setting an appropriate wavelength for 2P imaging of both, EGFP and TRITC (880-920 nm), several baseline videos were recorded until no or only little drifts in the scan field were observed. Tissue-depth was assessed with the help of autofluorescent hairs located in the dermis. For intravital recording, time-lapse images were taken every 60 sec for 1 - 2 h. Image resolution and scan speed were adjusted to allow one z-stack (focal distance of 3 μ m) per 60 sec. Videos were post-processed and analyzed using the Zeiss ZEN software and ImageJ.

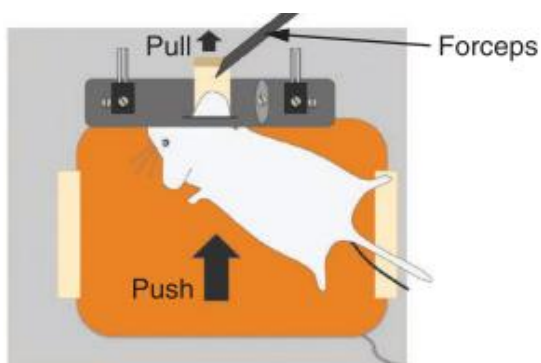


Figure 4.2 | Schematic overview of the custom-made stage used for IVM.

The anesthetized mouse is carefully placed on the custom-made IVM stage. First, a piece of tape, adhesive side up, is positioned midway through the slit and the ear is subsequently fixed onto it. Next, the ear is gently fed through the slit by pulling the tape with a pair of forceps, with the mouse body simultaneously brought closer to the stage. The tape is removed from the ear and the ventral side of the ear is moistened (PBS) and positioned flat on the stage. *Image modified after [146].*

4.3 Isolation and flow cytometry of skin immune cells

Ears of naïve or DNFB-treated mice (4 days post challenge) were harvested and stored in PBS on ice. Dorsal and ventral ear sides were separated and placed into a 12-well plate. Next, the samples were minced and digested in 500 μ l PBS supplemented with 0.154 mg/ml Liberase™ and 0.1 mg/ml DNase I. For digestion, minced tissue was incubated at 37°C for 90 minutes in a shaking incubator at 100 rpm. Following this, the lysate was further resuspended using a blunted 1000 μ l pipette tip and filtered through 100 μ m and 70 μ m filters (washed with 5 mL ice-cold PBS in between). Subsequently, the cell suspension was centrifuged at 4000 rpm for 10 min at 4°C. The cells were resuspended in 1 ml PBS and subjected to flow cytometric surface staining. The different antibody staining panels are depicted in **Tab. 4.2**. 250 μ l of the cell suspension were used for each staining (see **Tab. 4.2**), the remaining cells were used for single stainings or as an unstained control. Antibody staining was performed in FACS tubes. The cells were transferred to the FACS tubes through a 50 μ m filter. After another washing step, cells were first blocked using anti-CD16/32 antibodies for 5 min at 4°C. Next, the respective antibody mix was directly added to each tube and incubated at 4°C for 30 min. Following incubation the cells

were washed and resuspended in 280 μ l PBS. To determine the absolute cell number, 20 μ l counting beads were added.

Table 4-2 | Antibody staining panels used to characterize immune cells in the murine skin

Monocyte staining	Dendritic cell staining	T cell staining
Lineage - PE (L/D 1:1000, CD3 1:200, CD19 1:200, NK1.1 1:200, Ly-6G 1:200)	Lineage - APC-Cy7 (L/D 1:1000, CD3 1:200, B220 1:200)	Lineage - APC-Cy7 (L/D 1:1000)
anti-CD45 BV510 (1:400)	anti-CD45 BV510 (1:400)	anti-CD45 BV510 (1:400)
anti-CD24 BV421 (1:200)	anti-CD11c PerCP (1:100)	anti-CD3 PerCP (1:200)
anti-CD11b BV605 (1:200)	anti-MHCII APC (1:500)	anti-CD4 BV605 (1:400)
anti-Ly6C APC/Cy7 (1:200)	anti-CD11b BV605 (1:200)	anti-CD8 BV605 (1:200)
anti-CD64 PerCP (1:200)	anti-CD11b BV605 (1:200)	anti-TCR $\gamma\delta$ APC (1:200)
anti-CCR2 APC (1:100)	anti-CD103 PE (1:200)	anti-TCR β PE (1:200)
anti-MHCII PE/Cy7 (1:500)	anti-XCR1 BV421 (1:200)	-
<i>CCL17/EGFP in CCL17^{-EGFP} mice</i>	<i>CCL17/EGFP in CCL17^{-EGFP} mice</i>	<i>CCL17/EGFP in CCL17^{-EGFP} mice</i>

All samples were analyzed on a BD LSR II Cytometer. The following formula was used to calculate the absolute number of cells per ear:

$$\text{absolute cell number per ear} = \left[\left(\frac{\text{cell count} \times \text{beads volume}}{\text{bead count} \times \text{cell volume}} \right) \times \text{bead concentration} \right] \times 4$$

4.4 Isolation and flow cytometry of CNS mononuclear cells

PBS or LPS-treated mice were sacrificed and immediately perfused through the left cardiac ventricle with 25 ml ice-cold PBS. The brains were carefully dissected and transferred to 4 ml DMEM supplemented with Collagenase D (2.5 mg/ml) and DNase I (1 mg/ml). Brains were minced and digested at 37°C for 45 min. Following incubation, brain cells were triturated through a 19G cannula and passed through a 70 μ m cell strainer. For the isolation of leukocytes and microglia a Percoll density centrifugation was performed. Therefore, the cells were centrifuged and resuspended in 8 ml of a 40% Percoll/HBSS solution. Cells were transferred to FCS pre-coated 15 ml polypropylene round-bottom tubes and underlaid with 5 ml of 80% Percoll/HBSS solution using a glass pasteur pipette. The samples were centrifuged at 2800 rpm for 20' at 18°C (without brake and deceleration). Before collecting all mononuclear cells (MNC) at the 40/80% interphase, the top myelin layer was removed by aspiration. MNCs were transferred to FACS tubes and washed twice with HBSS. Cells were blocked using anti-CD16/32 antibodies for 5 min at 4°C before proceeding with antibody staining. Antibodies used for the analysis of brain leukocytes are depicted in **Tab. 4.3**. For staining, 100 μ l antibody mix were directly

added to the cells and incubated at 4°C for 30 min. Following antibody staining, cells were washed once with HBSS and resuspended in 280 µl HBSS. 20 µl counting beads were added to determine absolute cell numbers.

Table 4-3 | Antibodies used to characterizes brain leukocytes

Brain leukocyte staining	Dilution
anti-CD45 PE	1:100
anti-CD11b APC	1:200
anti-CD3 APC/Cy7	1:200
anti-Ly6G PE/Cy7	1:200
anti-Ly6C PerCP	1:200
<i>CCL17/EGFP in CCL17^{EGFP} mice</i>	-

Cells were analyzed on a BD FACSCanto II. The following formula was used to calculate the absolute number of cells per brain:

$$absolute\ cell\ number\ per\ brain = \left[\left(\frac{cell\ count \times beads\ volume}{bead\ count \times cell\ volume} \right) \times bead\ concentration \right]$$

4.5 Transwell migration assay

The capability of the aptamers to inhibit migration towards chemotactic CCL17 gradients was analyzed in a transwell migration assay. All experiments were performed using the BW5147.3 thymic lymphoma cell line (ATCC® TIB-47™), which has been previously demonstrated to specifically migrate towards recombinant murine CCL17 (mCCL17)¹⁴⁷. The day before the experiment, a vial of 1x10⁷ BW5147.3 cells was thawed and seeded at a density of 5x10⁵ cells/ml in complete RPMI media (10% FCS, 1% PenStrep). BW5147.3 cells were fed with 10 ml complete medium in the evening. The next morning, BW5147.3 cells were harvested by centrifugation (400g, 5 min) and resuspended in RPMI starvation media (0.5%FCS, 1% PenStrep). Cells were transferred back to the same flask and starved for 2 h at 37°C in the incubator. During starvation, aptamer dilutions were prepared as required and mixed with starvation media containing 100 ng/ml mCCL17. Following starvation, cells were harvested by centrifugation (400g, 5 min) and adjusted to 1x10⁶ cells/ml. Cell migration was analyzed in 12-well Costar® transwell plates (5µm pores). Therefore, lower chambers of transwell plates were filled with 600 µl starvation media with or without the addition of 100 ng/ml (±7.5 pmol) mCCL17. As a positive control, the CCL17 specific neutralizing antibody MAB529 was used at 1.88 µg/ml (±7.5 pmol). A scrambled version of MF35.47.m was used to analyze possible unspecific effects of the RNA aptamers. 100µl cell suspension (1x10⁵ cells) was transferred to the upper transwell chambers. Next, the plate was transferred to the incubator and cells were allowed to migrate for 2 h. Following migration the insert was carefully removed and the entire volume of the lower chamber was transferred to FACS tubes. Lower wells were washed with 500µl PBS which were also transferred to the corresponding FACS tube.

Subsequently, the cells were centrifuged (400g, 5 min) and 1 mL supernatant was removed carefully. Absolute numbers of transmigrated cells were determined in the remaining 100 μ l using flow cytometry (BD FACSCanto II). Results are depicted as percent of migration normalized to migration towards mCCL17 alone. All conditions were tested in duplicates or triplicates.

4.5.1 DNFB-induced contact hypersensitivity assay

The DNFB-induced mouse model of contact hypersensitivity (CHS) is separated into a sensitization and elicitation phase. For sensitization, mice were briefly anesthetized with a mixture of isoflurane and medical O₂, shaved on the belly before treating the abdominal skin with 70 μ l 0.25% w/v DNFB prepared in acetone:olive oil (5:1) on day d-8 or d-5 as indicated in the figure legends. The DNFB solution was evenly distributed on the abdominal the skin using yellow (20-200 μ l) pipette tips as

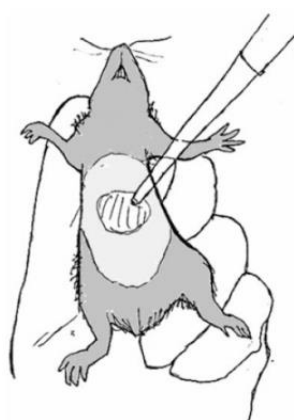


Figure 4.3 | DNFB application onto the shaved abdomen of the mouse.

Image modified after [158].

indicated in **Fig. 4. 3**. To prevent cross-contamination of DNFB-treated animals, mice were single housed for the course of the experiment. The following day the abdomen was treated with another 70 μ l 0.25% w/v DNFB solution. A baseline ear thickness was determined using a thickness-gauge caliper at d0. For DNFB challenge, mice were again anesthetized and dorsal and ventral sides of the right ear were treated epicutaneously with 10 μ l 0.3% w/v DNFB in acetone:olive oil, whereas dorsal and ventral sides of the left ear were treated with 10 μ l acetone:olive oil as a negative control. For aptamer experiments, mice were injected i.p. 1 h before and 12 h after DNFB challenge with aptamers diluted in 1xPBS. Control animals received i.p. injections of a

scrambled version of MF35.47.m. The course of ear swelling was assessed 24 h (day 1), 48 h (day 2) and 72 h (day 3) later. The absolute ear swelling response was calculated by subtracting the baseline thickness measured at day 0.

4.6 TLR-ligand stimulation

Mice were systemically treated with one of the following TLR-ligands, E. coli 0111:B4 LPS (6-150 μ g/animal), CpG ODN 1668 (32 μ g/animal) or Poly(I:C) (200 μ g/animal). All TLR ligands were diluted in PBS and injected i.p. (5 -6pm) in a volume of 200 μ l. For the analysis of gene expression in the hippocampus, mice were sacrificed 16 h later. Control animals received i.p. injections of 200 μ l PBS. To determine cytokine levels in the serum, blood was drawn from the cheek 3 hours after injection. Blood was collected in 1.5 ml Eppendorf® tubes and allowed to coagulate at RT for 30 - 60 min. Subsequently, samples were centrifuged at 16,000g for 10 min at RT. The clear serum was carefully collected, transferred into fresh 1.5 ml Eppendorf® tubes, and stored at -20°C until further use. Cytokine concentrations were measured by enzyme-linked immunosorbent assay (ELISA) according to the manufacturer's instructions (R&D systems).

4.7 Real Time semi-quantitative PCR (semi-qPCR)

4.7.1 RNA isolation

Hippocampi of naïve and TLR-ligand injected mice were carefully isolated as described by Beaudoin and colleagues¹⁴⁸. In brief, mice were sacrificed by cervical dislocation and brains were quickly harvested and washed in ice-cold PBS. Isolated brains were bisected along the longitudinal fissure (groove that separates the two cerebral hemispheres). The neocortex was resected to expose the hippocampus of each hemisphere, which was then isolated using two spatulas. Both hippocampi were directly homogenized in Qiazol® and RNA was isolated according to the manufacturer's instructions (Qiagen). The isolated RNA was further purified using the Zymo Research Direct-zol™ RNA MiniPrep Kit, which also included a DNase digestion step.

4.7.2 Determination of RNA concentration

The concentration of RNA was determined using the NanoDrop, ND-1000 spectrophotometer. Following equilibration, 2 µl sample were directly pipetted onto the detection area. The system measures absorbance at distinct wavelengths. Absorbance at 260 nm is used to determine the RNA concentration of the sample. Other wavelengths are used to check for DNA and/or protein contamination. If the RNA concentration exceeded 500 ng/µl, the sample was diluted DNase/RNase-free H₂O. Following dilution, samples were measured again and total amount of RNA was calculated. For subsequent experiments, the sample volume, containing 1000 ng RNA was calculated for each sample.

4.7.3 cDNA synthesis and RPS6 PCR

1 µg of the isolated total RNA was directly transcribed into complementary DNA (cDNA) using the RevertAid reverse transcriptase. Oligo(dT)₁₂₋₁₈ primers, which mainly bind to the 3' poly(A) tail of messenger RNAs (mRNA), were used for reverse transcription. To hybridize mRNAs and Oligo(dT)₁₂₋₁₈ primers, RNA was diluted with DNase/RNase-free H₂O, filled up to 10 µl with DNase/RNase-free H₂O, mixed with 3 µl Oligo(dT)₁₂₋₁₈ primers, and incubated at 70°C for 10 min. The samples were subsequently placed on ice to stop the hybridization reaction. Next, 27 µl cDNA master mix containing (per reaction), 9.4 µl DEPC H₂O, 8.0 µl 5xreverse transcription (RT) buffer, 4.0 µl dNTP (stock: 10 mM), 4.0 µl DTT (Dithiothreitol), 0.8 µl RiboLock (stock: 40U/ µl), and 0.8 µl reverse transcriptase (stock: 200U/ µl) were added to each sample and incubated for 1 hour at 40°C. To inactivate the reverse transcriptase, the reaction was incubated at 95°C for 5 min. Success and efficiency of cDNA synthesis was checked by performing a polymerase chain reaction (PCR) against the house-keeping gene RPS6 (ribosomal protein S6). The used RPS6 PCR mix and protocol are depicted in **Tab. 4.4**. The PCR product was visualized on a 2% agarose gel using SYBR® SAFE (Thermo Fisher Scientific). The intensity of the gel band was compared between all samples and samples which gave no or weak bands were either synthesized again or excluded from further analysis.

Table 4-4 | RPS6 PCR master mix and cycler program

Master mix (component)	Volume	Incubation time	Temperature	Cycles
ddH ₂ O	13.05 µl	5 min	95°C	1x
5xMyTag buffer	4.0 µl	1 min	95°C	35x
cDNA	1.5 µl	1 min	55°C	
RPS6 fwd primer	0.7 µl	1 min	72°C	
RPS6 rev primer	0.7 µl	10 min	72°C	1x
MyTaq DNA polymerase	0.05 µl			

4.7.4 semi-qPCR

Semi-qPCR was performed on the CFX93 Real-Time system. The previously synthesized cDNA was used as a template for amplification. The 2XSYBR-green ROX master mix contains, dNTPs, Thermo-Start DNA Polymerase and the SYBR Green I dye which intercalates with newly synthesized dsDNA and subsequently emits light at a wavelength of 520 nm. In addition, the SYBR ROX dye is included as a negative control. Primers were designed using the Universal Probe Library from Roche. The used semi-qPCR mix and protocol are depicted in **Tab. 4.5**. A melting curve analysis was performed to validate specificity of PCR primer. The melting curve is generated by progressively rising the temperature from 65°C to 95°C in 0.5°C steps, thereby the SYBR Green I dye dissociates from the DNA and the fluorescence signal is rapidly reduced as the temperature increases. Detection of more than one melting curve indicated the presence of several PCR products. In these cases, new primer pairs were designed and samples were analyzed again.

Table 4-5 | semi-qPCR master mix and cycler program

Master mix (component)	Volume	Incubation time	Temperature	Cycles
2XSYBR-green ROX mix	7.5 µl	15 min	95°C	1x
cDNA	5.0 µl	20 sec	95°C	44x
ddH ₂ O	1.9 µl	40 sec	60°C	
Fwd primer	0.3 µl	60 sec	40°C	
Rev primer	0.3 µl	10 min	72°C	1x

Expression levels of target genes were normalized to 18S ribosomal RNA (18S rRNA) before comparing expression of target genes between experimental groups. Fold changes were calculated using the standard $\Delta\Delta C_t$ method. Here, two normalization steps were performed. First, the C_t values of 18S rRNA were subtracted from the C_t values of target genes (ΔC_t). Second, the normalized C_t^{Control} values were subtracted from $C_t^{\text{Experiment}}$ values ($\Delta\Delta C_t$). Finally, the primer efficiency of each target gene was used to calculate the fold change of gene expression between control and experimental conditions.

The following formula was used: $\text{fold change} = 2^{(-\Delta\Delta Ct)}$

Using this formula, it is assumed that after each cycle the amount of cDNA is doubled and that the primers have an efficiency of 100% (2^\wedge), which is rarely the case. However, as most immune-relevant genes are strongly induced upon activation, slight differences in the primer efficiency (90 - 110%) will not significantly affect the expression levels. Nevertheless, exact primer efficiencies should be determined in future experiments.

4.8 Generation of primary hippocampal neurons

For the analysis of CCL17 secretion by hippocampal neurons it was necessary to establish a primary neuronal culture. Therefore, timed pregnancies were set up and successful mating was verified by the detection of a vaginal plug the day after starting the breeding. At embryonic day 14 (E14) pregnant mice were sacrificed by cervical dislocation as the use of anesthetic gases involves the danger of causing damage to brain cells¹⁴⁹. Subsequently, the embryos were harvested and placed in a petri dish filled with ice-cold PBS. The embryos were carefully decapitated using a fine pair of scissors and the embryonic brains were separated from the skull (under a dissecting microscope) and transferred into one drop of sterile, ice-cold HBSS. The meninges were removed as good as possible and the cerebral hemispheres were carefully separated using sharp forceps. The hippocampal tissue was isolated from each hemisphere and transferred to a drop of sterile, ice-cold DMEM medium. After processing all brains, hippocampi were further processed under the sterile bench. To dissociate hippocampal tissue, 6-10 hippocampi (isolated from 3-5 embryos) were pooled in a 15 ml conical tube with 1 ml of 0.25% Trypsin/EDTA solution (prewarmed to 37°C) and incubated for ~10 minutes at 37 °C. During dissociation, the tubes were inverted several times. Furthermore, the tissue was gently triturated 7-10 times. Digestion was stopped by adding 5 ml DMEM supplemented with 10% FCS. The cell suspension was centrifuged (300xg, 18°C, 6 min), supernatant was removed and the cells were resuspended in 5 mL Neurobasal medium with 1X B27 supplement (Life technologies). The cells were either plated in a 12-well plate at 4×10^5 cells/ well or in a 24-well plate at 2×10^5 cells/ well. The day before the experiment (E13.5) cell culture plates were coated with a mixture of 0.5-1 ml (12- & 24-well plate, respectively) laminin (2 µg/ml) and poly-D-lysine (200 µg/ml) in PBS for 1 hour at 37 °C and washed 3 times with 1 ml cold PBS. Coated plates were covered with PBS and placed in the fridge. After seeding, the cells were allowed to adhere for 15-20 min before carefully aspirating the medium completely and replacing it with fresh medium. This step was especially important as it removes slowly adhering cells, such as astrocytes and microglia. After one week of culture, half of the medium was replaced with fresh medium. At this point of time, the cells had already formed visible neural networks characterized by a triangular cell soma with extended axons (**Fig. 4.4**). Two weeks after establishing the cultures, mature neurons were stimulated with recombinant murine TNF (50 ng/ml), E. coli 0111:B4 LPS (100 ng/ml), or the combination of both for 96 h. Following this stimulation, supernatants were harvested

and the concentration of CCL17 and CX₃CL1 were determined by ELISA according to the manufacturer's instructions (R&D Systems).

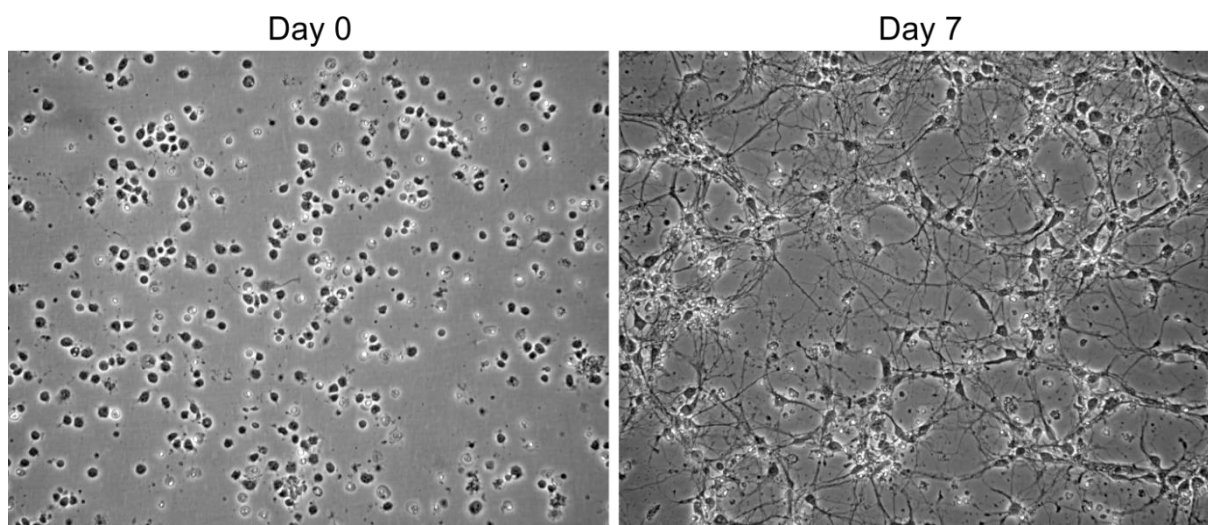


Figure 4.4 | Primary murine hippocampal neurons.

Images were taken immediately after seeding (Day 0) and after seven days in culture (Day 7).

4.9 Electrophysiological recordings of acute brain slices

Electrophysiological recordings were performed by B. Breithausen from the laboratory of Prof. Dr. C. Henneberger at the Institute of Cellular Neurosciences, University of Bonn Medical Center, Germany (IZN). Electrophysiological recordings were performed in acute brain slices as described previously^{144,150}. In brief, 300 μm thick acute hippocampal slices were generated from age-matched 8 to 12-week-old male WT and CCL17^{E/E} mice. Mice were injected i.p. with either 200 μl PBS or 150 μg E.coli 0111:B4 LPS diluted in 200 μl PBS 16h before the experiment. To perform electrophysiological recordings, PBS- and LPS-treated mice were transported to the IZN at the day of the experiment. At the IZN, horizontal slices were cut in an ice-cold slicing solution containing 60 mM NaCl, 105 mM sucrose, 2.5 mM KCl, 2.7 mM MgCl, 1.25 mM NaH₂PO₄, 1.3mM ascorbic acid, 3mM sodium pyruvate, 26 mM NaHCO₃, 0.5 mM CaCl₂, and glucose 10 (osmolarity 300-310 mOsm). To allow equilibration, slices were kept in this solution at 34 °C for 15 min. Next, slices were transferred to an extracellular bath solution containing 131 mM NaCl, 2.5 mM KCl, 1.3 mM MgSO₄, 1.25 mM NaH₂PO₄, 21 mM NaHCO₃, 2 mM CaCl₂, and 10 mM glucose (osmolarity adjusted to 297-303 mOsm) and stored at RT (21-23 °C) until the start of the experiment. To ensure sufficient oxygenation of the slices, all solutions were constantly supplied with 95% O₂/5% CO₂. After 1 h of incubation in the extracellular bathing solution, slices were transferred to an interface chamber for electrophysiological recordings. To record field excitatory postsynaptic potentials (fEPSP), a standard patch pipette (3-4 MOhm), filled with the extracellular bath solution, and was placed in the CA1 stratum radiatum (see **Fig. 4.5**). Using a bipolar concentric stimulation electrode (FHC), placed in the stratum radiatum at the border between the CA3/CA1 regions, fEPSPs were evoked by electrical stimulation of the CA3 to CA1 Schaffer collaterals

(SC) (see **Fig. 4.5**). Stimulation intensity was adjusted to generate fEPSPs with a ~50% maximum amplitude. The basal synaptic transmission (slope of the first fEPSP) and the paired pulse ratio (ratio of the slope of the second and first evoked fEPSP) were monitored using a paired stimuli (each 100 μ s,

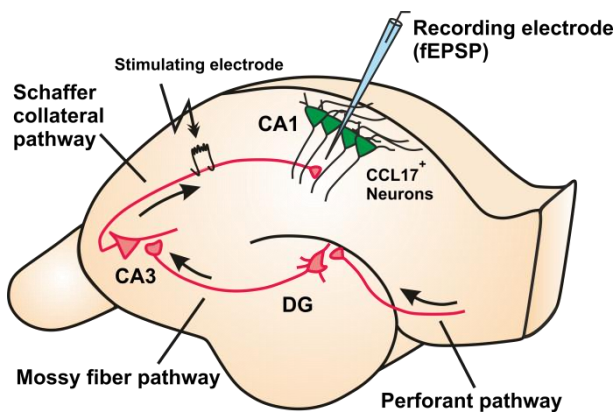


Figure 4.5 | Schematic overview of the setup used for electrophysiological recordings of murine acute brain slices.

(CA: Cornu Ammonis, DG: Dentate gyrus, fEPSP: field excitatory postsynaptic potential)

interstimulus, 50 ms interval between stimuli) every 15 s for at least 10 min before the induction of long-term potentiation (LTP) using a theta-burst stimulation (TBS). For TBS, 8 bursts consisting of 4 stimuli (100 Hz) were applied at 5 Hz. The TBS was delivered 3 times with an interval between stimuli of 1 min. To analyze the effect of the LTP induction, the fEPSP potentiation was subsequently probed by paired stimuli application for 30 min. All recorded signals were amplified and filtered (1000x, EXT-02B, NPI9, high-pass 0.1 Hz, low-pass 10 kHz),

digitalized at a sampling rate of 10 kHz and stored using WinWCP (Strathclyde Electrophysiology Software, University of Strathclyde Glasgow, Scotland). Final analysis of fEPSP slopes was performed by B. Breithausen using Clampfit (Molecular Devices, Sunnyvale, USA) and provided as a data table.

4.10 DT-mediated ablation of CCL17-expressing neurons

Mice received i.p. injections of 0.4 μ g Diphtheria toxin (DT) on three consecutive days (d-3 to d0) in 200 μ l 0.9% sodium chloride solution (saline). A 20 μ g/ml DT stock solution was prepared using Ampuwa® H₂O. For i.p. injections, DT stock solution was diluted to 2 μ g/ml using saline.

4.11 EEG recordings

EEG recordings CCL17^{DTR/+} mice were performed by Dr. P. Bedner and J. Müller from the laboratory of Prof. Dr. C. Steinhäuser at the Institute of Cellular Neurosciences, University of Bonn Medical Center, Germany. In brief, female CCL17^{DTR/+} mice also received 0.4 μ g DT (i.p.) on 3 consecutive days. Immediately after the last DT injection, the mice were anesthetized and a telemetric transmitter was transplanted into a subcutaneous pocket at the right abdominal wall. For the detection of electrographic seizures, surface electrodes were carefully implanted in the skull. Following surgery, mice received an analgesic and were returned to their cages. Telemetric signals, sent from the implanted transmitter, were captured by a radio signal receiver plate which was directly placed under individual cages. The recorded EEG data was manually screened for the occurrence of potential electrographic seizures by P. Bedner and was provided as a table depicting the number of seizures per day and mouse.

4.12 Statistical Analysis

All data was analyzed with GraphPad Prism 6 using, unpaired t-tests, one way or two way ANOVA with Bonferroni's post-hoc test for multiple comparisons. The level of significance for $p < 0.05$ was denoted as (*) or, for < 0.01 as (**), for $p < 0.001$ as (***), and for $p < 0.0001$ as (****), as indicated in the figure legends.

5. Results

5.1 Analysis of CCL17⁺ cells in murine skin

The chemokine CCL17 is known to be expressed in DCs of the skin, the intestine and the lung⁷³. It was demonstrated that expression of CCL17 is inducible in skin-resident myeloid cells in the context of allergic inflammation⁴⁹. Although it was previously demonstrated that CCL17⁺ DCs are present in the inflamed human and murine skin^{49,151,152}, it was less clear whether a population of CCL17⁺ cells is already present in the healthy skin. Therefore, ears of DNFB and solvent-treated CCL17^{E/+} mice were analyzed for the presence of CCL17/EGFP⁺ cells. Immunofluorescent staining, intravital microscopy, and multi-color flow cytometry were performed to get a comprehensive overview of the exact localization, morphology, and identity of CCL17⁺ cells in the skin.

5.1.1 CCL17⁺ cells are present in solvent and DNFB-treated murine skin

Confocal microscopy was performed with ears of solvent and DNFB-treated CCL17^{E/+} mice. Ears were excised, separated into dorsal and ventral halves and, following fixation, subjected to immunofluorescent staining. Whole-mount immunofluorescence of the entire dorsal halves was performed to ensure detection of all dermal and epidermal CCL17/EGFP⁺ cells. As depicted in the upper row of **Fig. 5.1A and B**, CCL17/EGFP⁺ cells were visible in the solvent as well as DNFB-treated skin. It has to be noted that the solvent-treated ears should not be considered naïve as it is possible that the solvent also induces CCL17. To identify the exact localization and identity of CCL17-expressing cells, ear halves were stained for Langerin (**Fig. 5.1A**) and CD3 (**Fig. 5.1B**). Whereas Langerin is expressed in LCs and dDCs, CD3 identifies several populations of skin T cells, in particular, epidermal DETCs and dermal $\gamma\delta$ T cell. As it is known that LCs leave the skin following activation, it was not surprising that less Langerin⁺ cells were detected after DNFB-treatment (see **Fig. 5.1A, second column**). Interestingly, no CCL17/EGFP/Langerin-positive cells could be observed (see **Fig. 5.1A, Merge**). Epidermal CD3⁺ DETCs were characterized by long cellular protrusions (see **Fig. 5.1B**) and, in contrast to LCs; application of DNFB had no apparent effect on their maintenance (see **Fig. 5.1B, second column**). It was previously demonstrated that murine DC are the predominant source of CCL17 in inflamed skin^{49,73} and as activated LCs and DCs leave the skin via lymphatic vessels (LVs), it was of interest whether CCL17⁺ cells would localize with LVs. Thus, ear halves were also stained with an anti-LYVE1 antibody to visualize LVs. As depicted in **Fig. 5.1A**, CCL17⁺ cells clustered around LVs, in particular under non-inflammatory conditions. Unexpectedly, these clusters appeared to disintegrate following DNFB-treatment whereas CCL17⁺ cells were still detected in close proximity to LVs. Furthermore, CCL17 and its receptor CCR4 were demonstrated to be essential for the recruitment and extravasation of peripheral T cells in the context of allergic inflammation^{86,153}. Staining with an anti-

Laminin antibody visualized the dense network of dermal blood vessels (BVs) (**Fig. 5.1B**). Strikingly, CCL17/EGFP⁺ cells also localized in close proximity to BVs (**Fig. 5.1B, Merge**). Naïve

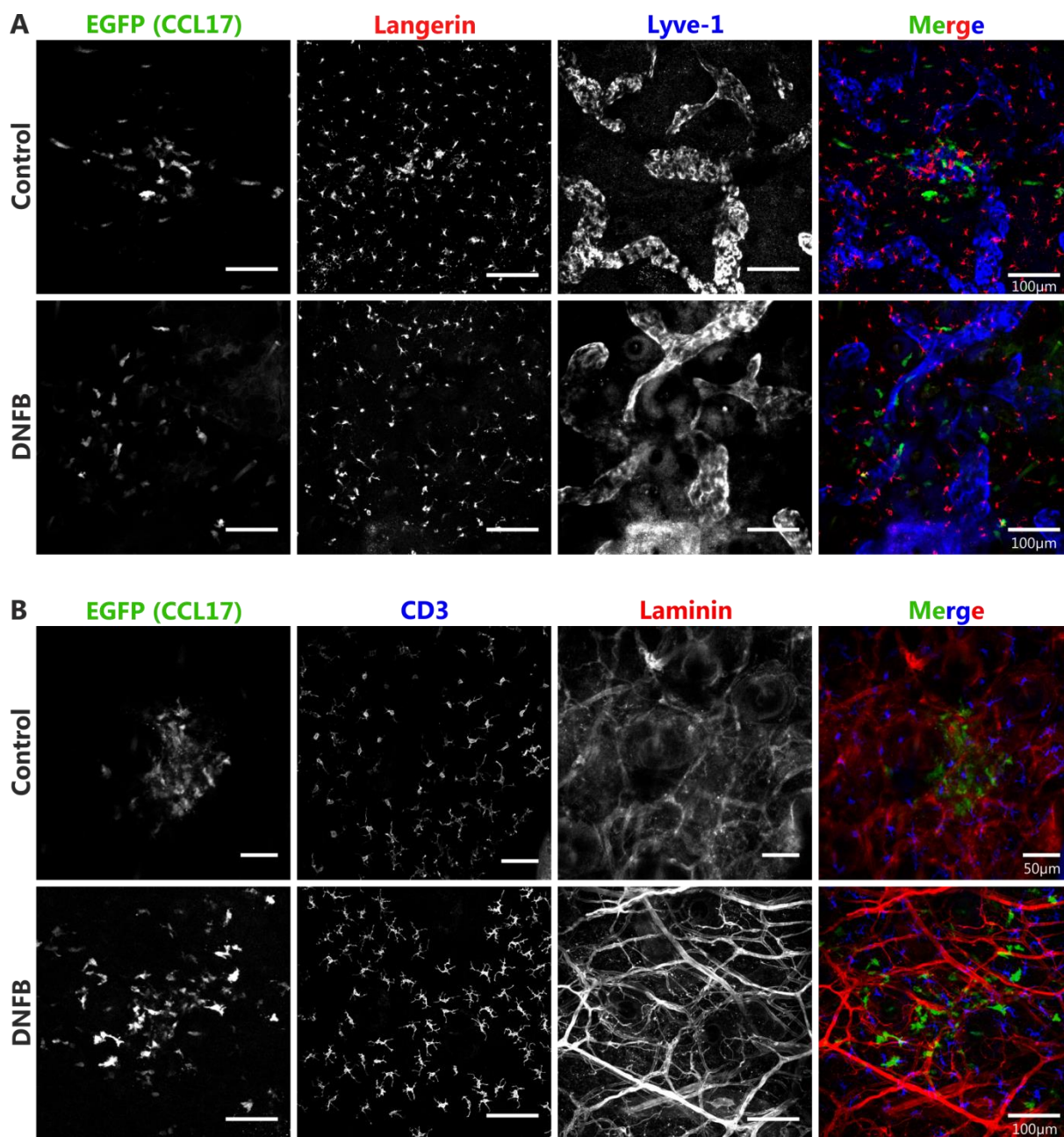


Figure 5.1 | CCL17⁺ cells localize to lymphatic and blood vessels in the murine skin.

CCL17^{E/+} mice were treated with 20 µl 0.3 % DNFB on the right ear (10 µl per ear half) or solvent (acetone:olive oil, 5:1) on the left ear. Ears were excised 24 h after treatment and subjected to immunofluorescent staining. A, B: Solvent (upper row) and DNFB-treated (lower row) ears of CCL17^{E/+} mice were stained with antibodies against Langerin and LYVE1 to visualize Langerhans cells or lymphatic vessels, respectively (**A**) or with a combination of anti-CD3 and anti-Laminin antibodies to visualize skin T cells or blood vessels, respectively (**B**). Endogenous reporter expression of EGFP in CCL17^{E/+} mice was used to detect CCL17-expressing cells. Pseudocolor merged image is depicted in the fourth column of A and B. Scale bars are indicated in pseudocolor image. Representative images are shown (n = 2).

In conclusion, these experiments confirmed the presence of CCL17⁺ cells in the inflamed skin but additionally identified CCL17⁺ skin cells in the absence of DNFB (solvent treated). Furthermore, CCL17⁺ cells localized in close proximity to dermal blood and lymphatic vessels.

5.1.2 Two behaviorally distinct CCL17⁺ cell populations are present in the murine dermis

Immunofluorescent (IF) staining of tissues often faces certain limitations, such as the need for fixation to prevent degradation of antigenic epitopes. In addition, immunofluorescent analyses only capture a snapshot of the tissue and do not provide information on cellular behavior or cell-cell interactions. Thus, it was decided to establish an intravital microscopy (IVM) setup to enable live-cell imaging of CCL17/EGFP⁺ cells in mouse ears¹⁵⁴. In CCL17^{E/+} and CCL17^{E/E} mice the bright expression of EGFP under the control of the CCL17 promoter allowed direct detection of CCL17/EGFP⁺ cells in their native environment. In addition, mice were injected i.v. with TRITC-dextran (155 kDa) to visualize dermal BVs¹⁵⁵. As depicted in **Fig. 5.2A**, CCL17/EGFP⁺ cells were widely distributed in the ear skin. Whereas some CCL17/EGFP⁺ cells were in close contact with BVs (red), others localized in the interstitium. The bright extended structures are autofluorescent hairs, which allow a rough determination of imaging depth. Detection of the hair follicles allowed to estimate the imaging depth to approximately 150 – 200 μm ¹⁵⁵.

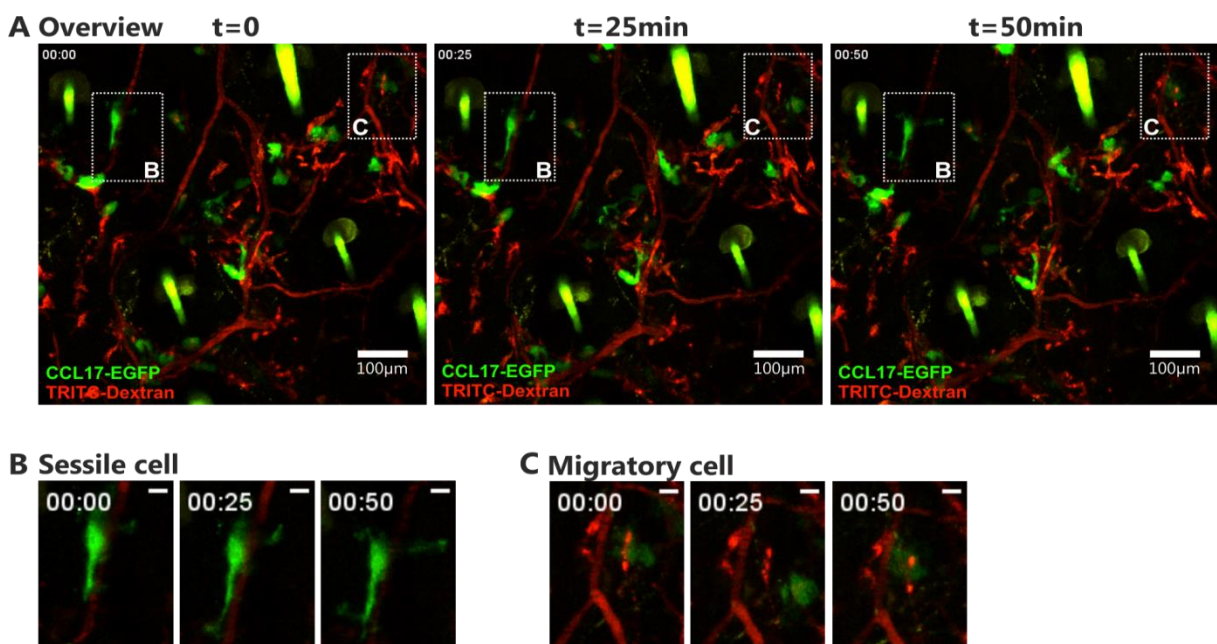


Figure 5.2 | Identification of different CCL17⁺ cells in the murine skin.

A: Video, still images of the ear of a CCL17^{E/+} mouse at different time-points after starting IVM recording. BV are visualized by injecting TRITC-Dextran (i.v.) prior to IVM. Scale bar is 100 μm . **B & C:** Magnification of the two behaviorally different CCL17⁺ cells identified in the murine skin. **B:** Sequential still images of a sessile CCL17⁺ cell in close proximity to a blood vessel. **C:** Sequential still images of a CCL17⁺ cell actively migrating in the interstitium. For B & C the same time points as in A are shown. Scale bar for B & C is 20 μm . Representative video (out of 5) was chosen to extract still images.

Interestingly, two behaviorally different populations of CCL17⁺ skin cells could be distinguished. The first, a more sessile CCL17⁺ cell population, was found in direct contact or close proximity to dermal BVs (see **Fig. 5.2A and B**). These non-migrating cells appeared to utilize cellular protrusions to directly interact with the dermal BVs (see **Fig. 5.2B**). A second CCL17⁺ cell population was found to actively

migrate through the interstitium (see **Fig. 5.2A and C**). In contrast to sessile CCL17⁺ cells, these migratory cells appeared smaller and exhibited a typical amoeboid monocyte morphology¹. In his master thesis, K. Knöpper extended these experiments and analyzed the migratory behavior of CCL17⁺ cells in heterozygous CCL17^{E/+} and CCL17-deficient CCL17^{E/E} mice. Although these are preliminary data, the migratory behavior of CCL17/EGFP⁺ skin cells, with regard to speed and directionality, was only marginally affected in the absence of CCL17¹⁵⁴.

In conclusion, these experiments confirmed the presence of CCL17⁺ cells in the naïve murine skin. Interestingly, IVM identified two behaviorally different CCL17⁺ cell populations, which underpinned the previous observation of CCL17⁺ cells located in close proximity to LVs and BVs (see **Fig. 5.1A and B**). Here, a more sessile CCL17⁺ cell population localized primarily to dermal BVs was identified and possibly represents a distinct population of dermal perivascular Mφs⁴³

5.1.3 CCL17 is expressed in defined subpopulations of skin-resident myeloid cells

The finding that two different CCL17⁺ populations with distinct migratory properties are present in the skin demanded a more comprehensive characterization of their identity. As stated previously, several studies already identified DCs as a major source of CCL17^{49,70,73,151,156}. However, the exact identity of CCL17-producing cells in the skin remained elusive. Here, a flow cytometric strategy based on Bouladoux et al.¹⁵⁷ was applied to clearly identify CCL17/EGFP⁺ DC populations in the skin of CCL17^{E/+} and CCL17^{E/E} mice (see **Fig. 5.3**). Wild-type (WT) mice were used as a control. The strategy comprised a live cell gate to exclude cellular debris and two gatings to remove doublets (see **Fig. 5.3B and C**). Next, a live/dead exclusion dye was combined with a lineage staining to exclude B and T cells (Lin⁻) (see **Fig. 5.3D**). CD45⁺ leukocytes were identified in all living and Lin⁻ cells (see **Fig. 5.3E**) and subsequently analyzed for CD11c and MHCII expression to identify myeloid cells. Total MHCII⁺ cells were then analyzed for the expression of CD11b and CD24 (see **Fig. 5.3F and G**). Whereas CD11b is expressed on several subsets of myeloid cells and is regulated upon activation, a high CD24 expression was found to be specific for epidermal LCs^{25,158}. Thus, staining for CD11b and CD24 enabled separation of four myeloid cell populations in the skin (see **Fig. 5.3G**), all of which were analyzed for CCL17/EGFP-expression (see **Fig. 5.3I-L**). Cells negative for CD11b and CD24 were identified as double-negative DC (DN DC)^{24,28}. CD24⁺CD11b⁻ cells represent cDC1,m whereas CD11b⁺CD24^{lo/int} cells comprise cDC2s as well as monocyte populations and were collectively referred to as CD11b⁺ cells. LCs were identified as CD11b⁺CD24^{hi} cells. In addition, cDC1 were further separated using CD103 as a marker of migratory DCs and XCR1 as a marker for cross-presenting DC (see **Fig. 5.3H**)¹⁵⁹.

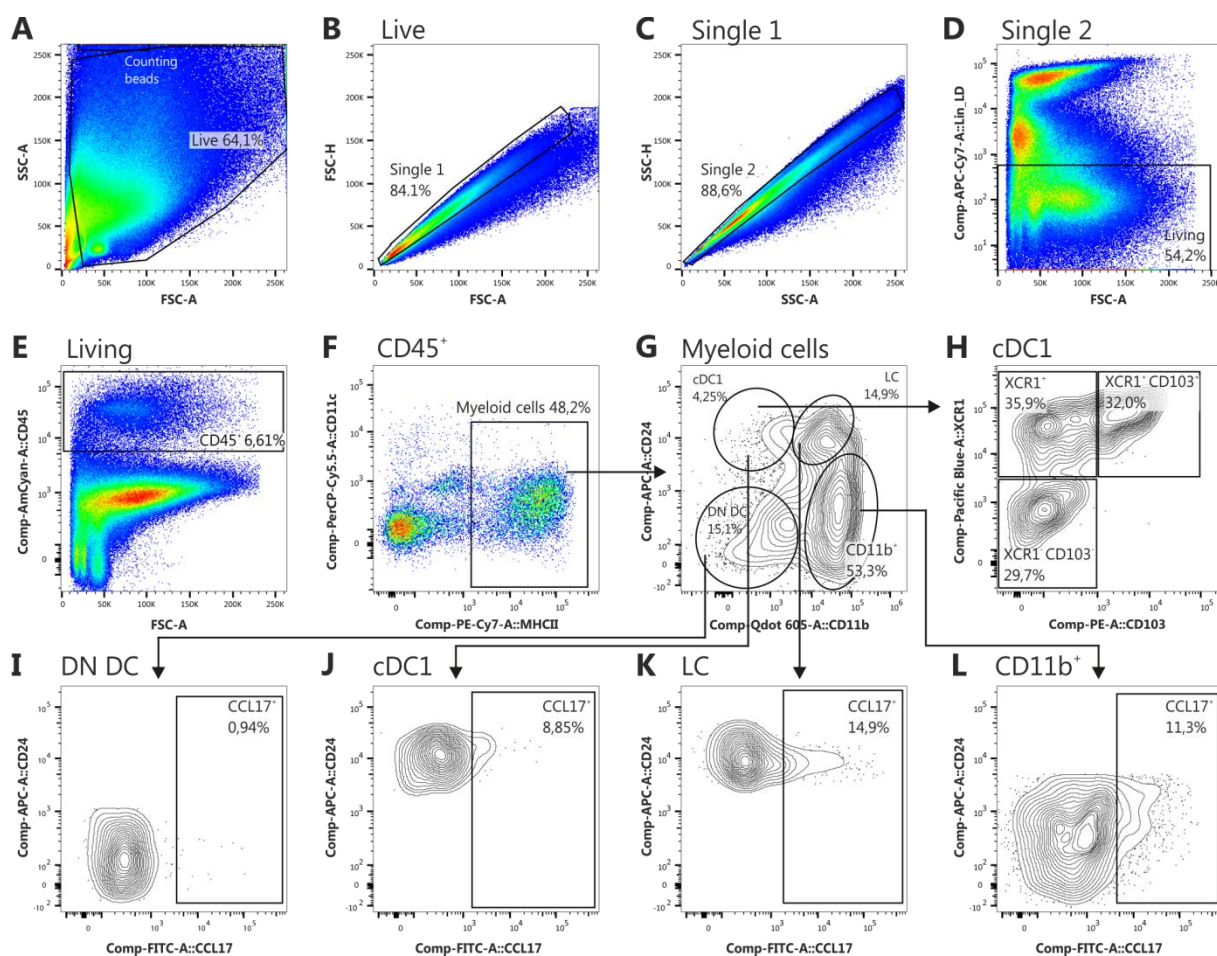


Figure 5.3 | Gating strategy to identify CCL17⁺ myeloid cell populations in the murine skin.

Skin cells were gated based on their characteristic FSC-A and SSC-A profiles (A). Two strategies to exclude doublets were applied (B-C). A viability dye was utilized to exclude dead cells from further analysis (D). Within all living cells CD45⁺MHCII⁺ cells were identified (E & F) and then further analyzed for CD24 and CD11b expression (F). Using these markers identified four skin myeloid cell populations were identified (G & I-L). cDC1 cells were further analyzed for the expression of CD103 and XCR1 (G & H). In all subpopulations the percentage of CCL17/EGFP⁺ cells was analyzed in comparison to wild-type control animals. Representative gating of a CCL17^{E/+} mouse is shown.

As depicted in **Fig. 5.3I-L** and **Fig. 5.4A**, CCL17/EGFP⁺ cells were present in variable frequencies in DN DC, cDC1, LCs and CD11b⁺ cells. In addition, it was of interest whether CCL17 itself would have an effect on the frequency of CCL17/EGFP⁺ cells, which could indicate autocrine regulation. To clarify this, the percentage of CCL17/EGFP⁺ cells in heterozygous CCL17^{E/+} mice was compared to CCL17-deficient CCL17^{E/E} mice. As depicted in **Fig. 5.4A**, the percentage of CCL17/EGFP⁺ cells was similar between the different experimental groups, which rules out autocrine regulation by CCL17. Interestingly, further analysis of cDC1 subpopulations revealed that only XCR1⁺CD103⁺ cells contained a considerable number of CCL17-expressing cells (see **Fig. 5B**). In contrast to immunofluorescent analysis and IVM, CCL17/EGFP⁺ cells were also detected in CD11b⁺CD24^{hi} LCs, which can probably be attributed to the higher sensitivity of the flow cytometer. Taken together, the analysis of skin myeloid cells revealed that CCL17 is expressed in XCR1⁺CD103⁺ cDC1, LCs and CD24^{lo-int}CD11b⁺ cells.

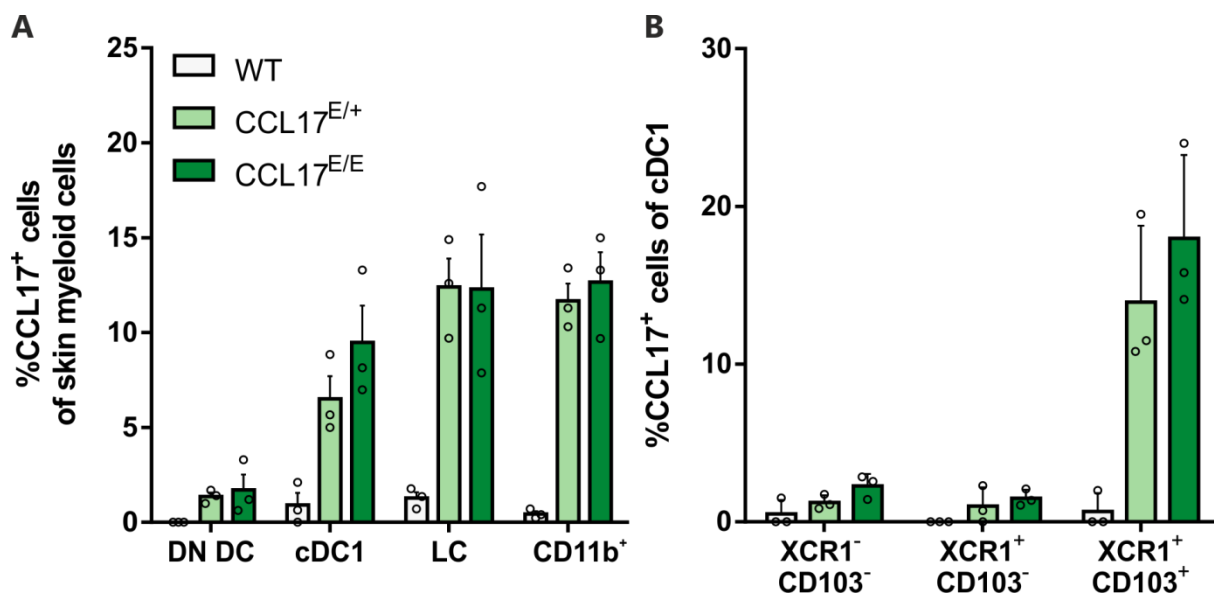


Figure 5.4 | CCL17⁺ cells are present in skin myeloid cell populations.

Ears of WT, CCL17^{E/+} and CCL17^{E/E} mice were separated into dorsal and ventral halves and mechanically disrupted. Single cell suspensions were obtained by enzymatic digestion. Skin cells were then subjected to antibody-mediated staining and subsequently analyzed by flow cytometry. The flow cytometric gating strategy is depicted in Fig. 5.3. **A:** Percentages of CCL17/EGFP⁺ cells within skin-resident myeloid cell populations (DN DC: Double-negative DC, cDC1: type 1 conventional DC, LC: Langerhans cells) **B:** Percentage of CCL17/EGFP⁺ cells in cDC1 subpopulations. (n=3 per group, mean ± SD). Circles represent data from individual mice.

5.1.4 Skin-resident monocytes and macrophages harbor substantial numbers of CCL17⁺ cells

The identification of CCL17⁺ cells within the very heterogeneous CD11b⁺ cell population (see **Fig. 5.3G & L**) demanded a more precise analysis of those cells. Thus, a second gating strategy, adopted from Bouladoux et al.¹⁵⁷ and Tamoutounour et al.⁴⁰, was used to discriminate CD11b⁺ DC from skin-monocytes and Mφs (see **Fig. 5.5**). As before, skin cells were isolated from CCL17^{E/+}, CCL17^{E/E} and WT mice. This gating strategy also excluded debris, doublets, dead and Lin⁻ cells (see **Fig. 5.5A-D**). In contrast to the previous staining, CD45⁺ leukocytes were directly analyzed for CD11b and CD24 expression, without a preceding exclusion of MHCII-negative cells (see **Fig. 5.5F**). The CD11b⁺CD24^{lo-int} cell population was further analyzed for the monocyte marker Ly6C and the Mφ marker CD64 (see **Fig. 5.5G**)²⁸. Here, the double-negative cells were identified as CD11b⁺ DC whereas the remaining monocytic cells were further analyzed for the expression of CCR2. As CCR2 is exclusively expressed on monocytes, it allowed separation of skin monocytes and Mφs (see **Fig. 5.5H**). CCR2⁺ monocytes and CCR2⁻ Mφs were subsequently analyzed for Ly6C and MHCII expression. Based on their expression levels, one monocyte (P1), two monocyte-derived DC (moDC) populations (P2 and P3) and two Mφ populations (P4 and P5) were identified (see **Fig. 5.5I and K**). In the last step, the frequency of CCL17/EGFP⁺ cells was analyzed in the different cell populations (see **Fig. 5.5J and L**).

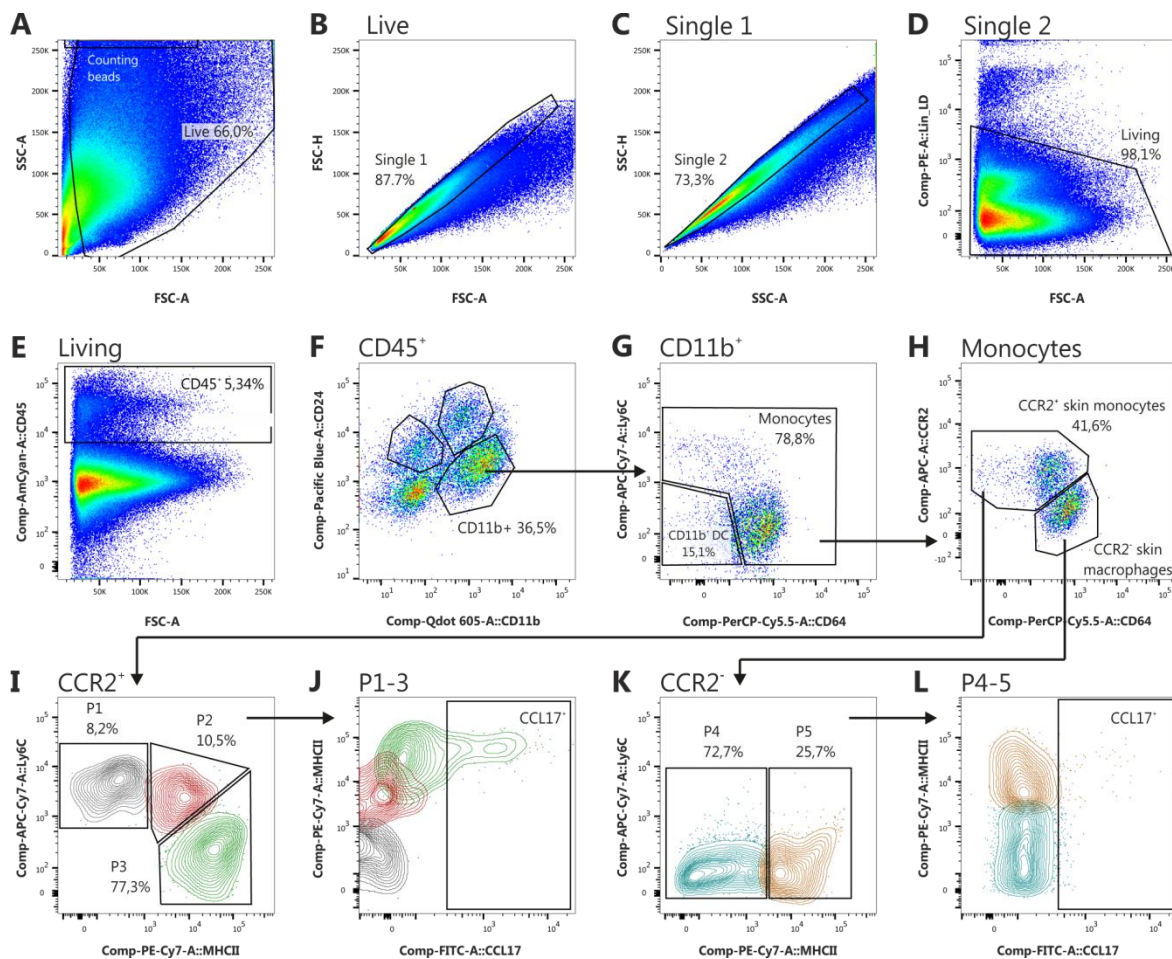


Figure 5.5 | Gating strategy to identify CCL17⁺ skin monocyte populations.

Skin lymphocytes were gated based on their characteristic FSC-A and SSC-A profiles (A). Two strategies to exclude doublets were applied (B-C). A viability and lineage stain was used to exclude dead and lineage⁺ cells from further analysis (D). All living, lineage⁻ and CD45⁺ cells were analyzed for CD24 and CD11b expression (E & F). The CD11b⁺CD24^{lo-int} fraction was further analyzed for Ly6C and CD64 expression. Ly6C⁻CD64⁻ cells were identified as CD11b⁺ DC (G). The remaining cells were further subdivided using CCR2 expression (H). The CCR2⁺ fraction is known to contain skin monocytes⁴⁰, whereas CCR2⁻ cells represent skin-resident macrophages⁴⁰. Using expression levels of Ly6C and MHCII, both fractions could be further subdivided into P1-P3 monocytes (I) and P4-P5 macrophages (K). Finally, the number of CCL17/EGFP⁺ cells was analyzed in all skin cell populations identified (exemplary gating depicted in J & L). Representative gating of a CCL17^{E/+} mouse is shown.

Percentages of CCL17/EGFP⁺ cells in all skin populations identified are depicted in Fig. 5.6. In line with the previous staining, approximately 14% of CD11b⁺ DC and monocytes were positive for CCL17. Strikingly, the majority of CCL17⁺ cells were found in P3 moDCs (CCR2⁺Ly6C⁻MHCII⁺), whereas only a few P5 Mφs (CCR2⁻Ly6C⁻MHCII⁺) were positive for CCL17. As expected from the previous staining, the number of CCL17/EGFP⁺ cells was comparable between CCL17^{E/+} and CCL17^{E/E} mice, which rules out a possible autocrine regulation of CCL17.

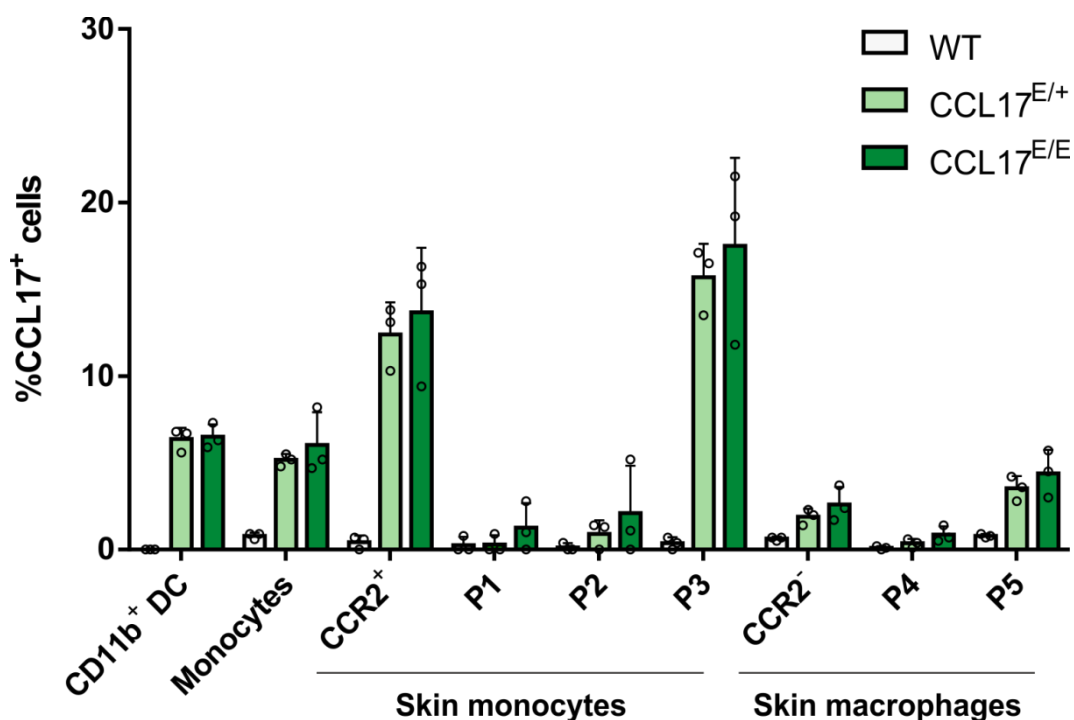


Figure 5.6 | Identification of CCL17⁺ cells in skin monocytes and macrophages.

Ears of WT, CCL17^{E/+} and CCL17^{E/E} mice were separated into dorsal and ventral halves and mechanically disrupted. Single cell suspensions were obtained by enzymatic digestion and subjected to antibody-mediated staining. Cells were subsequently analyzed by flow cytometry. The flow cytometric gating strategy is depicted in Fig. 5.5. Depicted are percentages of CCL17/EGFP⁺ cells in different populations of skin monocytes and macrophages (monocyte populations: P1: CCR2⁺Ly6C⁺MHCII⁺ P2: CCR2⁺Ly6C⁺MHCII⁺ P3: CCR2⁺Ly6C⁻MHCII⁺ and macrophages: P4: CCR2⁻Ly6C⁻MHCII⁺ and P5: CCR2⁻Ly6C⁻MHCII⁺). (n=3 per group, mean ± SD) Circles represent data from individual mice.

5.1.5 GM-CSF signaling differentially regulates CCL17 expression in skin dendritic cells and macrophages

It was previously demonstrated that the cytokine GM-CSF (granulocyte macrophage colony-stimulating factor) is a potent inducer of CCL17 expression in human monocytes as well as in murine Mφs⁷⁴. Thus, CCL17 expression in skin cells was monitored by flow cytometry in GM-CSF-deficient CCL17 reporter and knockout mice (GM-CSF^{-/-}CCL17^{E/+} and GM-CSF^{-/-}CCL17^{E/E} mice, respectively). The FACS gating strategies previously established for myeloid cells and monocytes were again used for the analysis of the percentages of CCL17/EGFP⁺ cells. To exclude that the loss of GM-CSF, CCL17, or both had an effect on the presence of skin cells, absolute skin cell were compared between the experimental groups (**Fig. 5.7A and B & Fig. 5.8A**). To account for variations between cell preparations, counting beads were used to determine absolute cell numbers. As depicted in **Fig. 5.7A and 5.8A**, total numbers of CD45⁺ leukocytes were comparable between all experimental groups. Also, the cell numbers in CD11c⁺MHCII⁺ skin DCs (see **Fig. 5.7A**) and CD11b⁺ monocyte populations (see **Fig. 5.8A**) in CCL17 and/ or GM-CSF-deficient mice were comparable to WT control mice. In contrast, there was a significantly reduced number of CCL17/EGFP⁺ cells in cDC1, LCs, and CD11b⁺ cell populations isolated from GM-CSF^{-/-}CCL17^{E/+} and GM-CSF^{-/-}CCL17^{E/E} mice (see **Fig. 5.7C**).

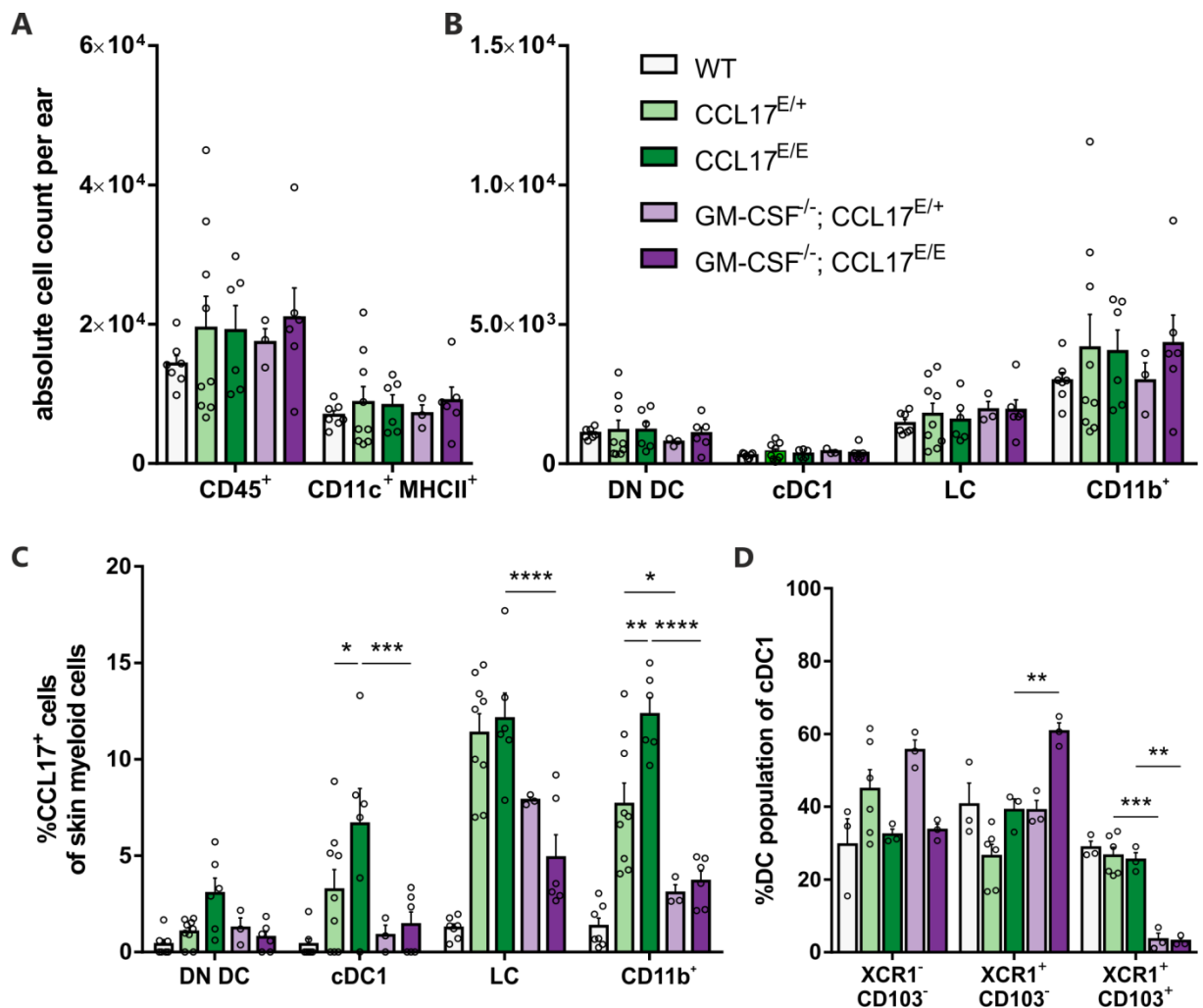


Figure 5.7 | GM-CSF regulates expression of CCL17 in skin myeloid cells.

Ears of WT, CCL17^{E/+}, CCL17^{E/E}, GM-CSF^{-/-}CCL17^{E/+} and GM-CSF^{-/-}CCL17^{E/E} mice were separated into dorsal and ventral halves and mechanically disrupted. Single cell suspensions were obtained by enzymatic digestion. Skin cells were then subjected to antibody-mediated staining and subsequently analyzed by flow cytometry. The flow cytometric gating strategy is depicted in Fig. 5.3. **A:** Absolute numbers of CD45⁺ and CD11c⁺MHCII⁺ cells present in a single mouse ear. **B:** Absolute numbers of different skin myeloid cell populations identified in CD11c⁺MHCII⁺ cells. **C:** Percentages of CCL17/EGFP⁺ cells in skin myeloid cell populations. **D:** Percentage of CCL17/EGFP⁺ cells in cDC1 subpopulations. (n=3-9, two experiments, mean ± SEM) Circles represent data from individual mice. Statistical significance was tested by 2-way ANOVA with Bonferroni's post-hoc test for multiple comparisons (****p<0.0001; ***p<0.001; **p<0.01; *p<0.05).

In line, GM-CSF-deficiency also resulted in a significant loss of CCL17-expressing cells in CD11b⁺ DCs and CCR2⁺ monocytes (see **Fig. 5.8C**). When comparing the monocyte subpopulations P1, P2, and P3, it was recognized that the highest number of cells represent P3 moDCs (see **Fig. 5.5I** and **Fig. 5.8B**). In addition, the percentage of CCL17/EGFP⁺ cells in P3 moDCs was significantly reduced in GM-CSF^{-/-}CCL17^{E/E} mice compared to CCL17^{E/E} mice (see **Fig. 5.8C**). Strikingly, the number of CCL17-expressing cells in CCR2⁻ Mφs, in particular P5 Mφs, was not affected by the loss of GM-CSF (see **Fig. 5.8C**). Aside from its potent role in regulating CCL17 expression, GM-CSF-signaling was also demonstrated to be critically involved in the development and maintenance of lung- and skin-resident CD103⁺ DC^{160,161}. In concordance, percentages of XCR1⁺CD103⁺ cDC1 were also found to be significantly reduced in GM-CSF^{-/-}CCL17^{E/+} and GM-CSF^{-/-}CCL17^{E/E} mice (see **Fig. 5.7D**). In contrast, no effect of CCL17-deficiency on cDC1 subpopulations was observed.

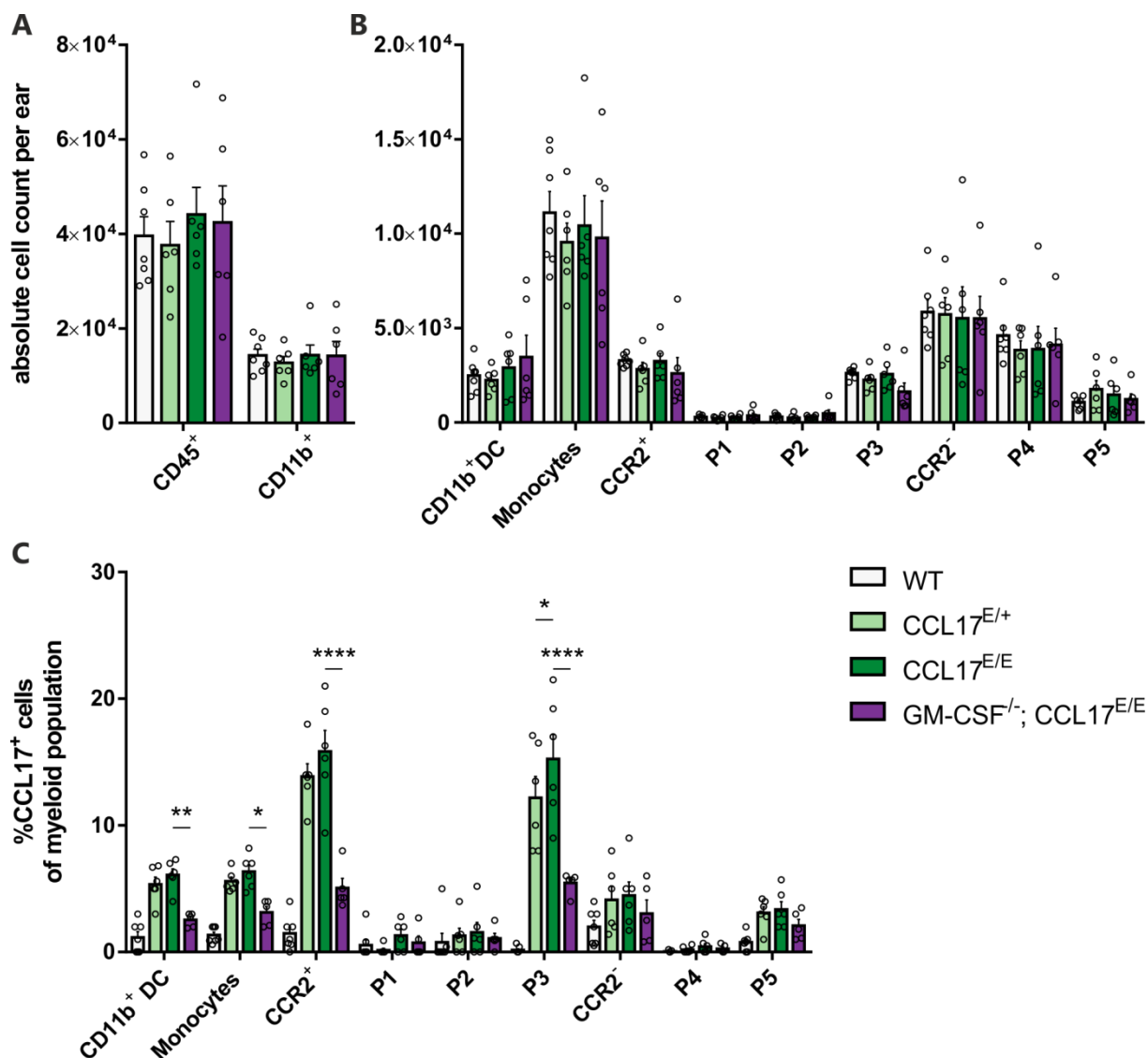


Figure 5.8 | GM-CSF-dependent regulation of CCL17 expression in skin monocyte populations.

Ears of WT, CCL17^{E/+}, CCL17^{E/E} and GM-CSF^{-/-}CCL17^{E/E} mice were separated into dorsal and ventral halves and mechanically disrupted. Single cell suspensions were obtained by enzymatic digestion. Skin cells were then subjected to antibody-mediated staining and subsequently analyzed by flow cytometry. The flow cytometric gating strategy is depicted in Fig. 5.5. **A:** Total CD45⁺ leukocytes and CD11b⁺ cells present in a single mouse ear. **B:** Numbers of skin monocyte populations identified in CD11b⁺ cells. **C:** Percentages of CCL17/EGFP⁺ cells in different populations of skin monocytes and macrophages (monocyte populations: P1: CCR2⁺Ly6C⁺MHCII⁺ P2: CCR2⁺Ly6C⁺MHCII⁺ P3: CCR2⁺Ly6C⁻MHCII⁺ and macrophages: P4: CCR2⁻Ly6C⁻MHCII⁻ and P5: CCR2⁻Ly6C⁻; MHCII⁺). (n=6-7, two experiments, mean \pm SEM) Circles represent data from individual mice. Statistical significance was tested by 2-way ANOVA with Bonferroni's post-hoc test for multiple comparisons (****p<0.0001; **p<0.01; *p<0.05).

5.1.6 CCL17-deficiency has only moderate effects on skin T cell numbers

Several studies highlighted an essential role of CCL17 for the recruitment of peripheral leukocytes into the skin^{50,86,162}. In this sense, it was of interest whether the total number of skin-resident T cells would be affected by the loss of CCL17. Thus, ears of naïve CCL17^{E/+}, CCL17^{E/E}, and WT mice were analyzed for the presence of different T cell populations using flow cytometry. The gating strategy has also been adopted from Bouladoux et al.¹⁵⁷ and is depicted in **Fig. 5.9**.

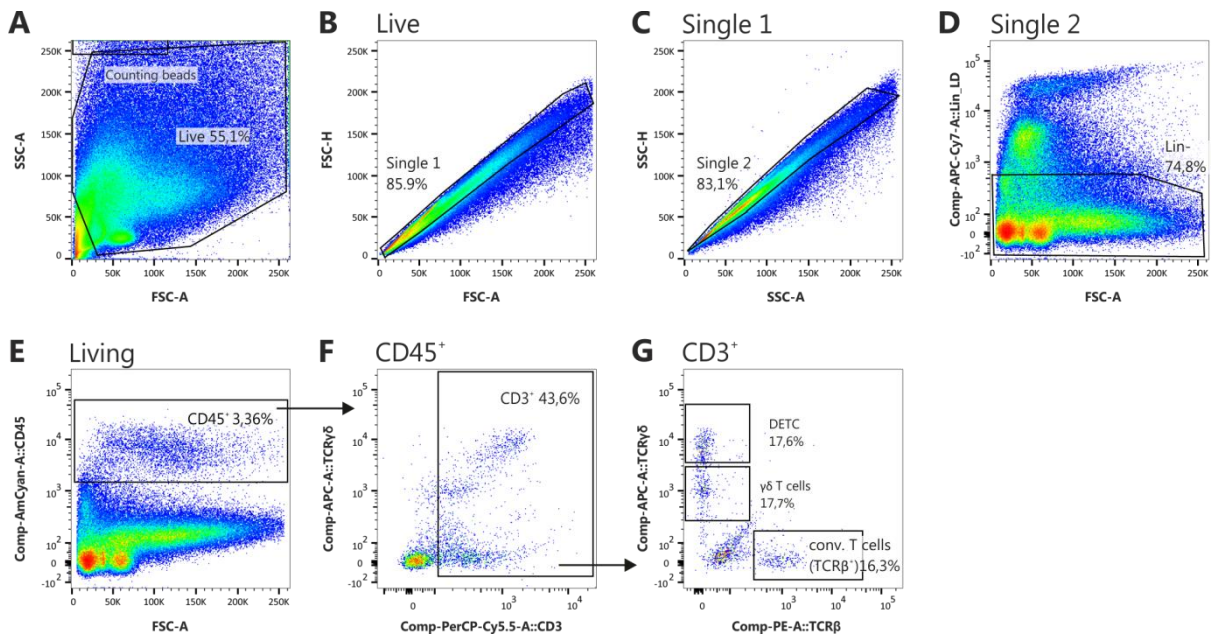


Figure 5.9 | Gating strategy to identify skin-resident T cell populations.

Skin cells were gated based on their characteristic FSC-A and SSC-A profiles (**A**). Two strategies to exclude doublets were applied (**B-C**). A viability stain was used to exclude dead cells (**D**). All living CD45⁺ cells were analyzed for CD3 and TCR $\gamma\delta$ expression (E & F). The CD3⁺TCR $\gamma\delta$ ^{+/+} fraction was further separated in TCR $\gamma\delta$ ^{hi} cells, representing dendritic epidermal T cells (DETC), dermal $\gamma\delta$ T cells and TCR $\gamma\delta$ TCR β ⁺ conventional T cells (G). No CCL17/EGFP⁺ cells were identified in T cell subsets. Representative gating of a WT mouse is shown.

As before, two strategies were used to identify single cells. Skin T cells were identified within all CD45⁺ leukocytes (no lineage stain) by the expression of CD3 and TCR $\gamma\delta$ (see **Fig. 5.9F**). CD3-negative cells were removed from further analysis. CD3⁺ cells were analyzed for the expression of TCR β and TCR $\gamma\delta$ (see **Fig. 5.9G**). Previously described DETCs (CD3⁺ cells in Fig. 5.1B) are characterized by high levels of TCR $\gamma\delta$, whereas dermal $\gamma\delta$ T cells express intermediate levels of TCR $\gamma\delta$ (see **Fig. 5.9G**)^{51,52}. In contrast, conv T cells exclusively express TCR β (see **Fig. 5.9G**).

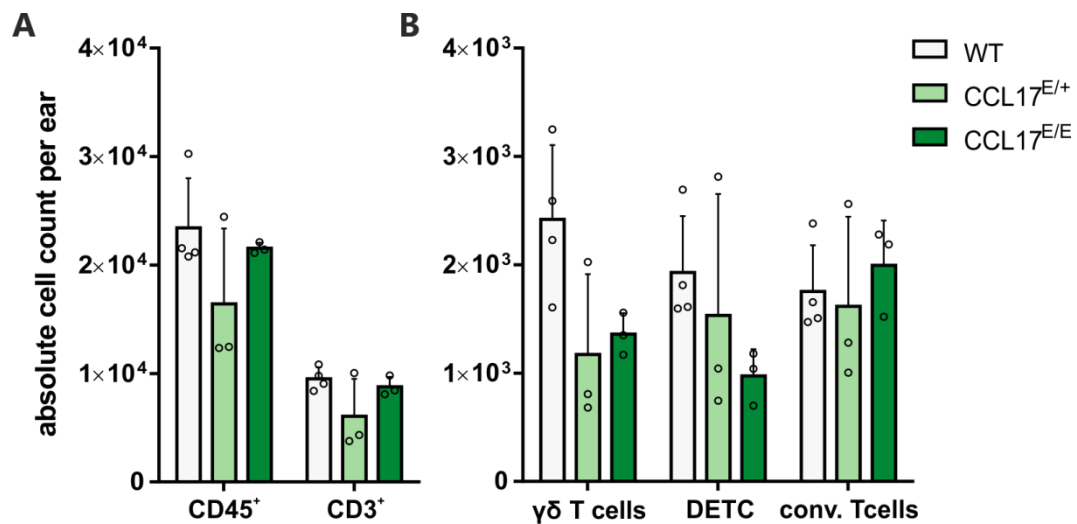


Figure 5.10 | Loss of CCL17 affects skin-resident $\gamma\delta$ T cells.

Ears of WT, CCL17^{E/+} and CCL17^{E/E} mice were separated in dorsal and ventral halves and mechanically disrupted. Single cell suspensions were obtained by enzymatic digestion and subjected to antibody-mediated staining. Cells were subsequently analyzed by flow cytometry. The flow cytometric gating strategy is depicted in Fig. 5.9. **A:** Absolute number of leukocytes (CD45⁺) and total T cells (CD45⁺CD3⁺) present in a single mouse ear. **B:** Absolute numbers of T cell subpopulations identified in total T cells ($\gamma\delta$ T cells: CD3⁺TCR β ⁺TCR $\gamma\delta$ ^{int}, DETC: CD3⁺TCR β ⁺TCR $\gamma\delta$ ^{hi}, conv T cells: CD3⁺TCR β ⁺TCR $\gamma\delta$). (n=3 per group, mean \pm SD) Circles represent data from individual mice.

Quantification of CD45⁺ leukocytes, total CD45⁺CD3⁺ T cells as well as T cell subsets are depicted in **Fig. 5.10**. In agreement with previous experiments, the total number of CD45⁺ leukocytes was similar between the experimental groups (see **Fig. 5.10A**). Also, the number of total CD3⁺ T cells was not significantly affected by the loss of CCL17. However, analysis of T cell subsets revealed reduced numbers of dermal $\gamma\delta$ T cells and DETCs in CCL17^{E/E} mice compared to WT mice, albeit not reaching statistical significance (see **Fig. 5.10B**). Surprisingly, the absolute number of conv T cells was similar between experimental groups. Unexpectedly, the loss of CCL17 had no apparent effect on conv T cells, but on dermal $\gamma\delta$ T cells and DETCs, indicating a role for CCL17 in the maintenance of $\gamma\delta$ T cells under homeostasis.

5.2 Inhibition of CCL17 ameliorates symptoms of contact hypersensitivity *in vivo*

Our lab previously demonstrated a pro-inflammatory role of CCL17 for the development of contact hypersensitivity (CHS) induced by DNFB⁷³. These results suggested that CCL17 may represent a drugable target for the treatment of allergic skin diseases. For the development and testing of new inhibitors, the CHS model is favored over other models of skin inflammation as it is very robust and can be analyzed in a relatively short time. The short-time frame reduces the amount of inhibitor required and is therefore more cost-effective. As stated in the introduction, CHS separates into a sensitization and a challenge phase¹⁶³. For sensitization, mice are treated with DNFB at the abdominal skin to prime a T cell-specific response. Several days later, the sensitized mice are challenged with DNFB on the ear. This induces a severe inflammatory reaction characterized by edema formation and

immune cell infiltration¹⁶⁴. Here, CHS was used to test the efficacy of two novel CCL17-neutralizing RNA aptamers to reduce the inflammatory responses associated with CHS. The two aptamers, MF11 & MF35, were isolated by Markus Funke (MF) from the group of Prof. Dr. Günter Mayer by employing the SELEX technology (Systematic Evolution of Ligands by EXponential enrichment) using a 2'-deoxy-2'-fluoro pyrimidine bearing RNA library⁵⁰. For *in vivo* application, the aptamers were chemically modified and underwent thorough *in vitro* testing regarding their immunogenicity and specificity. These experiments revealed a low immunogenic potential along with high specificity towards murine CCL17⁵⁰. As these experiments were performed in close collaboration with the group of Prof. Günter Mayer and were also published⁵⁰, only the experiments conducted by myself will be presented in the following sections.

5.2.1 MF11 and MF35 inhibit CCL17-dependent chemotaxis of BW cells

After aptamers were demonstrated to specifically bind murine CCL17⁵⁰ *in vitro*, it remained to be shown whether they would also inhibit CCL17-dependent cell migration. Thus, an *in vitro* transwell migration assay using the thymoma cell line BW5147.3 was established. BW5147.3 cells were previously shown to specifically migrate towards increasing gradients of CCL17⁷⁰. During establishment, a minimal concentration of 100 ng/ml murine CCL17 (mCCL17) (\approx 7.5 pmol per well) was found to be required for robust chemotaxis and was used in all further experiments⁵⁰. The transwell assay comprised three different control groups: a medium control without mCCL17, a control containing only mCCL17 and a second positive control which contained mCCL17 and the commercially available CCL17-specific neutralizing antibody MAB529 at a molar ratio of 1:1 (antibody:mCCL17). In all experiments, MAB529 and aptamers were added to the lower compartment of the transwell system which already contained 7.5 pmol mCCL17. Following 2 hours of migration, cells which had entered the lower compartment were harvested and counted using flow cytometry.

For analysis, the aptamer-mediated inhibition of migration was calculated as percentage of migrated cells in comparison to cells that migrated towards mCCL17 alone (set to 100%). Both aptamers were tested at a molar ratio of 1:1 (7.5 pmol/well) and 1:10 (0.75 pmol/well) (aptamer:mCCL17) and compared to bulk RNA sequences of the non-enriched library from selection cycle 1 of the SELEX⁵⁰. As expected, the addition of MAB529 almost completely inhibited the CCL17-dependent migration of BW5147.3 cells compared to the medium control (see **Fig. 5.11**). Strikingly, MF11 and MF35 also significantly inhibited transmigration of BW5147.3 cells at a molar ratio of 1:1. Of note, MF11 appeared to be more potent than MF35 as it was still able to inhibit migration at a molar ratio of 1:10. These results demonstrated that both aptamers are not only able to specifically bind mCCL17⁵⁰ but can also inhibit CCL17-dependent migration.

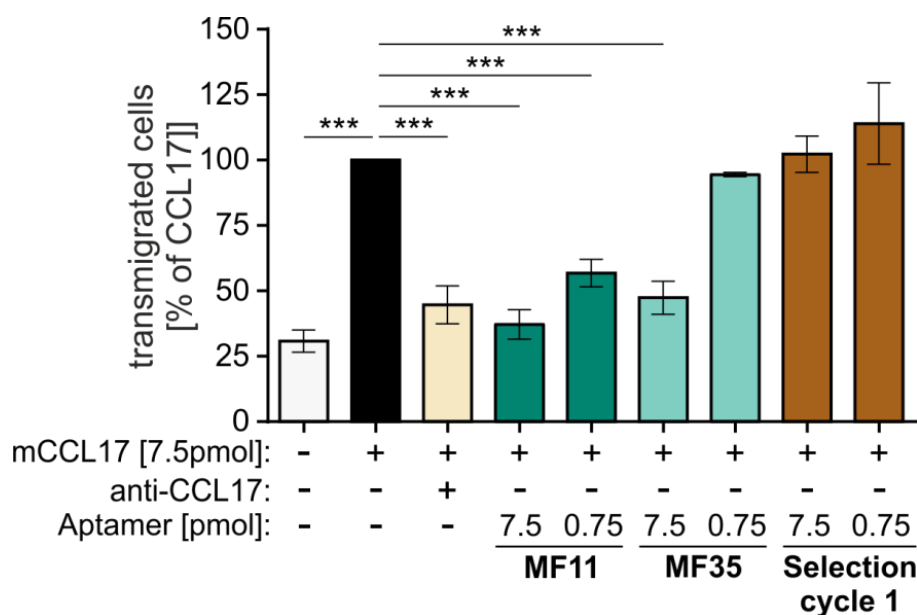


Figure 5.11 | Aptamers inhibit CCL17-dependent cell migration in vitro.

A transwell system was used to measure migration of BW5147.3 cells towards 100 ng/ml (7.5 pmol/well) mCCL17. The unmodified and full-length aptamers MF11 and MF35 as well as bulk RNA sequences from selection cycle 1 were tested at equimolar concentrations (7.5 pmol) and at a molar ratio of 1:10 (aptamer:mCCL17). As a control, 7.5 pmol of the anti-CCL17 monoclonal antibody MAB529 (1.88 μ g/ml) was added to the lower compartment. After 2h, transmigrated cells in the lower compartment were counted using flow cytometry and calculated as percent of migration towards mCCL17 alone ($n=3-5$, mean \pm SEM). Statistical significance was tested by One-way ANOVA with Bonferroni's post-hoc test for multiple comparisons (** $p < 0.001$).

5.2.2 CCL17-deficient mice are protected from CHS pathology

To demonstrate the efficacy of the two aptamers to neutralize CCL17 *in vivo*, CHS was performed in aptamer-treated WT mice and CCL17-deficient (CCL17^{E/E}) mice. The ear swelling response was measured on the right ear on days 1, 2, and 3 after DNFB challenge. Left ears were treated with vehicle (acetone:olive oil, 5:1) only and served as a control. As expected, CCL17^{E/E} mice showed a significantly reduced ear swelling response compared to control animals on day 1 and 2 after DNFB challenge (see **Fig. 5.12A**). Because of the postulated role of CCL17 in the recruitment of peripheral leukocytes into the skin, flow cytometry was used to analyze cell recruitment into challenged ears on day 4 after DNFB treatment (see **Fig. 5.12B and C**). In addition to the gating strategy used for skin-resident T cells (see **Fig. 5.9**), total CD3⁺ T cells were analyzed for the expression of CD8 (see **Fig. 5.12C**) as CD8⁺ cytotoxic T cells were demonstrated to be major effector cells of CHS^{165,166}. Compared to vehicle treated ears, a significant increase of CD45⁺ leukocytes and CD8⁺ T cells was observed in DNFB-treated ears isolated from both, WT and CCL17^{E/E} mice (see **Fig. 5.12B and C**). Strikingly, the ears of DNFB-treated CCL17^{E/E} mice harbored significantly fewer CD45⁺ leukocytes and CD8⁺ T cells compared to DNFB-treated WT mice. These results further strengthened the critical role of CCL17 for the recruitment of peripheral leukocytes and also allowed to test the inhibitory capacity of CCL17-specific aptamers *in vivo* using CCL17^{E/E} mice as a control group.

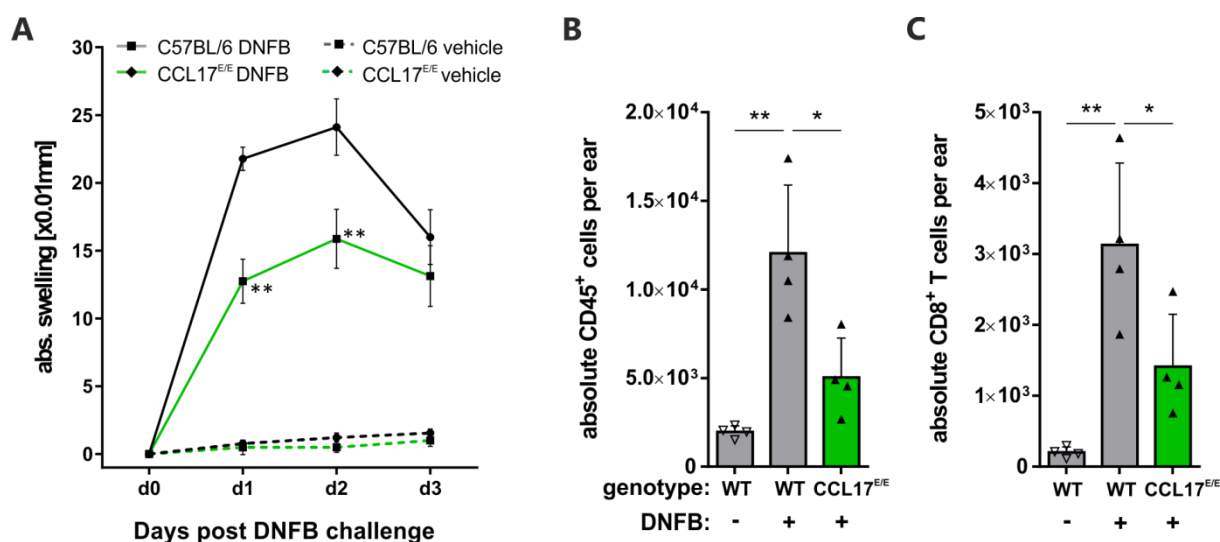


Figure 5.12 | CCL17-deficient mice are protected from contact hypersensitivity.

CHS was performed with C57BL/6 WT and CCL17^{E/E} mice. All mice were sensitized with DNFB on day -5 and -4. At d0, mice were challenged with DNFB at the right ear (solid lines in A), whereas the vehicle was applied to the left ear as a control (dashed lines in A) **A**: Time course of the ear swelling response at d1-d3 (24h-72h) post DNFB challenge of WT and CCL17^{E/E} mice. (n=8-9 animals per group, mean ± SEM). One representative of three experiments is shown. Data was tested for statistical significance by 2-way ANOVA with Bonferroni's post-hoc test for multiple comparisons (**p<0.01). **B & C**: Flow cytometric analysis of the ears. At day 4 the ears were digested and the isolated cells analyzed via flow cytometry. Absolute numbers of CD45⁺ leukocytes (B) and CD3⁺CD8⁺ T cells (C) per ear are depicted. (n=4 per group, mean ± SD). Data was tested for statistical significance by One-way ANOVA with Bonferroni's post-hoc test for multiple comparisons (**p<0.01; *p<0.05).

5.2.3 Aptamer-mediated inhibition of CCL17 reduces symptoms of CHS *in vivo*

As the originally selected aptamers, MF11 and MF35 were not optimized for *in vivo* use, it was decided to truncate and modify the aptamers⁵⁰. Without altering their secondary structure, both aptamers were shortened in a way that maintained the extended hairpin structure necessary to bind mCCL17⁵⁰. Additional details on the truncation process can be found in Fülle et al., 2017⁵⁰.

The shortened aptamers, MF11.46 and MF35.47, are less than 50 nucleotides (46 and 47 for MF11 and MF35, respectively) and were thus suitable for chemical synthesis⁵⁰. MF11.46 and MF35.47 were also tested for their capacity to specifically bind mCCL17. As for the original aptamers, a high specificity of MF11.46 and MF35.47 for mCCL17 was found⁵⁰. Whereas the truncation process yielded aptamers suitable for chemical synthesis, they presumably possess a rather short half-life *in vivo*⁵⁰. The introduction of a polyethyleneglycol (PEG)-tail and cap structures at the 5'- and 3'-terminal ends were previously demonstrated to significantly prolong the half-life of aptamers *in vivo*^{50,167}. The extended half-life is believed to result from an enhanced resistance towards exonuclease activity and reduced renal clearance¹⁶⁷. Thus, a 3'-dT-cap structure and a 20kDa 5'-PEG-tail were added to MF11.46 and MF35.47, generating modified versions of the shortened aptamers (MF11.46.m and MF35.47.m). As before, the functionality of the shortened and modified aptamers was also tested in the previously established transwell assay. Here, MF11.46.m and MF35.47.m were tested at molar ratios of 10:1 (only MF35.47.m) and 1:1, 1:10 and 1:100 (MF35.47.m & MF11.46.m), containing 75 pmol, 7.5 pmol, 0.75

pmol or 0.075 pmol aptamer per well, respectively. As depicted in **Fig. 5.13A**, both aptamers efficiently inhibited CCL17-dependent migration of BW5147.3 cells. Importantly, an equally modified, but non-functional scrambled aptamer (ctrl. apt.) did not inhibit migration of BW5147.3 cells, indicating that the shortening and the modifications had no impact on aptamer efficacy.

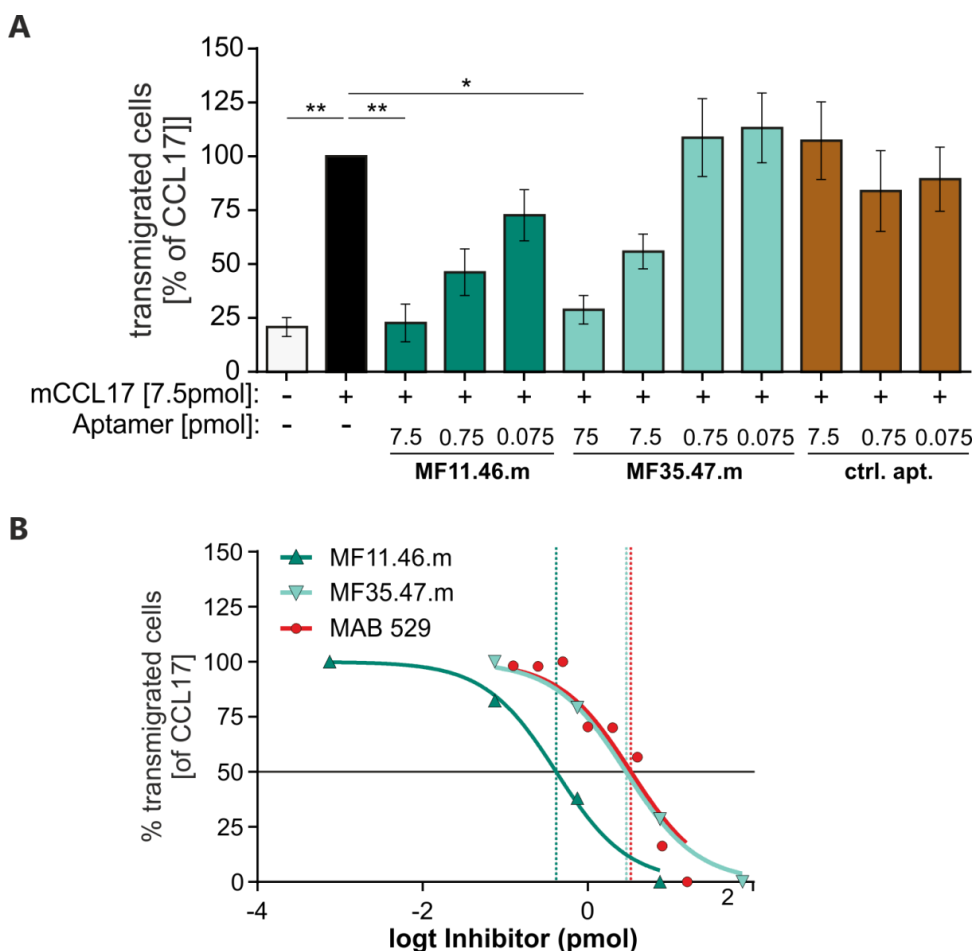


Figure 5.13 | MF11.46.m and MF35.47.m efficiently inhibit CCL17-dependent cell migration *in vitro*.

A: MF11.46.m and MF35.47.m were tested for their capacity to inhibit CCL17-dependent migration of BW5147.3 cells in a transwell system. Aptamers were tested at molar ratios of 1:1 (7.5pmol), 1:10 (0.75pmol) and 1:100 (0.075pmol) (aptamer:mCCL17). A non-functional control aptamer served as a negative control. The transmigrated cells were counted and calculated as percent of migration towards CCL17 alone (n=3, mean \pm SEM). Statistical significance was tested by One-way ANOVA with Bonferroni's post-hoc test for multiple comparisons (**p<0.01; *p<0.05). **B:** The half maximal inhibitory concentration (IC₅₀) of MAB529, MF11.46.m and MF35.47.m was determined using the transwell migration assay. Increasing concentrations of MAB529, MF11.46.m and MF35.47.m were tested to inhibit migration towards 100ng/ml mCCL17 (=7.5pmol). After 2h, the transmigrated cells were counted and total cell counts were normalized to the medium control and calculated as percent of migration towards mCCL17 alone. IC₅₀ values were calculated using GraphPad Prism 6. One representative experiment out of three is shown.

To this end, the IC₅₀ values (half maximal inhibitory concentration) of MF11.46.m and MF35.47.m were determined and directly compared to MAB529 (see **Fig. 5.13B**). The IC₅₀ value of MAB529 and MF35.47m was found to be very similar with 3.3 and 2.9 pmol, respectively. In contrast, MF11.46.m had a much higher binding efficiency with an approximately 8-fold lower IC₅₀ value of 0.42 pmol. This was in line with MF11.46.m also showing a much higher efficiency to inhibit CCL17-dependent migration *in vitro* (see **Fig. 5.13A**).

Before *in vivo* application, both aptamers were tested for their capability to induce an inflammatory response in immortalized murine embryonic Mφs. As aptamers could bind and activate cell surface or intracellular PRR, such as TLR3, 7 and 9 or RIG-I-like receptors, TNF levels were measured in the supernatant to determine the immunogenicity of the aptamers. The aptamers did not elicit TNF secretion and were therefore considered to be non-immunogenic⁵⁰.

After having demonstrated aptamer functionality *in vitro*, their potential to inhibit CCL17-dependent migration *in vivo* was tested. For this, the previously established CHS assay was used. Before testing the aptamers *in vivo*, the optimal time point to inhibit CCL17-mediated functions was determined using MAB529. Therefore, WT mice were injected i.p. with 200 µg of MAB529 either immediately before sensitization or before challenging the mice with DNFB. It turned out that neutralization of CCL17 shortly before DNFB challenge resulted in a reduction of the ear swelling response⁵⁰. Therefore, the efficacy of the aptamers to inhibit CCL17-induced responses was tested before DNFB challenge. To account for the shorter half-life of aptamers compared to monoclonal antibodies such as MAB529, WT mice received two i.p. injections of 5 nmol aptamer/mouse 1 h prior and 12 h post DNFB treatment of the ear. As a control, WT and CCL17^{E/E} mice were injected with PBS.

Treatment with MF35.47.m and MF11.46.m significantly inhibited the ear swelling response compared to mice which received the scrambled control aptamer (see **Fig. 5.14A**). Interestingly, treatment with MF35.47.m inhibited the ear swelling response more efficiently than MF11.46.m. This result was somehow unexpected as MF35.47.m was about 10-fold less efficient *in vitro* compared to MF11.46.m (see **Fig. 5.11 and 5.13A**). Consistent with previous experiments, CCL17^{E/E} mice displayed an attenuated ear swelling response. In line, flow cytometric analysis of the ears on day 4 post DNFB challenge revealed a clear reduction of CD45⁺ leukocytes in ear tissue of CCL17^{E/E} and MF35.47.m-treated mice and, to a lesser extent in MF11.46.m-treated mice (see **Fig. 5.14B**). Although only few CD8⁺ T cells are left in the swollen ear at day 4 after DNFB challenge, CCL17^{E/E} and MF35.47.m-treated mice harbored reduced amounts of CD8⁺ T cells compared to mice treated with the scrambled aptamer. In additional experiments, the dose of aptamer required to reduce CHS-associated symptoms was further titrated⁵⁰. Whereas a dose of 1 nmol aptamer per mouse resulted in a slight reduction of ear swelling, a minimal dose of 5 nmol per mouse proved to be necessary to observe significant differences compared to the scrambled aptamer⁵⁰. In conclusion, these experiments demonstrated that both aptamers are able to inhibit CCL17 functions *in vivo* albeit MF35.47.m proved to be more efficient than MF11.46.m.

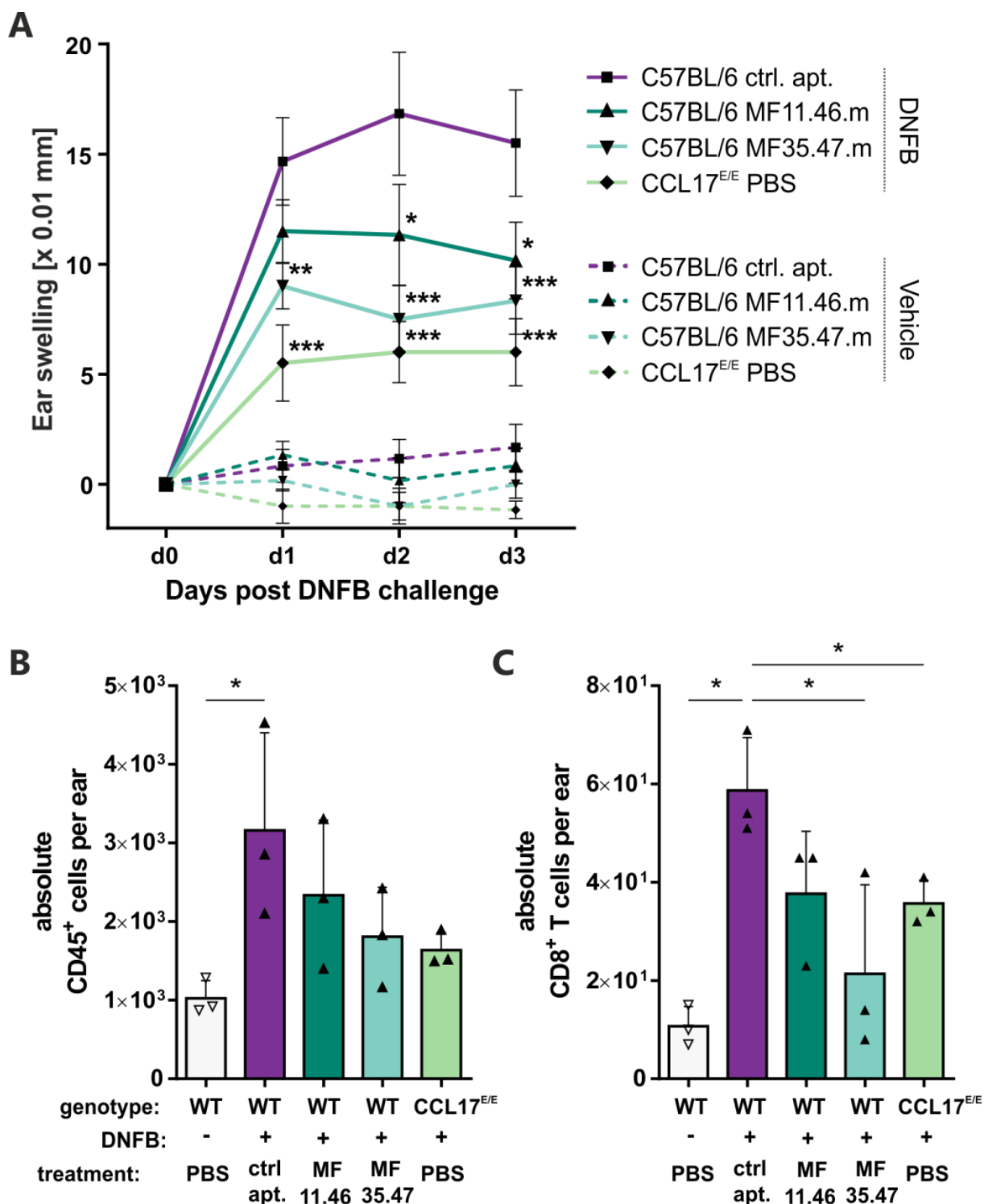


Figure 5.14 | Aptamer mediated inhibition of CCL17 reduces ear swelling and leucocyte infiltration.

CHS was performed with C57BL/6 WT and CCL17^{E/E} mice. All mice were sensitized with DNFB on day -8 and -7. WT mice received (i.p.) 5 nmol of MF11.46.m, MF35.47.m, or the control aptamer (in 200 μ l PBS) 1h before and 12h after DNFB challenge. CCL17^{E/E} mice were injected with 200 μ l PBS. **A**: Time course (24h-72h) of the ear swelling response of WT and CCL17^{E/E} mice after DNFB (solid lines) or vehicle (dashed lines) application. (n=6 per group, mean \pm SEM). One representative of three experiments is shown. Data was tested for statistical significance by 2-way ANOVA with Bonferroni's post-hoc test for multiple comparisons (**p<0.001; **p<0.01; *p<0.05). **B & C**: Flow cytometric analysis of ears biopsies. On day 4 after challenge the ears were digested and the isolated cells analyzed via flow cytometry. Absolute numbers of CD45⁺ (**B**) and CD3⁺CD8⁺ (**C**) cells per ear are depicted. (n=3 per group, mean \pm SD). Data was tested for statistical significance by One-way ANOVA with Bonferroni's post-hoc test for multiple comparisons (*p<0.05).

5.3 Opposing roles of CCR4 and its two known ligands in the context of contact hypersensitivity

The chemokines CCL17 and CCL22 are both ligands of the chemokine receptor CCR4. Interestingly, different immune regulatory functions have been attributed to the two chemokines. CCL17 has long been shown to promote various inflammatory and allergic diseases by being critically involved in the induction of T helper and cytotoxic T cell responses^{89,168}. In contrast, several studies found CCL22 to be present in immunosuppressive environments, for example, in various tumor tissues⁷⁹. Here, CCL22 was demonstrated to be produced by intratumoral DC and to dampen immune responses through the recruitment of regulatory T cells. With regard to CCR4 activation, it was shown that CCL22 induces a more rapid desensitization and internalization of CCR4 compared to CCL17^{81,169}. These differences of CCL17 and CCL22-induced signaling as well as the fact that CCR4-deficiency was not associated with amelioration of skin inflammation⁴⁵, underlined the need to perform a more comprehensive investigation of the CCL17/22-CCR4 axis *in vivo*. Thus, the TALEN (T_ranscription a_ctivator-l_ike e_ffector n_uclease) technology was employed to generate CCL17/22-double-deficient mice lines. To facilitate the process, it was decided to target the *Ccl22* locus in CCL17^{E/E} mice which would directly generate CCL17^{E/E}/22-double-deficient mice (referred to as CCL17^{E/E}/22^{-/-} mice). TALEN-mediated gene-targeting yielded several different CCL17^{E/E}/22^{-/-} mice lines, all harboring distinct mutations in the *Ccl22* locus. However, it was decided to perform the present experiments only with two lines, harboring either the "F" (CCL17^{E/E}/22^{F/F}) or "G" (CCL17^{E/E}/22^{G/G}) mutation (see 3.11.1 for details on the mutations). Loss of CCL17 and CCL22 was confirmed in several *in vitro* experiments, including ELISA measurements and transwell assays (data not shown). A comparison of the effect of two independent mutations of the same gene was performed to reduce the likelihood of possible off-target effects of the TALEN constructs, although this cannot be fully excluded.

As the experiments aimed to shed light on the opposing roles of CCR4 and its ligands, it was decided to directly compare CCL17^{E/E}/22^{-/-} mice with CCR4^{-/-} mice in the DNFB-induced CHS model. In all experiments, WT and CCL17^{E/E} mice were included as a control.

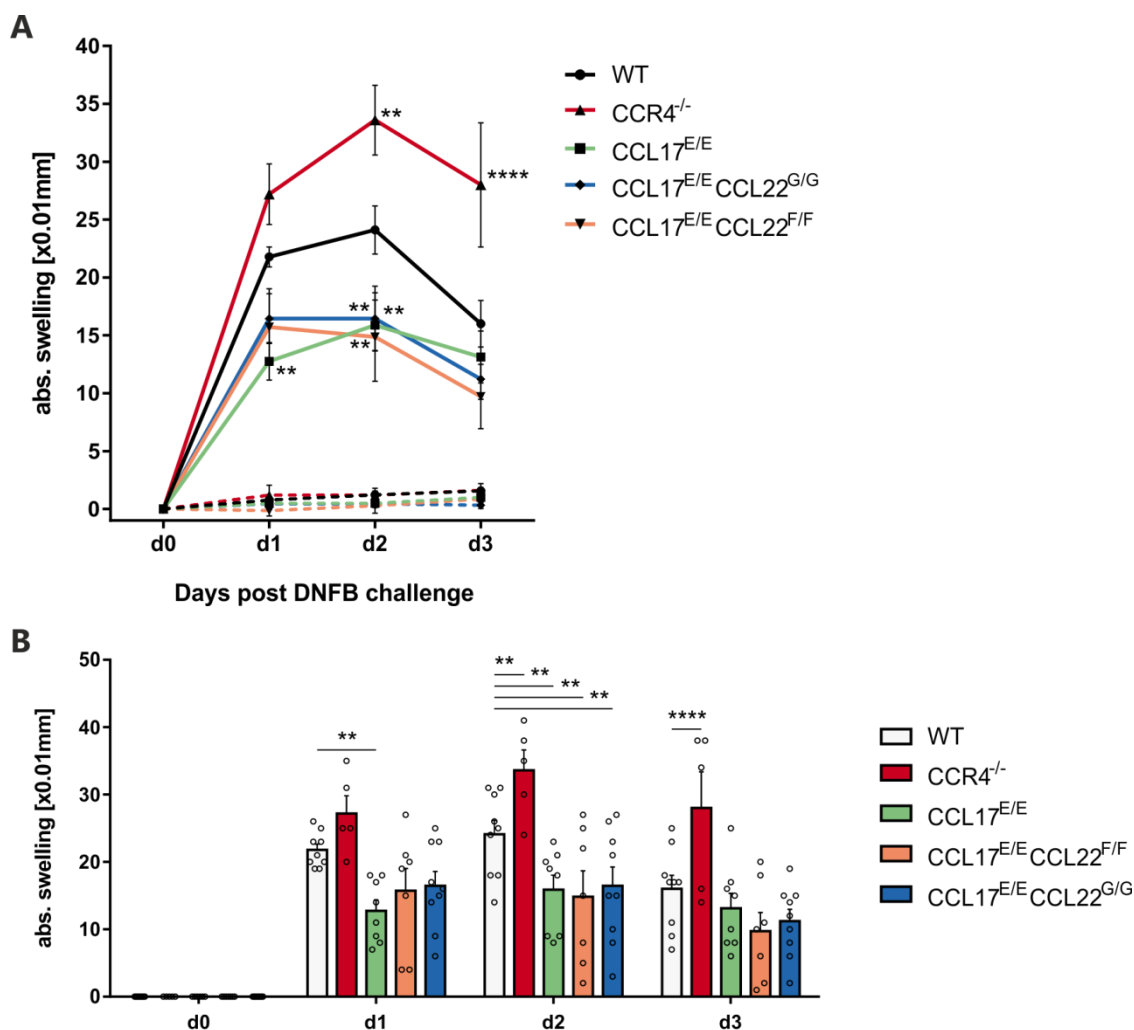


Figure 5.15 | Ongoing CHS reactions in CCR4-deficient and CCL17/22-double-deficient mice.

CHS was performed with C57BL/6 WT, CCR4^{-/-}, CCL17^{E/E}, CCL17^{E/E}CCL22^{F/F} and CCL17^{E/E}CCL22^{G/G} mice. All mice were sensitized with DNFB on day -5 and -4. On day 0 after sensitization ears were either treated with DNFB or solvent (acetone:olive oil, 5:1). **A**: Three day time course (24h-72h, respectively) of the ear swelling response of all experimental mice after DNFB (solid lines) or vehicle (dashed lines) treatment. **B**: Quantification of the ear swelling responses depicted in A. Circles represent data from individual mice. (n=5-9 per group, mean ± SEM). One representative of three experiments is shown. Data was tested for statistical significance by 2-way ANOVA with Bonferroni's post-hoc test for multiple comparisons (****p<0.0001; ***p<0.001; **p<0.01).

As depicted in **Fig. 5.15A and B**, DNFB treatment induced an ear swelling response in all experimental groups over the course of three days (d1-d3). In line with previous results, CCL17^{E/E} mice showed a milder progression of skin inflammation whereas CCR4-deficiency resulted in a significantly enhanced ear swelling response compared to WT mice. Unexpectedly, CCL17^{E/E}/22^{F/F} and CCL17^{E/E}/22^{G/G} mice also showed an amelioration of the ear swelling response, which was comparable to CCL17^{E/E} mice. Furthermore, it was noted, that the ear swelling response of WT mice returned to the thickness of CCL17^{E/E} and CCL17^{E/E}/22^{-/-} animals at day 3, whereas an increased swelling response persisted in three out of five CCR4^{-/-} mice.

5.4 Analysis of immune cell infiltrates after DNFB application

Similar to the characterization of CCL17⁺ cells in naïve murine skin (see 5.1) the composition and absolute numbers of immune cells were analyzed in the ears of CCL17^{E/E}/22^{F/F}, CCL17^{E/E}/22^{G/G}, CCR4^{-/-}, CCL17^{E/E} and WT mice after DNFB treatment. As before, ears were excised at day 4 after DNFB challenge and cells were subjected to staining for flow cytometry. To get a comprehensive overview of the cell composition present in the inflamed ear, the previously established gating strategies were utilized.

5.4.1 Analysis of T cells in ears of CCR4^{-/-}, CCL17^{E/E} and CCL17^{E/E}/22^{-/-} mice after DNFB treatment

To identify T cell subsets present in the inflamed skin, the same gating strategy as shown in **Fig. 5.9** was employed. As expected, all DNFB-treated ears harbored increased numbers of CD45⁺ leukocytes, total CD3⁺ T cells as well as CD3⁺TCRβ⁺ conv T cells compared to solvent-treated ears (see **Fig. 5.16A**). Strikingly, however, absolute numbers of CD45⁺ leukocytes were significantly higher in DNFB-treated CCR4^{-/-} mice compared to WT mice. Also, CCL17^{E/E}, CCL17^{E/E}/22^{F/F}, and CCL17^{E/E}/22^{G/G} mice contained significantly reduced numbers of CD45⁺ leukocytes compared to CCR4^{-/-} mice. Analysis of total T cells and conv T cell revealed a similar picture albeit not statistically significant. Interestingly, the ratio of infiltrating leukocytes and total CD3⁺ T cells somewhat reflected the ear swelling response as depicted in **Fig. 15B**, suggesting an important role of these cells for the opposing phenotypes observed in CCR4^{-/-} and CCL17^{E/E}/22^{-/-} mice. In contrast to conv T cells, overall numbers of dermal γδ T cells were not affected by DNFB application (see **Fig. 5.16B**). In line with the analysis of T cells in the naïve skin (see 5.1.6), absolute numbers of dermal γδ T cells were reduced in CCR4^{-/-}, CCL17^{E/E} and CCL17^{E/E}/22^{G/G} mice independently of DNFB treatment (see **Fig. 5.16B**). Interestingly, control ears of CCL17^{E/E}, CCL17^{E/E}/22^{F/F}, and CCL17^{E/E}/22^{G/G} mice contained less DETCs (TCRγδ^{hi}) compared to WT mice, whereas DNFB treatment resulted in reduced numbers of DETC in all experimental groups (see **Fig. 5.16B**). In conclusion, the experiments confirmed the critical role of CCL17 for the recruitment of T cells in the context of skin inflammation. However, loss of CCL17 and CCL22 in CCL17^{E/E}/22^{-/-} mice had no additional impact on T cells numbers in skin compared to CCL17^{E/E} mice.

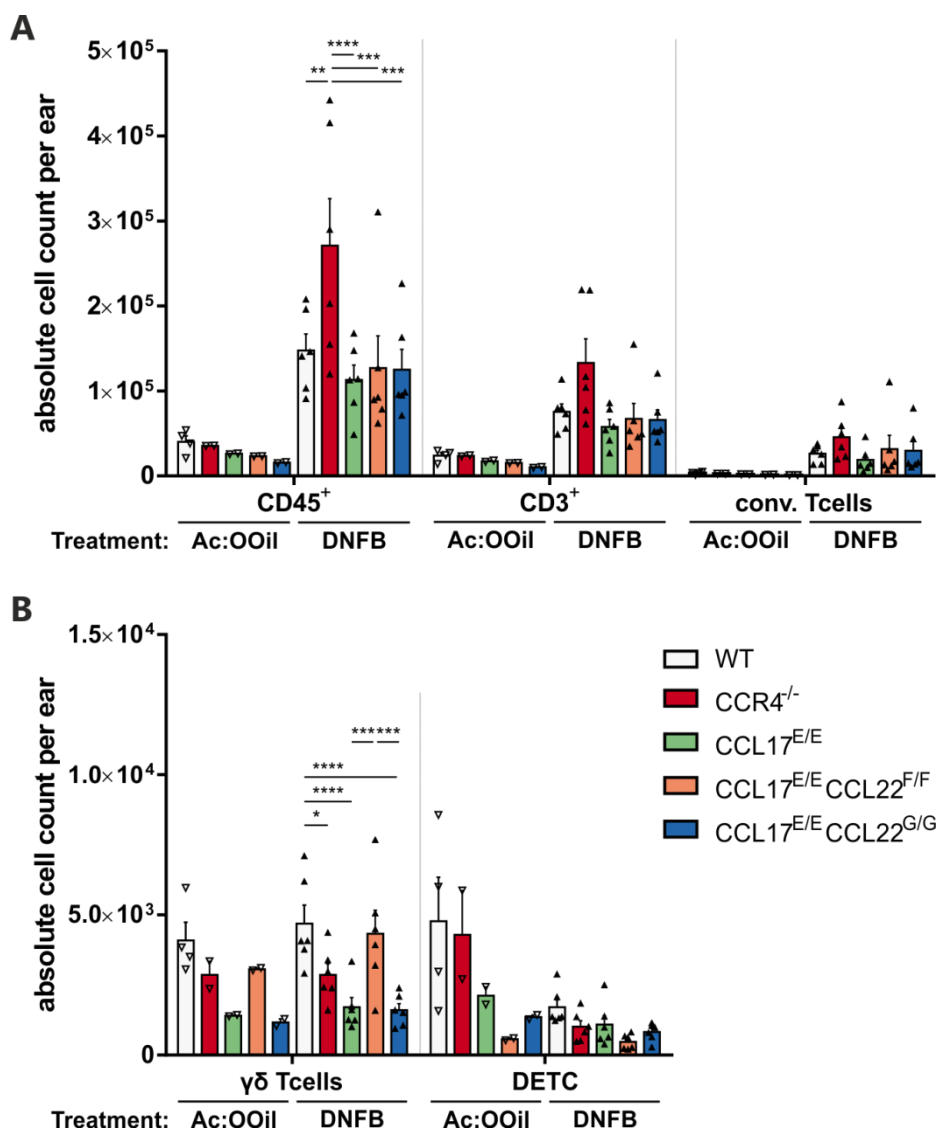


Figure 5.16 | Quantification of skin T cell subsets after DNFB treatment.

CHS assay was performed with C57BL/6 WT, CCR4^{-/-}, CCL17^{E/E}, CCL17^{E/E}CCL22^{F/F} and CCL17^{E/E}CCL22^{G/G} mice. Mice were sensitized with DNFB on day -5 and -4. On day 4 after DNFB challenge, ears were digested and isolated cells subjected to staining for flow cytometric analysis of. **A:** Absolute numbers of total CD45⁺ leukocytes, total CD3⁺ T cells and CD3⁺TCRβ⁺ conventional T cells. **B:** Absolute numbers of γδ T cells (TCRγδ^{int}) and TCRγδ^{hi} dendritic epidermal T cells (DETC). (n=2-4 for solvent treated groups (acetone:olive oil, 5:1), mean ± SD and n=5 for DNFB-treated groups, mean ± SEM). Only data from DNFB-treated groups were tested for statistical significance by 2-way ANOVA with Bonferroni's post-hoc test for multiple comparisons (****p<0.0001; ***p<0.001; **p<0.01).

5.4.2 Analysis of myeloid cells in ears of CCR4^{-/-}, CCL17^{E/E} and CCL17^{E/E}/22^{-/-} mice after DNFB treatment

For the analysis of myeloid cells in the skin of CCR4^{-/-} and CCL17^{E/E}/22^{-/-} mice, the previously established gating strategy for the analysis of naïve ears (see 5.1.3) was utilized. Confirming the analysis of T cells, CD45⁺ leukocytes were also strongly enriched in DNFB treated ears of all experimental groups albeit the variation within the groups was slightly higher compared to the T cell staining. DNFB treatment resulted in increased numbers of total CD11c⁺MHCII⁺ cells (see **Fig. 5.17A**) as well as DN DC, cDC1 and, in particular, CD11b⁺ cells (see **Fig. 5.17B**). Except for CD11b⁺ cells, no significant differences within the groups analyzed were found. In the case of CD11b⁺ cells, the absence of both chemokines, but not CCR4 led to significantly reduced numbers of CD11b⁺ cells after DNFB application compared to WT animals. In contrast, the absolute number of LCs was comparable between solvent and DNFB treated ears in all experimental groups. This was somehow unexpected as CCL17 was previously demonstrated to be required for the emigration of skin-resident LCs⁴⁹.

In addition to the absolute numbers of skin myeloid cells, the effect of DNFB treatment on CCL17 expression was analyzed. Thus, the percentage of CCL17/EGFP⁺ cells within the different myeloid cell subsets was determined (see **Fig. 5.18**). In concordance with previous analyses of naïve skin, CCL17/EGFP⁺ cells were identified in all myeloid cell subsets. Interestingly, the additional absence of CCL22 in CCL17^{E/E}/22^{F/F} and CCL17^{E/E}/22^{G/G} mice had no apparent effect on the number of CCL17/EGFP⁺ cells compared to CCL17^{E/E} mice. Whereas DNFB treatment led to increased numbers of DN DC, cDC1 and CD11b⁺ cells, the percentage of CCL17/EGFP⁺ cells was not or only slightly affected by DNFB application (see **Fig. 5.18**). Remarkably, however, LCs contained increased numbers of CCL17/EGFP⁺ cells after DNFB treatment.

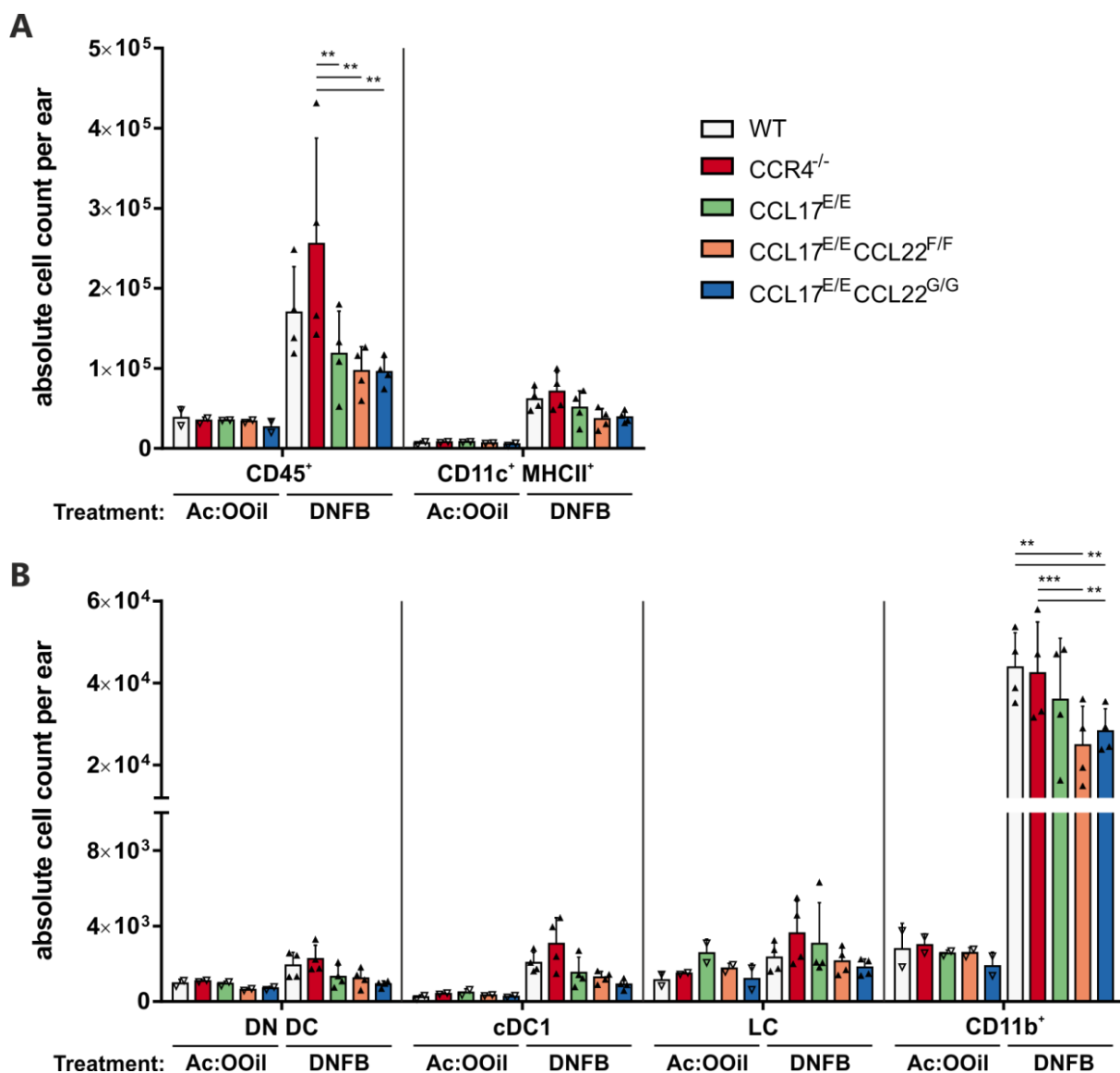


Figure 5.17 | Quantification of skin myeloid cell subsets after DNFB treatment.

CHS was performed with C57BL/6 WT, CCR4^{-/-}, CCL17^{E/E}, CCL17^{E/E}CCL22^{F/F} and CCL17^{E/E}CCL22^{G/G} mice. Mice were sensitized with DNFB on day -5 and -4. On day 0 after sensitization ears were either treated with DNFB or solvent (acetone:olive oil, 5:1). On day 4 after DNFB challenge ears were digested and isolated cells subjected to staining for flow cytometry. **A:** Absolute numbers of total CD45⁺ leukocytes and total CD11c⁺MHCII⁺ cells. **B:** Absolute numbers of CD24⁻CD11b⁻ double negative DC (DN DC), CD24⁺CD11b⁻ type 1 conventional DC (cDC1), CD24⁺CD11b^{hi} Langerhans cells (LC) and CD11b⁺ cells. (n=2-4 for solvent treated groups, mean ± SD and n=5 for DNFB-treated groups, mean ± SEM). Only data from DNFB-treated groups were tested for statistical significance by 2-way ANOVA with Bonferroni's post-hoc test for multiple comparisons (***p<0.001; **p<0.01).

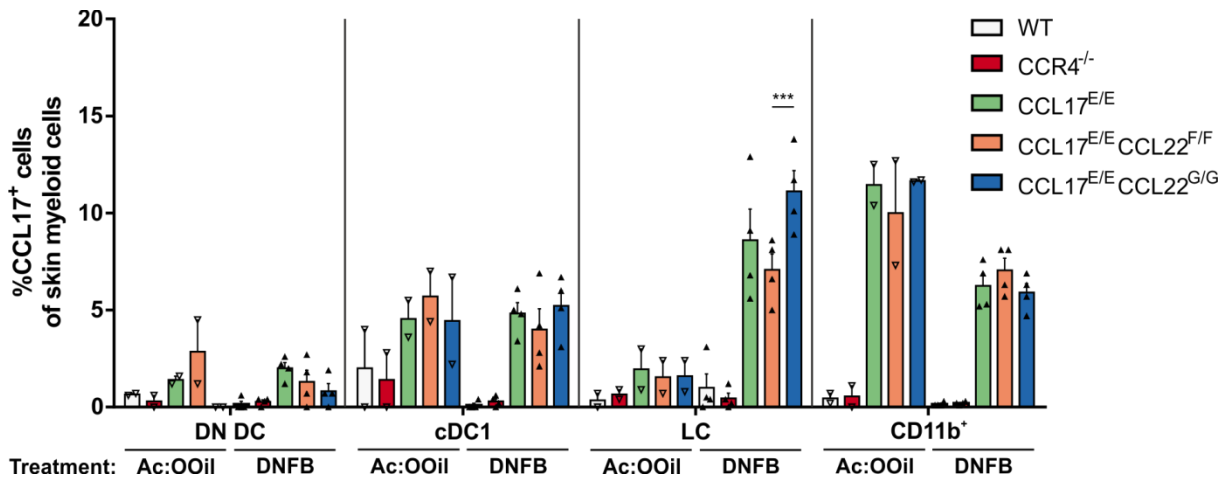


Figure 5.18 | Percentages of CCL17/EGFP⁺ cells within skin myeloid populations after DNFB treatment.

CHS was performed with C57BL/6 WT, CCR4^{-/-}, CCL17^{E/E}, CCL17^{E/E}CCL22^{F/F} and CCL17^{E/E}CCL22^{G/G} mice. Mice were sensitized with DNFB on day -5 and -4. On day 0 after sensitization ears were either treated with DNFB or solvent (acetone:olive oil, 5:1). On day 4 after DNFB challenge ears were digested and isolated cells subjected to staining for flow cytometry. Depicted are the percentages of CCL17/EGFP⁺ cells within the identified skin myeloid cell subsets. WT and CCR4^{-/-} mice served as negative controls and are depicted to indicate background fluorescence. (n=2-4 for solvent treated groups, mean ± SD and n=5 for DNFB-treated groups, mean ± SEM). Only data from DNFB-treated groups were tested for statistical significance by 2-way ANOVA with Bonferroni's post-hoc test for multiple comparisons (***) (***p<0.001).

5.4.3 Analysis of monocyte populations in ears of CCR4^{-/-}, CCL17^{E/E} and CCL17^{E/E}/22^{-/-} mice after DNFB treatment

As before, the heterogeneity of CD11b⁺ skin cells demanded a more precise analysis (see 5.1.4). Thus, the isolated cells of the inflamed ears were also subjected to the previously established monocyte staining. Consistent with previous analyses, the number of CD45⁺ leukocytes was strongly increased in DNFB treated ears of all experimental groups (see **Fig. 5.19A**) and CCR4^{-/-} mice showed highest numbers of CD45⁺ cells. Also, the absolute number of CD24^{lo}CD11b⁺ cells was enriched after DNFB treatment albeit no difference was detected between the analyzed groups (see **Fig. 5.19A**). Separation of CD11b⁺ cells into CD11b⁺ DC and total monocytes revealed that DNFB treatment also resulted in an increase of both cell types compared to solvent control (see **Fig. 5.19B**). Interestingly, CD11b⁺ DCs were increased in ear samples of DNFB-treated CCR4^{-/-} mice compared to WT controls.

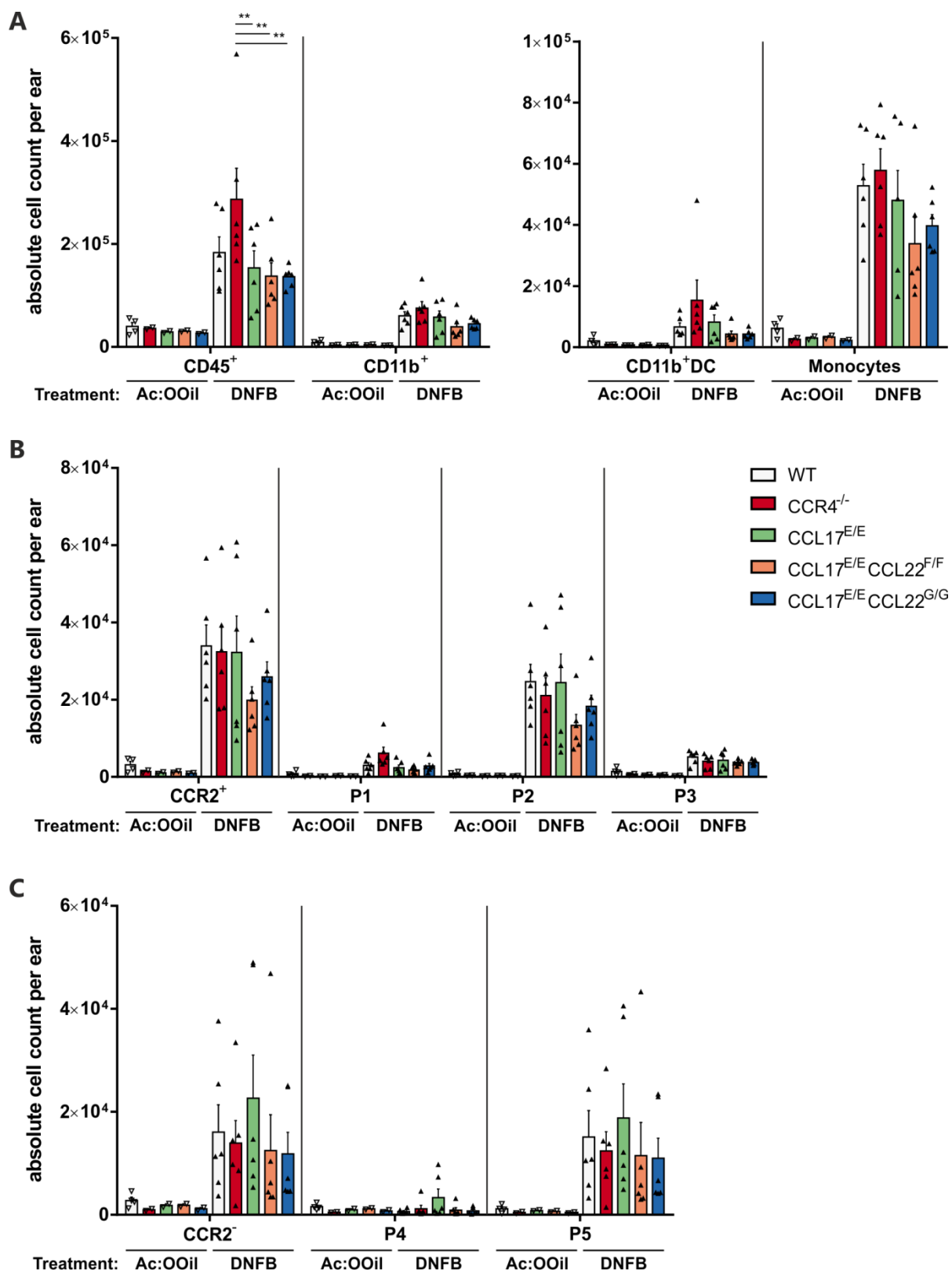


Figure 5.19 | Quantification of skin monocyte and macrophage subsets after DNFB treatment.

Legend on next page.

Further analysis of total monocytes revealed a strong DNFB-induced increase of CCR2⁺ and CCR2⁻ monocytes (see **Fig. 5.19B and C**). As stated earlier, CCR2⁺ cells comprise at least three distinct skin monocyte/ moDC populations (P1, P2, and P3) whereas CCR2⁻ cells constitute two distinct skin Mφ populations (P4 and P5)²⁸. Here, total CCR2⁺ cells, as well as P1, P2, and P3 cells increased following DNFB challenge (see **Fig. 5.19B**). Interestingly, the increase in CCR2⁺ cells mainly resulted from an increase in P2 moDCs. Furthermore, the DNFB-induced accumulation of total monocytes, in particular P2 moDCs, was less pronounced in CCL17^{E/E}/22^{-/-} mice (see **Fig. 5.19A right and Fig. 5.19B**). The DNFB-induced accumulation of total CCR2⁻ skin Mφs could be pinpointed to Ly6C⁻MHCII⁺ P5 Mφs (see **Fig. 5.19C**).

The percentage of CCL17/EGFP⁺ cells among CD11b⁺ DC and total monocytes was not affected by DNFB treatment (see **Fig. 5.20A**). It has to be noted, however, that the absolute number of CCL17-expressing cells increases following DNFB treatment as also the overall number of monocytes increases after DNFB application (see **Fig. 5.19A, right**). A comparison of CCL17-expressing CCR2⁺ monocytes and CCR2⁻ Mφs revealed an opposing picture. Whereas CCL17-expressing CCR2⁺ monocytes were not affected by DNFB, the percentage of CCL17-expressing CCR2⁻ Mφs increased (see **Fig. 5.20B**). Further analysis of the CCR2⁺ monocyte subsets demonstrated that especially cells in P1 and P3 contained less CCL17/EGFP⁺ cells after DNFB treatment (see **Fig. 5.20A**). In contrast, the number of CCL17/EGFP⁺ P5 Mφs increased after DNFB challenge and therefore explains the rise of CCL17-expressing cells in the CCR2⁻ fraction (see **Fig. 5.20B**).

In conclusion, flow cytometric analysis of skin immune cell infiltrates demonstrated that DNFB challenge results in an increase of distinct immune cell subsets in the murine skin, in line with the expectation the numbers of CD45⁺ leukocytes and conv T cells was markedly increased in CCR4^{-/-} mice compared to WT control mice. Furthermore, DNFB challenge strongly increased numbers of CCL17-expressing cells in various myeloid cell subsets, particularly CCR2⁺ Ly6C⁻ MHCII⁺ P3 moDCs and CCR2⁻ Ly6C⁻MHCII⁺ P5 Mφs.

Figure 5.19 Quantification of skin monocyte and macrophage subsets after DNFB treatment.

CHS was performed with C57BL/6 WT, CCR4^{-/-}, CCL17^{E/E}, CCL17^{E/E}CCL22^{F/F} and CCL17^{E/E}CCL22^{G/G} mice. Mice were sensitized with DNFB on day -5 and -4. On day 0 after sensitization ears were either treated with DNFB or solvent (acetone:olive oil, 5:1). On day 4 after DNFB challenge ears were digested and isolated cells subjected to staining for flow cytometry. **A, left:** Absolute numbers of total CD45⁺ leukocytes and total CD11b⁺ cells. **A, right:** Absolute numbers of CD11b⁺ DC and total skin monocytic cells. **B:** Absolute numbers of CCR2⁺ skin monocytes and corresponding P1, P2 and P3 subpopulations (for more details compare to Fig. 5H & I). **C:** Absolute numbers of CCR2⁻ skin macrophages and corresponding P4 and P5 subpopulations (for more details compare to Fig. 5H & K). (n=2-4 for solvent treated groups, mean ± SD and n=5 for DNFB-treated groups, mean ± SEM). Only data from DNFB-treated groups were tested for statistical significance by 2-way ANOVA with Bonferroni's post-hoc test for multiple comparisons (**p<0.01).

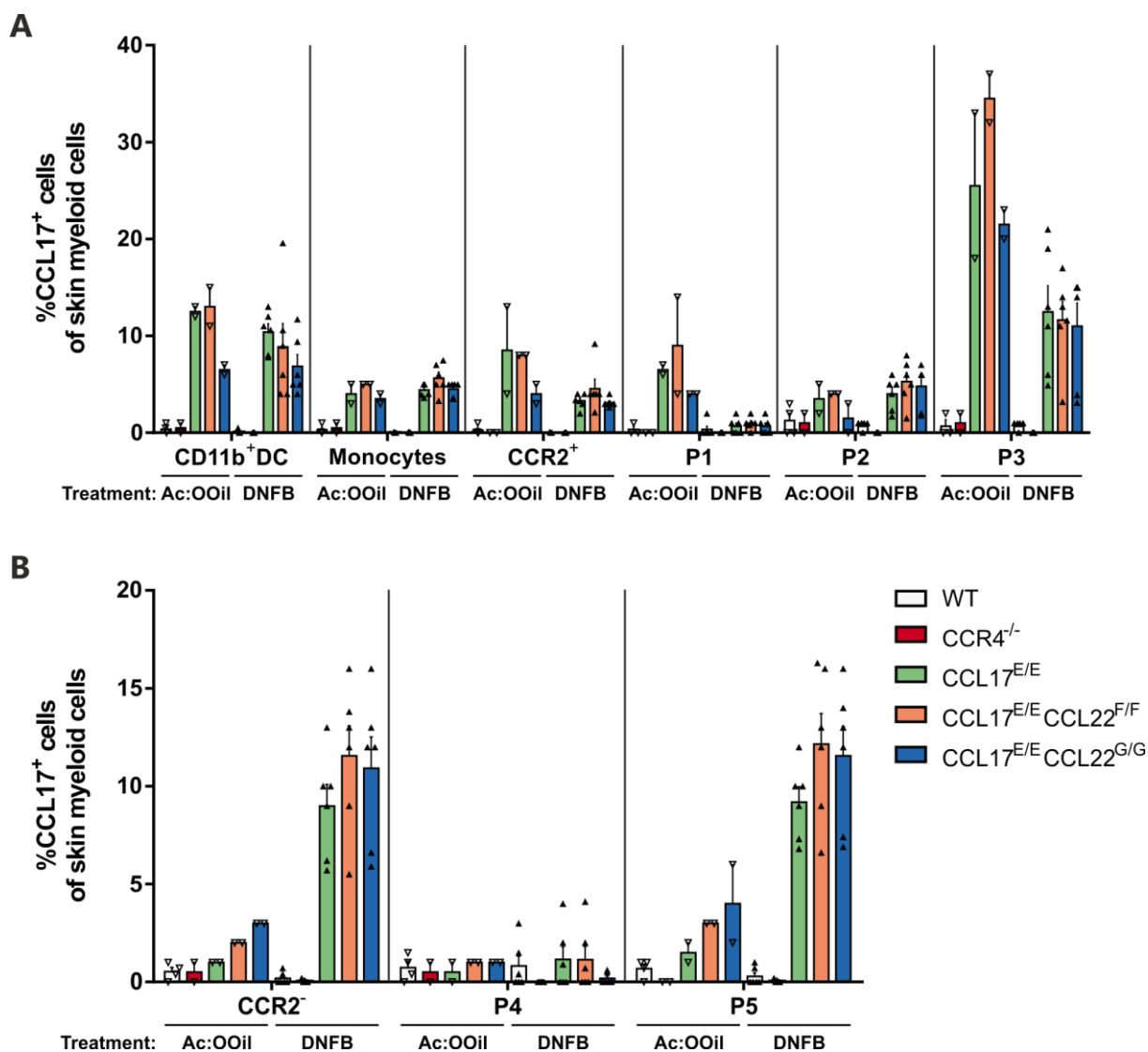


Figure 5.20 | Percentages of CCL17/EGFP⁺ cells within skin monocyte populations after DNFB treatment.

CHS assay was performed with C57BL/6 WT, CCR4^{-/-}, CCL17^{E/E}, CCL17^{E/E}CCL2^{F/F} and CCL17^{E/E}CCL2^{G/G} mice. Mice were sensitized with DNFB on day -5 and -4. On day 0 after sensitization ears were either treated with DNFB or solvent (acetone:olive oil, 5:1). On day 4 after DNFB challenge ears were digested and isolated cells subjected to staining for flow cytometry. **A:** Percentages of CCL17/EGFP⁺ cells within CD11b⁺ DC, total monocytic cells, CCR2⁺ monocytes and related monocyte subpopulations P1-P3. **B:** Percentages of CCL17/EGFP⁺ cells in CCR2⁻ skin macrophages and corresponding subpopulations P4 and P5. WT and CCR4^{-/-} mice served as negative controls and are depicted to indicate background fluorescence. (n=2-4 for solvent treated groups, mean ± SD and n=5 for DNFB-treated groups, mean ± SEM). Only data from DNFB-treated groups were tested for statistical significance by 2-way ANOVA with Bonferroni's post-hoc test for multiple comparisons.

5.5 CCL17 is a neuromodulatory chemokine in the CNS

In the previous section, the experiments were aimed to extend the knowledge on the immunoregulatory functions of CCL17 in skin immunity. Besides its expression in distinct skin-resident and infiltrating myeloid cells, CCL17 expression was found in other peripheral organs, particularly in the intestine and the lung^{72,170}. Both organs are in constant contact with the environment. As stated in the introduction, the mammalian CNS has long been viewed as an organ protected from the systemic circulation but this view is already obsolete for quite some time. The brain should be considered as an organ which is constantly in contact with at least two different environments. First, it integrates input from sensory neurons to generate a picture of the external environment, and second, it possesses highly specialized immune cells which closely monitor the body and brain. As chemokines, such as CCL17 and CCL22, are highly versatile messengers of the peripheral immune system it is probably not surprising that they were also identified in several brain regions, including the hypothalamus and the hippocampus¹²⁶. Interestingly, several studies already identified *Ccl17* expression in hypothalamic neurons and microglia¹⁷¹⁻¹⁷⁵. However, most of these studies used microarray or RNA sequencing approaches. In the present thesis, brains of CCL17-EGFP reporter mice (CCL17^{E/+}) were screened to identify cell-types expressing *Ccl17*.

5.5.1 CCL17 is expressed in a subset of hippocampal CA1 neurons

Initially, confocal microscopy was used to locate CCL17/EGFP⁺ cells in murine brain sections. Therefore, heterozygous CCL17^{E/+} mice and homozygous CCL17^{E/E} mice were compared to WT animals. As the endogenous EGFP expression in brain sections of CCL17^{E/+} and CCL17^{E/E} mice was very weak, antibody-mediated staining of EGFP was performed to detect CCL17/EGFP⁺ cells. In addition, brain sections were stained with the neuronal marker NeuN. As depicted in **Fig. 5.21B and C**, CCL17/EGFP⁺ cells were clearly identified in the hippocampal CA1 region in both heterozygous and homozygous mice.

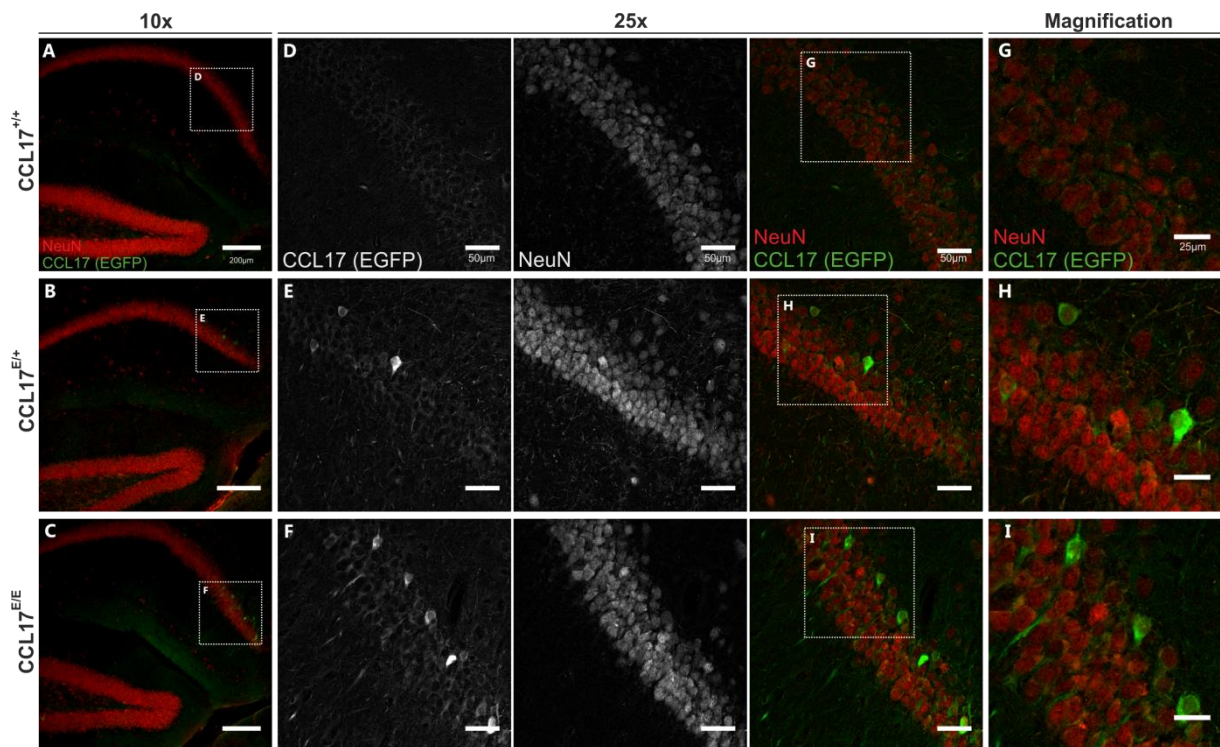


Figure 5.21 | Identification of CCL17⁺ cells in the distal hippocampal CA1 region.

A-C: Sagittal brain sections of naïve, adult CCL17^{+/+} (A, D and G), CCL17^{E/+} (B, E and H) and CCL17^{E/E} (C, F and I) mice. Sections were stained for NeuN (red) and EGFP (green). Scale Bar 200µm. Images were captured at 100x magnification. **D, E, F:** 250x magnification of the boxed areas depicted in A, B and C, respectively. Scale Bar 50µm. **G, H, I:** Digital magnification of boxed areas in D, E and F as indicated. Scale Bar 25µm. Representative images are shown.

As can be seen in **Fig. 5.21A, D & G** no unspecific staining was observed in CCL17^{+/+} mice. However, a higher proportion of CCL17/EGFP⁺ cells was detected in brain sections of CCL17^{E/E} mice (see **Fig. 5.21C, F and I**) compared to CCL17^{E/+} mice (see **Fig. 5.21B, E and H**). This can be probably explained by the stronger expression of EGFP encoded by both targeted alleles in CCL17^{E/E} mice. The CCL17/EGFP⁺ cells clearly possessed a NeuN⁺ nucleus and were thereby identified as neurons located in the hippocampal CA1 region. Interestingly, most CCL17/EGFP⁺ neurons were located in the distal stratum pyramidale of the CA1 region (see **Fig. 5.21B and C**). Here, the CCL17/EGFP⁺ neurons strongly oriented towards the stratum oriens (see **Fig. 5.21F and I**). In conclusion, the histological analysis of brain sections of CCL17^{E/+} and CCL17^{E/E} mice revealed distinct expression of *Ccl17* in hippocampal neurons.

5.5.2 Systemic inflammation induced by LPS upregulates expression of *Ccl17* and *Ccl22* in the brain

Although CCL17-expressing neurons in the hippocampus were consistently identified in several experiments, the intensity of EGFP (CCL17) staining varied between experiments. Previous studies by our lab found that TLR stimulation strongly upregulates CCL17 expression in peripheral organs, for example in skin-draining lymph nodes⁷³. Thus, neuronal *Ccl17* expression was analyzed after systemic TLR activation. Therefore, WT and CCL17^{E/+} mice were injected (i.p.) with various TLR-ligands or PBS as a control. The TLR-ligands are depicted in **Tab. 5-1**. 16 h after injection, CCL17^{E/+} mice were sequentially perfused with PBS and PFA before harvesting whole brains for microscopic analysis. Brain sections of PBS and TLR-ligand injected CCL17^{E/+} mice were stained for EGFP and DAPI as a counterstain (see **Fig. 5.22**). In PBS- and LPS-treated CCL17^{E/+} animals, CCL17/EGFP⁺ cells could be readily detected in the distal hippocampal CA1 region (see **Fig. 5.22A and B**). Strikingly, a strong increase in the number, as well as the staining intensity of CCL17/EGFP⁺ neurons was observed in LPS-treated CCL17^{E/+} mice compared to PBS-treated animals. In contrast, staining intensity of EGFP appeared to be slightly reduced in mice which received CpG or Poly(I:C) (see **Fig. 5.22C and D**).

Table 5-1 | Overview of the tested TLR ligands

Ligand	Receptor	Nature	Origin	Dose
Poly(I:C)	TLR3	dsRNA	Virus	200µg/ mouse
LPS	TLR4	Lipid/Polysaccharide	Gram-negative bacteria	150µg/ mouse
CpG-ODN	TLR9	dsDNA	Bacterial DNA & Virus	32µg/ mouse

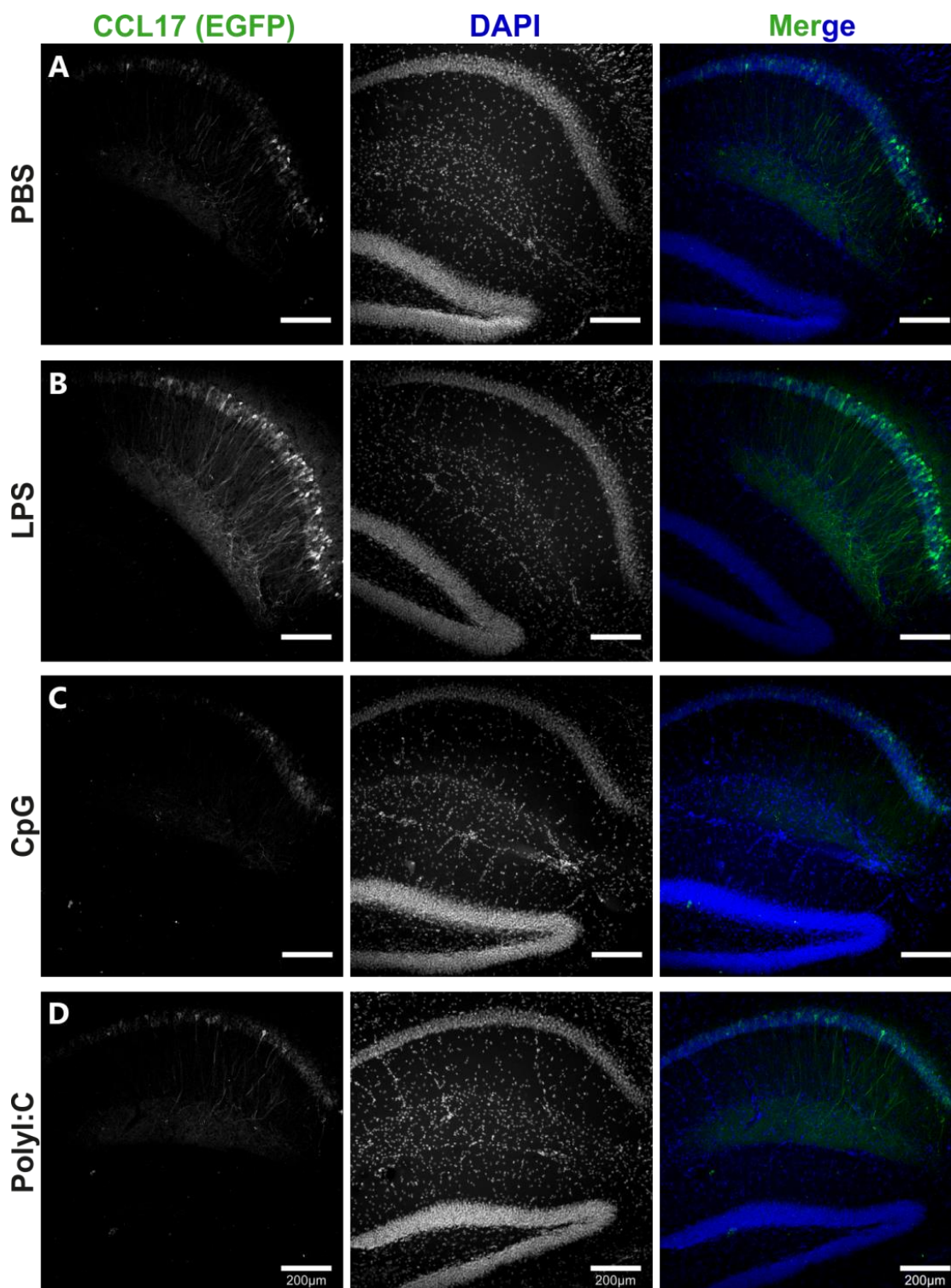


Figure 5.22 | Systemic LPS treatment enhances *Ccl17* and *Ccl22* expression in the hippocampus.

CCL17^{E/+} mice received i.p. injections of 200µl PBS (A), 150µg LPS (B), 32 µg CpG (C) or 150 µg Poly(I:C) (D) in 200µl PBS. Brains were isolated 16 h post injection, stained for EGFP and DAPI and scanned using confocal imaging analysis. (Left: EGFP staining; Middle: DAPI staining; Right: Pseudocolor merge: DAPI (blue), EGFP (green)). Scale bar, 200µm.

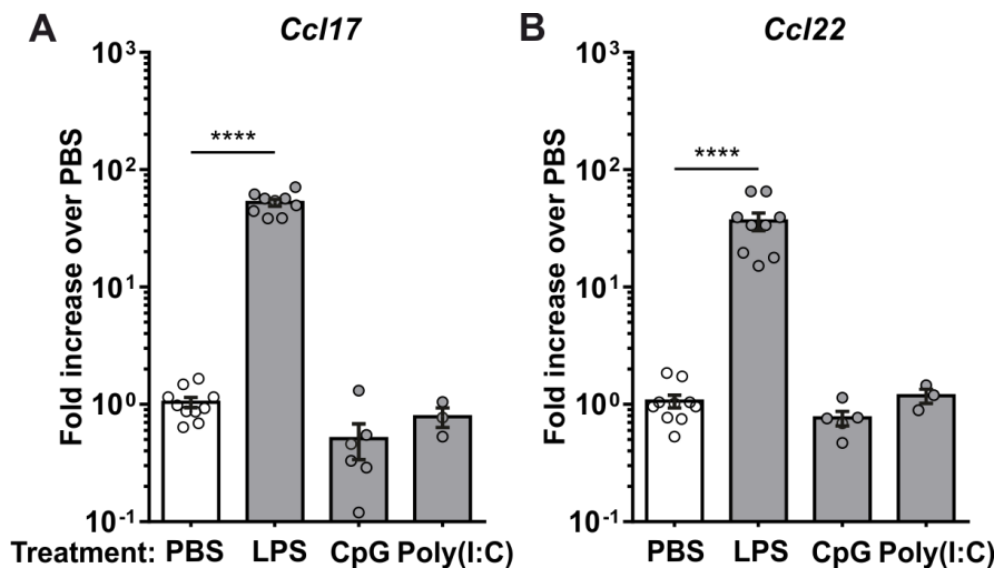


Figure 5.23 | Systemic LPS challenge enhances *Ccl17* and *Ccl22* expression in the hippocampus.

C57BL/6J WT mice were injected i.p. with 200 μ l PBS or the indicated TLR-ligand. **A, B:** RT-PCR analysis of *Ccl17* (A) and *Ccl22* (B) expression in hippocampi dissected from WT animals 16h post injection (n=3-10, mean \pm SEM). Circles represent individual mice. Statistical significance was tested using One-way ANOVA with Bonferroni's post-hoc test for multiple comparisons (****p<0.001 **p<0.01; *p<0.05).

In addition to the microscopic analysis, hippocampi of TLR ligand-treated WT mice and controls were freshly dissected and used for RNA extraction and RT-PCR analysis. RT-PCR analysis of WT mice revealed a similar TLR-dependent regulation of *Ccl17* expression in the brain as seen in the analysis of CCL17^{E/+} reporter mice (see **Fig. 5.23B**). Confirming the microscopic observations, only systemic LPS challenge resulted in significantly upregulated expression of *Ccl17* in the hippocampus (see **Fig. 5.23B**). Similar to the expression of *Ccl17*, LPS treatment also induced a significant upregulation of *Ccl22* mRNA (see **Fig. 5.23B**).

In conclusion, it could be demonstrated that the activation of TLR4 but not TLR3 or TLR9-related signaling pathways enhanced the expression of *Ccl17* and *Ccl22* above homeostatic expression.

5.5.3 Weak expression of CCL17 in cortical cells

In addition to the hippocampus, other brain regions, such as the cortex or the cerebellum were also analyzed for the presence of CCL17/EGFP⁺ cells. To increase the sensitivity of EGFP detection, only homozygous CCL17^{E/E} mice with or without prior stimulation with LPS were subjected to antibody staining and image analysis. As before, CCL17^{+/+} mice served as negative control.

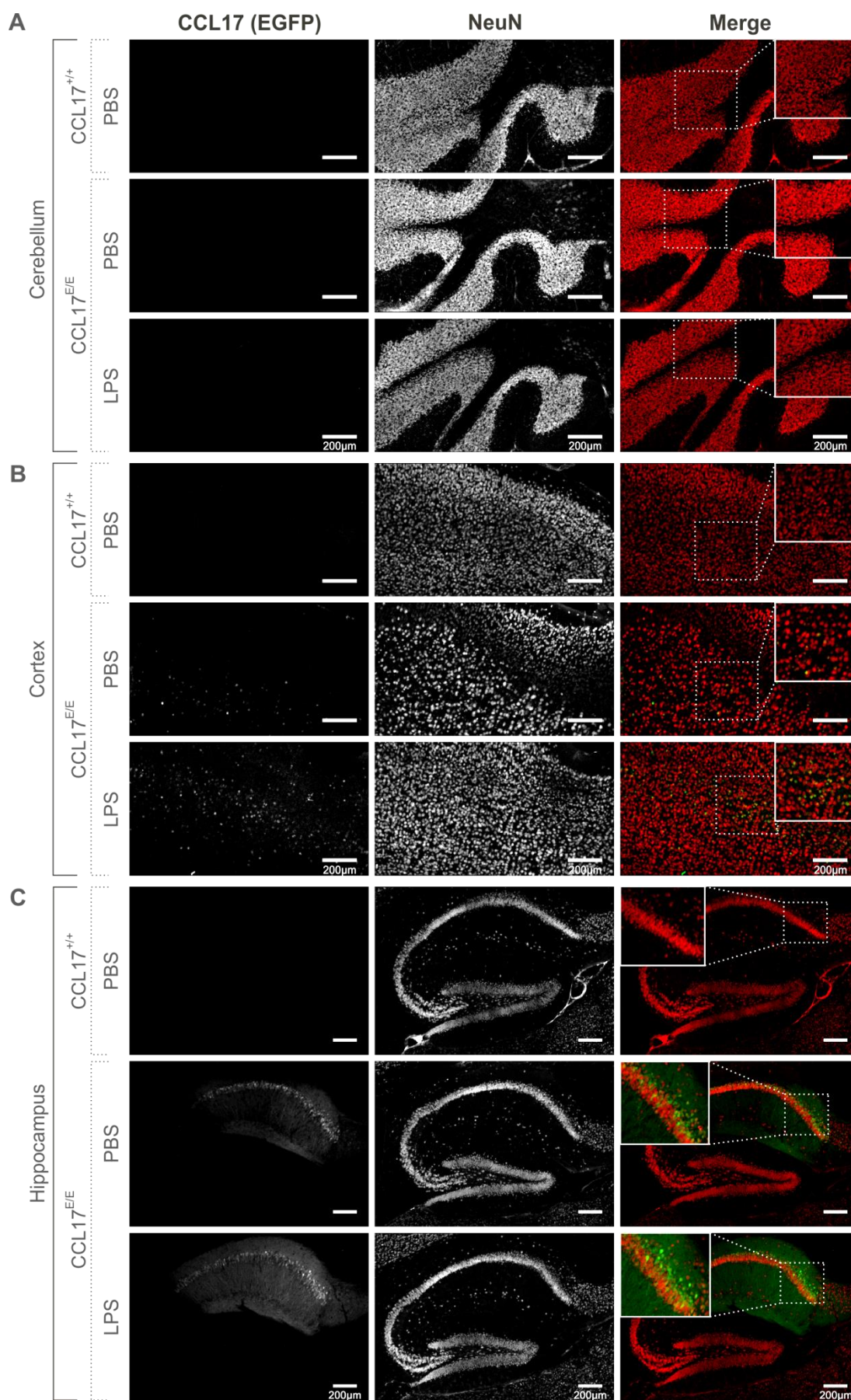


Figure 5.24 | Localization of CCL17/EGFP⁺ cells in different regions of the murine brain.

Legend on next page.

Fig. 5.24A shows that no CCL17/EGFP⁺ cells were detected in the cerebellum of CCL17^{E/E} mice. In contrast, few CCL17/EGFP⁺ cells could be observed in the cortex under homeostatic conditions as well as after LPS injection (**Fig. 5.24B**). Although LPS treatment led to visually increased numbers of CCL17/EGFP⁺ cells in the cortex, the intensity of EGFP staining appeared to be much weaker compared to hippocampal neurons (**Fig. 5.24C**). Some cells were clearly stained positive for NeuN and were thus identified as neurons. In conclusion, these experiments demonstrated that CCL17-expressing cells in the CNS are not exclusively found in the hippocampus but are also present at low numbers in the cortex, especially after LPS-induced systemic inflammation.

5.5.4 CCL17 is secreted from *in vitro* cultured hippocampal neurons

To investigate whether CCL17 is translated and secreted by hippocampal neurons, primary neurons were generated from hippocampi of E14 WT embryos. For this purpose, timed pregnancies were set up and the mice were sacrificed at day E14. Together with the master student N. Offermann, embryonic hippocampi were carefully dissected, and single cell suspensions were immediately plated on poly-D-lysine and laminin-coated culture dishes. To remove contaminating glia cells, a complete change of the medium was performed after 20 min. Following one week of culture, the cells acquired a typical neuronal morphology, characterized by a triangular cell body and elongated axons. After two weeks, the cells were treated with TNF, LPS or the combination of both and chemokine production was assessed by ELISA of culture supernatants. The chemokine fractalkine/ CX₃CL1, known to be produced by neurons, was measured as a positive control. As depicted in **Fig. 5.24A**, neurons produced high amounts of CX₃CL1 independent of LPS or TNF stimulation. In contrast, CCL17 was only detected in cells stimulated with TNF, LPS or both (see **Fig. 5.24B**). Although the concentration of CCL17 was very low compared to CX₃CL1, these experiments demonstrated that neurons are able to release CCL17 upon stimulation.

Figure 5.24 | Localization of CCL17⁺ cells in different regions of the murine brain.

Sagittal brain sections of CCL17^{+/+} or CCL17^{E/E} mice were stained for EGFP (first column) or NeuN (second column). Pseudocolor merge with NeuN in red and EGFP in green is shown in the third column. Cerebellum (**A**), cortex (**B**), or hippocampus (**C**) of PBS-treated CCL17^{+/+} (first row) and PBS- or LPS-treated CCL17^{E/E} mice (second & third row) as indicated. Scale Bar 200µm. Representative images are shown.

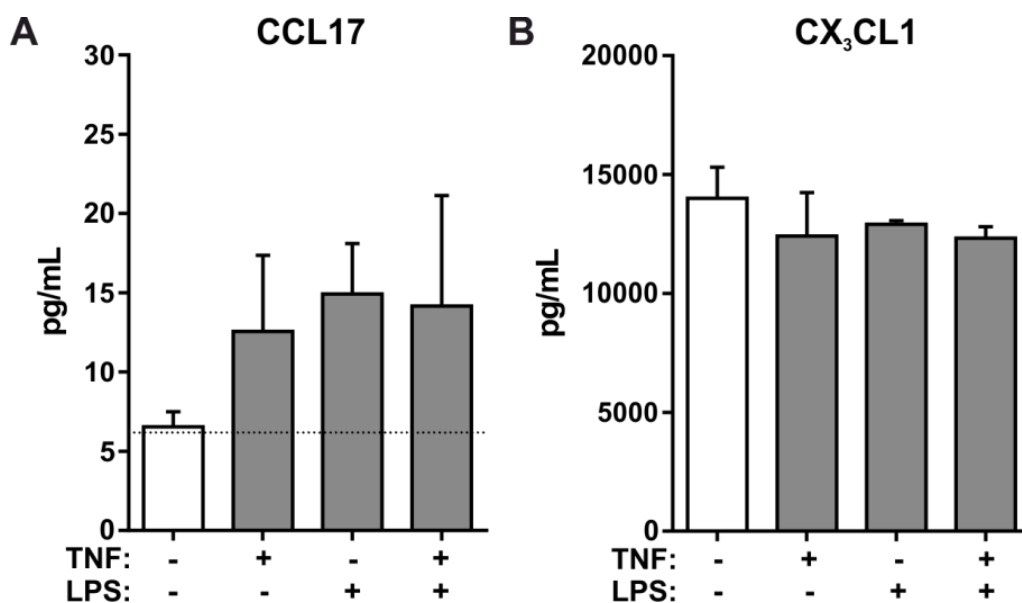


Figure 5.25 | TNF and LPS treatment of hippocampal neurons induces secretion of CCL17 and CX₃CL1 in vitro.

Neuronal cultures were established from E14.5 WT embryos. Mature neurons were stimulated with rmTNF [50ng/mL], LPS [100ng/mL], or the combination of both for 96h. Concentration of CCL17 (A) and CX₃CL1 (B) was determined in the supernatant by ELISA (n=2-5 independent experiments, n=2 per group in each experiment, mean ± SEM). The dashed line in A indicates the detection limit of the CCL17 ELISA.

5.5.5 Local TNF signaling regulates LPS-induced *Ccl17* expression in the hippocampus

The discovery that *Ccl17* and *Ccl22* are highly upregulated in the hippocampus after LPS treatment required clarification of the underlying regulatory pathways. It is well known that peripheral inflammation induced by LPS leads to elevated levels of pro-inflammatory cytokines in various organs, including the CNS¹¹⁹. Here, GM-CSF and TNF were of particular interest as both were demonstrated to regulate *Ccl17* expression in peripheral organs, such as the skin or the intestine^{72-74,168}. Thus, expression of *Csf2* and *Tnf* was analyzed in hippocampi of PBS or TLR-ligand treated WT mice. Whereas a high experimental variation of *Csf2* expression prevented reliable analysis (data not shown), LPS treatment resulted in robust expression of *Tnf* in the hippocampus (see **Fig. 5.26A**). In contrast, neither CpG nor Poly(I:C) had an effect on *Tnf* expression. As stated earlier, systemic LPS also induces the production of pro-inflammatory cytokines in the periphery. To ensure that the injected dosages of all TLR-ligands used induced immune activation, serum levels of TNF and IL-1 β were measured in WT mice 3 h after injection of TLR-ligands. As depicted in **Fig. 5.26B and C**, all three TLR-ligands provoked increased levels of TNF and IL-1 β in the serum albeit LPS treatment induced the strongest response.

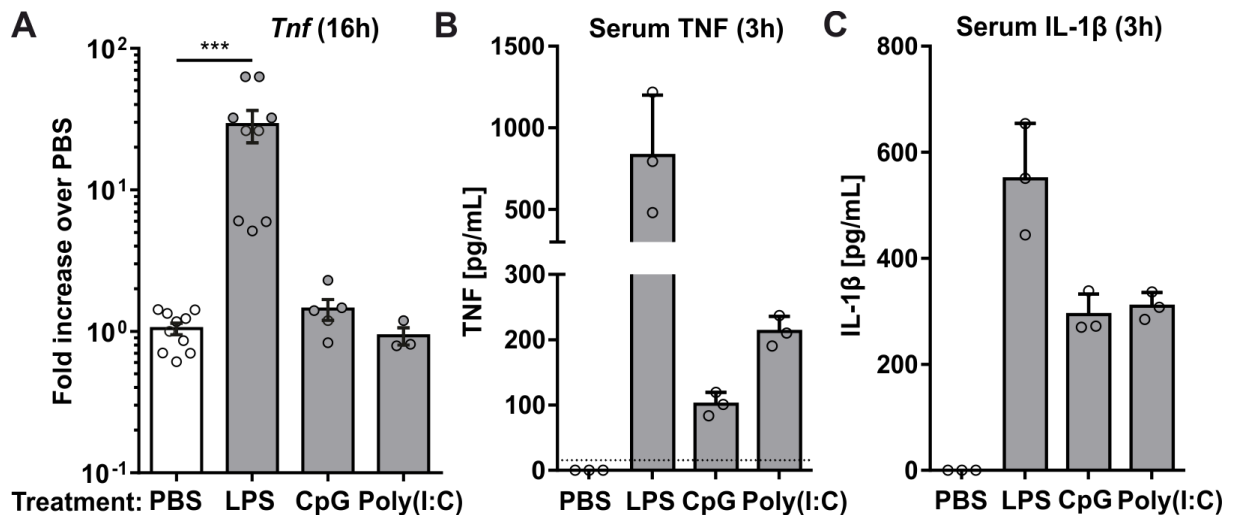


Figure 5.26 | Increased production of pro-inflammatory cytokines in the serum and CNS after systemic LPS treatment.

C57BL/6J WT mice were injected i.p. with 200 μ l PBS or the indicated TLR-ligand. **A:** RT-PCR analysis of *Tnf* expression in hippocampi dissected from WT animals 16h post injection (n=3-10, mean \pm SEM). **B, C:** Serum TNF (B) and IL-1 β (C) levels were measured 3h post injection (n=3, mean \pm SD). Circles represent individual mice. Statistical significance was tested using One-way ANOVA with Bonferroni's post-hoc test for multiple comparisons (**p<0.01; *p<0.05). The dashed line in B and C indicates the detection limit of the ELISA.

To further investigate a potential regulatory role of TNF for the expression of *Ccl17* in the hippocampus, TNF responses in the serum and CNS were analyzed in mice which received increasing doses of LPS. These experiments aimed to clarify whether severity of peripheral inflammation correlates with the level of serum TNF and/or the expression of *Tnf*, *Il-1 β* , and *Ccl17* in the hippocampus. As depicted in **Fig. 5.27A**, TNF levels in the serum increased independently of the injected LPS dose down to 6 μ g/mouse. Strikingly, however, the expression of *Tnf* in the hippocampus clearly correlated with the amount of injected LPS (see **Fig. 5.27B**). That was only partly true for expression of *Il-1 β* , as a pronounced expression could only be detected at doses of up to 18 μ g LPS/mouse whereas higher doses of LPS reversed the expression (see **Fig. 5.27C**). Interestingly, the increased expression of *Ccl17* and *Ccl22* required a minimal dose of 50 μ g LPS/mouse (see **Fig. 5.27D and E**). These experiments demonstrated that a certain threshold of peripheral inflammation had to be exceeded to strongly induce the expression of *Ccl17* and *Ccl22* in the hippocampus. In addition, a decisive role of peripheral TNF can be excluded, since all LPS doses caused a similar effect on TNF levels in the serum. This could be further confirmed by the i.p injection of recombinant murine TNF (rmTNF) in WT mice (see **Fig. 5.28A**). As depicted in **Fig. 5.28B and C**, even 5 μ g rmTNF/mouse failed to induce expression of *Ccl17* and *Ccl22* in the hippocampus.

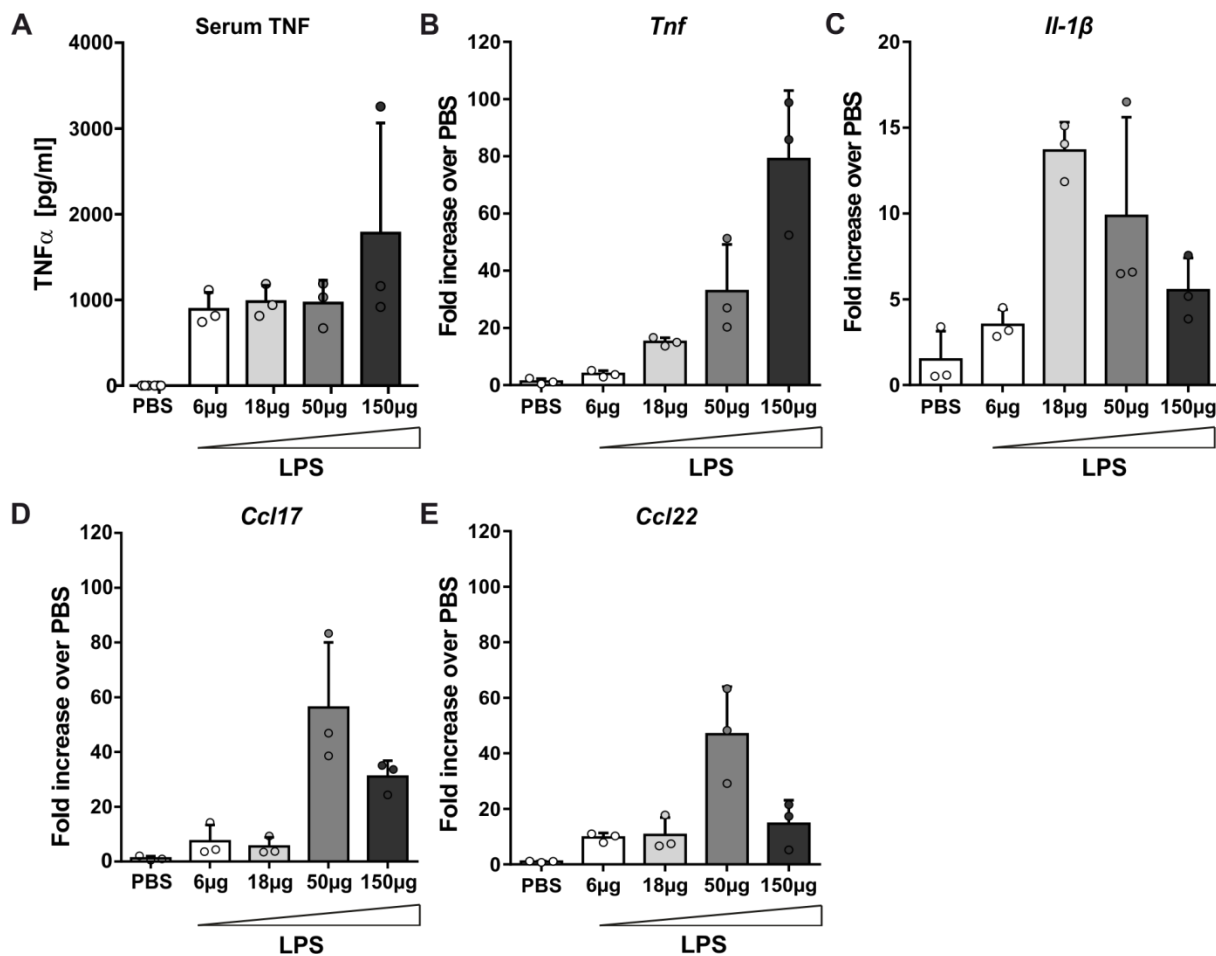


Figure 5.27 | Dose-response relationship between systemic LPS treatment and hippocampal expression of *Tnf*, *Il-1β*, *Ccl17* and *Ccl22*.

C57BL/6J mice were injected i.p. with 200 μl PBS or different doses of μg LPS/ mouse as indicated. **A:** Serum TNF levels were measured 3h post i.p. injection of WT mice with PBS or LPS. **B, C, D, and E:** RT-PCR analysis of *Tnf* (**B**), *Il-1β* (**C**), *Ccl17* (**D**) and *Ccl22* (**E**) expression in hippocampi dissected from WT animals 16h post 200 μl i.p. injection of PBS or LPS. (n=3, mean ± SD). Circles represent data from individual mice.

To confirm that TNF signaling is critically involved in the regulation of *Ccl17* expression in the brain, TNF receptor 1 (TNFR1^{-/-}) and TNF receptor 1 & 2 double-deficient animals (TNFR1/2^{-/-}) were injected i.p. with LPS (see **Fig. 5.29A**). Remarkably, LPS did not induce *Ccl17* expression in the hippocampi of TNFR1^{-/-} and TNFR1/2^{-/-} mice (see **Fig. 5.29B**). In addition, *Ccl22* mRNA was also reduced in the hippocampi of TNFR1^{-/-} and TNFR1/2^{-/-} mice albeit to a much lower extent than *Ccl17* (see **Fig. 5.29C**). In contrast, baseline expression of both chemokines did not appear to be impaired by the absence of TNFR. Taken together, these experiments identified local TNF signaling in the CNS to be the primary trigger for LPS-induced *Ccl17* expression in the hippocampus.

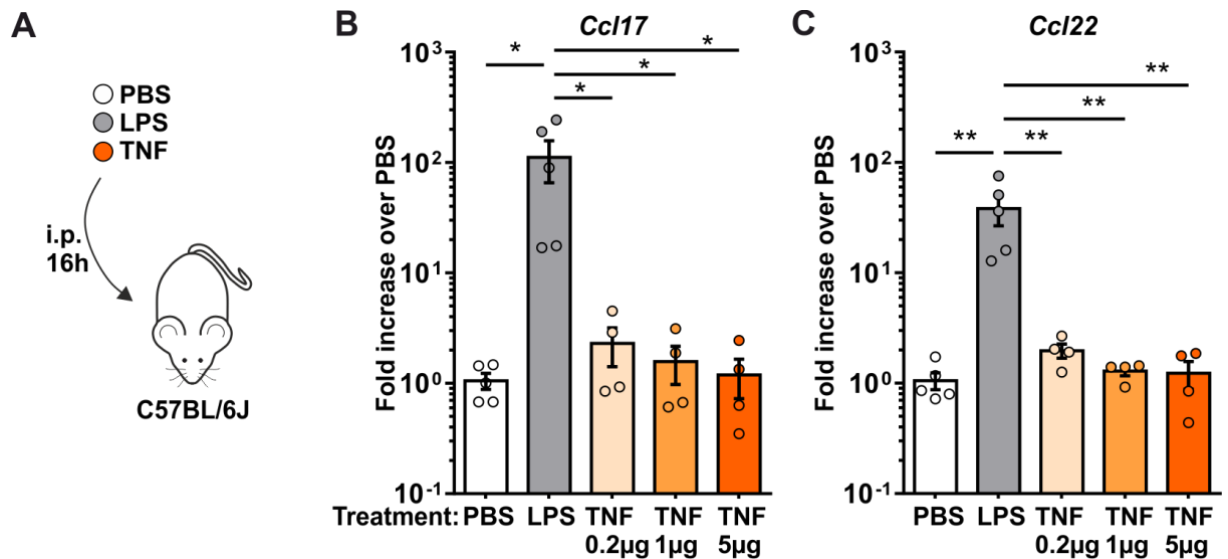


Figure 5.28 | Peripheral injection of rmTNF does induce *Ccl17* expression in the hippocampus.

A: C57BL/6J mice were injected i.p. with 200µl PBS or different doses of recombinant murine TNF as indicated 16h before isolating the hippocampus. B, C: RT-PCR analysis of *Ccl17* (B) and *Ccl22* (C) expression in the hippocampus (n=4, mean ± SEM). Circles represent data from individual mice. Statistical significance was tested using One-way ANOVA with Bonferroni's post-hoc test for multiple comparisons (**p<0.01; *p<0.05).

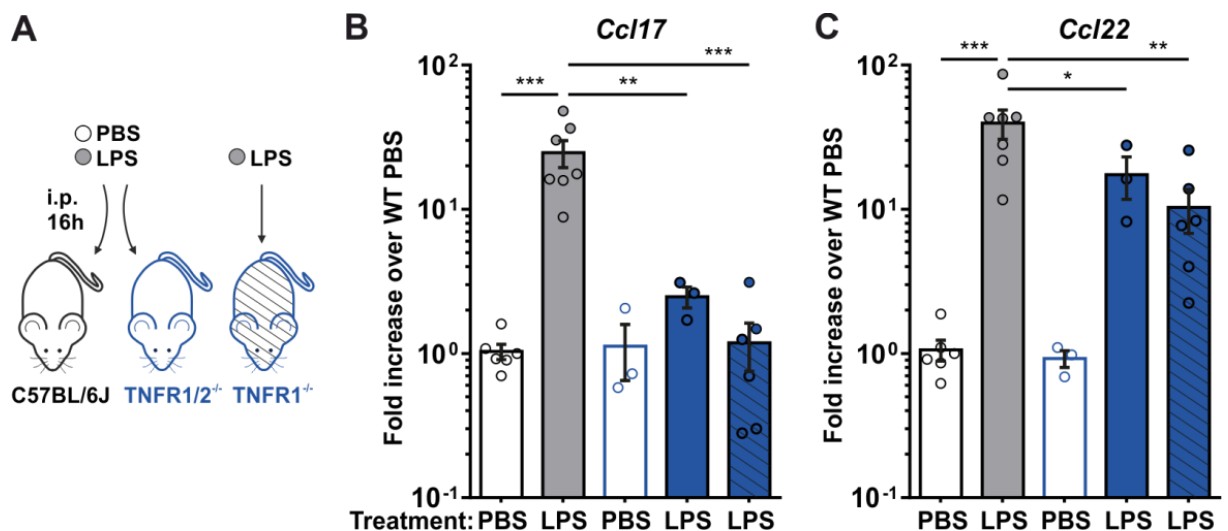


Figure 5.29 | TNFR-deficiency abrogates LPS-induced expression of CCL17 in the hippocampus.

A: C57BL/6J, TNFR1^{+/-} and TNFR1^{-/-} mice were injected i.p. with 200µl PBS or 150µg LPS 16h before isolating the hippocampus. B, C: RT-PCR analysis of *Ccl17* (B) and *Ccl22* (F) expression in hippocampi of WT, TNFR1^{-/-} and TNFR1^{+/-} mice as indicated in A (n=3-7, mean ± SEM). Circles represent data from individual mice. Statistical significance was tested using One-way ANOVA with Bonferroni's post-hoc test for multiple comparisons (**p<0.01; ***p<0.001; *p<0.05).

5.5.6 Cytokines rather than MyD88 signaling regulate the LPS-induced expression of *Ccl22* in the hippocampus

My previous experiments already provided evidence for a GM-CSF-dependent expression of *Ccl17* in skin cells (see 5.1.5). In addition, GM-CSF was identified to regulate CCL17-mediated arthritic pain⁷⁴. As the previous RT-PCR analysis of *Csf2* expression in the hippocampus did not yield informative data, expression of *Ccl17* and *Ccl22* was now analyzed in hippocampi of LPS-challenged GM-CSF^{-/-} mice (see **Fig. 5.30A**).

Comparable to the analysis of TNFR-deficient animals, the experiments also revealed a differential regulation of *Ccl17* and *Ccl22* by GM-CSF (see **Fig. 5.30B and C**). Whereas the LPS-induced *Ccl17* expression was only slightly affected by the loss of GM-CSF, *Ccl22* expression was more strongly reduced in GM-CSF^{-/-} mice (see **Fig. 5.30B and C**). In accordance with previous experiments, LPS-treated GM-CSF^{-/-} mice still expressed high levels of *Tnf* in the hippocampus (see **Fig. 5.30D**), which affirmed its essential role for the induction of *Ccl17* in the hippocampus.

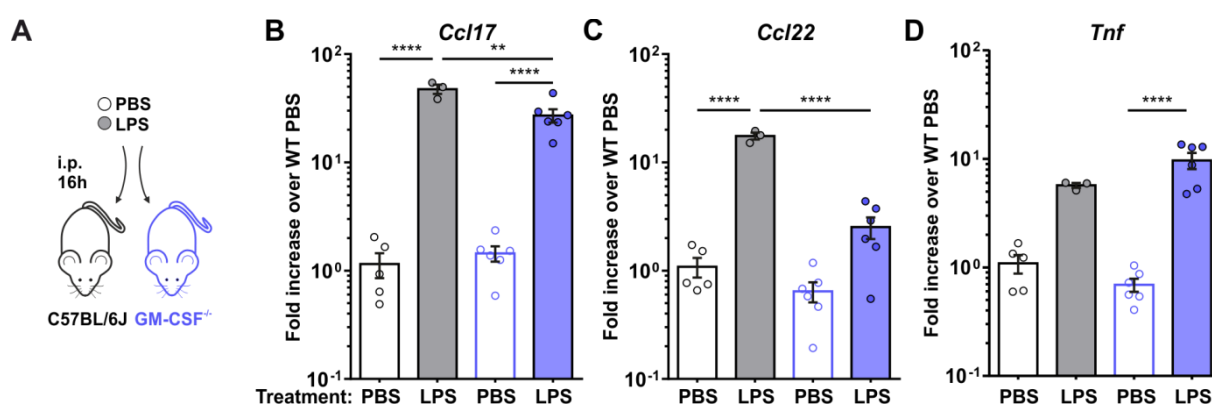


Figure 5.30 | The cytokine GM-CSF differentially regulates *Ccl17* and *Ccl22* expression in the hippocampus.

A: C57BL/6J WT and GM-CSF^{-/-} mice were injected i.p. with 200µl PBS or 150µg LPS/ mouse 16h before isolating the hippocampus. **B, C, D**: RT-PCR analysis of *Ccl17* (**B**), *Ccl22* (**C**) and *Tnf* (**D**) expression in hippocampi of WT and GM-CSF mice as indicated in A (n=3-6, mean ± SEM). Circles represent data from individual mice. Data was tested for statistical significance by One-way ANOVA with Bonferroni's post-hoc test for multiple comparisons (****p<0.0001; **p<0.01).

Next, it was tested whether the LPS/TNF-induced expression of *Ccl17* required activation of TLR-signaling pathways via Myd88. For this purpose, systemic LPS challenge was performed in mice lacking MyD88, a central adaptor protein of TLR signaling pathways (see **Fig. 5.31A**). As expected, LPS treatment of MyD88^{-/-} mice did not induce the expression of *Ccl17* in the hippocampus (see **Fig. 5.31B**). Strikingly, *Ccl22* was still induced after LPS treatment at levels comparable to WT mice (see **Fig. 5.31C**). It was somewhat puzzling that the expression of TNF in MyD88^{-/-} mice was still elevated after LPS challenge (see **Fig. 5.31D**) indicating that signal transduction via the adaptor TRIF downstream of TLR4 might be relevant for *Ccl22* expression. Interestingly, the baseline expression of *Ccl17*, *Ccl22* nor *Tnf* appeared not to be affected neither by the loss of GM-CSF nor MyD88 (see **Fig. 5.30** and **5.31**).

In conclusion, these experiments revealed the existence of distinct regulatory pathways differentially controlling the hippocampal expression of *Ccl17* and *Ccl22* in the context of LPS-induced systemic inflammation.

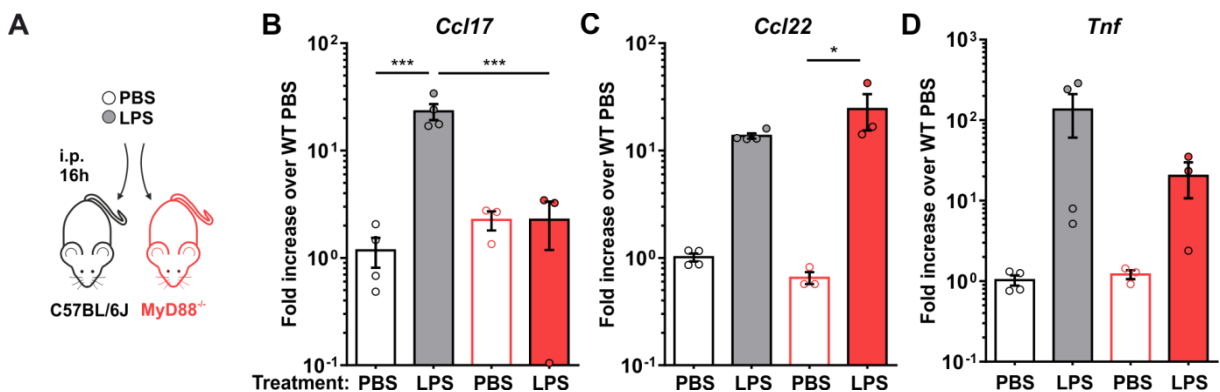


Figure 5.31 | MyD88-dependent signaling pathways differentially regulate *Ccl17* and *Ccl22* expression in the hippocampus.

A: C57BL/6J WT and MyD88^{-/-} mice were injected i.p. with 200μl PBS or 150μg LPS/ mouse 16h before isolating the hippocampus. **B, C, D:** RT-PCR analysis of *Ccl17* (**B**), *Ccl22* (**C**) and *Tnf* (**D**) expression in hippocampi of WT and MyD88^{-/-} mice as indicated in A (n=3, mean ± SEM). Circles represent individual mice. Data was tested for statistical significance by One-way ANOVA with Bonferroni's post-hoc test for multiple comparisons (***p<0.001; *p<0.05).

5.5.7 LPS-induced septic shock is not affected by the loss of CCL17

A previous report demonstrated that CCR4-deficient mice are less susceptible to LPS-induced endotoxin shock¹⁷⁶. For this reason, it was tested, whether the CCL17^{E/E} mice showed a normal systemic response to LPS by comparing the survival rate following high dose LPS injection (i.p.) [20mg/kg and 15mg/kg] in CCL17^{E/E} and WT mice (see **Fig. 5.32A**). In addition, serum of WT and CCL17^{E/E} mice which received 150 μg LPS/mouse was collected 3 h after i.p. injection and serum levels of TNF and IL-1β were determined. Interestingly, serum concentrations of TNF and IL-1β were comparable in mice from both experimental groups (see **Fig. 5.32B and C**). In line, evaluation of survival rates revealed no influence of CCL17 as both experimental groups were equally susceptible to LPS-induced septic shock (see **Fig. 5.32D and E**). These experiments demonstrated that CCL17 appears to play no role in the generation of peripheral immune responses in the LPS-shock model.

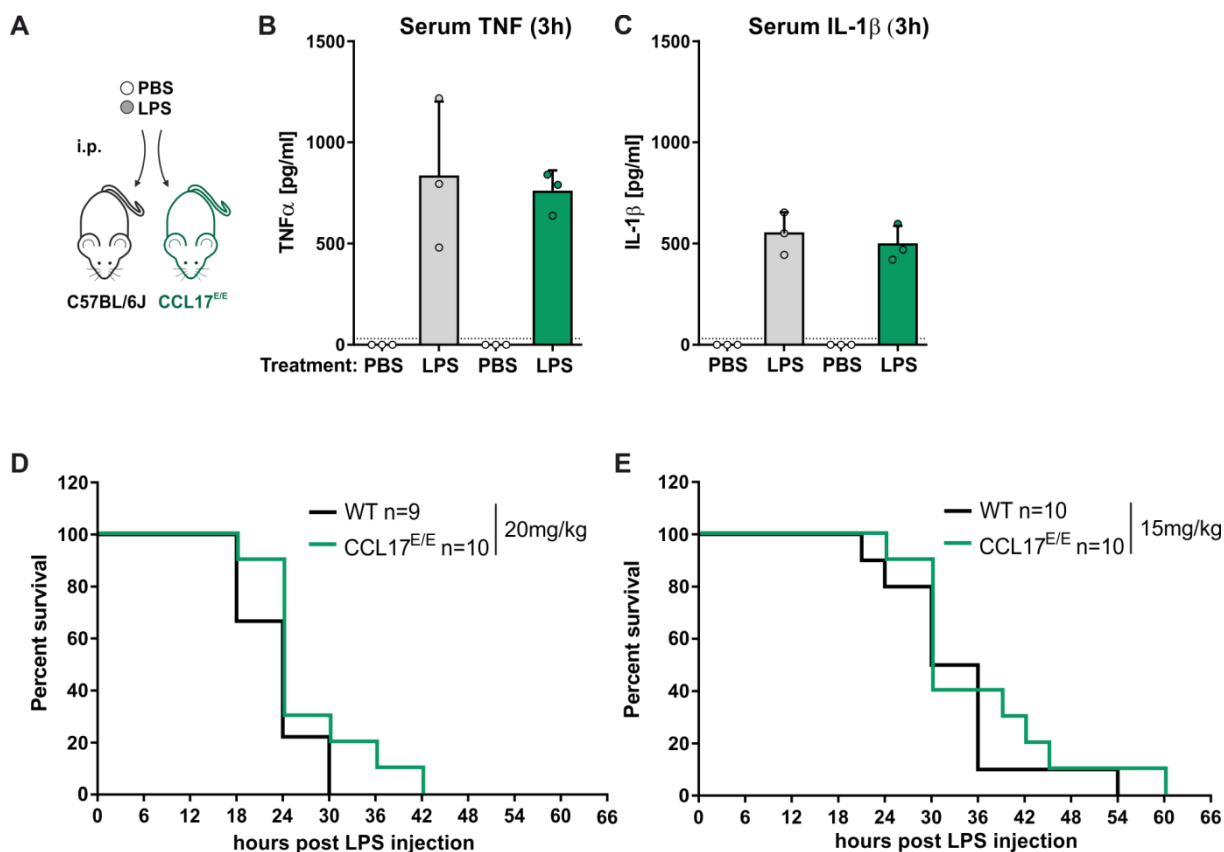


Figure 5.32 | LPS-induced septic shock is comparable in WT and CCL17-deficient animals.

A: C57BL/6J WT and CCL17^{E/E} mice were injected i.p. with 200 μ l PBS or different doses of LPS. **B, C:** Three hours post injection of 150 μ g LPS in 200 μ l PBS or 200 μ l PBS alone, serum levels of TNF (**B**) and IL-1 β (**C**) were determined in WT and CCL17^{E/E} mice (n=3 per group, mean \pm SD). **D, E:** Kaplan-Meier curve shows survival of WT and CCL17^{E/E} mice injected i.p. with 20mg/kg (**D**) or 15mg/kg (**E**) LPS i.p. (n=9-10 per group).

5.5.8 Absence of CCL17 reduces the number of microglia in the brain and affects monocyte activation

Based on the findings that CCL17^{E/E} mice responded normally to LPS in the peripheral immune system, I next analyzed the role of CCL17 in brain immune responses. First, flow cytometry was utilized to analyze the number and composition of brain-resident microglia and other hematopoietic cells in WT and CCL17^{E/E} mice under homeostatic as well as inflammatory conditions (see **Fig. 5.34A**). As in previous experiments, brains of WT and CCL17^{E/E} mice were isolated 16 h after i.p. injection of either 200 μ l PBS or 150 μ g LPS. After perfusion with ice-cold PBS, brains were dissociated by enzymatic digestion at 37°C and mechanically disrupted. Single cell suspensions were subjected to antibody staining and immediately analyzed by flow cytometry. A simplified gating strategy for the identification of microglia (CD45^{int} CD11b⁺CD3⁻), neutrophils (CD45^{hi}CD3⁻Ly6G⁺), inflammatory monocytes (CD45^{hi}Ly6G⁻CD11b⁺Ly6C⁺), and M ϕ s plus DC (CD45^{hi}CD3⁻Ly6G⁻CD11b⁺Ly6C⁻) was adapted from Pösel et al.¹⁷⁷ and is depicted in **Fig. 5.33**. The endogenous expression of the EGFP reporter in CCL17^{E/E} mice allowed the identification of CCL17-expressing cells.

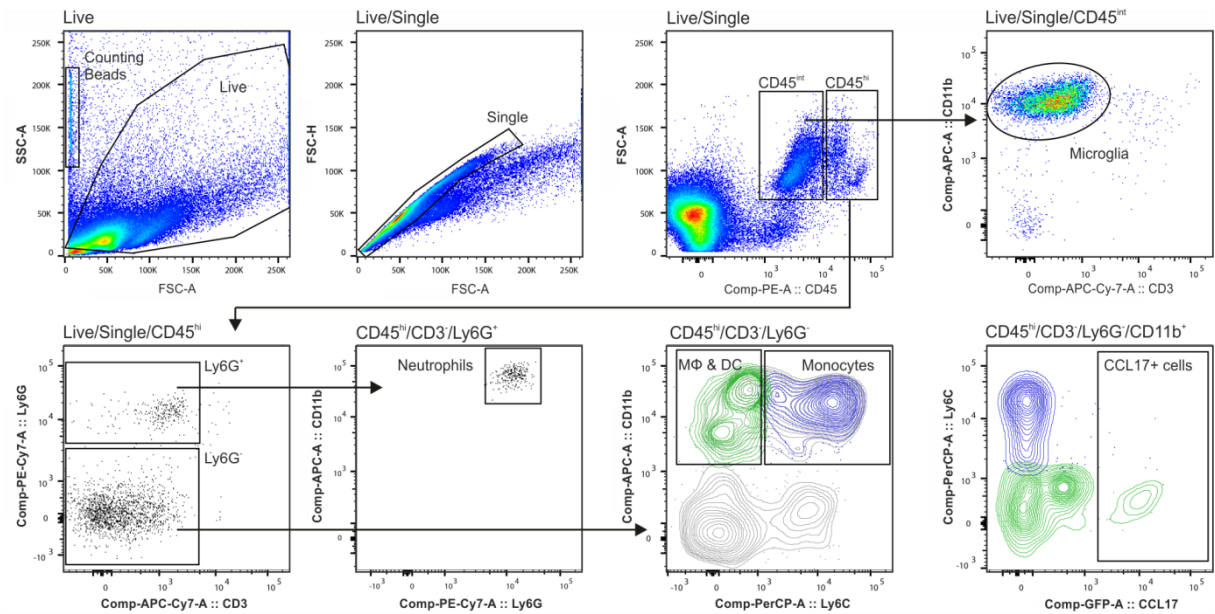


Figure 5.33 | Gating strategy for identification of microglia and immune cell infiltrates in the brain.

A live cell gate was set on the basis of FSC and SSC properties. Counting beads were identified based on their characteristic SSC profile and used to determine absolute cell numbers depicted in Fig. 5.34. From the live cell gate single cells were identified and subsequently separated in CD45^{int} and CD45^{hi} cells. Most CD45^{int} cells were also positive for CD11b and thus identified as microglia. CD45^{hi} leukocytes were further analyzed for Ly6G and CD3 expression. Neutrophils were identified as CD45^{hi}CD3⁻Ly6G⁺CD11b⁺ cells. The remaining CD3⁻Ly6G⁻ cells were further analyzed for CD11b and Ly6C expression. CD11b⁺Ly6C⁻ cells mainly comprised different subsets of DCs and MΦs and contained a substantial number of CCL17/EGFP-expressing cells. In contrast, no CCL17/EGFP⁺ cells were identified in CD11b⁺Ly6C⁺ inflammatory monocytes. A representative gating of a CCL17^{E/E} mouse is depicted.

In both experimental groups, LPS treatment resulted in significantly increased numbers of total CD45^{hi} leukocytes compared to PBS-injected control animals (see **Fig. 5.34B**). Further analysis of CD45^{hi} leukocytes also revealed a significant increase in neutrophils and inflammatory monocytes after systemic LPS challenge (see **Fig. 5.34D and F**, respectively). Despite not reaching statistical significance, numbers of MΦ and DC were also clearly increased following LPS injection (see **Fig. 5.34E**). Remarkably, LPS treatment also resulted in a significant increase of CCL17/EGFP⁺ cells (see **Fig. 5.34G**), which exclusively belonged to the MΦ and DC population (~20% of total MΦ and DC).

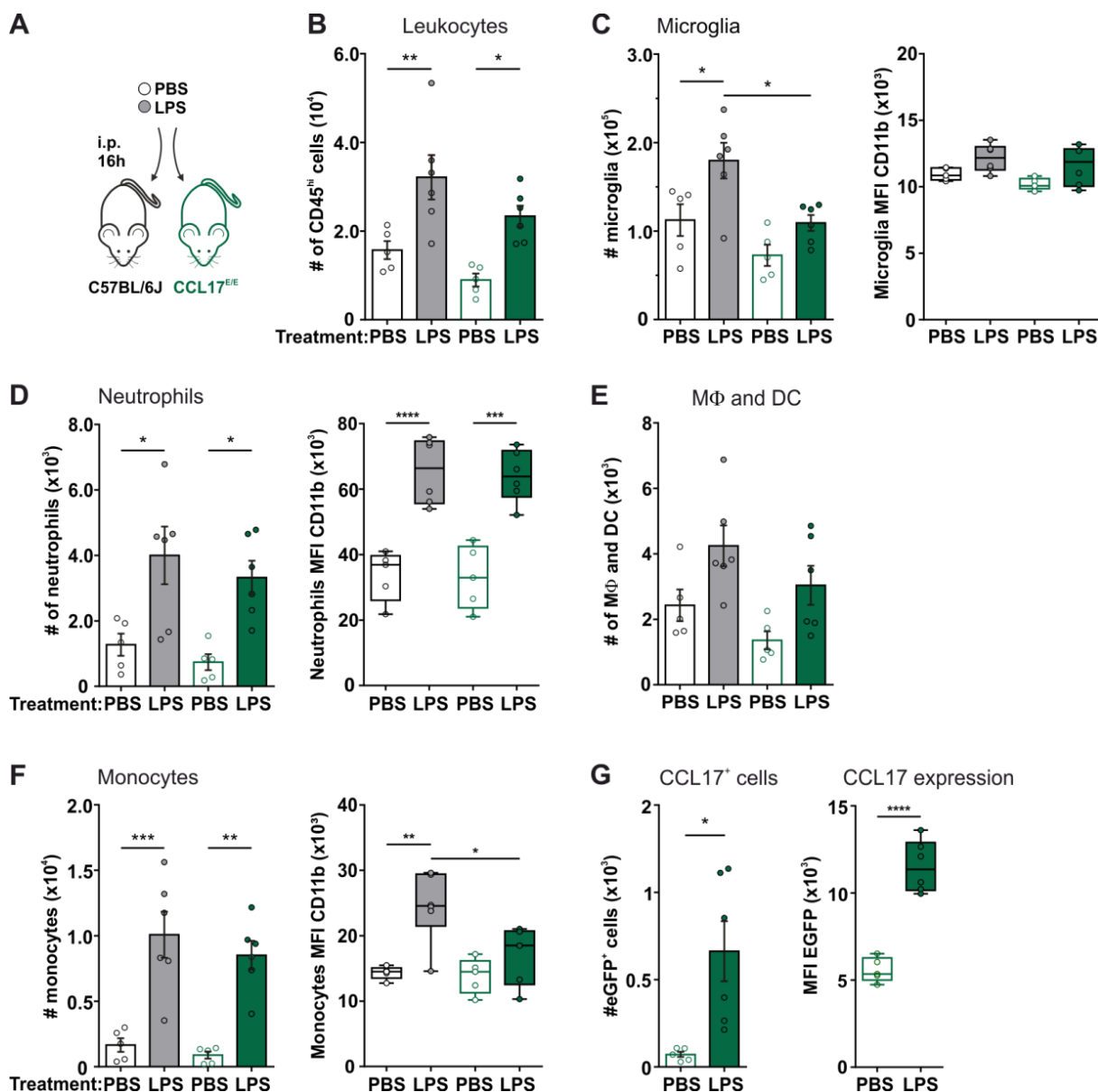


Figure 5.34 | CCL17-dependent modulation of resident and inflammatory immune cells in the brain.

A: C57BL/6J WT and CCL17^{E/E} mice were injected i.p. with 200μl PBS or 150μg LPS 16h before isolating the brain. Following in situ perfusion with PBS, brains were enzymatically digested and single cell suspensions subjected to staining for flow cytometry. With the help of counting beads, the absolute numbers of CD45^{hi} leukocytes (**B**), CD45^{int}CD11b⁺ microglia (**C**), CD45^{hi}CD3⁻Ly6G⁺, CD11b⁺ neutrophils (**D**), CD45^{hi}CD3⁻Ly6G⁻CD11b⁺ MΦs & DCs (**E**), and CD45^{hi}CD3⁻Ly6G⁻CD11b⁺ monocytes (**F**) was determined. The endogenous expression of EGFP in CCL17^{E/E} was used to identify CCL17-expressing cells. CCL17/EGFP⁺ cells were only present in inflammatory monocytes. Absolute numbers are depicted in **G**. In addition, mean fluorescence intensity (MFI) of CD11b staining was analyzed on microglia (**C**, right), neutrophils (**D**, right) and monocytes (**E**, right). MFI of EGFP was analyzed on CCL17/EGFP⁺ cells (**G**, right). (mean ± SEM, 3 independent experiments with n=5-6 per group) Circles represent individual mice. Data was tested for statistical significance by One-way ANOVA with Bonferroni's post-hoc test for multiple comparisons (****p<0.0001; ***p<0.001; **p<0.01; *p<0.05).

Regarding the CD45^{int}CD11b⁺ microglia, LPS treatment also led to increased numbers in both experimental groups, although CCL17^{E/E} mice had significantly fewer cells compared to WT mice (see **Fig. 5.34C**). Interestingly, reduced numbers of microglia were already observed under homeostatic conditions albeit the difference did not reach statistical significance. To determine the cellular activation status, the MFI of CD11b was analyzed. Under homeostatic conditions, CD11b expression

was comparable on microglia, monocytes, and neutrophils isolated from both experimental groups (see **Fig. 5.34C, D, and F, right**). As expected, LPS treatment induced a strong upregulation of CD11b on neutrophils and to a lesser extent on microglia of both genotypes. Strikingly, the absence of CCL17 abrogated the LPS-induced up-regulation of CD11b on inflammatory monocytes compared to WT mice.

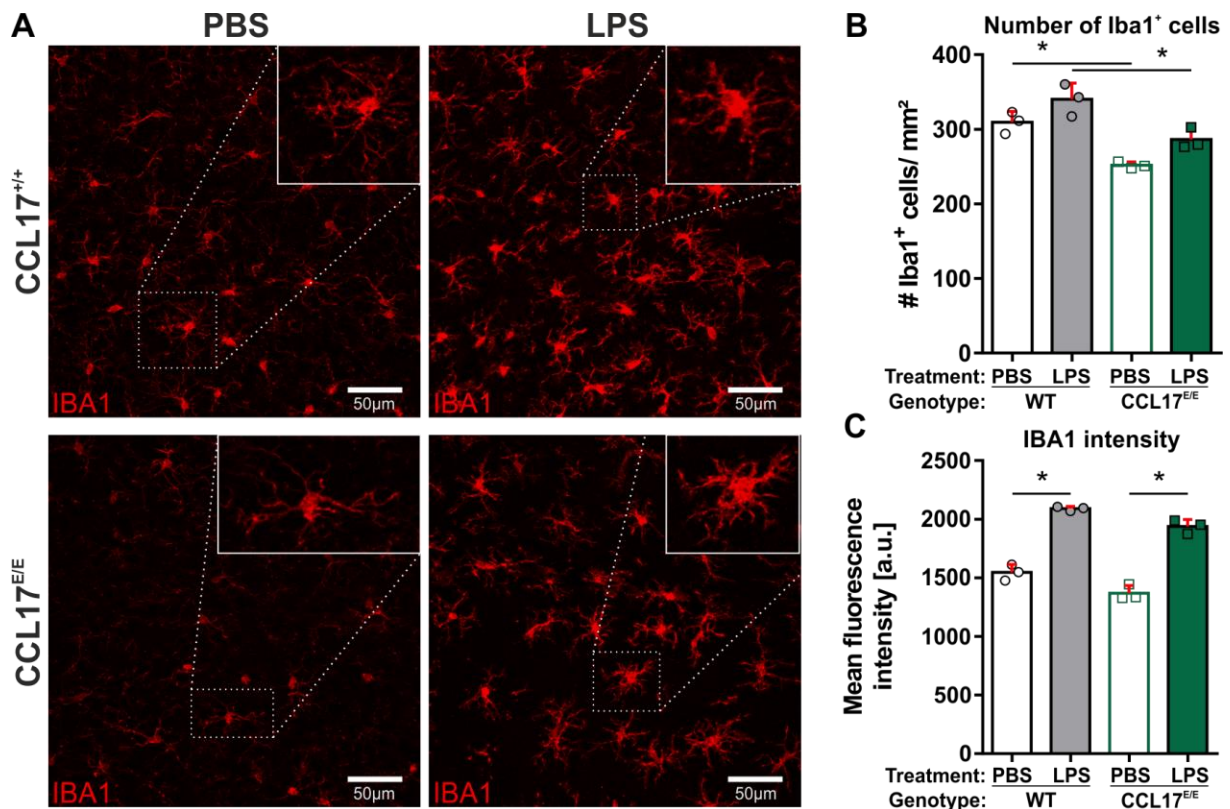


Figure 5.35 | Quantification of hippocampal microglia and IBA-1 expression in CCL17^{+/+} and CCL17^{E/E} mice.
A: Confocal images of IBA-1⁺ microglia in hippocampi of PBS- (first column) or LPS-treated (second column) CCL17^{+/+} (first row) and CCL17^{E/E} (second row) mice. Scale Bar is 50µm. Representative images are shown. **B:** Absolute number of hippocampal IBA-1⁺ cells in CCL17^{+/+} and CCL17^{E/E} mice. **C:** Quantification of the mean fluorescent intensity of IBA-1 staining in the hippocampus. Fluorescent intensity was determined using ImageJ plug-ins and normalized to the background. **B, C:** Analysis was performed using 9 images derived from 3 mice per genotype and treatment. Individual data points represent the mean values of 3 images/mouse. (mean ± SD) Statistical significance was determined using 2-way ANOVA with Bonferroni's post-hoc test for multiple comparisons (*p<0.05).

Flow cytometric analysis was performed on whole brains of WT and CCL17^{E/E} mice disregarding the fact that the strongest expression of CCL17 was observed in hippocampal CA1 neurons, especially in the context of systemic inflammation (see **Fig. 5.21 and 5.22B**). It was previously hypothesized that CCL17 exerts its effects predominantly within the hippocampal microenvironment in line with my own observations¹⁷⁵. Therefore, it was decided to analyze whether hippocampal microglia are specifically affected by the loss of CCL17. For this purpose, CCL17^{E/E} and littermate control animals (CCL17^{+/+}) were injected with 200 µl PBS or 150 µg LPS. 16 h later whole brains were isolated and vibratome sections were stained for the microglial marker IBA-1 (ionized calcium binding adaptor molecule 1) and analyzed by confocal microscopy.

IBA-1⁺ microglia were counted in confocal images of the hippocampus (see **Fig. 5.35A**). In addition, the MFI of IBA-1 was analyzed as an upregulation of IBA-1 was previously associated with microglia activation after systemic LPS challenge (see **Fig. 5.35C**)¹⁷⁸. In line with the flow cytometry data, the histological analysis also revealed significantly lower numbers of IBA-1⁺ microglia in PBS- and LPS-treated CCL17^{E/E} mice (see **Fig. 5.35B**). Comparable to the flow cytometric analysis of CD11b expression, LPS treatment also resulted in a significantly enhanced surface expression of IBA-1 (see **Fig. 5.35C**). However, upregulation of IBA-1 was comparable in WT and CCL17^{E/E} mice. In conclusion, these experiments demonstrated a potential role of CCL17 for the regulation of monocyte activation. In addition, loss of CCL17 appeared to affect microglia maintenance under homeostatic as well as inflammatory conditions.

5.5.9 Hippocampal microglia acquire an altered morphology in the absence of CCL17

The previous experiments indicated a role for CCL17 in regulating microglia maintenance. It was further recognized that IBA-1⁺ microglia appeared to acquire a slightly altered morphology in CCL17^{E/E} mice compared to littermate controls (see Fig. 5.35). To further investigate this observation, a more elaborate analysis of the morphology of IBA-1⁺ microglia was performed. To perform imaging analysis, a set of custom-written ImageJ plugins from J. N. Hansen from the group of Dr. Annett Halle was utilized (see section 4.1.4). Using these plugins, an in-depth morphological analysis of fluorescently labeled microglia within the hippocampal stratum radiale was carried out. As stated earlier, it was expected that the impact of CCL17 should be most prominent in the hippocampus, particularly after systemic LPS challenge. As in previous experiments, the morphological analysis was performed on IBA-1 stained brain sections generated from PBS- or LPS-treated (150 µg/mouse) male CCL17^{E/E} mice and corresponding littermate control animals (CCL17^{+/+}). The analysis focused on the hippocampus and representative cells are depicted in **Fig. 5.36**. The ImageJ plugins allowed the quantification of various morphological parameters, such as cell volume, cell surface or various skeleton parameters. For a detailed description of the parameters analyzed see Fülle et al., 2018¹⁴⁴.

For the analysis, single IBA-1⁺ cells were selected from the Z-stacks to generate a single cell image (see **Fig. 5.36, first column**). Next, a size-filtered binary image was created from this cell which removed background particles, smaller than 100 voxel (see **Fig. 5.36, second column**). This processed cell was then used to automatically extract the skeleton parameter (see **Fig. 5.36, third column**) and to reconstruct morphological parameters (see **Fig. 5.36, fourth and fifth column**).

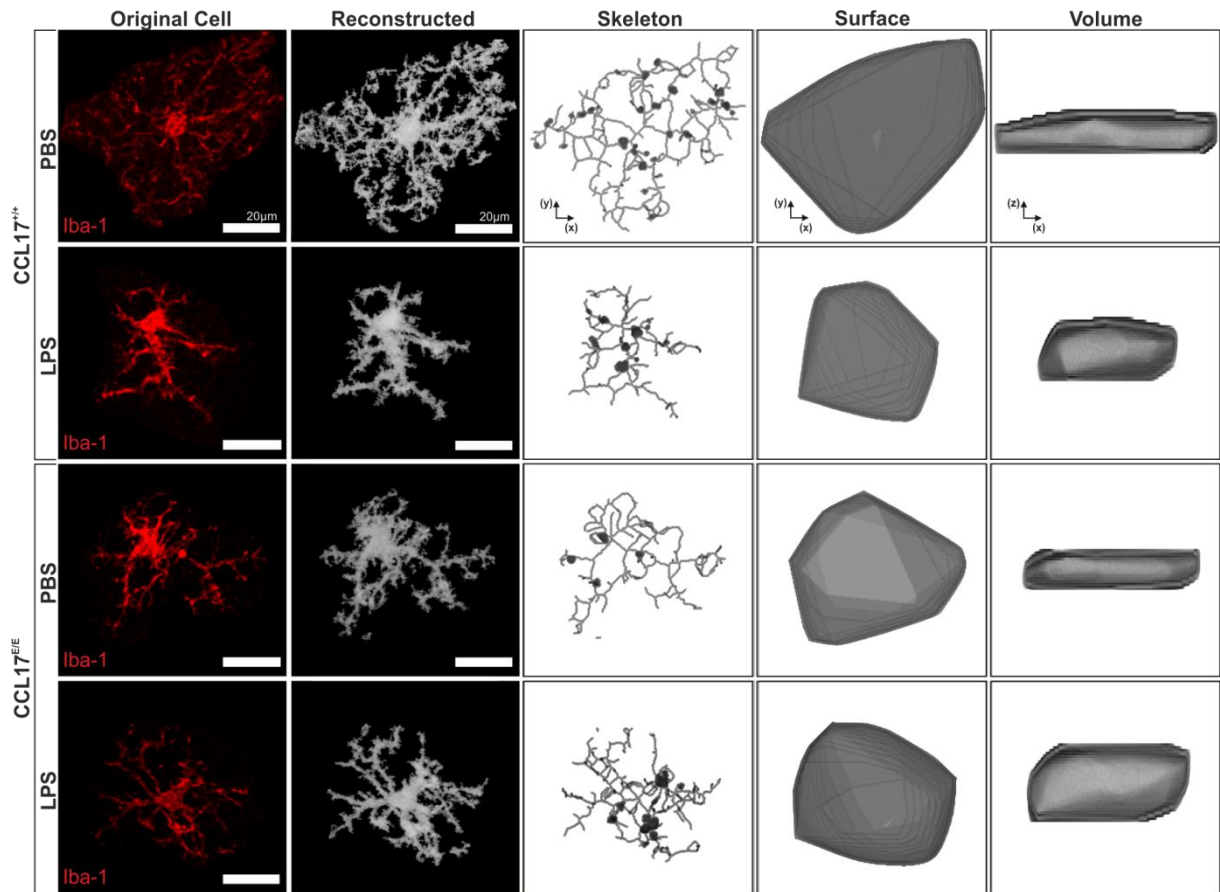


Figure 5.36 | Morphological analysis of hippocampal microglia in CCL17^{+/+} and CCL17^{E/E} mice.

CCL17^{+/+} and CCL17^{E/E} mice were injected (i.p.) with 200µl PBS or 150µg LPS. 16 h later mice were sequentially perfused with PBS and 4% PFA. Vibratome sections (40 µm) were stained for IBA-1 and z-stacks of hippocampal microglia were acquired using confocal microscopy. Resulting raw images were subjected to image analysis. Depicted are representative images of hippocampal microglia from PBS- or LPS-treated CCL17^{+/+} and CCL17^{E/E} mice. **First column:** Individual cells subjected to image analysis. Scale bar, 20µm. **Second column:** Reconstructed cell after image analysis. **Third column:** Skeletonized representation of the same cell. **Fourth column:** 3D representation of the determined cell surface area. **Fifth column:** 3D representation of the determined cell volume.

As can be already seen in the representative images, the surface area of microglia from PBS-treated CCL17^{E/E} mice appeared much smaller compared to PBS control microglia from CCL17^{+/+} mice (see **Fig. 5.36**). Whereas no apparent differences were observed between the experimental groups, systemic LPS challenge resulted in a striking increase of the cell volume (see **Fig. 5.36, fourth column**).

For a more comprehensive view of microglia morphology, 54 individual cells were analyzed for each genotype and condition (see **Fig. 5.37**). In addition to the quantification of cell volume and surface area, the total volume and area encompassed by the cell were calculated and are depicted as convex hull volume and convex hull area. In line with the microscopic evaluation, the cell volume and the convex hull volume of microglia from both experimental groups increased after LPS treatment (see **Fig. 5.37A and E**), whereas under control conditions (PBS injection) microglia of CCL17^{E/E} mice had a significantly smaller cell volume compared to microglia of CCL17^{+/+} mice. Also confirming the microscopic observations, systemic LPS challenge resulted in a significantly smaller surface area in control mice (see **Fig. 5.37B**). Strikingly, the surface area of microglia from PBS-treated CCL17^{E/E} mice was already much smaller than that of WT microglia. As anticipated, LPS treatment could not reduce this any further. Skeleton parameters were analyzed by implementing plugins from Arganda-Carreras and others¹⁷⁹ and included quantification of branches and junctions (see **Fig. 5.37C and D**) as well as analysis of the average branch length and the total tree length (see **Fig. 5.37G and H**). Comparable to the surface area, the number of branches and junctions, and the total tree length were also significantly lower in microglia from PBS-injected CCL17^{E/E} mice (see **Fig. 5.37C, D, and H**, respectively).

Ramification and polarity indices were calculated to get a better measure of the cellular activation status (see **Fig. 5.37I and J**). The ramification index describes the ratio of the cell surface area to the surface area of a theoretical sphere containing the same volume as the cell. As the sphere takes the cellular volume into account, it represents the minimum possible surface area an individual cell can achieve. As depicted in **Fig. 5.37I**, the overall ramification was reduced in both experimental groups after systemic LPS challenge. This is in line with several studies which also assessed the morphology of LPS-activated microglia *in vivo*¹¹¹. In contrast, the polarity index represents a measure for the homogeneity of microglia process distribution (see Methods for more details). A high polarity index is found in far-stretched microglia whereas a low polarity index is indicative of a more circular process distribution.

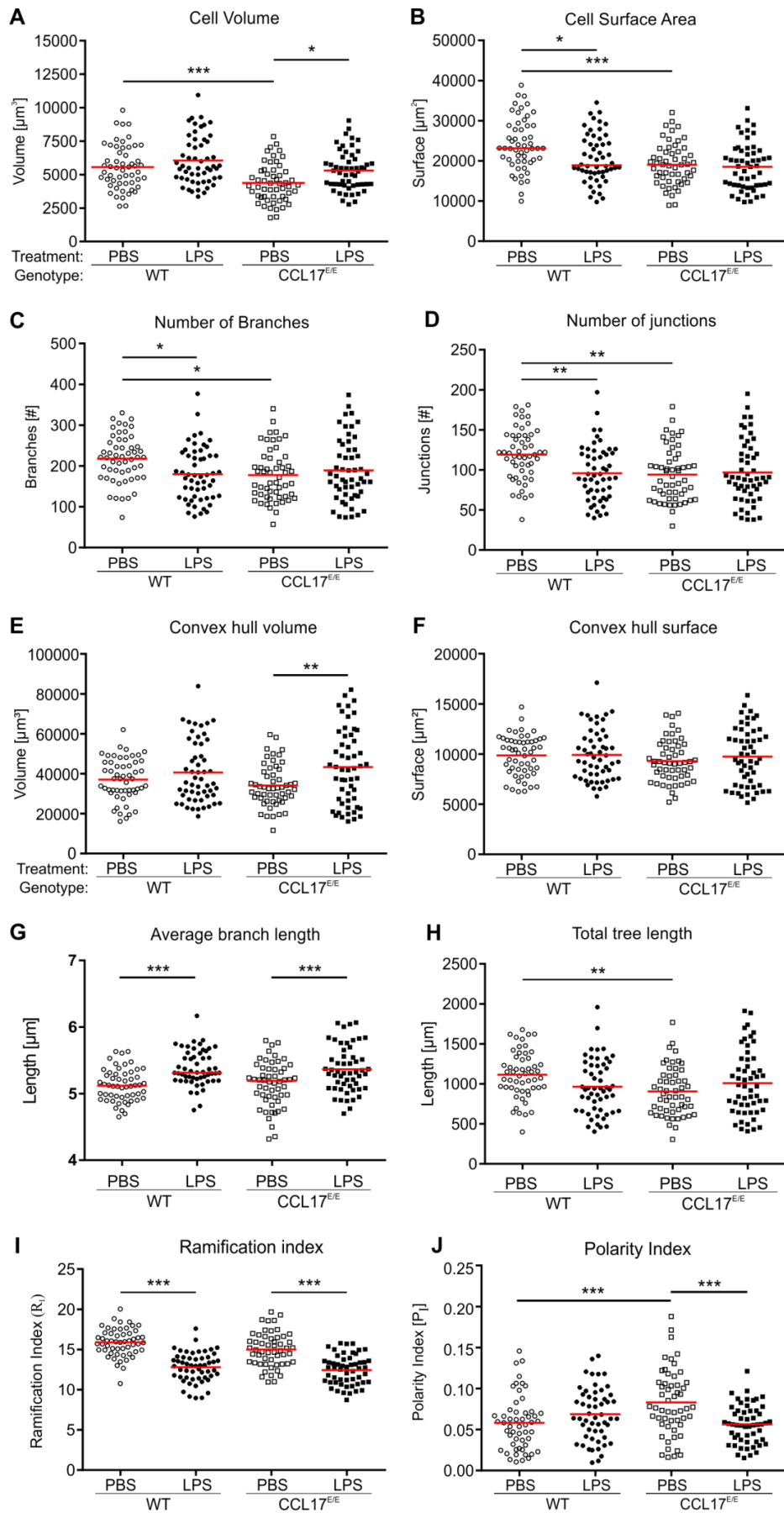


Figure 5.37 | Altered morphology of microglia in CCL17^{E/E} mice.

Legend on next page.

Interestingly, microglia of naïve CCL17^{E/E} mice displayed a remarkable increase in polarity compared to WT control mice. In contrast, systemic LPS challenge did not change the polarity of microglia from WT mice whereas microglia of CCL17^{E/E} mice lost their polarity after LPS treatment (see **Fig. 5.37J**).

The in-depth image analysis described above revealed a substantial role for CCL17 in regulating the morphology of hippocampal microglia. Regarding the cell surface area, the number of branches and junctions, and total tree length, the morphology of naïve microglia from CCL17^{E/E} mice resembled that of control microglia after systemic LPS challenge. In accordance with previous experiments, it can be concluded that hippocampal microglia, which developed in a microenvironment devoid of CCL17, were reduced in absolute numbers and had a significantly altered morphology already apparent under homeostatic conditions. It has to be noted, that systemic LPS treatment occluded the observed effects as microglia from both experimental groups acquired an activated morphology.

5.5.10 CCL17^{E/E} mice display an increased synaptic transmission at CA3-CA1 Schaffer collaterals

It is known that systemic inflammation leads to the activation of brain-resident microglia^{112,180}. In the healthy brain, quiescent or resting microglia continuously scan their environment, while also forming multiple immunological and neuronal synapses with neighboring glial cells and neurons. Other studies already found that under inflammatory conditions activated microglia engulf apoptotic cells and remove dysfunctional synapses¹¹¹. In light of the results described above which demonstrated robust expression of CCL17 in hippocampal neurons and further implicated CCL17 in the regulation of microglia morphology, it was decided to analyze synaptic transmission and plasticity in hippocampi of WT and CCL17^{E/E} mice. For this purpose, acute brain slices of male PBS- or LPS-treated CCL17^{E/E} mice or age-matched WT controls were prepared (see **Fig. 5.38A** and **5.39A**, respectively) and synaptic transmission was analyzed by B. Breithausen from the group of Dr. C. Henneberger from the Institute of Cellular Neurosciences, University of Bonn, Germany (IZN). CA3-CA1 Schaffer collaterals were stimulated electrically and field excitatory postsynaptic potentials (fEPSP) were recorded in the CA1 stratum radiatum. Strikingly, the basal synaptic transmission (slope of the first evoked fEPSP) was significantly higher in CCL17^{E/E} mice under homeostatic conditions (see **Fig. 5.38B**). This is also seen in the sample trace depicted in **Fig. 5.38A**. Analysis of the paired-pulse ratio (slope of the second fEPSP

Figure 5.37 | Altered morphology of microglia in CCL17^{E/E} mice.

Quantification of the morphological parameters of microglia depicted in Fig. 5.36. Confocal images of hippocampal IBA-1⁺ microglia from PBS- or LPS-treated CCL17^{+/+} and CCL17^{E/E} mice were subjected to image analysis. Z-stacks were acquired and analyzed using custom-written ImageJ plug-ins (see Methods for details). For both conditions and genotypes a total of 54 individual cells were analyzed (3 mice per group, 3 hippocampal images per mice with 6 cells per image). **A**: Cellular volume of single cells. **B**: 3D surface area of single cells. **C**: Absolute number of branches per single cell. **D**: Absolute number of junctions per single cell. **E**: Convex hull volume of individual cells. **F**: Convex hull surface of individual cells. **G**: Average branch length of individual cells. **H**: Total tree length of individual cell skeletons. **I**: Ramification index of individual cells. **J**: Polarity index of individual cells. The red line indicates mean value. Data was tested for statistical significance by 2-way ANOVA with Bonferroni's post-hoc test for multiple comparisons (**p<0.001; **p<0.01; *p<0.05).

divided by slope of the first fEPSP) did not reveal any differences between WT and CCL17^{E/E} animals. Corresponding to the morphological analysis of microglia, basal synaptic transmission was comparable in LPS-treated WT and CCL17^{E/E} mice (see **Fig. 5.39B** and sample trace in **Fig. 5.39A**).

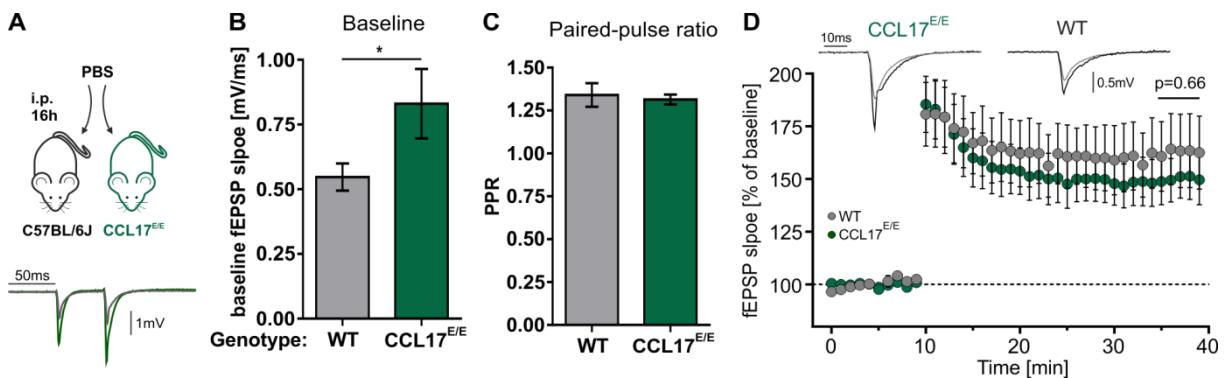


Figure 5.38 | Basal synaptic transmission is increased in CCL17^{E/E} mice under homeostatic conditions.

A: Male, age-matched WT and CCL17^{E/E} mice were injected (i.p.) with 200 μ l PBS. 16 h later acute brain slices were prepared and electrophysiological recordings were performed. Sample trace depicts characteristic baseline fEPSPs. **B:** Basal synaptic transmission as assessed by the slope of the first fEPSP evoked. The basal synaptic transmission significantly increased in slices of CCL17^{E/E} mice compared to WT mice (WT: 0.54 ± 0.05 mV/ms vs. CCL17^{E/E}: 0.87 ± 0.12 mV/ms; $n = 10-11$ slices from 3 animals; * $p < 0.05$ Mann-Whitney U-Test). **C:** Ratio of the second and first fEPSP evoked (Paired-pulse ratio) was not different between slices from WT and CCL17^{E/E} mice (WT: 1.34 ± 0.06 vs. CCL17^{E/E}: 1.31 ± 0.02 , $n = 10-11$ slices from 3 animals; $p = 0.72$, Mann-Whitney U-Test). **D:** Time-course of the fEPSP slopes during LTP measurements. The magnitude of LTP was quantified using the average fEPSP slope normalized to baseline over the last 5 min of the recording. TBS-induced fEPSP potentiation was not different between slices from WT and CCL17^{E/E} mice (WT: $162 \pm 16\%$ vs. CCL17^{E/E}: $150 \pm 10\%$, $n = 10-11$ slices from 3 animals; $p = 0.69$, Mann-Whitney U-Test). Sample traces show characteristic responses from WT or CCL17^{E/E} mice before (grey) and after (black) LTP induction. Data depicted as mean \pm SEM.

This experiment was performed by B. Breithausen (IZN).

As introduced earlier, the hippocampus has a crucial role in learning and memory formation. Although the exact molecular mechanisms remain elusive, it has long been known that repeated excitation improves communication between existing neurons by strengthening their synapses. This process is called long-term potentiation (LTP) and will produce lasting cellular changes that underlie synaptic plasticity and memory formation⁹⁶.

Here, LTP was induced using theta-burst stimulation (TBS) at hippocampal CA3-CA1 Schaffer collaterals (CA1-LTP). Under homeostatic and inflammatory conditions, TBS elicited a robust CA1-LTP that was comparable in CCL17^{E/E} and WT mice over the last 5 min of the recording (see **Fig. 5.38C** **PBS:** WT: $162 \pm 16\%$ vs. CCL17^{E/E}: $150 \pm 10\%$, $n = 10-11$ slices from 3 animals /group; $p = 0.69$, Mann-Whitney U-Test and **Fig. 5.39C** **LPS:** WT: $149 \pm 12\%$ vs. CCL17^{E/E}: $128 \pm 8\%$, $n = 10-12$ from 3 animals/group; $p = 0.15$, Mann-Whitney U-Test). It has to be noted, that the time-course of the baseline-normalized fEPSP slopes appeared to be reduced in slices of LPS-treated CCL17^{E/E} mice (see **Fig. 5.39C**).

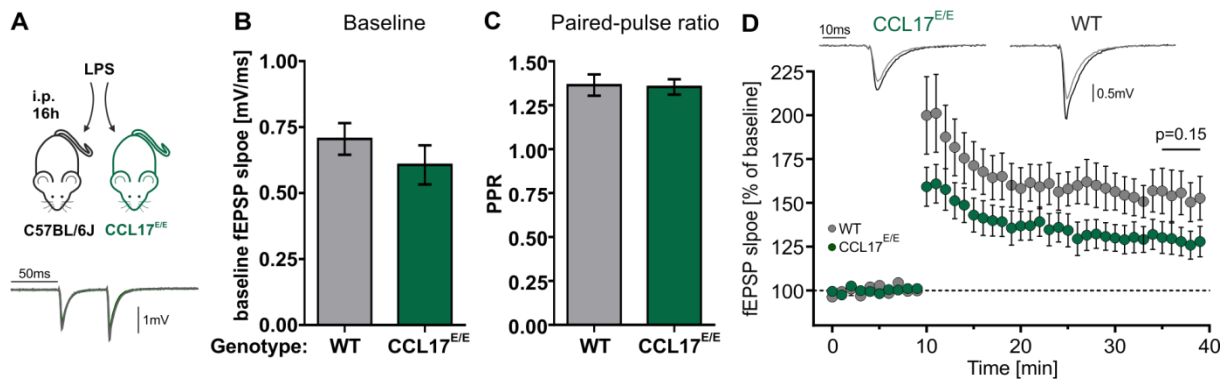


Figure 5.39 | After systemic LPS challenge neuronal signaling is comparable in WT and CCL17^{E/E} mice.

A: Male, age-matched WT and CCL17^{E/E} mice were injected (i.p.) with 150 µg LPS. 16 h later acute brain slices were prepared and electrophysiological recordings were performed. Sample trace depicts characteristic baseline fEPSPs. **B:** Basal synaptic transmission as assessed by the slope of the first fEPSP evoked. No significant difference was detected in slices of CCL17^{E/E} mice compared to WT mice (WT: 0.7 ± 0.06 mV/ms vs. CCL17^{E/E}: 0.6 ± 0.07 mV/ms; n = 10-12 slices from 3 animals; p=0.31, Mann-Whitney U-Test). **C:** Ratio of the second and first fEPSP evoked (Paired-pulse ratio) was not different between slices from WT and CCL17^{E/E} mice (WT: 1.36 ± 0.06 vs. CCL17^{E/E}: 1.35 ± 0.04, n = 10-12 slices from 3 animals; p=0.92, Mann-Whitney U-Test). **D:** Time-course of the fEPSP slopes during LTP measurements. The magnitude of LTP was quantified by taking the average fEPSP slope normalized to baseline over the last 5 min of the recording. TBS-induced fEPSP potentiation was not different between slices from WT and CCL17^{E/E} mice (WT: 149 ± 12% vs. CCL17^{E/E}: 128 ± 8 %, n = 10-12 slices from 3 animals; p=0.15, Mann-Whitney U-Test). Sample traces show characteristic responses from WT or CCL17^{E/E} mice before (grey) and after (black) LTP induction. Data depicted as mean ± SEM.

This experiment was performed by B. Breithausen (IZN).

In conclusion, these experiments revealed an enhanced basal synaptic transmission in the absence of CCL17. As the paired-pulse ratio was not affected by the loss of CCL17, which would indicate an increase probability of the presynaptic neuron to release neurotransmitters, the increase in basal synaptic transmission indicates a CCL17-dependent postsynaptic regulation of neuronal signaling. As for the analysis of microglia, this effect was occluded by systemic LPS challenge. In contrast, the absence of CCL17 had no significant effects on the induction of CA1-LTP, neither under homeostatic nor inflammatory conditions.

5.6 CCL17-DTR mice as a model system for the analysis of inducible neuroinflammation

The discovery that CCL17 is expressed in hippocampal CA1 neurons and has functional implications on microglia activation stimulated further research regarding the functional role of the CCL17-expressing neurons using CCL17-DTR mice (CCL17^{DTR/+} and CCL17^{DTR/DTR} mice). In these mice, the simian Diphtheria toxin receptor (DTR) was inserted into the second exon of the murine *Ccl17* locus by homologous recombination. Expression of the DTR under the control of the *Ccl17* promoter allows the inducible ablation of all CCL17-expressing cells following i.p. injection of diphtheria toxin (DT). Heterozygous CCL17^{DTR/+} mice carry only one functional *Ccl17* allele whereas homozygous CCL17^{DTR/DTR} mice are deficient for CCL17 but express the DTR from both targeted alleles. Importantly, DT is capable of crossing the blood-brain barrier and thus allows targeting of cells in the CNS¹⁸¹. Therefore, the ability of DT to ablate CCL17⁺ hippocampal neurons in CCL17^{DTR/+} mice was examined.

5.6.1 Strong fluctuations of body weight in DT-treated CCL17^{DTR/+} mice

Initially, both male and female mice were injected on three consecutive days with 0.4 µg DT/mouse/day or PBS as a control. To exclude unspecific effects of the DT treatment, WT control mice were also injected with DT or PBS. As depicted in **Fig. 5.40**, body weight monitoring revealed that both genders of DT-treated CCL17^{DTR/+} mice suffered from an early loss of body weight, starting the second day (day 0) after the first DT injection (day -2). Compared to PBS-injected CCL17^{DTR/+} mice, DTR mice continued to lose weight until a maximum was reached at day 5. At this time point, the mice had lost approximately 7-9% of their starting weight. Following this, the mice gained weight until they reached the weight of PBS-injected WT mice on day 7 (females, **Fig. 5.40A**) or day 11 (males, **Fig. 5.40B**). Once this point was overcome, all mice, independent of gender, genotype or treatment continued to gain weight. However, female DT-treated CCL17^{DTR/+} mice showed mild fluctuations in body weight over the entire course of the experiment. These fluctuations were accompanied by an increased sensitivity to stress, which manifested in increased locomotion and uncontrolled jumping behavior once the cage was opened. Approximately nine weeks after DT injection some of the female DT-treated CCL17^{DTR/+} mice also succumbed to the treatment. Interestingly, behavioral changes and lethality were rarely observed in male DT-treated CCL17^{DTR/+} mice.

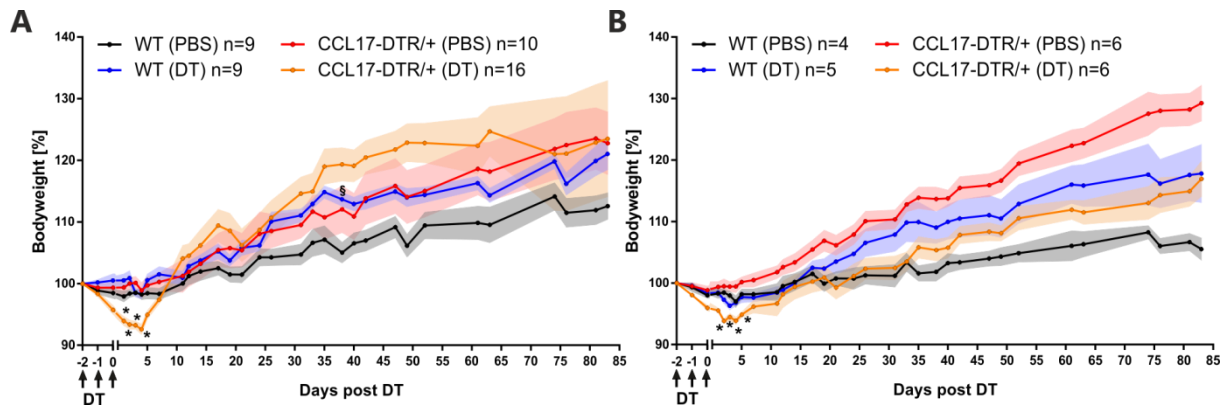


Figure 5.40 | Female and male CCL17^{DTR/+} mice show body weight fluctuations after DT treatment.

Female (**A**) and male (**B**) CCL17^{DTR/+} mice received three injections (i.p.) of 0.4 µg DT at d-2, d-1, and d0. Body weight was recorded every other day and calculated as percent of d-2. (Number of animals (n) is indicated in the figure, mean ± SEM). Statistical significance was tested using 2-way ANOVA with Bonferroni's post-hoc test for multiple comparisons (*p<0.05).

Three months after DT injection, all mice were sacrificed, and the brains were isolated as described previously. Following PFA-fixation, brains were embedded in paraffin, and 7 µm brain sections were prepared using a microtome. The brain sections were stained using hematoxylin and eosin (H&E) to analyze whether DT treatment of CCL17^{DTR/+} mice resulted in a loss of hippocampal neurons. Using light-microscopy, hippocampal sections of all experimental groups were visually inspected. As depicted in **Fig. 5.41A and B**, DT treatment of female and male CCL17^{DTR/+} mice resulted in an apparent reduction of pyramidal cells in the hippocampal CA1 region compared to all control groups. Importantly, hippocampi of DT-treated WT mice appeared normal.

The experiments indicated that in particular female, and to a lesser extent male CCL17^{DTR/+} mice, are affected by systemic DT treatment. At this point, however, it was difficult to attribute the early drop of body weight to the loss of CCL17⁺ neurons, especially keeping in mind that DT treatment will also ablate peripheral CCL17⁺ cells. In contrast, it was clearly demonstrated that DT treatment indeed resulted in diminished cell numbers in the hippocampal pyramidal cell layer three months after injection. The observed behavioral alterations could result from excessive neuronal activity in the hippocampus, which is often found in patients suffering from temporal lobe epilepsy.

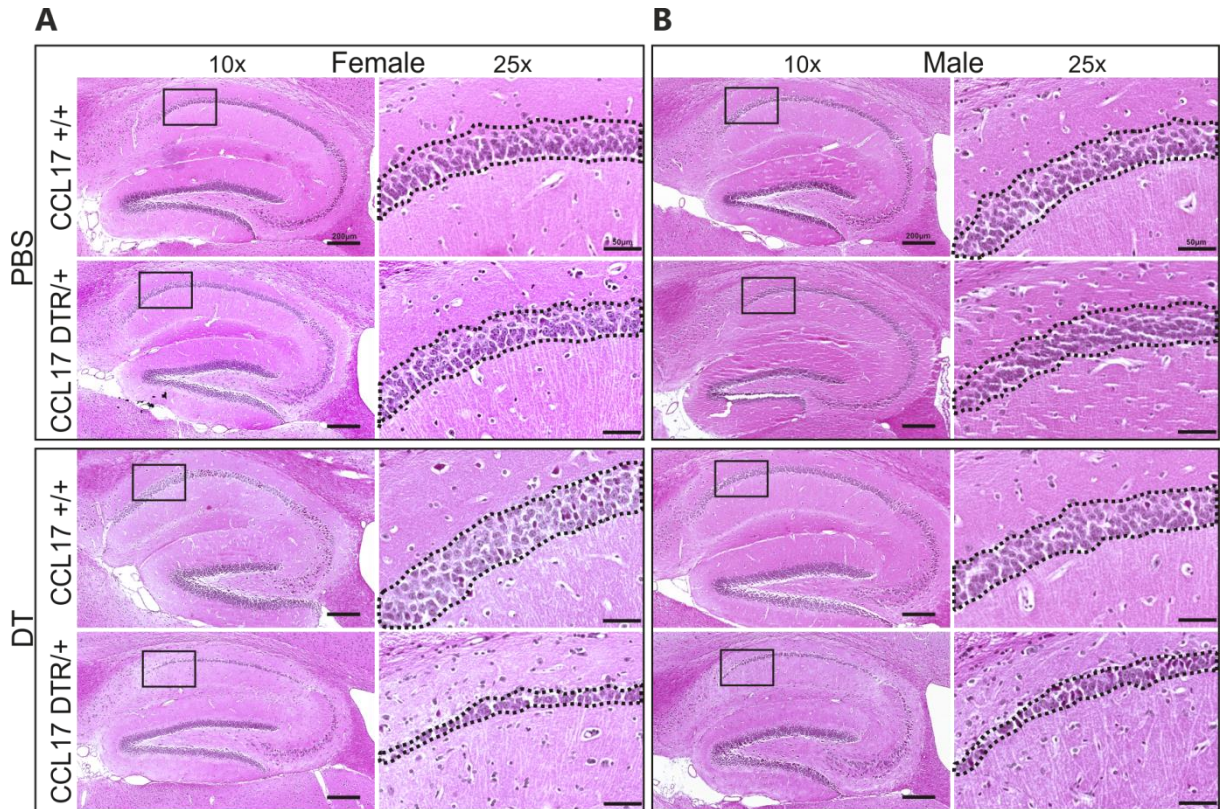


Figure 5.41 | Numbers of hippocampal pyramidal cells are reduced in $CCL17^{DTR/+}$ mice following long-term treatment with DT.

$CCL17^{DTR/+}$ mice received 0.4 μ g DT i.p. at d-2, d-1, and d0. Three months after injection, mice were perfused in situ and brains were isolated. After PFA fixation, brains were embedded in paraffin, and 10 μ m brain sections were prepared using a microtome. The brain sections were stained using hematoxylin and eosin (H&E). **A:** Hippocampi from female PBS or DT-treated $CCL17^{+/+}$ and $CCL17^{DTR/+}$ mice. **B:** Hippocampi from male PBS or DT-treated $CCL17^{+/+}$ and $CCL17^{DTR/+}$ mice. A & B: 100x and 250x magnification are depicted. Boxed areas indicate region analyzed at 250x magnification. Representative images are shown.

5.6.2 DT-induced ablation of $CCL17^+$ neurons takes approximately 14 days

Next, the dynamics of the DT-inducible ablation of $CCL17^+$ neurons were investigated. For this purpose, homozygous $CCL17$ -DTR mice ($CCL17^{DTR/DTR}$) were intercrossed with homozygous $CCL17$ -EGFP mice ($CCL17^{E/E}$). In the resulting F1 generation, $CCL17^{DTR/E}$ mice carried two targeted *Cc17* alleles and simultaneously expressed DTR and EGFP, both under the control of the *Cc17*-promoter. In $CCL17^{DTR/E}$ mice, the loss of $CCL17^+$ neurons post DT treatment can be followed by the loss of EGFP fluorescence. As before, $CCL17^{DTR/E}$ mice received three consecutive injections of 0.4 μ g DT/day (day -2, day -1, and day 0). To enhance the expression of DTR and EGFP mice received a single i.p injection of LPS (150 μ g) one day before isolating the brain (at day 3, day 6, or day 13). On day 4, day 7, or day 14 after the last DT injection, $CCL17^{DTR/E}$ mice were perfused *in situ*, and brains were isolated and prepared for confocal imaging. As before, sagittal brain sections were stained for EGFP. Further, a TUNEL (terminal deoxynucleotidyl transferase dUTP nick end labeling) stain was performed to detect DNA breaks present in apoptotic cells.

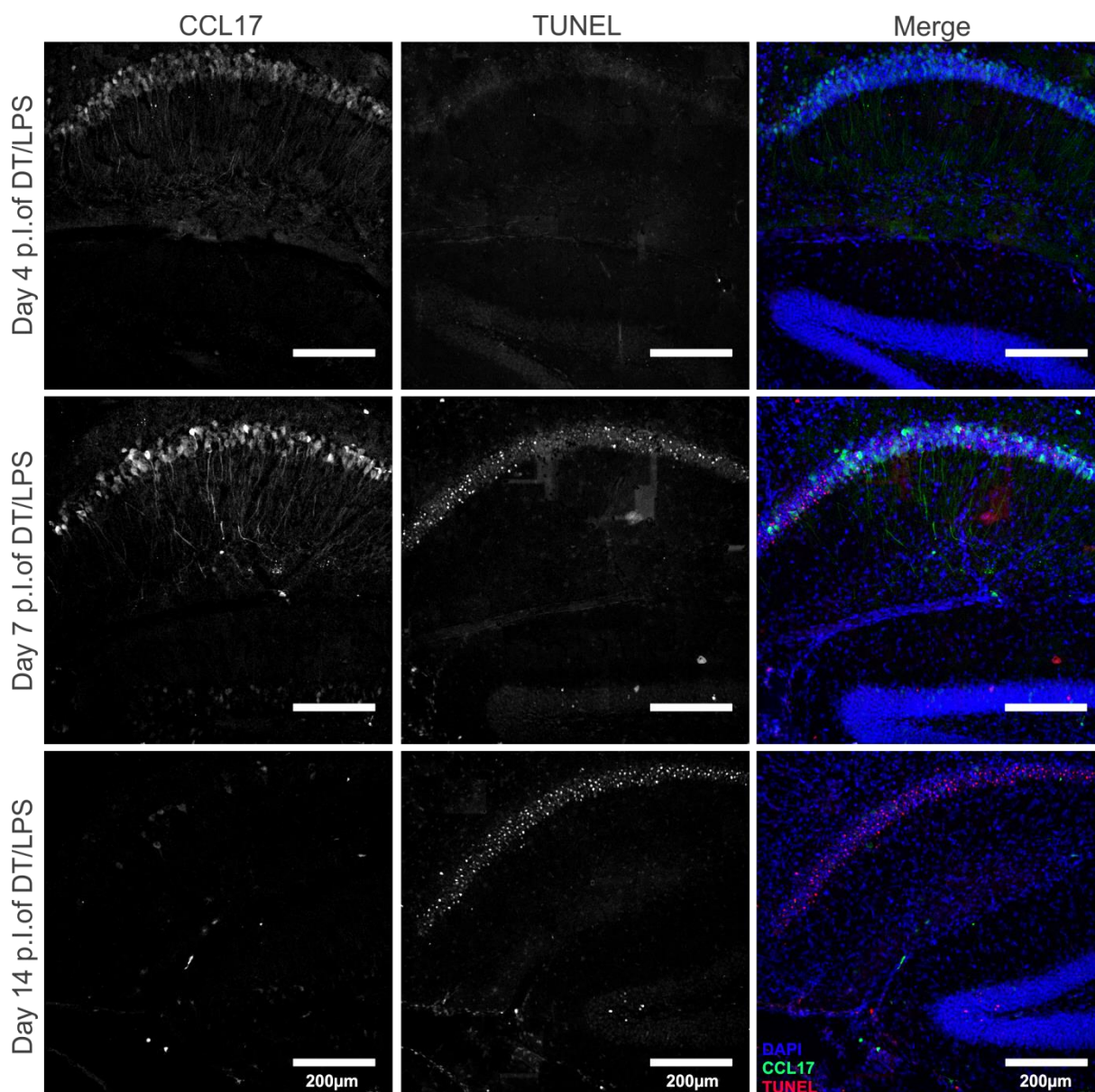


Figure 5.42 | DT treatment induces apoptosis of hippocampal CCL17⁺ neurons in CCL17^{DTR/E} mice.

CCL17^{DTR/E} mice received 0.4µg DT i.p. at day -2, day -1, and day 0. To enhance CCL17/EGFP expression, mice were injected i.p. with 150 µg LPS in 200 µl PBS on day 3, day 6, or day 13. Brains were isolated 16 post LPS injection and stained for EGFP and DAPI. Apoptotic cells were detected by TUNEL labeling (terminal deoxynucleotidyl transferase dUTP nick end labeling). Images were scanned using confocal microscopy (**Left**: CCL17/EGFP staining; **Middle**: TUNEL labeling; **Right**: Pseudocolor merge image: DAPI (blue), CCL17/EGFP (green) and TUNEL (red)). Scale bar, 200µm. Representative images are shown (n=2).

At day four after DT treatment, no TUNEL-positive cells could be detected in the hippocampi of DT-treated CCL17^{DTR/E} mice (see **Fig. 5.42, first row**). As expected, CCL17/EGFP⁺ hippocampal neurons were identified albeit the intensity of EGFP staining was relatively weak compared to previous experiments (see Fig. 5.22). In contrast, seven days after the last DT injection, a high number of apoptotic cells was present in the pyramidal cell layer of the hippocampal CA1 region (see **Fig.5.42, second row**). Also, a substantial number of CCL17/EGFP⁺ cells was still present in the hippocampus. Strikingly, two weeks after DT treatment (day 14) no CCL17/EGFP⁺ cells were detected in the hippocampus (see **Fig.5.42, third row**). In line, the number of TUNEL⁺ cells strongly increased

compared to the previous time point. In conclusion, these experiments confirmed that i.p. injection of DT in CCL17-DTR mice targets CCL17-expressing neurons in the hippocampus. Interestingly, CCL17/EGFP⁺ neurons were still detected one week after DT treatment whereas almost no EGFP-positive cells were left one week later.

5.6.3 Ablation of CCL17⁺ neurons causes severe micro- and astrogliosis in the hippocampus

To shed further light on the effects of the DT-induced ablation of CCL17⁺ neurons, brain sections of DT-treated CCL17^{DTR/+} mice were analyzed histologically at different time points after DT injection. As for the previous experiments, CCL17^{DTR/+} mice received three consecutive injections (i.p.) of 0.4 µg DT/mouse/day. Here, an emphasis was put on the histology of the hippocampus. As before, microglia were identified by IBA-1 staining. As astrocytes are also involved in the regulation of brain immunity, brain sections were also stained for the astrocyte marker GFAP (glial fibrillary acidic protein). Using confocal microscopy, Z-stacks of brain sections at day 4, day 7, day 14, day 21, and day 28 after DT treatment were recorded.

Visual inspection of IBA-1-stained brain sections indicated the development of severe microgliosis at day 7 after DT injection (see **Fig. 5.43, second row**). A high number of microglia was present in the pyramidal cell layer of the CA1 region, probably engulfing apoptotic neurons. Microglia numbers were still increased at day 14 after DT treatment albeit to a lesser extent compared with d7 (see **Fig. 5.43, third row**). These findings matched the results from the dynamics of the DT-induced ablation of CCL17-expressing neurons (see Fig. 5.42). Interestingly, the number of hippocampal microglia appeared to decrease at day 21 and day 28 after DT treatment (see **Fig. 5.43, fourth and fifth row**). This could indicate the efficient removal of apoptotic neurons and, therefore, a reduced recruitment/proliferation of microglia.

In contrast to the early microgliosis, numbers of astrocytes started to increase at day 7 after DT treatment but only developed into a severe astrogliosis 21 days after DT injection (see **Fig. 5.43 second and third row**). At day 21 and day 28 increased numbers of astrocytes localized to the pyramidal cell layer of the CA1 region. As astrocytes are commonly known for their essential role in tissue-repair, this indicates the formation of a glial scar probably in areas most severely affected by the DT-induced loss of CCL17/DTR-expressing CA1 neurons.

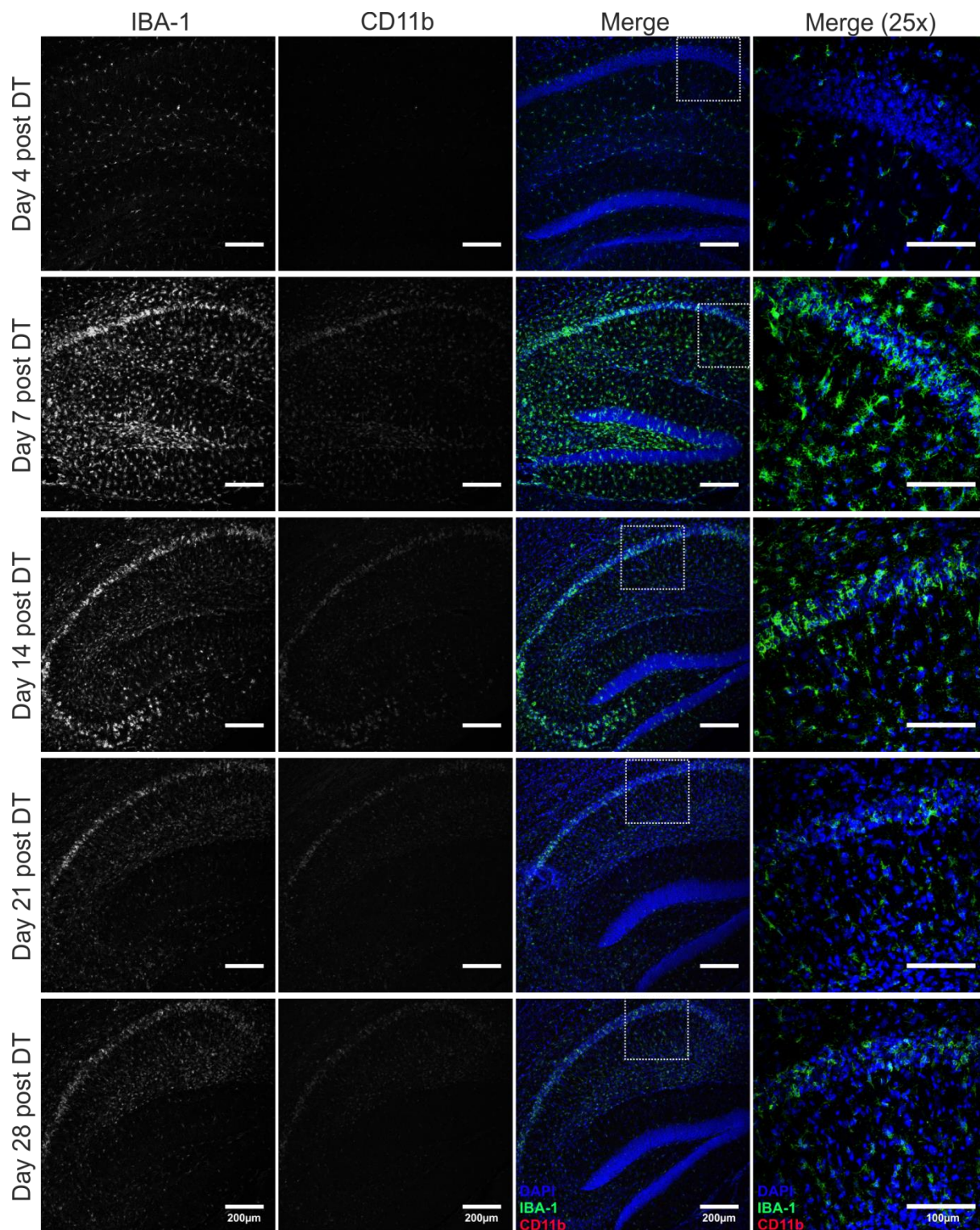


Figure 5.43 | DT treatment induces microgliosis in CCL17^{DTR/+} mice.

CCL17^{DTR/+} mice received 0.4 µg DT i.p. at day -2, day -1, and day 0. Brains were isolated at day 4 (first row), day 7 (second row), day 14 (third row), day 21 (fourth row), or day 28 (fifth row) after the last DT injection and stained for the microglia marker IBA-1. DAPI was used as a counterstain. Images were scanned using confocal microscopy. **(First column: IBA-1 staining. Second column: DAPI counterstain, Third column: Pseudocolor merge images: DAPI (blue) and IBA-1 (green). Boxed areas were analyzed at 250x magnification (fifth column).** Scale bar, 200µm. Representative images are shown (n=2).

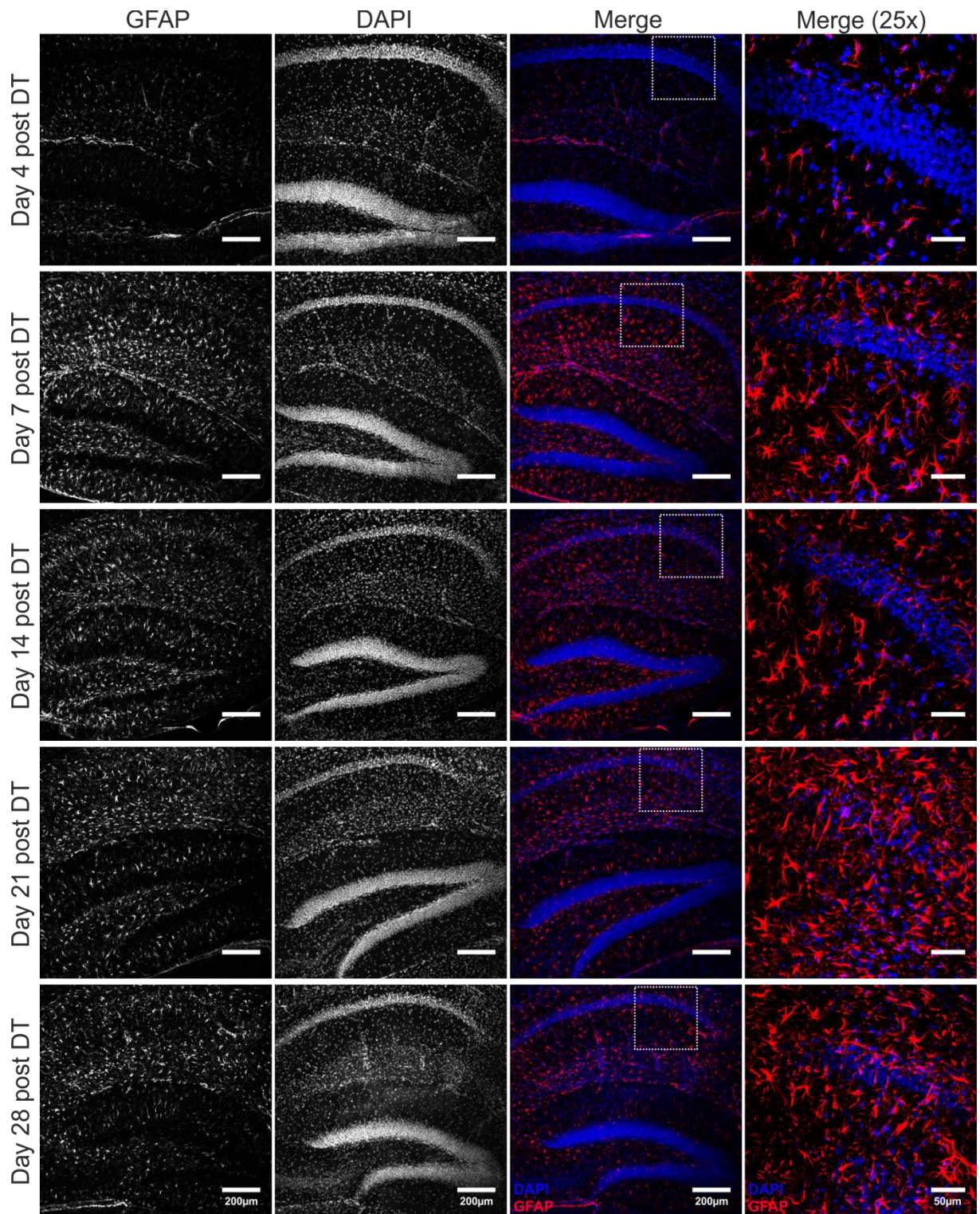


Figure 5.44 | DT treatment induces astroglial activation in CCL17^{DTR/+} mice.

CCL17^{DTR/+} mice received 0.4µg DT i.p. at day -2, day -1, and day 0. Brains were isolated at day 4 (first row), day 7 (second row), day 14 (third row), day 21 (fourth row), or day 28 (fifth row) after the last DT injection and stained for the astrocyte marker GFAP. DAPI was used as a counterstain. Images were scanned using confocal microscopy. **(First column: GFAP staining. Second column: DAPI counterstain. Third column: Pseudocolor merge images: DAPI (blue) and GFAP (red). Boxed areas were analyzed at 250x magnification (fifth column).** Scale bar, 200µm. Representative images are shown (n=2).

5.6.4 DT-treated CCL17^{DTR/+} mice develop epileptic seizures after an initial silent phase

During the preceding experiments it was demonstrated that DT treatment of CCL17^{DTR/+} mice induces apoptosis of CCL17⁺ hippocampal CA1 neurons. As a consequence, the mice developed a severe micro- and astrogliosis that was restricted to the hippocampus. In addition, CCL17-DTR mice experienced body weight fluctuations and showed behavioral abnormalities after DT-treatment. In particular, female CCL17^{DTR/+} mice displayed uncontrolled jerking movements and momentary losses of awareness. Neuronal death in the hippocampal CA1 region has long been associated with the development of mesial temporal lobe epilepsy (MTLE). In rodents, MTLE is characterized by epileptic seizures that result from spontaneous recurrent seizures (SRS) in the brain. Thus, it was hypothesized that the DT-induced ablation of CCL17⁺ neurons may lead to a functional destabilization of the hippocampus and consequently induces SRS and MTLE. To test this hypothesis, 12-week old female CCL17^{DTR/+} mice were injected (i.p) with DT and subsequently subjected to continuous telemetric EEG monitoring. Since the applied DT treatment regimen did not affect WT mice in previous experiments, it was decided to test only CCL17^{DTR/+} mice. The experiment was performed in collaboration with J. Müller and Dr. P. Bedner from the group of Prof. Steinhäuser at the IZN.

In accordance with previous experiments, CCL17^{DTR/+} mice received three daily i.p. injections of 0.4 µg DT. Immediately after the last DT injection, telemetric transmitters were transplanted and EEG recordings were started. The recorded EEG data was manually screened for the occurrence of potential electrographic seizures by Dr. P. Bedner and was provided as a table depicting the number of seizures per day and mouse. Unfortunately, two mice did not recover from anesthesia and one mouse died shortly after the start of the experiment. Thus, only two mice could be monitored for three months post DT injection.

In **Fig. 5.45** the numbers of daily seizures per individual mouse are depicted. Strikingly, the analysis revealed a series of 15-17 high-frequency and high-amplitude seizures at day 5 or day 6 after DT treatment in mouse#1 and mouse#2, respectively (see **Fig. 5.45A and B**). In both animals, the number of seizures decreased on the next day, while seizures came to a complete halt at day 7 or day 8 in mouse#1 and #2, respectively. After this one day latent period, both mice developed generalized SRS over the course of the experiment. The number of SRS varied between the animals, ranging from 0-6 seizures/day in mouse#1 and 0-8 seizures/day in mouse#2 (mean of: 2.771 ± 1.399 seizures/ day/ mouse).

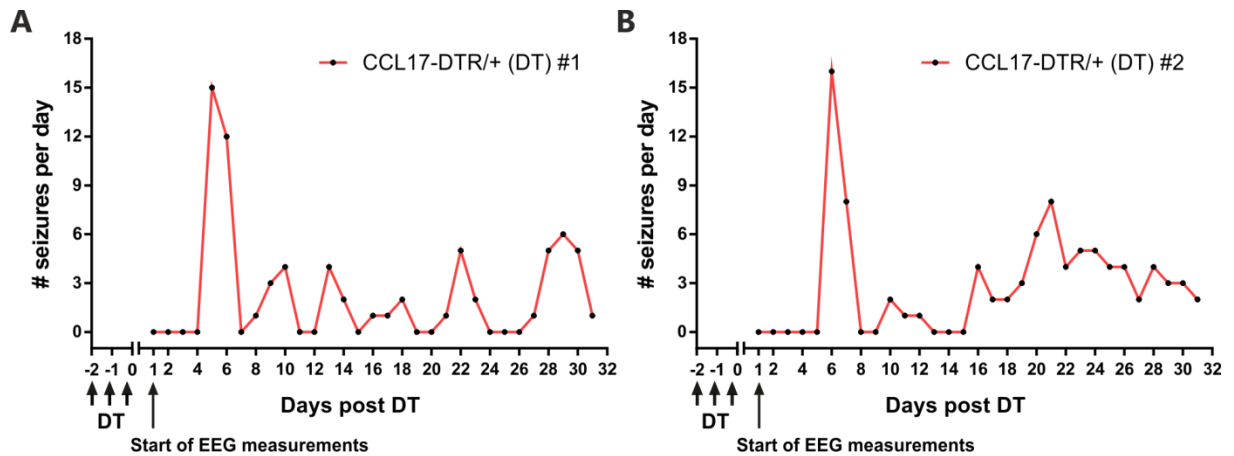


Figure 5.45 | DT-treated CCL17^{DTR/+} mice develop epileptic seizures after DT treatment.

Female CCL17^{DTR/+} mice received 0.4 μ g DT i.p. at day -2, day -1, and day 0. At day 0, mice were anesthetized and a telemetric transmitter was placed into a subcutaneous pocket in the right abdominal wall. Skull surface electrodes were implanted to record electrographic seizures. Individual mice were placed on radio receiving plates, which captured signals from the electrodes and sent them to an input exchange matrix. The digital output of the receiver was converted in real-time into a calibrated analog output. **A, B:** Number of epileptic seizures/day, recorded in mouse#1 (**A**) and mouse#2 (**B**). The sudden appearance of seizures at days 5-7 was followed by a strong decrease in the frequency of SRS on the following days (mean of 2.771 ± 1.399 / seizures/ day/ mouse).

In conclusion, it could be demonstrated that five to six days after DT treatment, CCL17^{DTR/+} mice indeed developed epileptic seizures. The initial silent period could be explained by the previous experiments in which apoptotic cells appear only as late as day 7 after DT treatment. Although more experiments have to be performed, CCL17-DTR mice may serve as a new model for the analysis of epilepsy and inducible neuroinflammation in the future.

6. Discussion

The chemokine CCL17 has been implicated in the development of inflammatory diseases of all major barrier organs, including the skin, the gut, and the lung. In the skin, CCL17 was shown to be crucial for the development of atopic dermatitis^{69,73,152,164,182}, lupus erythematosus¹⁸³ and contact hypersensitivity (CHS)^{49,50,90}. In the gut, it promotes intestinal inflammation of the colon⁷², and in the lung, CCL17 exacerbated allergic asthma^{71,80,184,185}. Using CCL17/EGFP reporter (CCL17^{E/+}) mice, we previously demonstrated that DCs are the primary source of CCL17 under both, homeostatic and inflammatory conditions^{73,168}. Key functions of CCL17 include the recruitment of T cells to sites of inflammation^{50,186} and the initiation of T cell-DC interactions required to trigger adaptive immune responses⁸⁹. In particular, CCL17 production by natural killer T (NKT) cell-licensed DCs was shown to recruit cytotoxic T cells via cross-presentation of external antigens⁸⁹. In mice, the designated receptor of CCL17 is CCR4, whereas in humans CCR4 as well as CCR8 were described to interact with CCL17⁷⁶. In mice, CCR4 was demonstrated to be expressed on thymic CD4/CD8 double-positive thymocytes & CD4 single positive T cells¹⁸⁷. In addition, CCR4 is also found on skin-homing CLA⁺ T cells, Th2 cells and regulatory T cells^{45,48}. Interestingly, CCR4-induced signaling pathways have also been associated with regulation the of DC functions⁸⁵.

CCL22, the second ligand of CCR4, was mainly shown to be involved in autoimmune disorders^{188,189}, allergic reactions of the skin^{77,190}, and recruitment of regulatory T cells into the tumor microenvironment^{78,191}. Similar to CCL17, CCL22 expression was detected in the thymus¹⁸⁷ and distinct subsets of myeloid cells, with alternatively activated Mφs showing the highest expression¹⁹². Strikingly, CCL22 expression by intratumoral Mφs is associated with a tumor immune-escape response mechanism through the recruitment of CCR4⁺ regulatory T cells and the subsequent suppression of tumor-specific T cell immunity¹⁹³.

In the first part of the present thesis, the functional relevance of the CCL17/CCL22-CCR4 axis was investigated in the context of skin inflammation. Therefore our newly generated CCL17/22-double-deficient mice were analyzed in CHS, the murine model of allergic contact dermatitis (ACD), and compared to CCR4-deficient animals. In addition, a potential therapeutic application of inhibiting CCL17 using an aptamer-based approach was investigated.

Besides the immunostimulatory and immunoregulatory roles of CCL17 and CCL22, several reports already indicated a function of the two chemokines in the CNS^{84,85,194,195}. As these studies focused on the functional relevance of CCL17 production outside the CNS, in the second part of the thesis, I analyzed CCL17 expression in the brain and examined its function in the context of systemic inflammation.

6.1 CCL17 in the context of skin immunity

In previous studies of our group, a critical role of CCL17 in the development of DNFB-induced CHS was identified^{49,73}. The analysis of CCL17-deficient (CCL17^{E/E}) mice revealed a function for CCL17 during both phases of the CHS response. During the afferent phase, emigration of LCs from the skin to draining LNs was shown to require autocrine signaling of CCL17 via a CCR4-independent signaling pathway⁴⁹. The impaired migration of LCs resulted in reduced transport of cutaneous antigens to LNs and consequently less efficient priming of naïve T cells. As a result, reduced numbers of memory effector T cells home back to the skin⁵⁰ and the second exposure to DNFB causes an attenuated inflammatory response in CCL17^{E/E} mice compared to control mice⁵⁰. During the elicitation phase of CHS, the expression of CCL17 in the skin strongly increases possibly to recruit CLA⁺ CCR4⁺ effector T cells^{46,47,87}. In the absence of CCL17, mice show less severe allergic reactions of the skin due to an impaired sensitization and reduced recruitment of CCR4⁺ leukocytes. Surprisingly, an opposite phenotype was observed in CCR4-deficient (CCR4^{-/-}) mice^{91,196}, with CCR4^{-/-} mice showing an exaggerated skin inflammation. This observation points to more complex regulatory mechanisms, potentially involving a second receptor for CCL17 and/ or another ligand of CCR4, such as CCL22, CCL2, CCL3, or CCL5^{176,197}.

6.1.1 Analysis of CCL17-expressing cells in the murine skin

In mice, CCL17 is strongly expressed in CD8 α ⁻ CD11b⁺ cDC2 under homeostatic as well as inflammatory conditions^{73,168}. These CCL17-producing cDC2s are mainly found in peripheral LNs, mucosal tissues, and other non-lymphoid organs⁷³. Interestingly, CCL17 expression was nearly absent in the healthy spleen and skin^{73,168}. However, we found that α -galactosylceramide-activated NKT cells induce CCL17 expression also in splenic CD8 α ⁻ cDC2 as well as CD8 α ⁺ cDC1¹⁶⁸ in a GM-CSF-and IL-4-dependent manner¹⁶⁸. In contrast, IFN γ caused a significant suppression of CCL17 expression in splenic DCs¹⁶⁸. These findings demonstrated that CCL17 is strongly regulated in an inflammation- and organ-specific manner.

The earlier studies mainly focused on the analysis of CCL17-expressing cells in the epidermis^{49,73}. In the present work, however, entire dorsal ear halves from CCL17^{E/+} mice were analyzed for the presence of CCL17/EGFP⁺ cells in both compartments of the skin. Using a combination of highly sensitive confocal and intravital microscopy (IVM) it was possible to detect a small number of CCL17/EGFP⁺ cells even in murine skin which was not treated with DNFB (see section 5.1). These cells might have been overlooked previously due to technical limitations^{49,73}. As another consideration, the skin samples analyzed in this thesis have been treated with the solvent acetone:olive oil for confocal microscopy or with a hair-removal cream for IVM which may have induced CCL17 expression to some extent. Interestingly, CCL17/EGFP⁺ cells appeared to mostly assemble in small cellular clusters in close proximity to lymphatic and/or blood vessels (BVs). This finding was somewhat surprising, as CCL17 was

expected to be mostly expressed in dermal DCs (dDCs) which are known to distribute diffusely in the healthy skin⁶⁰. Nevertheless, it is conceivable that the distinct location of CCL17/EGFP⁺ cells, which likely represent also perivascular Mφs (pvMφs), in close proximity to post-capillary venules is required to recruit peripheral leukocytes, such as neutrophils or memory effector T cells^{87,185,198}. In line, the analysis of non-inflamed human skin revealed co-expression of CCL17 and the adhesion molecules, E-selectin and ICAM-1, in defined areas of dermal vessels⁸⁶. These areas are likely to represent 'dermal hotspots' for extravasating leukocytes. Here, a single application of DNFB on the ears of non-sensitized CCL17^{E/+} mice induced a more dispersed distribution of CCL17-expressing cells, which either suggests an activation induced increase in CCL17 expression, enhanced migratory capacity of existent CCL17⁺ cells, or the infiltration of peripheral CCL17-producing cells. Interestingly, treatment of alternatively-activated BM-Mφs with IL-1α was shown to induce the expression of several chemokines including CCL17⁶⁰. In line, treatment of human keratinocytes (KCs) with various contact sensitizers was previously shown to induce inflammasome activation which results in the massive release of IL-1α¹⁹⁹. Furthermore, murine KCs are capable of secreting large amounts of IL-1α in response to mechanical and inflammatory stimuli^{57,200,201}. Thus, it is possible that DNFB treatment results in the release of IL-1α from KCs, which in turn upregulates CCL17 expression in dDCs and pvMφs.

As introduced earlier, skin immune cells display a sequential activation pattern during inflammation, which leads to the formation of distinct immune cell clusters known as iSALT for **inducible skin-associated lymphoid tissue**^{58,202}. These clusters are not present under homeostatic conditions but are essential for the local activation of memory effector T cells under inflammatory conditions⁶⁰. In the present work, the presence of CCL17/EGFP⁺ cells directly adjacent to dermal BVs under homeostatic as well as inflammatory conditions potentially indicates an important role for CCL17 in the formation of iSALT through the recruitment of skin-homing CCR4⁺ leukocytes. Thus, further experiments should address whether CCR4⁺ leukocytes actually extravasate in dermal areas juxtaposed to CCL17-expressing cells.

Behaviorally distinct CCL17⁺ cells are present in the murine skin.

To examine the migratory kinetics of CCL17/EGFP⁺ skin cells *in vivo*, I performed IVM using ears of CCL17^{E/+} mice. Interestingly, IVM revealed the presence of at least two CCL17/EGFP⁺ cell populations in the dermis (see section **5.1.2**), which differed in motility.

A more sessile cell population with an elongated, dendritic shape localized directly adjacent to post-capillary venules. These cells showed no active migratory behavior but displayed a continuous movement of their dendrites along the vessel wall. In light of previous studies, these cells possibly represent a subset of CCL17⁺ pvMφs^{42,60}. In the skin, pvMφs express typical Mφ surface markers, including CD45, CD11b, F4/80, and CD64⁴⁰. Strikingly, pvMφs were found to cover approximately 40% of the length of dermal venules and to be essential for the induction of iSALT through the recruitment

of CXCR2⁺ DCs via secretion of CXCL2^{42,60}. Interestingly, sessile CCL17/EGFP⁺ cells appeared to localize at random positions along the BVs. Thus, although speculative at this point, sessile CCL17/EGFP⁺ cells probably influence the adhesive and transmigratory activity of crawling blood leukocytes and thereby contribute to their extravasation in areas juxtaposed to sessile CCL17/EGFP⁺ cells. Fittingly, their elongated dendrites appeared to reach directly into the vessel lumen. Alternatively, this interaction could also indicate some kind of sampling mechanism of the capillary content. However, Geissmann and colleagues demonstrated, that in contrast to other tissue Mφs, dermal Mφs, LCs, microglia and alveolar Mφs do not take up circulating proteins from adjacent capillary beds²⁰³. Thus, it seems unlikely that the sessile CCL17/EGFP⁺ cells in the skin actually sample the capillary content, but rather interact with endothelial to mediate extravasation of blood leukocytes. Assuming that CCL17 is required for the recruitment of infiltrating leukocytes, it remains elusive how CCL17 is transported to the intraluminal side of the BV. In recent years, atypical chemokine receptors (ACKRs) have gained much attention as silent partners in the regulation of chemokine function²⁰⁴. ACKRs are structurally similar to conventional chemokine receptors as they also possess seven transmembrane- spanning helices and an extracellular domain that binds multiple chemokines with high or low affinity²⁰⁵. In contrast to chemokine receptors, ACKRs lack an intracellular G protein signaling domain and are not able to activate signal transduction pathways normally activated by G-protein coupled receptors²⁰⁵. In the organism, ACKRs are implicated in chemokine scavenging, local buffering of chemokine release, shaping of chemokine gradients, chemokine sequestration, and transcellular transport of chemokines²⁰⁴⁻²⁰⁷. Prominent examples of ACKRs that were shown to bind CCL17 include the Duffy Antigen Receptor for Chemokines (DARC) also known as ACKR1^{205,207-209}, and D6, also known as chemokine-binding protein 2 (ccbp2) or ACKR2^{135,205}. Strikingly, expression of both, DARC and D6 has been reported on resting and inflamed blood endothelial cells (BECs) of post-capillary venules and lymphatic endothelial cells (LECs)^{204,207,210,211}. However, a major difference of DARC and D6 function was demonstrated with regard to skin inflammation. Whereas overexpression of DARC on BECs resulted in elevated chemokine-mediated leukocyte extravasation into the skin and enhanced CHS reactions^{206,210}, deficiency of D6 also led to exaggerated skin inflammation²¹². The current view of D6 function mostly implicates scavenging of chemokines during inflammation. Therefore, enhanced inflammatory reactions in D6-deficient mice were mostly attributed to a slower resolution of chemokine availability and the prolonged recruitment of inflammatory cells²¹². In contrast, DARC expression on BECs is strongly associated with transcytosis of chemokines across endothelial cells^{205,206,210}, including those of the blood-brain barrier²⁰⁷. Considering the close association of sessile CCL17-producing skin cells with dermal BVs, it is possible that DARC mediates transcellular transport of CCL17 from the skin interstitium to the intraluminal side of dermal BVs. Thus, future experiments should specifically address whether infiltrating leukocytes actually extravasate in areas juxtaposed to sessile CCL17⁺ skin cells and whether CCL17 presentation on BECs requires shuttling via DARC.

The second population of CCL17/EGFP⁺ cells identified by IVM displayed an amoeboid morphology and showed active migratory behavior, which is typical for skin monocytes or DCs⁶⁰ (see **Fig. 5.2**). The ability to migrate implies a functional difference compared to the sessile CCL17/EGFP⁺ cells. Whereas the sessile CCL17-expressing cells in the skin probably assist in the extravasation of blood leukocytes, skin-infiltrating leukocytes may be further guided by chemokine cues produced by the migratory population of CCL17-producing cells. In support of this theory, distinct skin-resident DC subsets were shown to promote unique T cell responses against the same antigen²¹³. For example, Langerin⁺CD103⁺ dDCs were demonstrated to specifically enhance Th1 cell responses while simultaneously inhibiting Th17 cell responses in a mouse model of *C. albicans* infection²¹³. In contrast, functions of Langerin⁻CD103⁻dDCs, which include both, CD11b⁺ and CD11b⁻ dDCs²⁷, are generally less well understood. However, in skin-draining LNs, CD103⁻ dDCs were found to constitutively produce retinoic acid and may be important for the generation of regulatory T cells²¹⁴. Of note, Tamoutounour and colleagues previously demonstrated that pvMφs isolated from the skin were not able to induce T cell proliferation but are essential for their recruitment to the skin^{40,60}. A possible role of migrating CCL17⁺ cells for the activation of distinct T cell subsets is corroborated by the finding that only NKT-cell-licensed DCs recruit a population of CCR4⁺ cytotoxic T leukocytes (CTLs) via the production of CCL17⁸⁹.

CCL17 is expressed in distinct subsets of skin myeloid cells

Flow cytometric analysis of naïve ears from CCL17^{E/+} and CCL17^{E/E} mice (see **5.1.3**) revealed that CCL17 is expressed in all major DC populations (cDC1 and cDC2), CCR2⁺Ly6C^{int/lo}MHCII^{int/hi} monocytes (P2 & 3 monocyte DC), and CCR2⁻Ly6C⁻CD64⁺MHCII⁺ dermal Mφs (P5 dMφs).

Strikingly, further characterization of cDC1 subpopulations revealed that CCL17 was only expressed in XCR1⁺CD103⁺ cells. It has become increasingly clear that distinct DC subsets are responsible for the activation of specific T cell subsets²¹³. cDC1 are superior in priming CD8⁺ T cells²¹⁵, whereas cDC2 specialize in CD4⁺ T cell priming²⁴. In particular, CD103⁺ cDC1 were demonstrated to be highly migratory and efficient in presenting keratinocyte-derived antigens to CD8⁺ T cells^{159,215,216}. Furthermore, the additional expression of XCR1⁺ allows CD103⁺ cDC1 to efficiently cross-present exogenous antigens to CD8⁺ T cells²¹⁵. Thus, the expression of CCL17 in CD103⁺XCR1⁺ cDC1s suggests that in the skin CCL17 potentially recruits a distinct subset of CD8⁺ T cells. Further analysis of this particular cDC1 subset under inflammatory conditions could reveal exciting insights for the development of therapies targeting CD8⁺ T cell-dependent diseases such as ACD^{165,166}.

It is conceivable that the population of CCL17⁺ P5 dMφs identified by flow cytometry represents the population of sessile CCL17/EGFP⁺ cells identified by IVM, whereas the CCL17⁺ P2 & 3 moDC population possibly reflect the migratory population of CCL17⁺ cells identified by IVM. In future experiments the exact cellular identity of CCL17⁺ cells identified by IVM should be clarified.

In contrast to microscopy, flow cytometry also identified CCL17/EGFP⁺ Langerhans cells (LCs). In the present study, skin myeloid cells that displayed a high CD11b and CD24a expression were identified as LCs (see **Fig. 5.3**). Historically, LCs were distinguished from dDCs by the expression of Langerin (CD207), which was later found to correlate strictly with a high CD24a expression²⁵. In later studies, CD207 was identified to be also expressed on a subset of dDCs^{26,217,218} and could therefore no longer be used as a reliable marker for the identification of LCs. Here, flow cytometric gating of LCs proved to be difficult as cDC1 (CD11b⁻CD24⁺) and monocytes/cDC2 (CD11b⁺CD24^{lo-int}) populations were directly adjacent to CD11b⁺CD24a^{hi} LCs. Thus, it is possible that some neighboring cDC1s, monocytes, or cDC2s are present in the LC gate. Given the high frequency of CCL17/EGFP⁺ cells in cDC1, cDC2, and monocytes (see **Fig. 5.4A**), and the absence of CCL17/EGFP⁺ cells in the epidermis (microscopy), it is possible that the identified CCL17/EGFP⁺ LCs are actually cDC1s, cDC2s, or monocytes. Alternatively, the CCL17/EGFP⁺CD11b⁺CD24a^{hi} cells could be activated LCs which are on transition through the dermis, migrating towards lymphatic vessels. It is also possible that LCs express only low levels of CCL17 which are not readily detected by microscopy, but only by more sensitive methods such as flow cytometry, or that the procedure to isolate skin cells for FACS analysis induced CCL17 expression in otherwise CCL17-negative LCs. Thus, in future experiments, the epidermal and dermal compartment should be analyzed separately to be able to clearly separate LC from DC populations. Furthermore, the analysis of additional surface markers of CCL17-expressing cells, such as F4/80, CD205, CD207, or CD209 will also prove useful to further characterize CCL17-expressing cells in the skin.

Interestingly, flow cytometric analysis of naïve ears of CCL17-deficient mice (CCL17^{E/E}) did not show major differences compared to heterozygous CCL17^{E/+} mice, which excludes an autocrine regulatory loop of CCL17 expression by itself. In line, the absolute number of various skin myeloid cells was not affected by the loss of CCL17 (see **Fig. 5.7** & **Fig. 5.8**). Thus, under steady state conditions CCL17 does not seem to regulate trafficking of skin-resident myeloid cells but may do so under inflammatory conditions as demonstrated by Stutte et al.⁴⁹.

6.1.2 GM-CSF regulates CCL17 expression in dDCs and monocytes

Granulocyte-macrophage colony-stimulating factor (GM-CSF) was previously demonstrated to induce CCL17 expression in DCs, Mφs, and monocytes in an IFN regulatory factor 4 (IRF4)-dependent manner^{74,168}. The hematopoietic-specific transcription factor IRF4 was shown to be critical for the development of distinct myeloid and lymphoid lineages, in particular, development of cDC2s³⁷. In the present work, the role of GM-CSF in the regulation of CCL17 expression in skin myeloid cells was investigated by flow cytometry using untreated GM-CSF-deficient CCL17^{E/+} (GM-CSF^{-/-}CCL17^{E/+}) mice (see section **5.1.5**). Whereas the absolute numbers of various skin myeloid cells was not affected by the loss of GM-CSF, the number of CCL17-expressing cDC1s, cDC2s, LCs, and P3 moDCs was significantly reduced in the absence of GM-CSF. In contrast, CCL17/EGFP⁺ dermal P5 Mφs were not

affected by the absence of GM-CSF. This result was somehow expected as a publicly available microarray dataset of all major murine skin myeloid cells (GEO accession: GSE49358) revealed that only dDCs and P1-P3 monocytes express the GM-CSF receptor, *Csf2rb* (colony stimulating factor 2 receptor, beta, low affinity)⁴⁰. Taken together, the selective induction of CCL17 by GM-CSF in dDCs and monocytes clearly points to a highly regulated mechanism controlling the expression of CCL17 in distinct subsets of skin-resident immune cells. As discussed earlier, KCs probably have a major role in the regulation of CCL17 expression in the skin through the production of various cytokines. Under inflammatory conditions, murine KCs were not only shown to release IL-1 α ²⁰⁰, but also produce increasing amounts of GM-CSF²¹⁹. Thus, it is likely that KC-derived cytokines regulate CCL17 expression in various immune cells, but a more specific regulation of CCL17 expression is achieved through a cell-type specific expression of cytokine receptors. In another study conducted in our lab, we previously demonstrated that MyD88-deficient KCs produce significantly less IL-1 α in a mouse model of atopic dermatitis (AD)²²⁰, which further suggests a role for TLR-mediated regulation of CCL17 expression in dM ϕ s cells via IL-1 α . It has to be noted, however, that the analysis of CCL17-expressing cells in MyD88-deficient mice is biased by the fact that MyD88 is also required for signaling downstream of the IL-1 and IL-18 receptors¹².

6.1.3 CCL17 regulates the abundance of dermal $\gamma\delta$ T cells

One of the major functions of CCL17 is the recruitment of CCR4-expressing leukocytes to sites of inflammation⁷⁵. For this reason, I performed a rough analysis of the major T cells present in untreated ears of WT, CCL17^{E/+}, and CCL17^{E/E} mice. Whereas the absolute number of CD3⁺TCR β ⁺ conventional T cells (conv T cells) was not affected by the loss of CCL17, CD3⁺TCR $\gamma\delta$ ^{hi} dendritic epidermal T cells (DETCs) and CD3⁺TCR $\gamma\delta$ ^{int} T cells ($\gamma\delta$ T cells) were both present at reduced numbers in CCL17^{E/E} mice, although the difference did not reach statistical significance (see **Fig. 5.10**). One important difference of conv T cells in comparison to DETCs is the time point when these cells appear in the skin for the first time. Whereas DETCs seed the skin during embryonic development^{221,222}, conv T cells mostly home to the skin after being activated by cognate antigen in draining LNs²²³. Only after this priming conv T cell subsets were shown to induce the expression of CCR4 and are able to respond to CCL17 produced in the skin^{45,224}. As here only naïve mice were analyzed, no significant role for CCL17 in the regulation of conv T cells was expected.

In contrast to conv T cells, DETCs are generated in the fetal thymus during embryonic development and are exported sequentially in distinct waves to the skin at E14^{51,225,226}. In the fetal thymus, V γ 5⁺ DETC precursor cells that survived positive selection were shown to induce the expression of the chemokine CCR10. In turn, CCR10 expression proved to be essential for the migration of DETC precursors towards the chemokine CCL27 produced by keratinocytes in the epidermis^{221,227}. Consequently, CCR10-deficient mice display reduced numbers of DETCs in the epidermis but show a

reciprocal accumulation of DETC precursor cells in the dermis²²⁸. Thus, the CCR10/CCL27 signaling axis seems to be critical to mediate the migration of DETC precursors from the dermis into the epidermis. In contrast, CCR4 was shown to be necessary for the *in situ* maintenance of DETCs in adult mice^{221,229}. Thus, in CCR4-deficient mice, the absolute number of DETCs in the epidermis slowly diminished with increasing age²²⁹. For the present thesis, the CCR4-dependency of adult DETCs to maintain themselves is of particular interest as it could explain the necessity to produce CCL17 in the naïve skin. As DETCs require CCR4 signaling for *in situ* maintenance and CCL17 is a potent ligand of CCR4, it is possible that CCL17 produced by dermal immune cells also reaches the epidermis to regulate maintenance of DETCs. In the present work, the mice analyzed had an average age of 8-12 weeks which might be too young to observe a stronger effect of CCL17-deficiency on DETCs. Thus, in future experiments DETCs should be analyzed in aged (>24 weeks) CCL17^{E/E} mice.

The second population of $\gamma\delta$ T cells present in the skin is characterized by an intermediate expression of TCR $\gamma\delta$ (see **Fig. 5.9**) and likely represents dermal $\gamma\delta$ T cells²³⁰. Interestingly, expression of CCR10 and CCR4 was also reported on dermal $\gamma\delta$ T cells²³¹, although no definitive function has been assigned, yet. As discussed previously, CCR10 and CCR4 ligands (CCL27 and CCL17, respectively) have been implicated in skin homing of $\gamma\delta$ T cells^{221,228}. Whereas CCL27 is continuously expressed in the epidermis⁶¹ and therefore probably regulates homeostatic trafficking of $\gamma\delta$ T cells, CCL17 is known to be strongly upregulated during skin inflammation^{49,69,73}. However, in light of the presented results, constitutive expression of CCL17 might also regulate homeostatic trafficking of dermal $\gamma\delta$ T cells to the skin.

6.1.4 Aptamer-mediated inhibition of CCL17 represents a promising treatment strategy for ACD

As introduced earlier, serum levels of CCL17 serve as a biomarker for the severity of AD^{69,182,232,233}. Furthermore, we and others already demonstrated that the absence of CCL17 is associated with beneficial responses in mouse models of allergic skin inflammation^{58,78} as well as several other inflammatory disease models^{72,183,186}. In addition, inhibition of CCL17 function with CCL17-specific neutralizing antibodies reduced atheroprogession in atherosclerosis-prone mice¹⁸⁶. Due to the large promiscuity of the chemokine system, targeting a single chemokine may cause less unwanted side-reactions compared to inhibition of chemokine receptor function²³⁴. The difference becomes obvious when comparing CHS reactions in CCL17^{E/E} and CCR4-deficient (CCR4^{-/-}) mice. Whereas CCL17^{E/E} mice developed a reduced ear swelling response^{49,50}, CCR4-deficiency resulted in an enhanced CHS response⁹¹ (see also **Fig. 5.15**).

In the present work, two previously isolated high-affinity RNA aptamers specific for murine CCL17 were tested for their potential to inhibit CCL17 function *in vitro* and *in vivo*⁵⁰. The two aptamers, namely MF11.46 and MF35.47, showed a very high binding affinity for murine CCL17 of 0.9 nM and 7.5 nM,

respectively⁵⁰. First, both aptamers were tested for their ability to inhibit CCL17-dependent migration of the murine T lymphoma cell line BW5147.3 in an *in vitro* transwell assay. In line with its higher affinity, MF11.46 showed a maximal inhibition of BW cell migration at a molarity 10-fold lower than that of MF35.47 (see **Fig. 5.13**). Also, the IC₅₀ of MF11.46 (0.42 pmol) was found to be approximately 8-fold lower than that to MF35.47 (2.9 pmol) and the CCL17-specific neutralizing antibody MAB529 (3.3 pmol). Surprisingly, and in contrast to the *in vitro* results, MF35.47 proved to be more efficient than MF11.46 *in vivo* (see Fig. 5.14). These results could be explained by a shorter *in vivo* half-life of MF11.46, a potential absorbance of MF11.46 by certain tissues, or could indicate different modes of inhibition of the two aptamers. For example, it was proposed that efficient signaling through CCR4 requires the engagement of two distinct binding domains on CCL17⁸⁰. In this study, the authors generated two chimeric anti-mouse CCL17 surrogate antibodies, B202 and B225, which both inhibited CCL17 function *in vitro* and *in vivo*. Nevertheless, there was a large difference regarding the affinities of the two antibodies for CCL17 of 685 pM and 4.9 nM for B202 and B225, respectively. Furthermore, only B202 also displayed weak binding to CCL22. Thus, the authors concluded that the two antibodies bind CCL17 at different binding sites and that inhibition of only one site is sufficient to prevent effective engagement with CCR4⁸⁰. Regarding MF35.47 and MF11.46, a role for the additional inhibition of CCL22 can be excluded as both aptamers were found to specifically bind murine CCL17 only⁵⁰. However, it is still possible that the two aptamers engage with different binding sites on CCL17, one of which might be more accessible *in vivo*. As introduced earlier, the formation of inducible skin-associated lymphoid tissue (iSALT) was demonstrated to be crucial for the initiation of the CHS immune response⁶⁰. The initial formation of iSALT depends on the early activation of pMφs by KCs. In turn, pMφs produce increasing amounts of chemokines, such as CXCL2 and CCL17 to recruit specific subsets of dermal CXCR2⁺ DCs and memory effector T cells⁶⁰. In the present work, infiltration of CD8⁺ T cells following DNFB treatment was significantly reduced in CCL17^{E/E} mice and WT mice that received i.p. injections of MF35.47 or MF11.46. This parenteral administration into the circulatory system ensures that the aptamers can act systemically and likely reach the bloodstream. Regarding the formation of iSALT, it is therefore possible that the aptamers inhibited the extravasation of T cells and/or the interaction of dDCs and T cells.

In conclusion, the aptamer-based approach to inhibit CCL17 function was very successful and appears advantageous over the use of neutralizing antibodies for the following reasons: 1. large scale GMP production of aptamers is more cost-effective than antibody production as they can be readily synthesized chemically¹⁶⁷, 2. nucleic acid aptamers have a minimal immunogenicity, and 3. the small size and secondary structure of aptamers may facilitate direct entry into the epidermal and dermal compartments and could potentially also directly applied onto the skin²³⁵. The relatively short half-life of aptamers *in vivo* (hours to days) makes aptamers particularly suited for the treatment of acute inflammatory response as no or few side-reactions are expected caused by a prolonged presence of

the drug in the systemic circulation⁵⁰. Thus, in future experiments the aptamers will be tested for their potential to inhibit CCL17 in the skin by epicutaneous application. In addition, the aptamers should be tested to for their ability to ameliorate other inflammatory reactions in murine disease models in which CCL17 was shown to be involved, such as asthma⁷¹, atherosclerosis¹⁸⁶ or intestinal inflammation⁷².

6.1.5 Opposing roles of CCR4 and its two known ligands CCL17 & CCL22

In humans and mice, CCL17 and CCL22 are both potent ligands of CCR4⁷⁵. In contrast to the immunostimulatory roles that have been assigned to CCL17, CCL22 has more often been associated with an immunosuppressive function¹⁸⁸. Several studies already demonstrated a critical role for CCL22 in the recruitment of regulatory T cells. Fittingly, CCR4 was detected on both, murine and human regulatory T cells^{75,191}. In mice, treatment with anti-CCL22 antibodies specifically reduced recruitment of regulatory T cells into ovarian cancers⁷⁹, whereas in humans, the CCR4-specific monoclonal antibodies mogamulizumab and mAb1567 displayed potent anti-tumor effects^{236,237}. Interestingly, however, in late 2014 mogamulizumab was found to cause the development of a serious skin rash in some treated patients^{75,238}. Regarding the activation of CCR4-induced signaling, CCL22 was found to interact at a different binding domain than CCL17⁸². In addition, CCL22 induces a more rapid desensitization and internalization of CCR4 compared to CCL17^{80-82,239}.

As mentioned earlier, in a murine model of oxazolone-induced CHS, CCR4^{-/-} mice displayed an enhanced ear swelling response compared to control mice^{91,196}, which is in strong contrast to the reduced CHS response observed in CCL17^{E/E} mice^{50,73}. Based on these findings, it was hypothesized that in the absence of CCL17 a dominant, immunosuppressive CCL22-CCR4 interactions suppress the CHS response, whereas in CCR4^{-/-} mice the absence of CCL22/CCR4 signaling exacerbates the CHS response. Therefore, we analyzed the CHS response in two of our newly generated CCL17/CCL22-double-deficient mice strains (CCL17^{E/E}/22^{F/F} and CCL17^{E/E}/22^{G/G}) in comparison it to CCR4^{-/-} and CCL17^{E/E} mice. It should be noted, that the ameliorated CHS response observed in CCL17^{E/E} mice (see **Fig. 5.15**) may be caused by the decreased emigration of antigen-bearing LCs to skin-draining LNs resulting in an impaired sensitization to DNFB^{49,73} and the reduced recruitment of effector memory T cells into the skin during the elicitation phase on the other hand⁵⁰.

Confirming the findings by Lehtimäki et al., CCR4^{-/-} mice displayed an increased ear swelling over the course of three days after DNFB challenge compared to WT control mice. Interestingly, the ear swelling of CCR4^{-/-} mice even increased 48h after DNFB application, whereas it progressively decreased in WT mice. Surprisingly, both strains of CCL17^{E/E}/22^{-/-} mice also developed a markedly reduced ear swelling response, comparable to the one observed for CCL17^{E/E} mice. Thus, it is conceivable that the sole absence of CCL17 in CCL17^{E/E} and CCL17^{E/E}/22^{-/-} mice is sufficient to confer protection against DNFB-induced CHS. As our group previously demonstrated a critical role of CCL17 in the emigration of LCs

after DNFB sensitization⁴⁹, it is possible that also CCL17^{E/E}/22^{-/-} mice are affected by an impaired sensitization. Although the CCL22-CCR4 axis was previously demonstrated to be critically involved in the recruitment of regulatory T cells to the skin²⁴⁰, an impaired sensitization phase in CCL17^{E/E}/22^{-/-} mice probably precludes the necessity to recruit regulatory T cells during the elicitation phase. At this point, however, it cannot be ruled out that the absence of CCL22 alone would have detrimental effects on the development of CHS. Thus, further experiments are required to unambiguously demonstrate an impaired sensitization phase in CCL17^{E/E} as well as CCL17^{E/E}/22^{-/-} mice. Therefore, it would be of great interest to isolate the primed T cells from sensitized WT, CCL17^{E/E} or CCL17^{E/E}/22^{-/-} mice and adoptively transfer them into non-sensitized WT recipients to compare the ear swelling responses following DNFB-challenge. If the recipient WT mice injected with T cells isolated from CCL17^{E/E} or CCL17^{E/E}/22^{-/-} mice will develop no or reduced ear swelling compared to control mice, CCL17 would be identified as a critical factor already required during the sensitization phase of CHS.

In contrast, the exaggerated ear swelling response in CCR4^{-/-} mice is probably due to the increased infiltration of leukocytes into the skin as demonstrated by quantification of CD45⁺ leukocytes and CD3⁺ T cells (see **Fig. 5.16A**). These results are in line with findings from Lehtimäki et al. who also observed increased numbers of CD4⁺ T cells in ears of Oxazolone-treated CCR4^{-/-} mice⁹¹. In disagreement with the assumption that the CCR4-CCL22 interaction is responsible for the recruitment of regulatory T cells to the skin²⁴⁰, Lehtimäki and colleagues found increased numbers of CD3⁺FoxP3⁺ regulatory T cells in the ears of Oxazolone-treated CCR4^{-/-} mice compared to control mice. Furthermore, the enhanced infiltration of leukocytes in CCR4^{-/-} mice strongly suggests the presence of a second receptor which compensates for the loss of CCR4. As discussed earlier, CCR10 and its ligand CCL27 were often implicated in the migration of skin-homing leukocytes to the skin^{61,140,228,241}. In line, combined treatment of WT mice with anti-CCL17, anti-CCL22, and anti-CCL27 antibodies, or treatment of CCR4^{-/-} mice with anti-CCL27 antibodies during CHS, resulted in diminished ear swelling responses^{48,140}, suggesting additive roles of CCR4 and CCR10 in murine CHS. It remains, enigmatic, however, why such compensation through CCR10-CCL27 should not occur in CCL17/22^{-/-} double-deficient mice.

Alternatively, the enhanced inflammatory response observed in CCR4^{-/-} mice could be caused by an unrelated defect during T cell development as suggested by a study from Hu and colleagues¹⁸⁷. In this study, the authors identified a critical role of CCR4 for the efficient negative selection of autoreactive T cells in the murine thymus¹⁸⁷. The authors demonstrated that CCR4 is specifically expressed on immature CD69⁺CD4⁺ single positive (SP) and CD69⁺CD4⁺CD8⁺ double positive (DP) thymocytes that just underwent positive selection in the thymic cortex and were about to enter the medulla. Upon further maturation of SP thymocytes CCR4 expression is lost. The subsequent analysis of CCR4^{-/-} mice revealed that CCR4-deficient SP and DP thymocytes do not accumulate in the thymic medulla as CCR4 is required for the interaction with medullary DCs which present low-affinity autoantigens to induce tolerance and clonal deletion^{1,187}. Most strikingly, the impaired ability of CCR4-deficient thymocytes to

undergo negative selection resulted in the accumulation of autoreactive T cells and concomitantly reduced numbers of regulatory T cells in secondary lymphoid organs. We and others have previously demonstrated that the CCR4 ligands, CCL17 and CCL22 are expressed in the thymus^{70,242,243}. In the study conducted by Hu et al., SIRP α -expressing thymic medullary DCs were specifically identified to express high levels of CCL17 and CCL22¹⁸⁷. Although, the authors used an *in vitro* transwell system to demonstrate that both, SP and DP thymocytes migrate towards CCL17 and CCL22 in a CCR4-dependent manner, they do not provide data regarding the specific roles of the two chemokines *in vivo*. In light of the exacerbated CHS reaction observed in CCR4^{-/-} mice, the paper by Hu et al. suggests that a paucity of regulator T cells and the accumulation of autoreactive T cells in CCR4^{-/-} mice could explain the increased infiltration of T cells in DNFB-treated ears. Interestingly, CCL17^{E/E} mice were shown to possess higher numbers of regulatory T cells than WT mice^{72,186}, in line with the diminished CHS responses in this background.

There is one conceptual problem with this explanation. In the present work, CCL17^{E/E}/22^{-/-} and CCR4^{-/-} mice also displayed an opposing phenotype in the CHS model. Assuming that CCR4-expressing SP and DP thymocytes are recruited to medullary SIRP α ⁺ DCs via CCL17 or CCL22, a similar phenotype of CCR4^{-/-} and CCL17^{E/E}/22^{-/-} mice would be expected. Thus, a possible explanation would be that CCR4-expressing thymocytes respond to a so far unknown ligand of CCR4. Possible ligands described in humans include CCL2¹⁹⁷, CCL3^{176,197}, and CCL5¹⁹⁷. However, no direct evidence for a specific contribution of these chemokines to thymocyte development has been demonstrated so far. Therefore, further experiments that elucidate the complex interplay of CCR4 and its ligands are required.

6.1.6 Increased abundance of CCL17-expressing macrophages during CHS

In addition to T cells, it is well-known that the epicutaneous application of haptens such as DNFB also results in the recruitment of blood-derived Ly6C^{hi} monocytes to the inflamed skin¹⁶³. Furthermore, a study published by the lab of Bernard Malissen found that a single DNFB treatment triggers a rapid and massive increase in dermal CD11b⁺ cells, even in the absence of sensitization⁴⁰. Nevertheless, the influence of DNFB on CCL17 expression in dermal myeloid cells remained elusive. Thus, in the present work the composition of skin myeloid cells was analyzed in sensitized WT, CCL17^{E/E}, CCL17^{E/E}/22^{-/-}, and CCR4^{-/-} mice 4 days after DNFB challenge. In line with the study conducted by the Malissen lab⁴⁰, dermal CD11b⁺ cells were strongly enriched in DNFB-treated ears compared to ears which had only been treated with solvent (see **Fig. 5.17**). Strikingly, WT, CCL17^{E/E}, and CCR4^{-/-} mice showed comparable numbers of CD11b⁺ cells, whereas significantly fewer CD11b⁺ cells infiltrated the ears of DNFB-treated CCL17^{E/E}/22^{-/-} mice. The heterogeneous dermal CD11b⁺ cells were resolved into cDC2s, three monocyte-derived DC populations P1-P3, and two populations of dM ϕ s P4 and P5. The overall

increase, irrespective of the genotype, in P2 moDCs following DNFB application was somewhat expected, as these cells were shown to develop from infiltrating Ly6C^{hi} blood monocytes (P1 monocytes)^{28,40}. In accordance, the rather late analysis of cellular composition at day 4 after DNFB challenge suggested that most P1 monocytes had undergone maturation into P2 moDCs. As discussed previously, it is possible that the absence of CCL22 or the combined loss of CCL17 and CCL22 regulates the migration of mainly CCR2⁺ monocytes. Whereas skin DC and monocyte populations are continuously replenished from bone marrow-derived preDCs and Ly6C^{hi} cells, respectively, dMφs originate from at least two distinct precursor pools^{102,244}. In contrast to DCs in the skin, which develop in an Flt3L-dependent and CCR2-independent manner³⁸, P1-P3 monocytes, and to a lesser extent dermal P4 and P5 Mφs, develop in a CCR2-dependent manner⁴⁰. It has to be noted, however, that a substantial proportion of dMφs already establishes during embryonic development in a CCR2-independent manner⁴⁰. As only CCR2⁺ monocytes were affected by the loss of CCL17 and CCL22 but not by the absence of CCR4, this suggests the presence of a CCL22-dependent/ CCR4-independent signaling mechanism regulating monocyte functions in the skin. Although a second receptor for CCL22 was not described yet, some evidence for CCR4-independent signaling mechanisms of CCL22 has been reported¹³⁵. In addition to the regulatory roles of ACKRs discussed above, post-translational modifications of chemokines represent another mechanism to enhance or dampen chemokine-driven inflammatory responses²⁴⁵. In the case of CCL22, the ubiquitously expressed dipeptidyl peptidase IV (DPP4 or CD26) was found to excise the NH₂-terminal Gly1-Pro2 and Tyr3-Gly4 dipeptides from CCL22 generating a truncated version of CCL22(5-69)²⁴⁶. Compared to full-length CCL22, the DPP4-processed CCL22(5-69) was shown to display reduced chemotactic activity for human lymphocytes and moDCs, but not for monocytes²⁴⁶. In addition, CCR4-transfected HOS cells (human osteosarcoma) showed reduced mobilization of intracellular Ca²⁺ and desensitization after application of CCL22(5-69), whereas monocytes appeared to bind CCL22(5-69) and full-length CCL22 similarly^{135,246}. Although no such function was reported for murine CCL22, it is conceivable that DPP4 has a similar role in the regulation of murine CCL22 function. Thus, future experiments should analyze the specific expression and function of DPP4 on murine WT and CCR4^{-/-} monocytes. Furthermore, it would be of great interest to identify a possible second receptor that preferentially binds truncated CCL22(5-69).

As for the analysis of naïve ears (see 5.1.3 & 5.1.4), the proportion of CCL17/EGFP⁺ cells was analyzed for all myeloid cell subsets after DNFB challenge. CCL17/EGFP⁺ cells were found within all DC as well as monocyte subsets. Interestingly, in sensitized mice, DNFB challenge resulted in a marked increase in CCL17/EGFP⁺ LCs. This is in line with previous studies conducted in our lab where increased numbers of CCL17-expressing LCs were also detected in skin-draining LNs following skin irritation^{49,73}. In contrast, P1 monocytes were devoid of CCL17/EGFP⁺ cells after DNFB treatment. This suggests that early extravasated Ly6C^{hi} monocytes do not express CCL17 when they enter the skin but only upregulate CCL17 expression once they mature to P2 and P3 moDCs and acquire a transcriptome that

is more reminiscent of CD11b⁺ cDC2s as shown by Tamoutounour and colleagues⁴⁰. Most strikingly, the overall number of P5 dMφs as well as their proportion of CCL17/EGFP⁺ cells (see **Fig. 5.19C & 5.20B**) was strongly increased 4 days after DNFB challenge. In light of previous suggestions concerning their potential role in the recruitment of skin-homing CCR4⁺ T cells, the increased number of CCL17-expressing P5 dMφs after DNFB treatment supports this scenario. It has to be noted, however, that the present analysis was conducted at day 4 after DNFB challenge and that future experiments should carefully dissect the kinetics of CCL17 expression in P5 dMφs at earlier time points after DNFB challenge. In addition, the specific cytokines regulating CCL17 expression in P5 dMφs should be investigated. As demonstrated by Natsuaki et al.⁶⁰ and Didovic et al.²²⁰ KC-derived IL-1α appears to be a good candidate as it was able to induce CCL17 expression in bone-marrow derived Mφs.

Taken together, the present work significantly extended the previous knowledge on CCL17 in the context of regulation of skin immunity. In addition, distinct subsets of CCL17-expressing cells were identified in the naïve as well as inflamed murine skin and an aptamer-based approach to inhibit CCL17 function in a murine model of ACD was established. Finally, the opposing phenotypes of CCR4^{-/-} and CCL17^{E/E}/22^{-/-} mice in the CHS model suggest the existence of yet another CCR4 ligand as well as a possible second receptor for CCL22.

6.2 CCL17 in the context of brain immunity

Early evidence for CCL17 expression in the brain was already demonstrated nearly 20 years ago when Ivo Lieberam analyzed CCL17 expression in various cell types and tissues⁷⁰. He found that BM-DCs expressed the highest levels of CCL17, whereas an about 100-fold lower expression was detected in the thymus, the lung, and the brain. In particular, regarding the expression of CCL17 in the lung, CCL17 has nowadays been proven to be a critical factor in the development of many inflammatory lung diseases such as allergic asthma⁷¹. Additional experiments conducted in our lab using CCL17^{E/+} mice confirmed CCL17 expression in the brain. However, the exact cellular localization as well as the function of CCL17 in the brain remained elusive.

6.2.1 CCL17 is expressed in hippocampal CA1 neurons and affects microglia morphology and synaptic transmission

Imaging of brain sections of CCL17^{E/+} mice revealed a cell-type specific expression of *Ccl17* in a subset of hippocampal CA1 neurons. As chemokines in the brain are known to affect microglia activation¹⁰⁷, the abundance and morphology of microglia was also analyzed in CCL17^{E/E} mice. Strikingly, compared to WT mice, microglia in naïve CCL17^{E/E} mice were reduced in number and acquired a more reactive morphology (see **Fig. 5.36**) based on the analysis of morphological parameters generally associated with activated microglia²⁴⁷. In the absence of CCL17 microglia displayed a reduced cell volume, reduced branching, overall reduced tree length and a higher polarity compared to WT control mice

(see **Fig. 5.37**). In previous studies, we demonstrated that CCL17 expression in secondary lymphoid organs is upregulated in response to systemic inflammation^{89,168}. Here, the systemic treatment with LPS strongly induced the expression of *Ccl17* in hippocampal neurons, whereas neither the TLR3 ligand PolyI:C nor the TLR9 ligand CpG enhanced *Ccl17* expression. Peripheral inflammation is commonly known to influence normal brain function¹²⁰. In particular, microglia respond to increased production of peripheral cytokines following systemic inflammation and assume a highly reactive morphology^{111,248,249}. Interestingly, systemic LPS stimulation in CCL17^{E/E} mice did not impose further changes on microglia morphology, whereas microglia in WT mice acquired a highly reactive morphology. Aside from modulating microglia activation, chemokines in the brain were also demonstrated to influence neuronal signaling comparable to neuropeptides such as BDNF¹²⁹. Indeed, naïve CCL17^{E/E} mice displayed an elevated basal synaptic transmission between Schaffer collaterals and pyramidal CA1 neurons (see **Fig. 5.38**). Thus, it is tempting to speculate that CCL17 is able to downmodulate synaptic transmission either via direct neuromodulatory effects or indirectly via the modulation of microglia functions, such as pruning or the secretion of other neuromodulatory factors.

One possibility is that the highly localized expression of CCL17 in hippocampal neurons helps to prevent premature activation of hippocampal microglia. The hippocampus represents one of the brains' most vulnerable regions to injury, inflammatory insult, or CNS disorders¹²⁶. Therefore, it is reasonable to assume that the hippocampus possesses unique capabilities to keep microglia in their non-pathogenic, tissue-surveilling state. CCL17 may exert its function on microglia using one of two possible routes. First, CCL17 may directly act on microglia via its receptor CCR4. In line, we and others have previously demonstrated that microglia indeed express CCR4^{133,144,250}. Furthermore, during the revision process of our paper on the function of CCL17 in the murine brain¹⁴⁴ I was able to demonstrate that microglia are able to directly bind CCL17 on their surface (data not shown), which supports the idea of a direct neuron-microglia communication via CCL17 and CCR4. In addition to a direct effect, it is also conceivable that CCL17-expressing immune cells outside the CNS acquire various defects in the absence of CCL17 as shown for a population of CCL17-expressing DCs that fail to immigrate into the CNS in a mouse model of experimental autoimmune encephalomyelitis (EAE) a model of human multiple sclerosis^{84,194}. Interestingly, the chemokine CX₃CL1 was previously identified to exhibit a similar inhibitory influence on microglia activation as CCL17 via CX₃CR1^{251,252}. However, in sharp contrast to CCL17, CX₃CL1 is widely expressed in neurons of the hippocampus, the striatum, and the cortex and is, therefore, able to regulate microglia activation in the entire brain²⁵¹. It is of interest here, that upon LPS stimulation a weak CCL17/EGFP signal was also detected in cortical neurons (see **Fig. 5.24**) and potentially a low level expression of CCL17 can also occur in other regions of the brain under steady state conditions.

The LPS-induced upregulation of *Ccl17* in hippocampal neurons was abrogated in MyD88-deficient mice. Interestingly, the baseline expression of *Ccl17* was found to be MyD88-independent suggesting

that neither LPS nor other PAMPs derived from commensal bacteria signal via the TLR4/MyD88-dependent pathway to maintain the constitutive expression of *Ccl17* in the hippocampus. However, it is still possible that TLR4 regulates baseline expression of *Ccl17* via the MyD88-independent TRIF pathway¹². The constitutive expression of *Ccl17* in the hippocampus indicates a role for CCL17 in maintaining normal brain function. In support of this theory, histological analysis of hippocampal brain sections from naïve and LPS-treated CCL17^{E/E} mice revealed a significant reduction in microglia numbers compared to WT mice (see **Fig. 5.35**). Given the localized expression of CCL17 in the hippocampus, it was expected that CCL17 exerts its strongest effects in the hippocampus. Intriguingly, flow cytometric quantification of microglia isolated from the entire brain also revealed reduced microglia numbers in mice lacking CCL17 compared to WT mice. Thus, it is possible that the low expression of CCL17 in brain regions other than the hippocampus affects microglia globally. Furthermore, the lack of CCL17 expression in peripheral immune cells could also indirectly influence microglia function. For example, alterations in the intestinal microbiota have been recently described to affect microglia morphology^{253,254}. Thus, a direct or indirect effect of systemically produced CCL17 on microglia cannot be excluded at this point.

In line with previous work conducted by Ruland and colleagues⁸⁴, flow cytometric analysis of hematopoietic cells in the CNS also identified CCL17/EGFP⁺ cells only within the DC/M ϕ population, whereas microglia did not express CCL17 (see **Fig. 5.34**). This finding is in contrast to other studies which already indicated expression of *Ccl17* in microglia¹⁷¹. In the present study, CCL17-driven EGFP expression was indicative of active *Ccl17* transcription, whereas other studies used RNA-sequencing (RNA-seq) to detect *Ccl17* in microglia¹⁷¹. As microglia continuously shape neurons by synaptic pruning and also phagocytose dying neurons, it is conceivable that they might have taken up *Ccl17* RNA passively from surrounding neurons. Along the same line, another study conducted by the Jung lab also demonstrated that conventional RNA-seq analysis of microglia often produce results compromised by artifacts introduced by different methods of tissue-dissociation²⁵⁵. In addition, absolute numbers of brain infiltrating CD45^{hi} leukocytes as well as the level of CD11b surface expression on infiltrating monocytes were markedly reduced in LPS-injected CCL17^{E/E} mice compared to control mice. These findings suggest that CCL17 is potentially involved in priming/ sensitizing monocytes upon TLR-stimulation. The reduced recruitment of CD45⁺ leukocytes into the brain in CCL17^{E/E} mice can be partially explained by previous studies which found that DCs require CCL17 to cross the BBB after induction of EAE⁸⁴. Furthermore, brain-derived CCL17 may exert direct chemotactic effects on peripheral immune cells such as regulatory T cells^{100,256}. Surprisingly, no T cells (CD3⁺ cells) were detected in the brain. As numerous studies already demonstrated the presence of T cells in the brain¹⁰⁰, the failure to detect T cells in the present work can probably be attributed to a weak CD3 antibody staining. Thus, future studies should analyze additional T cell surface markers to unambiguously characterize brain T cells in CCL17^{E/E} and WT mice.

6.2.2 Locally produced TNF regulates *Ccl17* expression in the brain

As, the LPS-induced upregulation of *Ccl17* in the brain was completely abolished in TNFR-deficient mice (see **Fig. 5.29**), a prominent role for TNF in the regulation of *Ccl17* was apparent. In line, LPS-injected WT mice also displayed a strong increase in *Tnf* expression in the hippocampus. Unexpectedly, LPS treatment also induced upregulation of *Tnf* in the hippocampus of MyD88-deficient mice, although less pronounced compared to WT mice. As MyD88-deficient mice failed to upregulate *Ccl17* following LPS injection this suggests that a certain amount of locally produced TNF in the brain is required to induce *Ccl17* expression above baseline. To address this, *Ccl17* expression was analyzed in WT mice that were injected i.p. with increasing doses of LPS. This titration experiment revealed that the level of *Tnf* expression in the hippocampus directly correlated with the injected dose of LPS. Interestingly, a minimum dose of 50µg LPS was required to upregulate *Ccl17* expression above baseline. In contrast, serum levels of TNF strongly increased independently of the LPS dose over a range of 6 to 150 µg/ mouse, suggesting that the LPS-induced expression of *Ccl17* in the brain strongly depends on local TNF-signaling. In line, WT mice that received i.p. injections of recombinant TNF did not upregulate *Ccl17* in the brain (see **Fig. 5.28**).

In the brain, LPS is primarily sensed by microglia and astrocytes that express TLR4^{112,257,258}. Interestingly, it was previously demonstrated that small amounts of LPS are not able to cross an intact BBB but instead bind to TLR4 expressed on brain endothelial cells which then propagate a proinflammatory signal into the brain^{93,115,121}. On the contrary, high doses of LPS as well as repeated small doses of LPS were shown to induce disruption of the BBB in particular in the frontal cortex, thalamus, pons, medulla, and cerebellum⁹³. In response to LPS, microglia and astrocytes produce increasing amounts of TNF which is associated with an enhanced excitatory activity of neurons^{259,260}. In the present work, LPS-induced expression of *Ccl17* in hippocampal neurons potentially causes some kind of TNF-dependent microglia-neuron cross-talk which prevents excessive activation of neuronal-signaling under inflammatory conditions.

6.2.3 *Ccl22* is expressed in microglia and regulated by GM-CSF signaling

CCL22, the second ligand of CCR4, was also found to be expressed in the hippocampus of WT mice. Similar to *Ccl17*, systemic LPS treatment strongly enhanced the expression of *Ccl22*, whereas neither CpG nor PolyI:C had an effect on *Ccl22* expression. Analysis of hippocampal gene expression in LPS-injected GM-CSF- and TNF-deficient mice revealed a dominant role for GM-CSF in regulating *Ccl22* expression (see **Fig. 5.29 & 5.30**). In contrast, GM-CSF-deficiency had only minor effects on the LPS-induced expression of *Ccl17*, suggesting a differential regulation of *Ccl17* and *Ccl22* in the murine hippocampus. Conversely, previous studies demonstrated an essential role for GM-CSF in the regulation of *Ccl17* expression in myeloid cells⁷⁴. Thus, it seems likely that a distinct cytokine receptor

expression profile on neurons and myeloid cells regulates *Ccl17* and *Ccl22* expression. Whereas CCL17/EGFP⁺ neurons could be readily identified by means of CCL17/EGFP reporter mice, the cell type producing *Ccl22* has yet to be identified. If *Ccl22* was also produced in hippocampal neurons the observed finding could reflect a distinct cytokine responsiveness of the *Ccl17* and *Ccl22* promoters in neurons. Analysis of *Ccl22* expression in a publicly available brain transcriptome database (<http://www.brainmaseq.org/>), however, revealed highest expression of *Ccl22* in the microglia/ M ϕ group (see **Fig. 6.1**).

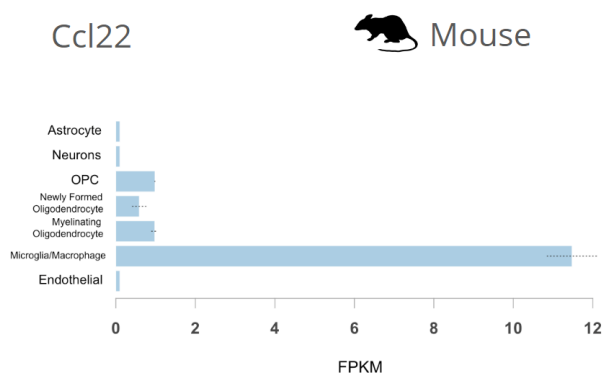


Figure 6.1 | *Ccl22* expression in different murine brain cell types.

Brain cells were isolated via FACS and subjected to whole-cell RNA sequencing. According to the original publication, a FPKM (Fragments Per Kilobase Million) value of 0.1 represents the noise threshold of the data.

Data was downloaded from the brain RNA-seq database (brainmaseq.org).

Whereas this finding should be confirmed by analyzing CCL22 protein production in the brain, it indicates that the differential cytokine dependence of *Ccl17* and *Ccl22* expression is likely due to their expression in distinct cell types. In previous work conducted by our group, IFN γ was identified to specifically repress *Ccl17* expression in splenic DCs¹⁶⁸. Interestingly, analysis of *Ifngr1* (Interferon gamma receptor 1) expression in the brain RNA-seq database revealed nearly exclusive expression in the microglia/ M ϕ group, potentially explaining the absence of CCL17/EGFP⁺ microglia in CCL17^{E/+} mice. Taken together, the additional expression of *Ccl22* in the hippocampus represents a very interesting finding and its potential neuromodulatory functions should be investigated in future studies.

6.2.4 Synaptic transmission is altered in the absence of CCL17

Apart from regulating neuron-microglia interaction, the homeostatic and localized expression of *Ccl17* in pyramidal neurons of the hippocampal CA1 region also indicated a role for the CCL17-CCR4 axis in modulating neuronal activity. Electrophysiological field recordings in the CA1 region revealed an enhanced basal synaptic transmission at CA3-CA1 Schaffer collaterals in brain sections isolated from CCL17^{E/E} mice (see **Fig. 5.38**). This finding appeared to depend on a post-synaptic mechanism as the paired-pulse ratio (ratio of the second and first evoked fEPSP) was not different between slices from WT and CCL17^{E/E} mice¹⁴⁴. As the field electrode was directly placed in the hippocampal CA1 region (where CCL17-expressing neurons are located), this further suggests an autocrine signaling mechanism of CCL17. Interestingly, a recent study by McGill et al. found *Ccl17* to be specifically expressed in glutamatergic neurons of the hippocampus¹⁷⁵. As glutamatergic neurons represent the brains' main class of excitatory neurons, the increased basal synaptic transmission observed in CCL17^{E/E} mice

implied an autocrine inhibitory function of CCL17. In line, a study performed by Meucci et al. previously demonstrated that various chemokines, including CCL17 and CCL22, were able to evoke or reduce intracellular Ca^{2+} oscillations ($[\text{Ca}^{2+}]_i$) in distinct subsets of primary cultured hippocampal neurons from rat embryos¹³³. These studies demonstrate that chemokines, such as CCL17 and CCL22, are able to directly modulate neuronal activity which likely becomes even more important in the context of systemic inflammation. Interestingly, a previous study by Li et al. in zebra fish found that active neurons can release factors enhancing microglia-neuron interactions which in turn reduce the activity of contacted neurons^{261,262}. Surprisingly, following *in vivo* LPS treatment the basal synaptic transmission was comparable in WT and CCL17^{E/E} mice, presumably because systemic inflammation is generally known to stimulate synaptic transmission^{248,260} possibly through mechanisms that may overcome an inhibitory function of CCL17 in the healthy brain.

In preceding studies by J. Alferink and colleagues^{84,194}, the functional relevance of the neuronal CCL17/22-CCR4 axis could already be demonstrated^{84,85,194}. Strikingly, CCR4-deficient mice displayed an impaired locomotor activity and less efficient nest building behavior compared to CCL17-deficient and WT mice²⁶³. In contrast, CCL17-deficient mice showed an increased exploratory behavior in the dark-light and object recognition tests, whereas CCR4-deficient mice exhibited an overall diminished exploratory behavior²⁶³. Furthermore, in the elevated plus-maze test CCR4 but not CCL17-deficient mice exhibited a reduced anxiety-related behavior. These opposing phenotypes suggest that the remaining expression of CCL22 and CCR4 in CCL17^{E/E} mice potentially modulates synaptic signaling which manifests in an altered behavioral response. Interestingly, in a study previously performed by Osborn et al. CCL22 was found to directly act as a prostaglandin-dependent pyrogen when injected into the anterior hypothalamus²⁶⁴. As a consequence of this CCL22 injection into the hypothalamus, a systemic hyperthermic response was induced via activation of brown adipose tissue. This study indicates that CCL22 is able to directly affect normal brain function independently of CCL17. Although the existing studies already indicate an important role for the CCL17/22-CCR4 axis in regulating distinct behavioral responses, the relative contributions of the two CCR4 ligands in the CNS should be further analyzed in future studies utilizing CCL22-deficient and CCL17/22-double-deficient mice.

Intriguingly, elevated levels of CCL17 and CCL22 were also found in the serum of patients suffering from autism spectrum disorders (ASD)^{195,265}. Here, serum levels of CCL17 and CCL22 directly correlated with severity of ASD. It is also tempting to speculate that the CCL17/22-CCR4 interaction is involved in the regulation of some of the TNF-dependent symptoms of sickness syndrome, such as depression or decreased locomotor activity, that are induced by peripheral inflammation^{120,266}. Thus, the identification of CCL17 and CCL22 expression in the hippocampus represents an important and so far unrecognized finding that adds the CCL17/22-CCR4 axis to the list of chemokine/receptor pairs controlling CNS function under homeostatic as well as inflammatory conditions.

6.3 CCL17-DTR mice can be used as a new model for the analysis of temporal lobe epilepsy

Expression of the simian diphtheria toxin receptor (DTR) under control of the *Ccl17* promoter in CCL17-DTR (CCL17^{DTR/+}) mice offers the interesting possibility to study the consequences of a specific ablation of CCL17-expressing neurons *in vivo*. Similar to CCL17^{E/+} mice, CCL17-DTR mice have been generated by targeting the second exon of the CCL17 locus. Thus, in heterozygous CCL17^{DTR/+} mice functional CCL17 is still produced from one allele, whereas the DTR is expressed from the second allele allowing inducible ablation of all CCL17-expressing cells through systemic treatment with diphtheria toxin (DT). In nature, DT is produced by *Corynebacterium diphtheria*²⁶⁷. DT is a polypeptide consisting of two subunits, DT-A and DT-B. Whereas DT-B mediates binding to DTR on the cell surface and receptor-mediated endocytosis, DT-A catalyzes the transfer of an ADP-ribose moiety of nicotinamide adenine dinucleotide (NAD⁺) to a modified histidine residue on the protein elongation factor 2 (EF-2) in the cytoplasm²⁶⁷. This results in the inactivation of EF-2 and subsequently in the inhibition of protein synthesis and apoptotic cell death. It is of interest here that the DTR has been identified as a membrane-bound form of the heparin-binding EGF-like growth factor (HB-EGF)²⁶⁸, which is endogenously expressed in many different species, including humans, monkeys, and mice²⁶⁹. In contrast to the human and monkey HB-EGF, however, the murine variant does not bind DT-B, rendering murine cells at least 105 times more resistant to DT treatment than human cells²⁷⁰. Thus, the generation of transgenic mice expressing the gene for the simian DTR under the control of a tissue/cell-specific promoter (here *Ccl17*) allows the specific ablation of the DTR-expressing cells²⁷¹.

Earlier experiments performed by other lab members already showed that systemic DT treatment of CCL17^{DTR/E} mice efficiently depletes CCL17-expressing cells in secondary lymphoid organs such as skin-draining lymph nodes. This depletion occurred, however, only transiently as CCL17 is mainly expressed in hematopoietic cells⁷³, which are continually replenished by blood-borne precursors. In contrast, loss of neurons is usually permanent, as the majority of neurons cannot regenerate and only two brain regions show signs of weak neurogenesis^{96,124,272}. Thus, it was reasoned that systemic DT treatment of CCL17^{DTR/+} mice could be used to specifically and permanently ablate CCL17-expressing neurons in the hippocampal CA1 region. To monitor the loss of CCL17-expressing hippocampal neurons, homozygous CCL17^{E/E} were intercrossed with CCL17^{DTR/DTR} mice. In the resulting offspring (CCL17^{DTR/E} mice), the DT-mediated loss of CCL17-expressing neurons could be easily monitored by the loss of EGFP fluorescence. Interestingly, no apparent effect on CCL17-expressing neurons was observed as early as 3 days following DT treatment (see **Fig. 5.42**). This is likely due to slow diffusion of DT over the BBB^{181,273} as well as weak expression of the CCL17-DTR construct in naïve CCL17^{DTR/+} mice. Nevertheless, this is in line with other studies reporting an estimated time of 3-5 days for DT-induced neuronal cell death²⁷³. Interestingly, DT treatment of female, and to a lesser extent male CCL17^{DTR/+}

mice resulted in an early loss of bodyweight (~8-10%) compared to control mice (see **Fig. 5.40**). DT-treated CCL17^{DTR/+} mice of both genders continued to lose weight until day 5 after the last DT injection before gaining weight again. Approximately 10 days after DT treatment female and male CCL17^{DTR/+} mice displayed a body weight comparable to control animals, whereas female mice showed an accelerated weight gain over the entire course of the experiment (>80days) compared to control mice. Although only speculative at this point, it is possible that the early drop in body weight observed in DT-treated CCL17^{DTR/+} mice is related to a rapid depletion of peripheral CCL17-expressing cells because no apoptotic cells were detected in the hippocampus at day 3 post-DT treatment. It is conceivable that CCL17-expressing cells present in adipose tissues directly affect lipid metabolism as shown for resident adipose tissue Mφs which take up triglycerides from over-burdened adipocytes in an attempt to buffer fatty acid release into the circulation²⁷⁴. In contrast, the subsequent increase in body weight observed in DT-treated CCL17^{DTR/+} mice is possibly due to the progressive loss of CCL17-expressing neurons. Thus, histological analysis of the brains at the end of the experiment revealed a strongly diminished number of hippocampal CA1 neurons in male and female DT-treated CCL17^{DTR/+} mice (see **Fig. 5.41**). It is of interest here that *Ccl17* was previously identified by Henry F.E. and others to be strongly upregulated in the hypothalamic arcuate nucleus (ARC) of mice that had been food-deprived for 24h¹⁷⁴. In the ARC, *Ccl17* was found to be specifically expressed in neurons that express Agouti-related protein (AGRP neurons). Together with Proopiomelanocortin-producing neurons (POMC neurons), AGRP neurons are known to mediate whole-body energy homeostasis by sensing circulating levels of the metabolic hormones insulin, leptin, and grehlin¹⁷⁴. In the same study, the authors also demonstrated that the chronic overexpression of *Ccl17* in AGRP neurons resulted in a progressive increase in body weight compared to control mice, suggesting a potential role for neuronal CCL17 in the regulation of energy homeostasis. Thus, it is possible that DT-treated CCL17^{DTR/+} mice also upregulate *Ccl17* expression in AGRP neurons as a response to the early loss in body weight. The concomitant expression of the DT receptor in AGRP neurons would then also result in their depletion and likely manifest in a disturbed energy homeostasis. Although apoptotic cells in DT-treated CCL17^{DTR/E} mice were only detected in the hippocampus, it is possible that an effect of DT treatment on CCL17/EGFP⁺ AGRP neurons was overlooked due to their overall low abundance¹⁷⁴. Therefore, it will be interesting to investigate the expression of *Ccl17* in the ARC of food-deprived CCL17^{E/+} mice in the future, while also analyzing the specific role of neuronal CCL17 in the regulation of energy homeostasis.

It was further predicted that the DT-mediated ablation of CCL17-expressing neurons in CCL17^{DTR/+} mice would result in the activation of microglia and astrocytes. Indeed, immunofluorescent staining of the microglial marker IBA-1 at distinct time points after DT treatment revealed a strong increase in IBA-1 immunoreactivity 7 and 14 days after the last DT injection (see **Fig. 5.43**). Microglia numbers particularly increased in the hippocampal pyramidal layer of the CA1 region, suggesting that they

actively engulfed apoptotic CCL17-expressing neurons, which appeared at around the same time after DT treatment (compare **Fig. 5.42 & Fig. 5.43**). In the unperturbed hippocampus, neurons in the hippocampal pyramidal layer form a very dense and tight band of somata, which is normally devoid of microglia¹²². Here, the DT-mediated neuronal death of CCL17/DTR-expressing neurons appeared to cause a marked increase of microglial infiltration or proliferation in the CA1 region. It is generally accepted that in the injured brain microglia migrate to the site of inflammation to phagocytose and eliminate dead cells and debris³¹. In the injured area microglia also become hyper-proliferative and undergo drastic morphological changes characterized by a less ramified, highly phagocytic amoeboid morphology²⁷⁵. In turn, microglia form fewer contacts with neurons and their synaptic surveillance functions are diminished^{276,277}. Thus, in addition to an increased migration to the pyramidal layer, microglia in DT-treated CCL17^{DTR/+} mice likely acquire an increased proliferative potential. The exact contribution of microglial infiltration or proliferation should be addressed in future experiments. Analysis of the astrocytic marker GFAP also revealed an increased immunoreactivity 7 days after DT treatment, which slowly increased over the course of the experiment, peaking at around 21 days after DT treatment (see **Fig. 5.44**). In the healthy brain, astrocytes are known to fulfill multiple functions, such as the uptake of neurotransmitters, metabolic support of neurons, maintenance of the BBB, and the modulation of synaptic transmission^{96,278}. Interestingly, astrocytes also play an essential role in CNS regeneration²⁷⁹. Upon nerve injury, astrocytes proliferate in the injured area and form a glial scar. Therefore, it is reasonable to assume that in DT-treated CCL17^{DTR/+} mice astrocytes fill up the space in the pyramidal layer and form a glial scar once microglia removed the CCL17-expressing neurons.

During initial monitoring of DT-injected mice, it became apparent that female DT-treated CCL17^{DTR/+} mice in particular displayed an abnormal behavior characterized by increased sensitivity to stress and elevated locomotion. Depending on the brain region, injuries can lead to the development of spontaneous recurrent seizures (SRS), a process known as epileptogenesis²⁷³. The hippocampus is well-known for its association with epilepsy²⁸⁰. Given that DT-treatment of CCL17^{DTR/+} mice most strongly affected neurons in the pyramidal CA1 layer it was decided to perform EEG measurements in female DT-treated CCL17^{DTR/+} mice. Unfortunately only two mice could be analyzed at the time; however, both mice displayed a sporadic occurrence of more than 15 seizures 5 to 6 days after DT treatment. Development of first SRS nearly coincided with the first appearance of apoptotic neurons (compare **Fig. 5.42 & Fig. 5.45**), suggesting that the death of CCL17-expressing neurons is directly responsible for the development of SRS in DT-treated CCL17^{DTR/+} mice. The delay of 5-6 days between the last DT administration and the occurrence of the first SRS was likely due to the time required for DT to traverse the BBB and kill CCL17/DTR-expressing neurons^{181,273}. It is of interest here, that in a recent study *Ccl17* expression was specifically identified in hippocampal glutamatergic neurons¹⁷⁵. Glutamatergic neurons are the brains main excitatory neurons, which use glutamate as a neurotransmitter. Prolonged excitation of neurons through glutamate was found to induce cell death

in a process known as “excitotoxicity” and is often associated with the pathology of epilepsy²⁸¹⁻²⁸³. Therefore, it is possible that the DT-mediated ablation of CCL17-expressing glutamatergic neurons results in a sudden release of glutamate which in turn induces excitotoxicity of neighboring neural and non-neural cells. In the unperturbed brain, astrocytes are critical to buffer synaptic glutamate levels and possess specific glutamate transporters, such as GLAST and GLT-1 to remove excessive glutamate from the synapse²⁸⁴. During epileptogenesis and increased seizure activity, however, extracellular glutamate levels rise and contribute to the reactive astrogliosis observed in epileptic patients. Here, further investigation of the exact contributions of neuronal cell death and gliosis to the development of SRS in the CCL17-DTR model may provide novel insights into the process of epileptogenesis. In addition, CCL17-DTR mice may represent a new valuable model system for the analysis of inducible neuroinflammation in the hippocampal CA1 region.

7. Acknowledgments

First of all I want to thank Prof. Irmgard Förster for giving me the opportunity to conduct my PhD thesis in her laboratory and for the chance to work and thrive in a very independent manner. She always provided me with useful thoughts and stimulating discussions giving me the chance to solve arising problems by my own. I also want to thank Prof. Waldemar Kolanus for agreeing to be my second examiner.

Further I would like to thank everybody from the Förster and Weighardt laboratory. In particular Heike, who had always an open ear and good advices on my experiments. Furthermore, she shared my passion for endless speculations. Especially in the early month of my thesis, I have to thank all the "Förster girls", Nancy, Martina, Rieke, Theresa, and Olga. I'm particularly grateful for all the intense discussions we had on experiments or just daily things. Most of the times these discussions provided me with new perspectives, whereas sometime I was just left confused as only one of three men. With respect to the men, I really have to thank Philip who will always be a great antipole to myself (most intense discussions I ever had), and Björn who is one of the most meticulous and helpful persons I've met so far. Special thanks go to our secretary Christiane who helped me with almost any problem and always provided me with the newest gossip. I also thank our animal caretakers Tamara and Mirjam, who got never tired of my many wishes concerning the organization of mouse experiments.

I am also very grateful to our collaboration partner who significantly contributed to the success of our two publications. In particular, Julia, Franzi, and Günter from the Department of Chemical Biology and Aptamers, University of Bonn, Germany, to Björn and Christian from the Institute of Cellular Neuroscience (IZN), University of Bonn, Germany, Jan and Annett from the German Center for Neurodegenerative Diseases (DZNE), Bonn, Germany, and Julia and Peter also from the IZN.

I also want to thank some other people from the LIMES institute, in particular Lucia and Felix E. for being the best companions during my PhD, Thomas Q. for every discussion and help with microscopic techniques, Andreas Schoofs, Sebastian, Anton, Lorenzo and Paul for great discussions during smoking breaks, Andreas Schlitzer and Elvira Mass for sharing their thoughts on my experiments and manuscript and for introducing me to some scientific big shots. All these people (and many more) contributed to the very good experience I had during my PhD. Although, there is much more I am grateful for, I just want to say that I have the feeling to have worked with some truly nice and inspiring people.

A big thank you goes to my lovely girlfriend Nina for always keeping me motivated, literally helping me with many experiments, sharing thoughts, and being my best friend. She really is one of the most impressive characters I've ever met and I am grateful for every day we spend together.

Last but not least, I want to thank my family, my siblings Judith and Adrian and my parents Horst and Beatrix who always supported me, tried to understand my personal AND experimental problems, and just for always being there for me!

Special thanks go to all of my friends from earlier times (they know), I promise I will have more time for all of you once the thesis is submitted!

8. References

1. Murphy, K. & Weaver, C. *Janeway's Immunobiology, 9th edition*. (Garland Science, 2016).
2. Dranoff, G. Cytokines in cancer pathogenesis and cancer therapy. *Nat. Rev. Cancer* **4**, 11–22 (2004).
3. Takeuchi, O. & Akira, S. Pattern Recognition Receptors and Inflammation. *Cell* **140**, 805–820 (2010).
4. Deczkowska, A. *et al.* Disease-Associated Microglia: A Universal Immune Sensor of Neurodegeneration. *Cell* **173**, 1073–1081 (2018).
5. Matzinger, P. The danger model: a renewed sense of self. *Science* **296**, 301–5 (2002).
6. Eberl, G. Immunity by equilibrium. *Nat. Rev. Immunol.* **16**, 524–532 (2016).
7. Bergthaler, A. & Menche, J. The immune system as a social network. *Nat. Immunol.* **18**, 481–482 (2017).
8. Surendran, S., Hückesfeld, S., Wäschle, B. & Pankratz, M. J. Pathogen-induced food evasion behavior in *Drosophila* larvae. *J. Exp. Biol.* **220**, 1774–1780 (2017).
9. Curtis, V. A. Infection-avoidance behaviour in humans and other animals. *Trends Immunol.* **35**, 457–64 (2014).
10. Park, J. H., Schaller, M. & Crandall, C. S. Pathogen-avoidance mechanisms and the stigmatization of obese people. *Evol. Hum. Behav.* **28**, 410–414 (2007).
11. Buchmann, K. Evolution of Innate Immunity: Clues from Invertebrates via Fish to Mammals. *Front. Immunol.* **5**, 459 (2014).
12. Takeda, K., Kaisho, T. & Akira, S. Toll-like receptors. *Annu. Rev. Immunol.* **21**, 335–376 (2003).
13. Takeda, K. & Akira, S. TLR signaling pathways. *Semin. Immunol.* **16**, 3–9 (2004).
14. Kanneganti, T.-D. Central roles of NLRs and inflammasomes in viral infection. *Nat. Rev. Immunol.* **10**, 688–98 (2010).
15. Lamkanfi, M. & Dixit, V. M. Mechanisms and functions of inflammasomes. *Cell* **157**, 1013–22 (2014).
16. Netea, M. G. *et al.* Trained immunity: A program of innate immune memory in health and disease. *Science (80-.).* **352**, aaf1098-aaf1098 (2016).
17. de Boer, R. J. & Hogeweg, P. Immunological discrimination between self and non-self by precursor depletion and memory accumulation. *J. Theor. Biol.* **124**, 343–69 (1987).
18. Tay, S. S., Roediger, B., Tong, P. L., Tikoo, S. & Weninger, W. The Skin-Resident Immune Network. *Curr. Dermatol. Rep.* **3**, 13–22 (2014).
19. Nestle, F. O., Di Meglio, P., Qin, J. Z. & Nickoloff, B. J. Skin immune sentinels in health and disease. *Nat. Rev. Immunol.* **9**, 679–691 (2009).
20. Pasparakis, M., Haase, I. & Nestle, F. O. Mechanisms regulating skin immunity and inflammation. *Nat. Rev. Immunol.* **14**, 289–301 (2014).
21. Worbs, T., Hammerschmidt, S. I. & Förster, R. Dendritic cell migration in health and disease. *Nat. Rev. Immunol.* **17**, 30–48 (2017).
22. Abraira, V. E. & Ginty, D. D. The Sensory Neurons of Touch. *Neuron* **79**, 618–639 (2013).
23. Merad, M., Ginhoux, F. & Collin, M. Origin, homeostasis and function of Langerhans cells and other langerin-expressing dendritic cells. *Nat. Rev. Immunol.* **8**, 935–947 (2008).
24. Kashem, S. W., Haniffa, M. & Kaplan, D. H. Antigen-Presenting Cells in the Skin. *Annu. Rev. Immunol.* **35**, 469–499 (2017).

25. Stutte, S., Jux, B., Esser, C. & Förster, I. CD24a expression levels discriminate Langerhans cells from dermal dendritic cells in murine skin and lymph nodes. *J. Invest. Dermatol.* **128**, 1470–1475 (2008).
26. Bursch, L. S. *et al.* Identification of a novel population of Langerin+ dendritic cells. *J. Exp. Med.* **204**, 3147–3156 (2007).
27. Henri, S. *et al.* CD207+ CD103+ dermal dendritic cells cross-present keratinocyte-derived antigens irrespective of the presence of Langerhans cells. *J. Exp. Med.* **207**, 189–206 (2010).
28. Malissen, B., Tamoutounour, S. & Henri, S. The origins and functions of dendritic cells and macrophages in the skin. *Nat. Rev. Immunol.* **14**, 417–428 (2014).
29. Nayak, D., Roth, T. L. & McGavern, D. B. Microglia Development and Function. *Annu. Rev. Immunol.* **32**, 367–402 (2014).
30. Greter, M. *et al.* Stroma-Derived Interleukin-34 Controls the Development and Maintenance of Langerhans Cells and the Maintenance of Microglia. *Immunity* **37**, 1050–1060 (2012).
31. Colonna, M. & Butovsky, O. Microglia Function in the Central Nervous System During Health and Neurodegeneration. *Annu. Rev. Immunol.* **35**, 441–468 (2017).
32. Kaplan, D. H., Jenison, M. C., Saeland, S., Shlomchik, W. D. & Shlomchik, M. J. Epidermal Langerhans Cell-Deficient Mice Develop Enhanced Contact Hypersensitivity. *Immunity* **23**, 611–620 (2005).
33. Bennett, C. L. *et al.* Inducible ablation of mouse Langerhans cells diminishes but fails to abrogate contact hypersensitivity. *J. Cell Biol.* **169**, 569–576 (2005).
34. Shklovskaya, E. *et al.* Langerhans cells are precommitted to immune tolerance induction. *Proc. Natl. Acad. Sci.* **108**, 18049–18054 (2011).
35. Seré, K. *et al.* Two Distinct Types of Langerhans Cells Populate the Skin during Steady State and Inflammation. *Immunity* **37**, 905–916 (2012).
36. Steinman, R. M. & Cohn, Z. A. Identification of a novel cell type in peripheral lymphoid organs of mice. I. Morphology, quantitation, tissue distribution. *J. Exp. Med.* **137**, 1142–62 (1973).
37. Schlitzer, A. *et al.* IRF4 Transcription Factor-Dependent CD11b+ Dendritic Cells in Human and Mouse Control Mucosal IL-17 Cytokine Responses. *Immunity* **38**, 970–983 (2013).
38. Schlitzer, A. *et al.* Identification of cDC1- and cDC2-committed DC progenitors reveals early lineage priming at the common DC progenitor stage in the bone marrow. *Nat. Immunol.* **16**, 718–728 (2015).
39. Karsunky, H., Merad, M., Cozzio, A., Weissman, I. L. & Manz, M. G. Flt3 ligand regulates dendritic cell development from Flt3+ lymphoid and myeloid-committed progenitors to Flt3+ dendritic cells in vivo. *J. Exp. Med.* **198**, 305–13 (2003).
40. Tamoutounour, S. *et al.* Origins and functional specialization of macrophages and of conventional and monocyte-derived dendritic cells in mouse skin. *Immunity* **39**, 925–938 (2013).
41. Mass, E. *et al.* Specification of tissue-resident macrophages during organogenesis. *Science (80-.).* **353**, aaf4238–aaf4238 (2016).
42. Abtin, A. *et al.* Perivascular macrophages mediate neutrophil recruitment during bacterial skin infection. *Nat. Immunol.* **15**, 45–53 (2014).
43. Barreiro, O. *et al.* Pivotal role for skin transendothelial radio-resistant anti-inflammatory macrophages in tissue repair. *Elife* **5**, 1–33 (2016).
44. Roberts, S. & Girardi, M. Conventional and unconventional T cells. *Clin. Basic Immunodermatology* 85–104 (2008). doi:10.1007/978-1-84800-165-7_6
45. Al-Banna, N. A., Vaci, M., Slauenwhite, D., Johnston, B. & Issekutz, T. B. CCR4 and CXCR3 play different roles in the migration of T cells to inflammation in skin, arthritic joints, and lymph nodes. *Eur. J. Immunol.*

- 44**, 1633–1643 (2014).
46. Riis, J. L. *et al.* Kinetics and differential expression of the skin-related chemokines CCL27 and CCL17 in psoriasis, atopic dermatitis and allergic contact dermatitis. *Exp. Dermatol.* **20**, 789–794 (2011).
 47. Kusumoto, M. *et al.* Expression of Chemokine Receptor CCR4 and Its Ligands (CCL17 and CCL22) in Murine Contact Hypersensitivity. *J. Interf. Cytokine Res.* **27**, 901–910 (2007).
 48. Reiss, Y., Proudfoot, A. E., Power, C. A., Campbell, J. J. & Butcher, E. C. CC chemokine receptor (CCR)4 and the CCR10 ligand cutaneous T cell-attracting chemokine (CTACK) in lymphocyte trafficking to inflamed skin. *J. Exp. Med.* **194**, 1541–7 (2001).
 49. Stutte, S. *et al.* Requirement of CCL17 for CCR7- and CXCR4-dependent migration of cutaneous dendritic cells. *Proc. Natl. Acad. Sci.* **107**, 8736–8741 (2010).
 50. Fülle, L. *et al.* RNA Aptamers Recognizing Murine CCL17 Inhibit T Cell Chemotaxis and Reduce Contact Hypersensitivity In Vivo. *Mol. Ther.* **26**, 95–104 (2018).
 51. Sutoh, Y., Mohamed, R. H. & Kasahara, M. Origin and Evolution of Dendritic Epidermal T Cells. *Front. Immunol.* **9**, 1059 (2018).
 52. Sumaria, N. *et al.* Cutaneous immunosurveillance by self-renewing dermal gammadelta T cells. *J. Exp. Med.* **208**, 505–18 (2011).
 53. Halim, T. Y. F. *et al.* Group 2 innate lymphoid cells license dendritic cells to potentiate memory TH2 cell responses. *Nat. Immunol.* **17**, 57–64 (2015).
 54. Li, Z. *et al.* Epidermal Notch1 recruits RORγ+ group 3 innate lymphoid cells to orchestrate normal skin repair. *Nat. Commun.* **7**, 11394 (2016).
 55. Streilein, J. W. Skin-associated lymphoid tissues (SALT): origins and functions. *J. Invest. Dermatol.* **80 Suppl**, 12s–16s (1983).
 56. Bienenstock, J. & Befus, D. Gut- and bronchus-associated lymphoid tissue. *Am. J. Anat.* **170**, 437–445 (1984).
 57. Kaplan, D. H., Igyártó, B. Z. & Gaspari, A. A. Early immune events in the induction of allergic contact dermatitis. *Nat. Rev. Immunol.* **12**, 114–124 (2012).
 58. Ono, S. & Kabashima, K. Proposal of inducible skin-associated lymphoid tissue (iSALT). *Exp. Dermatol.* **24**, 630–631 (2015).
 59. Mueller, S. N. Skin DCs cluster for efficient T cell activation. *Nat. Immunol.* **15**, 1004–1005 (2014).
 60. Natsuaki, Y. *et al.* Perivascular leukocyte clusters are essential for efficient activation of effector T cells in the skin. *Nat. Immunol.* **15**, 1064–1069 (2014).
 61. Homey, B. *et al.* CCL27–CCR10 interactions regulate T cell-mediated skin inflammation. *Nat. Med.* **8**, 157–165 (2002).
 62. Honda, T. & Kabashima, K. Novel concept of iSALT (inducible skin-associated lymphoid tissue) in the elicitation of allergic contact dermatitis. *Proc. Jpn. Acad., Ser. B* **92**, 20–28 (2016).
 63. Sasseville, D. Occupational contact dermatitis. *Allergy Asthma. Clin. Immunol.* **4**, 59–65 (2008).
 64. Gell, P. G. h. & Coombs, R. R. A. *The classification of allergic reactions underlying disease. Clinical Aspects of Immunology* (Blackwell, 1963).
 65. Zlotnik, A. & Yoshie, O. Chemokines: a new classification system and their role in immunity. *Immunity* **12**, 121–127 (2000).
 66. von Hundelshausen, P. *et al.* Chemokine interactome mapping enables tailored intervention in acute and chronic inflammation. *Sci. Transl. Med.* **9**, eaah6650 (2017).

67. Tan, S.-Y., Roediger, B. & Weninger, W. The role of chemokines in cutaneous immunosurveillance. *Immunol. Cell Biol.* **93**, 337–346 (2015).
68. Griffith, J. W., Sokol, C. L. & Luster, A. D. Chemokines and Chemokine Receptors: Positioning Cells for Host Defense and Immunity. *Annu. Rev. Immunol.* **32**, 659–702 (2014).
69. Stutte, S., Gerbitzki, N., Novak, N. & Förster, I. in *Atopic Dermatitis - Disease Etiology and Clinical Management* (ed. Esparza-Gordillo, J.) (InTech, 2012). doi:10.5772/25704
70. Lieberam, I. & Förster, I. The murine beta-chemokine TARC is expressed by subsets of dendritic cells and attracts primed CD4+ T cells. *Eur. J. Immunol.* **29**, 2684–94 (1999).
71. Yahia, S. A. *et al.* CCL17 Production by Dendritic Cells Is Required for NOD1-mediated Exacerbation of Allergic Asthma. *Am. J. Respir. Crit. Care Med.* **189**, 899–908 (2014).
72. Heiseke, A. F. *et al.* CCL17 promotes intestinal inflammation in mice and counteracts regulatory T cell-mediated protection from colitis. *Gastroenterology* **142**, 335–345 (2012).
73. Alferink, J. *et al.* Compartmentalized production of CCL17 in vivo: strong inducibility in peripheral dendritic cells contrasts selective absence from the spleen. *J Exp Med* **197**, 585–599 (2003).
74. Achuthan, A. *et al.* Granulocyte macrophage colony-stimulating factor induces CCL17 production via IRF4 to mediate inflammation. *J. Clin. Invest.* **126**, 3453–3466 (2016).
75. Yoshie, O. & Matsushima, K. CCR4 and its ligands: From bench to bedside. *Int. Immunol.* (2015). doi:10.1093/intimm/dxu079
76. Panina-Bordignon, P. *et al.* The C-C chemokine receptors CCR4 and CCR8 identify airway T cells of allergen-challenged atopic asthmatics. *J. Clin. Invest.* **107**, 1357–1364 (2001).
77. Elhussein Mohamed, O. Y., Elazomi, A., Mohamed, M. S. & Abdalla, F. B. Local elevation of CCL22: A new trend in immunotherapy (skin model). *J. Cell. Immunother.* **2**, 1–6 (2016).
78. Wiedemann, G. M. *et al.* Cancer cell-derived IL-1 α induces CCL22 and the recruitment of regulatory T cells. *Oncoimmunology* **5**, e1175794 (2016).
79. Curiel, T. J. *et al.* Specific recruitment of regulatory T cells in ovarian carcinoma fosters immune privilege and predicts reduced survival. *Nat Med* **10**, 942–949 (2004).
80. Santulli-Marotto, S. *et al.* Engagement of Two Distinct Binding Domains on CCL17 Is Required for Signaling through CCR4 and Establishment of Localized Inflammatory Conditions in the Lung. *PLoS One* **8**, e81465 (2013).
81. Santulli-Marotto, S. *et al.* Surrogate Antibodies That Specifically Bind and Neutralize CCL17 But Not CCL22. *Monoclon. Antib. Immunodiagn. Immunother.* **32**, 162–171 (2013).
82. Santulli-Marotto, S. *et al.* CCL22-specific Antibodies Reveal That Engagement of Two Distinct Binding Domains on CCL22 Is Required for CCR4-mediated Function. *Monoclon. Antib. Immunodiagn. Immunother.* **34**, 373–380 (2015).
83. Rajagopal, S. *et al.* Biased agonism as a mechanism for differential signaling by chemokine receptors. *J. Biol. Chem.* **288**, 35039–48 (2013).
84. Ruland, C. *et al.* Chemokine CCL17 is expressed by dendritic cells in the CNS during experimental autoimmune encephalomyelitis and promotes pathogenesis of disease. *Brain. Behav. Immun.* **66**, 382–393 (2017).
85. Poppensieker, K. *et al.* CC chemokine receptor 4 is required for experimental autoimmune encephalomyelitis by regulating GM-CSF and IL-23 production in dendritic cells. *Proc. Natl. Acad. Sci.* **109**, 3897–3902 (2012).
86. Chong, B. F., Murphy, J.-E., Kupper, T. S. & Fuhlbrigge, R. C. E-Selectin, Thymus- and Activation-Regulated Chemokine/CCL17, and Intercellular Adhesion Molecule-1 Are Constitutively Coexpressed in Dermal

- Microvessels: A Foundation for a Cutaneous Immunosurveillance System. *J. Immunol.* **172**, 1575–1581 (2004).
87. Kupper, T. S. & Fuhlbrigge, R. C. Immune surveillance in the skin: mechanisms and clinical consequences. *Nat. Rev. Immunol.* **4**, 211–222 (2004).
 88. Campbell, J. J. *et al.* The chemokine receptor CCR4 in vascular recognition by cutaneous but not intestinal memory T cells. *Nature* **400**, 776–780 (1999).
 89. Semmling, V. *et al.* Alternative cross-priming through CCL17-CCR4-mediated attraction of CTLs toward NKT cell-licensed DCs. *Nat. Immunol.* **11**, 313–320 (2010).
 90. Tsunemi, Y. *et al.* CCL17 transgenic mice show an enhanced Th2-type response to both allergic and non-allergic stimuli. *Eur. J. Immunol.* **36**, 2116–2127 (2006).
 91. Lehtimäki, S. *et al.* Absence of CCR4 Exacerbates Skin Inflammation in an Oxazolone-Induced Contact Hypersensitivity Model. *J. Invest. Dermatol.* **130**, 2743–2751 (2010).
 92. Abbott, N. J., Patabendige, A. A. K., Dolman, D. E. M., Yusof, S. R. & Begley, D. J. Structure and function of the blood–brain barrier. *Neurobiol. Dis.* **37**, 13–25 (2010).
 93. Varatharaj, A. & Galea, I. The blood-brain barrier in systemic inflammation. *Brain. Behav. Immun.* **60**, 1–12 (2017).
 94. Brankatschk, M. & Eaton, S. Lipoprotein particles cross the blood-brain barrier in *Drosophila*. *J. Neurosci.* **30**, 10441–7 (2010).
 95. Kaur, C. & Ling, E.-A. The circumventricular organs. *Histol. Histopathol.* **32**, 879–892 (2017).
 96. Kandel, E. R., Schwartz, J. H., Siegelbaum, S. A. & Hudspeth, A. J. *Principles of neural science*. (McGraw-Hill, New York, 2013).
 97. Li, Q. & Barres, B. A. Microglia and macrophages in brain homeostasis and disease. *Nat. Rev. Immunol.* **18**, 225–242 (2018).
 98. Prinz, M. & Priller, J. Microglia and brain macrophages in the molecular age: From origin to neuropsychiatric disease. *Nat. Rev. Neurosci.* **15**, 300–312 (2014).
 99. Theoharides, T. C., Tsilioni, I., Patel, A. B. & Doyle, R. Atopic diseases and inflammation of the brain in the pathogenesis of autism spectrum disorders. *Transl. Psychiatry* **6**, e844 (2016).
 100. Xie, L., Choudhury, G. R., Winters, A., Yang, S.-H. & Jin, K. Cerebral regulatory T cells restrain microglia/macrophage-mediated inflammatory responses via IL-10. *Eur. J. Immunol.* **45**, 180–191 (2015).
 101. Herz, J., Filiano, A. J., Smith, A., Yogev, N. & Kipnis, J. Myeloid Cells in the Central Nervous System. *Immunity* **46**, 943–956 (2017).
 102. Ginhoux, F. & Williams, M. Tissue-Resident Macrophage Ontogeny and Homeostasis. *Immunity* **44**, 439–449 (2016).
 103. Ginhoux, F. *et al.* Fate mapping analysis reveals that adult microglia derive from primitive macrophages. *Science* **330**, 841–5 (2010).
 104. Ginhoux, F., Lim, S., Hoeffel, G., Low, D. & Huber, T. Origin and differentiation of microglia. *Front. Cell. Neurosci.* **7**, 45 (2013).
 105. Salter, M. W. & Stevens, B. Microglia emerge as central players in brain disease. *Nat. Med.* **23**, 1018–1027 (2017).
 106. Hashimoto, D. *et al.* Tissue-Resident Macrophages Self-Maintain Locally throughout Adult Life with Minimal Contribution from Circulating Monocytes. *Immunity* **38**, 792–804 (2013).
 107. Wolf, S. A., Boddeke, H. W. G. M. & Kettenmann, H. Microglia in Physiology and Disease. *Annu. Rev.*

- Physiol.* **79**, 619–643 (2017).
108. Kettenmann, H., Kirchhoff, F. & Verkhratsky, A. Microglia: New Roles for the Synaptic Stripper. *Neuron* **77**, 10–18 (2013).
 109. Parkhurst, C. N. *et al.* Microglia Promote Learning-Dependent Synapse Formation through Brain-Derived Neurotrophic Factor. *Cell* **155**, 1596–1609 (2013).
 110. Keren-Shaul, H. *et al.* A Unique Microglia Type Associated with Restricting Development of Alzheimer's Disease. *Cell* **169**, 1276–1290.e17 (2017).
 111. Gyoneva, S. *et al.* Systemic inflammation regulates microglial responses to tissue damage *in vivo*. *Glia* **62**, 1345–1360 (2014).
 112. Qin, L. *et al.* Systemic LPS causes chronic neuroinflammation and progressive neurodegeneration. *Glia* **55**, 453–462 (2007).
 113. Krstic, D. *et al.* Systemic immune challenges trigger and drive Alzheimer-like neuropathology in mice. *J. Neuroinflammation* **9**, 151 (2012).
 114. Ajmone-Cat, M. A., Bernardo, A., Greco, A. & Minghetti, L. Non-Steroidal Anti-Inflammatory Drugs and Brain Inflammation: Effects on Microglial Functions. *Pharmaceuticals (Basel)*. **3**, 1949–1965 (2010).
 115. Seruga, B., Zhang, H., Bernstein, L. J. & Tannock, I. F. Cytokines and their relationship to the symptoms and outcome of cancer. *Nat. Rev. Cancer* **8**, 887–899 (2008).
 116. Chavan, S. S., Pavlov, V. A. & Tracey, K. J. Mechanisms and Therapeutic Relevance of Neuro-immune Communication. *Immunity* **46**, 927–942 (2017).
 117. Andersson, U. & Tracey, K. J. Reflex Principles of Immunological Homeostasis. *Annu. Rev. Immunol.* (2011). doi:10.1146/annurev-immunol-020711-075015
 118. Sundman, E. & Olofsson, P. S. Neural control of the immune system. *Adv. Physiol. Educ.* **38**, 135–9 (2014).
 119. Becher, B., Spath, S. & Goverman, J. Cytokine networks in neuroinflammation. *Nat. Rev. Immunol.* **17**, 49–59 (2017).
 120. Dantzer, R., O'Connor, J. C., Freund, G. G., Johnson, R. W. & Kelley, K. W. From inflammation to sickness and depression: when the immune system subjugates the brain. *Nat. Rev. Neurosci.* **9**, 46–56 (2008).
 121. Johnson, R. H., Kho, D. T., O'Carroll, S. J., Angel, C. E. & Graham, E. S. The functional and inflammatory response of brain endothelial cells to Toll-Like Receptor agonists. *Sci. Rep.* **8**, 10102 (2018).
 122. Strange, B. A., Witter, M. P., Lein, E. S. & Moser, E. I. Functional organization of the hippocampal longitudinal axis. *Nat. Rev. Neurosci.* **15**, 655–669 (2014).
 123. Smith, D. M. & Mizumori, S. J. Y. Hippocampal place cells, context, and episodic memory. *Hippocampus* **16**, 716–729 (2006).
 124. Vescovi, A. L., Galli, R. & Reynolds, B. A. Brain tumour stem cells. *Nat. Rev. Cancer* **6**, 425–436 (2006).
 125. Sternberg, E. M. Neural regulation of innate immunity: a coordinated nonspecific host response to pathogens. *Nat. Rev. Immunol.* **6**, 318–28 (2006).
 126. Williamson, L. L. & Bilbo, S. D. Chemokines and the hippocampus: A new perspective on hippocampal plasticity and vulnerability. *Brain. Behav. Immun.* **30**, 186–194 (2013).
 127. Bilbo, S. D., Block, C. L., Bolton, J. L., Hanamsagar, R. & Tran, P. K. Beyond infection - Maternal immune activation by environmental factors, microglial development, and relevance for autism spectrum disorders. *Exp. Neurol.* **299**, 241–251 (2018).
 128. de Haas, A. H., van Weering, H. R. J., de Jong, E. K., Boddeke, H. W. G. M. & Biber, K. P. H. Neuronal Chemokines: Versatile Messengers In Central Nervous System Cell Interaction. *Mol. Neurobiol.* **36**, 137–

- 151 (2007).
129. Rostène, W., Kitabgi, P. & Parsadaniantz, S. M. Chemokines: a new class of neuromodulator? *Nat. Rev. Neurosci.* **8**, 895–903 (2007).
 130. Lieberam, I., Agalliu, D., Nagasawa, T., Ericson, J. & Jessell, T. M. A Cxcl12-Cxcr4 Chemokine Signaling Pathway Defines the Initial Trajectory of Mammalian Motor Axons. *Neuron* **47**, 667–679 (2005).
 131. Mimura-Yamamoto, Y. *et al.* Dynamics and function of CXCR4 in formation of the granule cell layer during hippocampal development. *Sci. Rep.* **7**, 5647 (2017).
 132. Guyon, A. & Nahon, J.-L. Multiple actions of the chemokine stromal cell-derived factor-1 on neuronal activity. *J. Mol. Endocrinol.* **38**, 365–376 (2007).
 133. Meucci, O. *et al.* Chemokines regulate hippocampal neuronal signaling and gp120 neurotoxicity. *Proc. Natl. Acad. Sci. U. S. A.* **95**, 14500–14505 (1998).
 134. Sanchez, A. B. *et al.* CXCL12-induced neurotoxicity critically depends on NMDA receptor-gated and L-type Ca²⁺ channels upstream of p38 MAPK. *J. Neuroinflammation* **13**, 252 (2016).
 135. Bonecchi, R. *et al.* Differential recognition and scavenging of native and truncated macrophage-derived chemokine (macrophage-derived chemokine/CC chemokine ligand 22) by the D6 decoy receptor. *J. Immunol.* **172**, 4972–6 (2004).
 136. Stafstrom, C. E. in *Epilepsy and the Ketogenic Diet* 3–29 (Humana Press, 2004). doi:10.1007/978-1-59259-808-3_1
 137. Scharfman, H. E. The neurobiology of epilepsy. *Curr. Neurol. Neurosci. Rep.* **7**, 348–54 (2007).
 138. Kandratavicius, L. *et al.* Animal models of epilepsy: use and limitations. *Neuropsychiatr. Dis. Treat.* **10**, 1693–705 (2014).
 139. Bouilleret, V. *et al.* Recurrent seizures and hippocampal sclerosis following intrahippocampal kainate injection in adult mice: electroencephalography, histopathology and synaptic reorganization similar to mesial temporal lobe epilepsy. *Neuroscience* **89**, 717–29 (1999).
 140. Mirshahpanah, P., Li, Y. Y., Burkhardt, N., Asadullah, K. & Zollner, T. M. CCR4 and CCR10 ligands play additive roles in mouse contact hypersensitivity. *Exp. Dermatol.* **17**, 30–34 (2008).
 141. Peschon, J. J. *et al.* TNF receptor-deficient mice reveal divergent roles for p55 and p75 in several models of inflammation. *J. Immunol.* **160**, 943–52 (1998).
 142. Stanley, E. *et al.* Granulocyte/macrophage colony-stimulating factor-deficient mice show no major perturbation of hematopoiesis but develop a characteristic pulmonary pathology. *Proc. Natl. Acad. Sci. U. S. A.* **91**, 5592–6 (1994).
 143. Adachi, O. *et al.* Targeted disruption of the MyD88 gene results in loss of IL-1- and IL-18-mediated function. *Immunity* **9**, 143–50 (1998).
 144. Fülle, L. *et al.* CCL17 exerts a neuroimmune modulatory function and is expressed in hippocampal neurons. *Glia* **in press**, (2018).
 145. Arganda-Carreras, I., Fernández-González, R., Muñoz-Barrutia, A. & Ortiz-De-Solorzano, C. 3D reconstruction of histological sections: Application to mammary gland tissue. *Microsc. Res. Tech.* **73**, 1019–1029 (2010).
 146. Li, J. L. *et al.* Intravital multiphoton imaging of immune responses in the mouse ear skin. *Nat. Protoc.* **7**, 221–234 (2012).
 147. Kremer, L. *et al.* The transient expression of C-C chemokine receptor 8 in thymus identifies a thymocyte subset committed to become CD4⁺ single-positive T cells. *J. Immunol.* **166**, 218–25 (2001).
 148. Beaudoin, G. M. J. *et al.* Culturing pyramidal neurons from the early postnatal mouse hippocampus and

- cortex. *Nat. Protoc.* **7**, 1741–1754 (2012).
149. Stratmann, G., Sall, J. W., May, L. D. V, Loepke, A. W. & Lee, M. T. Beyond anesthetic properties: the effects of isoflurane on brain cell death, neurogenesis, and long-term neurocognitive function. *Anesth. Analg.* **110**, 431–7 (2010).
 150. Minge, D. *et al.* Heparan Sulfates Support Pyramidal Cell Excitability, Synaptic Plasticity, and Context Discrimination. *Cereb. Cortex* **27**, 903–918 (2017).
 151. Xiao, T. *et al.* Thymus and activation-regulated chemokine (TARC/CCL17) produced by mouse epidermal Langerhans cells is upregulated by TNF-alpha and IL-4 and downregulated by IFN-gamma. *Cytokine* **23**, 126–32
 152. Gros, E., Bussmann, C., Bieber, T., Förster, I. & Novak, N. Expression of chemokines and chemokine receptors in lesional and nonlesional upper skin of patients with atopic dermatitis. *J. Allergy Clin. Immunol.* **124**, 14–16 (2009).
 153. Wang, X. *et al.* Visualizing CD4 T-cell migration into inflamed skin and its inhibition by CCR4/CCR10 blockades using *in vivo* imaging model. *Br. J. Dermatol.* **162**, 487–496 (2010).
 154. Knöpper, K. Characterization of CCL17+ cells in the skin using imaging and functional analysis. (Rheinische Friedrich-Wilhelms Universität Bonn, 2017).
 155. Nakamizo, S., Egawa, G., Bing, J. T. K. & Kabashima, K. Intravital imaging of cutaneous immune responses. *Cell. Immunol.* 0–1 (2018). doi:10.1016/j.cellimm.2018.05.006
 156. Shoda, T. *et al.* Expression of thymus and activation-regulated chemokine (TARC) by human dermal cells, but not epidermal keratinocytes. *J. Dermatol. Sci.* **76**, 90–95 (2014).
 157. Bouladoux, N. *et al.* in *Inflammation: methods and protocols* 21–36 (2017). doi:10.1007/978-1-4939-6786-5_2
 158. Clausen, B. E. & Laman, J. D. *Inflammation - Methods and Protocols.* **1559**, (Springer New York, 2017).
 159. Crozat, K. *et al.* Cutting edge: expression of XCR1 defines mouse lymphoid-tissue resident and migratory dendritic cells of the CD8 α + type. *J. Immunol.* **187**, 4411–5 (2011).
 160. Zhan, Y. *et al.* GM-CSF increases cross-presentation and CD103 expression by mouse CD8+ spleen dendritic cells. *Eur. J. Immunol.* **41**, 2585–2595 (2011).
 161. Greter, M. *et al.* GM-CSF controls nonlymphoid tissue dendritic cell homeostasis but is dispensable for the differentiation of inflammatory dendritic cells. *Immunity* **36**, 1031–46 (2012).
 162. Vestergaard, C., Deleuran, M., Gesser, B. & Larsen, C. G. G. Thymus- and activation-regulated chemokine (TARC/CCL17) induces a Th2-dominated inflammatory reaction on intradermal injection in mice. *Exp. Dermatol.* **13**, 265–271 (2004).
 163. Honda, T., Egawa, G., Grabbe, S. & Kabashima, K. Update of Immune Events in the Murine Contact Hypersensitivity Model: Toward the Understanding of Allergic Contact Dermatitis. *J. Invest. Dermatol.* **133**, 303–315 (2013).
 164. Saeki, H. & Tamaki, K. Thymus and activation regulated chemokine (TARC)/CCL17 and skin diseases. *J. Dermatol. Sci.* **43**, 75–84 (2006).
 165. Vocanson, M. *et al.* CD8+ T Cells Are Effector Cells of Contact Dermatitis to Common Skin Allergens in Mice. *J. Invest. Dermatol.* **126**, 815–820 (2006).
 166. Saint-Mezard, P., Berard, F., Dubois, B., Kaiserlian, D. & Nicolas, J.-F. The role of CD4+ and CD8+ T cells in contact hypersensitivity and allergic contact dermatitis. *Eur. J. Dermatol.* **14**, 131–8
 167. Ni, S. *et al.* Chemical Modifications of Nucleic Acid Aptamers for Therapeutic Purposes. *Int. J. Mol. Sci.* **18**, 1683 (2017).

168. Globisch, T. *et al.* Cytokine-dependent regulation of dendritic cell differentiation in the splenic microenvironment. *Eur J Immunol* **44**, 500–510 (2014).
169. Mariani, M., Lang, R., Binda, E., Panina-Bordignon, P. & D'Ambrosio, D. Dominance of CCL22 over CCL17 in induction of chemokine receptor CCR4 desensitization and internalization on human Th2 cells. *Eur J Immunol* **34**, 231–240 (2004).
170. Belperio, J. A. *et al.* The role of the Th2 CC chemokine ligand CCL17 in pulmonary fibrosis. *J. Immunol.* **173**, 4692–8 (2004).
171. Varol, D. *et al.* Dicer Deficiency Differentially Impacts Microglia of the Developing and Adult Brain. *Immunity* **46**, 1030–1044.e8 (2017).
172. Zhang, Y. *et al.* An RNA-Sequencing Transcriptome and Splicing Database of Glia, Neurons, and Vascular Cells of the Cerebral Cortex. *J. Neurosci.* **34**, 11929–11947 (2014).
173. Srinivasan, K. *et al.* Untangling the brain's neuroinflammatory and neurodegenerative transcriptional responses. *Nat. Commun.* **7**, 11295 (2016).
174. Henry, F. E., Sugino, K., Tozer, A., Branco, T. & Sternson, S. M. Cell type-specific transcriptomics of hypothalamic energy-sensing neuron responses to weight-loss. *Elife* **4**, 1–30 (2015).
175. McGill, B. E. *et al.* Abnormal Microglia and Enhanced Inflammation-Related Gene Transcription in Mice with Conditional Deletion of *Ctcf* in *Camk2a-Cre* -Expressing Neurons. *J. Neurosci.* **38**, 0936–17 (2017).
176. Chvatchko, Y. *et al.* A key role for CC chemokine receptor 4 in lipopolysaccharide-induced endotoxic shock. *J. Exp. Med.* **191**, 1755–64 (2000).
177. Pösel, C., Möller, K., Boltze, J., Wagner, D.-C. & Weise, G. Isolation and Flow Cytometric Analysis of Immune Cells from the Ischemic Mouse Brain. *J. Vis. Exp.* 53658 (2016). doi:10.3791/53658
178. Hoogland, I. C. M., Houbolt, C., van Westerloo, D. J., van Gool, W. A. & van de Beek, D. Systemic inflammation and microglial activation: systematic review of animal experiments. *J. Neuroinflammation* **12**, 114 (2015).
179. Arganda-Carreras, I., Fernández-González, R., Muñoz-Barrutia, A. & Ortiz-De-Solorzano, C. 3D reconstruction of histological sections: Application to mammary gland tissue. *Microsc. Res. Tech.* **73**, 1019–1029 (2010).
180. Qin, L., Liu, Y., Hong, J.-S. & Crews, F. T. NADPH oxidase and aging drive microglial activation, oxidative stress, and dopaminergic neurodegeneration following systemic LPS administration. *Glia* **61**, 855–868 (2013).
181. Wrobel, C. J., Wright, D. C., Dedrick, R. L. & Youle, R. J. Diphtheria toxin effects on brain-tumor xenografts. Implications for protein-based brain-tumor chemotherapy. *J. Neurosurg.* **72**, 946–950 (1990).
182. Kataoka, Y. Thymus and activation-regulated chemokine as a clinical biomarker in atopic dermatitis. *J. Dermatol.* **41**, 221–229 (2014).
183. Okamoto, H., Koizumi, K., Yamanaka, H., Saito, T. & Kamatani, N. A role for TARC/CCL17, a CC chemokine, in systemic lupus erythematosus. *J. Rheumatol.* **30**, 2369–73 (2003).
184. Perros, F., Hoogsteden, H. C., Coyle, A. J., Lambrecht, B. N. & Hammad, H. Blockade of CCR4 in a humanized model of asthma reveals a critical role for DC-derived CCL17 and CCL22 in attracting Th2 cells and inducing airway inflammation. *Allergy* **64**, 995–1002 (2009).
185. Thanabalasuriar, A., Neupane, A. S., Wang, J., Krummel, M. F. & Kubes, P. iNKT Cell Emigration out of the Lung Vasculature Requires Neutrophils and Monocyte-Derived Dendritic Cells in Inflammation. *Cell Rep.* **16**, 3260–3272 (2016).
186. Weber, C. *et al.* CCL17-expressing dendritic cells drive atherosclerosis by restraining regulatory T cell homeostasis in mice. *J Clin Invest* **121**, 2898–2910 (2011).

187. Hu, Z., Lancaster, J. N., Sasiponganan, C. & Ehrlich, L. I. R. CCR4 promotes medullary entry and thymocyte-dendritic cell interactions required for central tolerance. *J. Exp. Med.* **212**, 1947–1965 (2015).
188. Montane, J. *et al.* Prevention of murine autoimmune diabetes by CCL22-mediated Treg recruitment to the pancreatic islets. *J. Clin. Invest.* **121**, 3024–3028 (2011).
189. Bischoff, L. *et al.* Cellular Mechanisms of CCL22-Mediated Attenuation of Autoimmune Diabetes. *J. Immunol.* **194**, 3054–3064 (2015).
190. Katou, F. *et al.* *Am. J. Pathol.* **158**, 1263–70 (2001).
191. Gobert, M. *et al.* Regulatory T Cells Recruited through CCL22/CCR4 Are Selectively Activated in Lymphoid Infiltrates Surrounding Primary Breast Tumors and Lead to an Adverse Clinical Outcome. *Cancer Res.* **69**, 2000–2009 (2009).
192. Martinez, F. O., Helming, L. & Gordon, S. Alternative Activation of Macrophages: An Immunologic Functional Perspective. *Annu. Rev. Immunol.* **27**, 451–483 (2009).
193. Li, Y.-Q. *et al.* Tumor Secretion of CCL22 Activates Intratumoral Treg Infiltration and Is Independent Prognostic Predictor of Breast Cancer. *PLoS One* **8**, e76379 (2013).
194. Scheu, S., Ali, S., Ruland, C., Arolt, V. & Alferink, J. The C-C chemokines CCL17 and CCL22 and their receptor CCR4 in CNS autoimmunity. *Int. J. Mol. Sci.* **18**, (2017).
195. AL-Ayadhi, L. Y. & Mostafa, G. A. Elevated serum levels of macrophage-derived chemokine and thymus and activation-regulated chemokine in autistic children. *J. Neuroinflammation* **10**, 1 (2013).
196. Sells, R. E. & Hwang, S. T. Paradoxical Increase in Skin Inflammation in the Absence of CCR4. *J. Invest. Dermatol.* **130**, 2697–2699 (2010).
197. Power, C. A. *et al.* Molecular cloning and functional expression of a novel CC chemokine receptor cDNA from a human basophilic cell line. *J. Biol. Chem.* **270**, 19495–500 (1995).
198. Gilet, J. *et al.* Role of CCL17 in the Generation of Cutaneous Inflammatory Reactions in Hu-PBMC-SCID Mice Grafted with Human Skin. *J. Invest. Dermatol.* **129**, 879–890 (2009).
199. Watanabe, H. *et al.* Activation of the IL-1 β -Processing Inflammasome Is Involved in Contact Hypersensitivity. *J. Invest. Dermatol.* **127**, 1956–1963 (2007).
200. Murphy, J.-E., Robert, C. & Kupper, T. S. Interleukin-1 and Cutaneous Inflammation: A Crucial Link Between Innate and Acquired Immunity. *J. Invest. Dermatol.* **114**, 602–608 (2000).
201. Lee, R. T. *et al.* Mechanical deformation promotes secretion of IL-1 alpha and IL-1 receptor antagonist. *J. Immunol.* **159**, 5084–8 (1997).
202. Ono, S. & Kabashima, K. Novel insights into the role of immune cells in skin and inducible skin-associated lymphoid tissue (iSALT). *Allergo J. Int.* **24**, 170–179 (2015).
203. Stamatiades, E. G. *et al.* Immune Monitoring of Trans-endothelial Transport by Kidney-Resident Macrophages. *Cell* **166**, 991–1003 (2016).
204. Hansell, C. A. H., Hurson, C. E. & Nibbs, R. J. B. DARC and D6: silent partners in chemokine regulation? *Immunol. Cell Biol.* **89**, 197–206 (2011).
205. Nibbs, R. J. B. & Graham, G. J. Immune regulation by atypical chemokine receptors. *Nat. Rev. Immunol.* **13**, 815–829 (2013).
206. Pruenster, M. *et al.* The Duffy antigen receptor for chemokines transports chemokines and supports their promigratory activity. *Nat. Immunol.* **10**, 101–108 (2009).
207. Minten, C. *et al.* DARC shuttles inflammatory chemokines across the blood–brain barrier during autoimmune central nervous system inflammation. *Brain* **137**, 1454–1469 (2014).

208. Kashiwazaki, M. *et al.* A high endothelial venule-expressing promiscuous chemokine receptor DARC can bind inflammatory, but not lymphoid, chemokines and is dispensable for lymphocyte homing under physiological conditions. *Int. Immunol.* **15**, 1219–1227 (2003).
209. Gardner, L., Patterson, A. M., Ashton, B. A., Stone, M. A. & Middleton, J. The human Duffy antigen binds selected inflammatory but not homeostatic chemokines. *Biochem. Biophys. Res. Commun.* **321**, 306–312 (2004).
210. Peiper, S. C. *et al.* The Duffy antigen/receptor for chemokines (DARC) is expressed in endothelial cells of Duffy negative individuals who lack the erythrocyte receptor. *J. Exp. Med.* **181**, 1311–7 (1995).
211. Singh, M. D. *et al.* Elevated expression of the chemokine-scavenging receptor D6 is associated with impaired lesion development in psoriasis. *Am. J. Pathol.* **181**, 1158–64 (2012).
212. Jamieson, T. *et al.* The chemokine receptor D6 limits the inflammatory response in vivo. *Nat. Immunol.* **6**, 403–411 (2005).
213. Igyártó, B. Z. *et al.* Skin-resident murine dendritic cell subsets promote distinct and opposing antigen-specific T helper cell responses. *Immunity* **35**, 260–72 (2011).
214. Guilliams, M. *et al.* Skin-draining lymph nodes contain dermis-derived CD103⁻ dendritic cells that constitutively produce retinoic acid and induce Foxp3⁺ regulatory T cells. *Blood* **115**, 1958–1968 (2010).
215. Dorner, B. G. *et al.* Selective Expression of the Chemokine Receptor XCR1 on Cross-presenting Dendritic Cells Determines Cooperation with CD8⁺ T Cells. *Immunity* **31**, 823–833 (2009).
216. Guilliams, M. *et al.* From skin dendritic cells to a simplified classification of human and mouse dendritic cell subsets. *Eur. J. Immunol.* **40**, 2089–2094 (2010).
217. Ginhoux, F. *et al.* Blood-derived dermal langerin⁺ dendritic cells survey the skin in the steady state. *J. Exp. Med.* **204**, 3133–3146 (2007).
218. Poulin, L. F. *et al.* The dermis contains langerin⁺ dendritic cells that develop and function independently of epidermal Langerhans cells. *J. Exp. Med.* **204**, 3119–3131 (2007).
219. Pastore, S. *et al.* Granulocyte macrophage colony-stimulating factor is overproduced by keratinocytes in atopic dermatitis. Implications for sustained dendritic cell activation in the skin. *J. Clin. Invest.* **99**, 3009–3017 (1997).
220. Didovic, S., Opitz, F. V., Holzmann, B., Förster, I. & Weighardt, H. Requirement of MyD88 signaling in keratinocytes for Langerhans cell migration and initiation of atopic dermatitis-like symptoms in mice. *Eur. J. Immunol.* **46**, 981–992 (2016).
221. Jiang, X., Campbell, J. J. & Kupper, T. S. Embryonic trafficking of T cells to skin is dependent on E/P selectin ligands and CCR4. *Proc. Natl. Acad. Sci.* **107**, 7443–7448 (2010).
222. Jiang, X. *et al.* Dermal $\gamma\delta$ T Cells Do Not Freely Re-Circulate Out of Skin and Produce IL-17 to Promote Neutrophil Infiltration during Primary Contact Hypersensitivity. *PLoS One* **12**, e0169397 (2017).
223. Mueller, S. N., Gebhardt, T., Carbone, F. R. & Heath, W. R. Memory T Cell Subsets, Migration Patterns, and Tissue Residence. *Annu. Rev. Immunol.* **31**, 137–161 (2013).
224. Iellem, A. *et al.* Unique chemotactic response profile and specific expression of chemokine receptors CCR4 and CCR8 by CD4⁽⁺⁾CD25⁽⁺⁾ regulatory T cells. *J. Exp. Med.* **194**, 847–53 (2001).
225. Leandersson, K., Jaensson, E. & Ivars, F. T cells developing in fetal thymus of T-cell receptor α -chain transgenic mice colonize $\gamma\delta$ T-cell-specific epithelial niches but lack long-term reconstituting potential. *Immunology* **119**, 134–142 (2006).
226. Tigelaar, R. E., Lewis, J. M. & Bergstresser, P. R. TCR γ/δ ⁺ dendritic epidermal T cells as constituents of skin-associated lymphoid tissue. *J. Invest. Dermatol.* **94**, 58S–63S (1990).
227. Jin, Y. *et al.* Cutting edge: Intrinsic programming of thymic $\gamma\delta$ T cells for specific peripheral tissue

- localization. *J. Immunol.* **185**, 7156–60 (2010).
228. Jin, Y., Xia, M., Sun, A., Saylor, C. M. & Xiong, N. CCR10 Is Important for the Development of Skin-Specific T Cells by Regulating Their Migration and Location. *J. Immunol.* **185**, 5723–5731 (2010).
229. Nakamura, K. *et al.* Differential Requirement for CCR4 in the Maintenance but Not Establishment of the Invariant V γ 5+ Dendritic Epidermal T-Cell Pool. *PLoS One* **8**, e74019 (2013).
230. O'Brien, R. L. & Born, W. K. Dermal $\gamma\delta$ T cells--What have we learned? *Cell. Immunol.* **296**, 62–9 (2015).
231. Vrieling, M., Santema, W., Van Rhijn, I., Rutten, V. & Koets, A. T Cell Homing to Skin and Migration to Skin-Draining Lymph Nodes Is CCR7 Independent. *J. Immunol.* **188**, 578–584 (2012).
232. Gu, C.-Y., Gu, L. & Dou, X. Serum levels of thymus and activation-regulated chemokine can be used in the clinical evaluation of atopic dermatitis. *Int. J. Dermatol.* **54**, e261–e265 (2015).
233. Thijs, J. L. *et al.* A panel of biomarkers for disease severity in atopic dermatitis. *Clin. Exp. Allergy* **45**, 698–701 (2015).
234. Solari, R. & Pease, J. E. Targeting chemokine receptors in disease - A case study of CCR4. *Eur. J. Pharmacol.* **763**, 169–177 (2015).
235. Lenn, J. D. *et al.* RNA Aptamer Delivery through Intact Human Skin. *J. Invest. Dermatol.* **138**, 282–290 (2018).
236. Ishida, T. *et al.* Defucosylated Anti-CCR4 Monoclonal Antibody (KW-0761) for Relapsed Adult T-Cell Leukemia-Lymphoma: A Multicenter Phase II Study. *J. Clin. Oncol.* **30**, 837–842 (2012).
237. Chang, D.-K. *et al.* Humanization of an Anti-CCR4 Antibody That Kills Cutaneous T-Cell Lymphoma Cells and Abrogates Suppression by T-Regulatory Cells. *Mol. Cancer Ther.* **11**, 2451–2461 (2012).
238. Ishida, T. *et al.* Stevens-Johnson Syndrome associated with mogamulizumab treatment of adult T-cell leukemia / lymphoma. *Cancer Sci.* **104**, 647–650 (2013).
239. Viney, J. M. *et al.* Distinct Conformations of the Chemokine Receptor CCR4 with Implications for Its Targeting in Allergy. *J. Immunol.* **192**, 3419–3427 (2014).
240. Eby, J. M. *et al.* CCL22 to Activate Treg Migration and Suppress Depigmentation in Vitiligo. *J. Invest. Dermatol.* **135**, 1574–1580 (2015).
241. Xiong, N., Fu, Y., Hu, S., Xia, M. & Yang, J. CCR10 and its ligands in regulation of epithelial immunity and diseases. *Protein Cell* **3**, 571–580 (2012).
242. Chantry, D. *et al.* Macrophage-derived chemokine is localized to thymic medullary epithelial cells and is a chemoattractant for CD3(+), CD4(+), CD8(low) thymocytes. *Blood* **94**, 1890–8 (1999).
243. Bleul, C. C. & Boehm, T. Chemokines define distinct microenvironments in the developing thymus. *Eur. J. Immunol.* **30**, 3371–3379 (2000).
244. Lavin, Y., Mortha, A., Rahman, A. & Merad, M. Regulation of macrophage development and function in peripheral tissues. *Nat. Rev. Immunol.* **15**, 731–44 (2015).
245. Mortier, A., Gouwy, M., Van Damme, J., Proost, P. & Struyf, S. CD26/dipeptidylpeptidase IV-chemokine interactions: double-edged regulation of inflammation and tumor biology. *J. Leukoc. Biol.* **99**, 955–969 (2016).
246. Proost, P. *et al.* Truncation of macrophage-derived chemokine by CD26/ dipeptidyl-peptidase IV beyond its predicted cleavage site affects chemotactic activity and CC chemokine receptor 4 interaction. *J. Biol. Chem.* **274**, 3988–93 (1999).
247. Hristovska, I. & Pascual, O. Deciphering Resting Microglial Morphology and Process Motility from a Synaptic Prospect. *Front. Integr. Neurosci.* **9**, 73 (2015).

248. Riazi, K. *et al.* Microglial activation and TNF production mediate altered CNS excitability following peripheral inflammation. *Proc. Natl. Acad. Sci.* **105**, 17151–17156 (2008).
249. Hoogland, I. C. M., Houbolt, C., van Westerloo, D. J., van Gool, W. A. & van de Beek, D. Systemic inflammation and microglial activation: systematic review of animal experiments. *J. Neuroinflammation* **12**, 114 (2015).
250. Flynn, G., Maru, S., Loughlin, J., Romero, I. A. & Male, D. Regulation of chemokine receptor expression in human microglia and astrocytes. *J. Neuroimmunol.* **136**, 84–93 (2003).
251. Kim, K.-W. *et al.* In vivo structure/function and expression analysis of the CX3C chemokine fractalkine. *Blood* **118**, e156–e167 (2011).
252. Cardona, A. E. *et al.* Control of microglial neurotoxicity by the fractalkine receptor. *Nat. Neurosci.* **9**, 917–924 (2006).
253. Thion, M. S. *et al.* Microbiome Influences Prenatal and Adult Microglia in a Sex-Specific Manner. *Cell* **172**, 500–516.e16 (2018).
254. Erny, D. *et al.* Host microbiota constantly control maturation and function of microglia in the CNS. *Nat. Neurosci.* **18**, 965–977 (2015).
255. Haimon, Z. *et al.* Re-evaluating microglia expression profiles using RiboTag and cell isolation strategies. *Nat. Immunol.* **19**, 636–644 (2018).
256. Maruyama, T. *et al.* CCL17 and CCL22 chemokines within tumor microenvironment are related to infiltration of regulatory T cells in esophageal squamous cell carcinoma. *Dis. Esophagus* **23**, no-no (2010).
257. Chen, Z. *et al.* Lipopolysaccharide-Induced Microglial Activation and Neuroprotection against Experimental Brain Injury Is Independent of Hematogenous TLR4. *J. Neurosci.* **32**, 11706–11715 (2012).
258. Parajuli, B. *et al.* GM-CSF increases LPS-induced production of proinflammatory mediators via upregulation of TLR4 and CD14 in murine microglia. *J. Neuroinflammation* **9**, 268 (2012).
259. Pascual, O., Ben Achour, S., Rostaing, P., Triller, A. & Bessis, A. Microglia activation triggers astrocyte-mediated modulation of excitatory neurotransmission. *Proc. Natl. Acad. Sci. U. S. A.* **109**, E197–205 (2012).
260. Schäfers, M. & Sorkin, L. Effect of cytokines on neuronal excitability. *Neurosci. Lett.* **437**, 188–193 (2008).
261. Li, Y., Du, X., Liu, C., Wen, Z. & Du, J. Reciprocal Regulation between Resting Microglial Dynamics and Neuronal Activity In Vivo. *Dev. Cell* **23**, 1189–1202 (2012).
262. Panatier, A. & Robitaille, R. The Soothing Touch: Microglial Contact Influences Neuronal Excitability. *Dev. Cell* **23**, 1125–1126 (2012).
263. Ambrée, O. *et al.* Reduced locomotor activity and exploratory behavior in CC chemokine receptor 4 deficient mice. *Behav. Brain Res.* **314**, 87–95 (2016).
264. Osborn, O. *et al.* Ccl22/MDC, is a prostaglandin dependent pyrogen, acting in the anterior hypothalamus to induce hyperthermia via activation of brown adipose tissue. *Cytokine* **53**, 311–319 (2011).
265. Bashir, S. & Al-Ayadhi, L. Y. Effect of camel milk on thymus and activation-regulated chemokine in autistic children: Double-blind study. *Pediatr. Res.* **75**, 559–563 (2014).
266. Dantzer, R. Cytokine, Sickness Behaviour, and Depression. *Immunol. Allergy Clin. North Am.* **29**, 247–264 (2009).
267. Collier, R. J. Diphtheria toxin: mode of action and structure. *Bacteriol. Rev.* **39**, 54–85 (1975).
268. Vinante, F. & Rigo, A. Heparin-binding epidermal growth factor-like growth factor/diphtheria toxin receptor in normal and neoplastic hematopoiesis. *Toxins (Basel)* **5**, 1180–1201 (2013).
269. Mitamura, T., Higashiyama, S., Taniguchi, N., Klagsbrun, M. & Mekada, E. Diphtheria toxin binds to the

- epidermal growth factor (EGF)-like domain of human heparin-binding EGF-like growth factor/diphtheria toxin receptor and inhibits specifically its mitogenic activity. *J. Biol. Chem.* **270**, 1015–9 (1995).
270. Moehring, J. M. & Moehring, T. J. Comparison of diphtheria intoxication in human and nonhuman cell lines and their resistant variants. *Infect. Immun.* **13**, 221–8 (1976).
 271. Saito, M. *et al.* Diphtheria toxin receptor–mediated conditional and targeted cell ablation in transgenic mice. *Nat. Biotechnol.* **19**, 746–750 (2001).
 272. Kempermann, G., Song, H. & Gage, F. H. Neurogenesis in the Adult Hippocampus. *Cold Spring Harb. Perspect. Biol.* **7**, a018812 (2015).
 273. Spampinato, J. & Dudek, F. E. Targeted Interneuron Ablation in the Mouse Hippocampus Can Cause Spontaneous Recurrent Seizures. *eNeuro* **4**, (2017).
 274. Xu, X. *et al.* Obesity Activates a Program of Lysosomal-Dependent Lipid Metabolism in Adipose Tissue Macrophages Independently of Classic Activation. *Cell Metab.* **18**, 816–830 (2013).
 275. Davis, E. J., Foster, T. D. & Thomas, W. E. Cellular forms and functions of brain microglia. *Brain Res. Bull.* **34**, 73–8 (1994).
 276. Eyo, U. B., Murugan, M. & Wu, L. J. Microglia–Neuron Communication in Epilepsy. *Glia* **65**, 5–18 (2017).
 277. Biber, K., Neumann, H., Inoue, K. & Boddeke, H. W. G. M. Neuronal ‘On’ and ‘Off’ signals control microglia. *Trends Neurosci.* **30**, 596–602 (2007).
 278. Allen, N. J. & Eroglu, C. Cell Biology of Astrocyte–Synapse Interactions. *Neuron* **96**, 697–708 (2017).
 279. Anderson, M. A. *et al.* Astrocyte scar formation aids central nervous system axon regeneration. *Nature* **532**, 195–200 (2016).
 280. Drexel, M. *et al.* Selective Silencing of Hippocampal Parvalbumin Interneurons Induces Development of Recurrent Spontaneous Limbic Seizures in Mice. *J. Neurosci.* **37**, 8166–8179 (2017).
 281. Cho, C.-H. New mechanism for glutamate hypothesis in epilepsy. *Front. Cell. Neurosci.* **7**, 127 (2013).
 282. Dantzer, R. & Walker, A. K. Is there a role for glutamate-mediated excitotoxicity in inflammation-induced depression? *J. Neural Transm.* 925–932 (2014). doi:10.1007/s00702-014-1187-1
 283. Meldrum, B. S. Excitotoxicity and Selective Neuronal Loss in Epilepsy. *Brain Pathol.* **3**, 405–412 (1993).
 284. Blanco-Suárez, E., Caldwell, A. L. M. & Allen, N. J. Role of astrocyte–synapse interactions in CNS disorders. *J. Physiol.* **595**, 1903–1916 (2017).